Measuring Dental Implant Stability with the Advanced System for Implant Stability Testing (ASIST)

by

Chester Jar

A thesis submitted in partial fulfillment of the requirements for the degree of

Master of Science

Department of Mechanical Engineering
University of Alberta

Abstract

A clinical way to non-invasively assess dental implant stability is important for long-term success of the implant. Dental implants are typically screw shaped prosthetics which fuse with the surrounding jaw bone through a process known as osseointegration, where newly formed bone is deposited on the implant surface, forming a direct structural connection. Following sufficient healing, the implant is used to hold a dental restoration in place, which serves to replace the function and appearance associated with the missing tooth. The risk of implant failure is generally highest before any osseointegration has taken place, which has resulted in the development of various techniques to measure implant stability. Many of these techniques, developed over the last few decades, relate the stability of an implant to the stiffness of the bone-implant interface.

The Advanced System for Implant Stability Testing (ASIST) is a recently developed device that was shown to evaluate the stability of bone anchored hearing aid implants as well as natural teeth. The device couples an impact technique with an analytical model of the system, such that the measured signal can be correlated with the analytical response by determining the model parameters, including the interfacial stiffness, which minimizes the Euclidean norm between the model response and fitted data as quantified by an R^2 value. This stiffness is non-dimensionalized and reported as the ASIST Stability Coefficient (ASC). The current work presents the development of the ASIST towards dental implant systems. The device was evaluated using *in vitro* laboratory testing with polyurethane foam as an artificial bone substitute. A refined analytical model was also developed, which accounts for the different mechanical properties of the cortical and cancellous bone layers.

It was found that the ASIST was able to consistently estimate the interfacial stiffness on a given implant installation with various abutments and crowns. This provides evidence that the analytical model is able to account for the geometric and inertial properties of different system components, and that ASIST approach can isolate the stiffness of a given interface. Further tests were done to evaluate the correlations between the ASC and other methods of measuring stability. This includes the commercially available Osstell® device, in addition to the insertion torque (IT) and the force required to pull the implant out of its socket. The ASIST was able to detect differences in stability corresponding to changes in substrate properties and implant bonding. Additionally, the ASIST was found to have several advantages over the Osstell® device. Compared to the Osstell® device, the ASIST was shown to retain its sensitivity across a wider range of stability, and possessed a stronger correlation to the insertion torque and pullout force.

To better reflect the physiological structure of bone, the analytical model was then further refined to model the mechanical properties of the cortical and cancellous layers and used to evaluate the effects of cortical density and thickness on primary stability. The ASIST was then compared to the Osstell® in terms of their correlations to IT and pullout strength. Compared to the ISQ, the ASC showed stronger correlations with IT and pullout values. This implies that the analytical model is an accurate representation of the implant's mechanical stability, and can potentially be used to measure the stability of implants in a clinical setting.

This work shows that the ASIST device is mainly sensitive to changes in the interface conditions, and possesses several advantages over current measurement techniques. The ASIST shows promising preliminary results as a method of measuring dental implant stability. With further research into the device's performance with implant systems in real bone, the device could potentially provide clinicians with an improved non-invasive method of measuring the stability and health of dental implants over time.

Preface

This thesis is an original work by Chester Jar.

Portions of Chapter 3 were presented at the 2022 Annual Alberta Biomedical Conference:

Jar C, Archibald A, Gibson M, Westover L. (2022). Measuring dental implant stability with the Advanced System for Implant Stability Testing (ASIST). *23rd Annual Alberta Biomedical Engineering Conference*, Banff, Canada, October 21 – 22, 2023 (Podium).

Acknowledgements

In writing this thesis, I would like to acknowledge and thank the following people:

Dr. Lindsey Westover for giving me the opportunity to volunteer in your research before becoming my MSc supervisor. Thank you for guiding me throughout my degree and for the honour of working with you.

Dr. Samer Adeeb for giving me support ever since I worked with you in the summer of 2017. Thank you for introducing me to Dr. Westover and for being a career mentor since my days as an undergraduate student.

My fellow graduate students and lab members: Thank you Tod, Eric, Mostafa, Maha, Nada, Robert, Mostafa and Cass, for making my degree so enjoyable. It has been a privilege with work alongside you.

To Jessica, for being supportive and encouraging of my studies. Thank you for listening to me (even if what I say doesn't make sense sometimes).

Lastly, and most of all, to my mother and father. Thank you for supporting me, and I hope you are both proud of my work.

Table of Contents

List of Tables

List of Figures

Chapter 1 : Introduction

1.1 Background

Dental restorations, such as a single crown or dental arch, provide functional and aesthetic improvements for patients with missing teeth. These restorations are supported by dental implants, which are typically titanium screw shaped fixtures that are surgically inserted into the bone of the maxilla or mandible. The implant acts as a support and attachment point for an abutment, which acts as a connection piece onto which the dental restoration is placed. The type of implant used vary according to its location in the mouth and the type of tooth being replaced.

Implants undergo osseointegration, a biological process in which bone reformation occurs around the implant and results in a structural integration of the implant with the bone (Brånemark et al., 1985). Osseointegration is a result of the healing and formation of bone surrounding the fixture, followed by natural remodelling of bone due to mechanical stimuli in the form of occlusal forces (Jayesh & Dhinakarsamy, 2015). Integration is not guaranteed but is promoted through biocompatible implant materials (such as titanium) and factors related to the surgical placement of the implant, related to its placement and damage to the surrounding bone. Moreover, it is important that the implant is not subject to significant loads or forces before it is adequately secured in the bone (Brånemark et al., 1985).

Long term success of dental implants is largely dependent on the extent and quality of osseointegration at the bone-implant interface. Successful outcomes involve the absence of clinically detectable implant mobility and pain when subject to forces such as mastication (Zix & Hug, 2008). Unsuccessful outcomes are also attributed to patient-relevant factors including underlying bone quality. For example, dental implant failure rates generally fall around 2 – 6% (Beschnidt et al., 2018; Brånemark et al., 1985; Yang et al., 2021), while orbital implants (ie. around the eye) have failure rates of up to 47% (Roumanas et al., 2002), with even higher rates in irradiated bone (Ganström, 2005).

A common cause of implant failure is loosening due to crown placement and functional loading before being properly integrated (Esposito et al., 1998), with the majority of implant failures occurring in the early stages (Staedt et al., 2020; Yang et al., 2021). Guidelines on required times between implant placement and loading exist, ranging from 1 week to more than 2 months following implant placement (Donos et al., 2021). The relatively larger occurrence of early implant failures and uncertainty in loading time implies that a definitive threshold to begin functional loading of the implant has yet to be determined (Yang et al., 2021). Therefore, monitoring the progression of the implant during healing is important to identify areas at risk of failure.

It is generally accepted that the stability of an implant is largely dependent on its osseointegration, and is related to changes in the stiffness of the bone-implant interface (Atsumi et al., 2007; Swain et al., 2008b). In this context, stiffness is denoted as the mechanical stiffness of a material, which determines the amount of deformation under a corresponding external force, while implant stability refers to the absence of any detectable clinical mobility. Materials with a higher stiffness subsequently deform less than less stiff materials when subjected to the same load. As a result, a stiffer interface provides greater stability by restricting the implant's mobility in the bone under loading. The effective interfacial stiffness is due to several factors, including osseointegration, and the properties of the surrounding bone. Interface stiffness and stability are interchangeable in the context of this work – a stiff interface will deform less, resulting in decreased movement of the implant and therefore increased stability.

The work presented in this thesis aims to develop and validate an approach to non-invasively measure stability by relating the dynamic behaviour of the implant system to its surrounding mechanical properties.

The Advanced System for Implant Stability Testing (ASIST) was developed as a non-invasive method to measure the stability of percutaneous implants through vibrational analysis. By applying a percussive strike to the implant system, the vibrational response is recorded and used to estimate the mechanical stiffness of the bone-implant interface. The interface stiffness is determined by analysing the experimentally measured response and approximating the implant system with an analytical model, giving a corresponding estimate of stability. This allows the ASIST to detect relative changes in stiffness and monitor implant stability over time. The ASIST was previously utilized to detect longitudinal stability for bone anchored hearing aid (BAHA) implants (Westover et al., 2018b), and to estimate the stiffness of the periodontal ligament during orthodontic alignment and cuspid retraction (Westover et al., 2016b). This work therefore aims to evaluate the applicability of the ASIST for measuring the stability of dental implants.

1.2 Research Objectives and Specific Aims

The objective of this research is the development and experimental validation of the ASIST as a device for the non-invasive measurement of dental implant stability. To address the weaknesses in currently used methods, the ASIST should meet the established specific aims (SA).

SA #1:

A dental implant system analytical model must be developed. With the analytical model, the ASIST should also be able to properly isolate the interfacial stiffness, as the analytical model accounts for the specific properties of the implant and abutment. As a result, the ASC score for a specific implant installation should be essentially independent of the attached abutment and yield consistent ASC measurements.

SA #2:

The ASIST should be able to measure and differentiate between different stages of stability. This translates to detecting changes in the interfacial properties, which includes bonding between the implant and substrate and factors pertaining to the osteotomy.

SA #3:

The final objective of this work is to compare the ASC to current methods of measuring stability. Clinically, the initial stability of a newly placed implant is assessed by the insertion torque, and the Osstell® ISQ is subsequently used to monitor the implant's progression. Additionally, destructive mechanical testing has been used to characterize the interfacial properties in studies performed *ex-vivo* or *in-vitro*. This serves to, in part, validate the ASIST and its clinical feasibility, if the ASC is strongly correlated to current methods used by both clinicians and researchers.

1.3 Literature Review

This section presents a literature review to establish background information on clinical factors relevant to dental implants. An overview of various methods of evaluating implant stability established in research is also presented to gain an overall understanding of the techniques and developments for assessing these methods.

1.3.1 Bone and Osseointegration

Bone is a connective tissue whose matrix consists of inorganic and organic components. The inorganic component comprises approximately 60% of the matrix, mainly consisting of hydroxyapatite crystals made from calcium and phosphate, while the organic component, consisting of proteins, cells, and water, contributes the remaining 40% (Feng, 2009). Bone is constantly remodelled in response to external mechanical stresses, which occurs via osteoclast and osteoblast activity (Florencio-Silva et al., 2015). Osteoblasts are responsible for the formation of new bone by synthesizing and releasing osteoid, the proteins and organic components of bone matrix. This activity stimulates the deposition of calcium salts onto released osteoid, followed by its crystallization, resulting in the formation of new bone matrix (Florencio-Silva et al., 2015). Osteoclasts resorb bone through enzyme secretion, which results in the dissolution of bone and subsequent release of calcium into the bloodstream. Released calcium from osteoclast activity is used by osteoblasts to form new bone matrix to accommodate mechanical stresses (Feng, 2009).

Bone quality is a key consideration in planning clinical procedures such as implant installation, as bone strength is positively related to its density and increases the initial retention of newly placed implants before osseointegration has taken place (Chugh et al., 2013). While different categorizations of bone quality exist, Table 1.1 outlines a typical schematic that focuses on the bone density (Lekholm & Zarb, 1985). Implant placement and loading vary for each type, depending on the bone condition prior to surgery and immediate implant placement and loading is often prescribed for exceptionally strong bones (Type 1). A decrease in the bone-implant contact area is observed for lower density bone, which increases the overall stress transferred to the bone and risk of implant failure (Chugh et al., 2013).

Table 1.1: Bone classification system by Lekholm and Zarb (1985).

Bone Type	Description
Type 1	Hard, dense bone; homogeneous cortical bone
Type 2	Thick layer of cortical bone surrounding a dense cancellous core
Type 3	Thin layer of cortical bone surrounding a dense cancellous core
Type 4	Weak bone; thin cortical layer surrounding a low-density cancellous core

Successful treatments using dental implants rely on proper osseointegration of the implant into the living bone. Insufficient osseointegration leads to implant failure due to loosening of the implant in its bed and has significant clinical importance. Osseointegration occurs when bone growth occurs directly onto the implant surface, effectively fusing the implant to the living bone (Brånemark et al., 1985; LeGeros & Craig, 1993). Developments in clinical practice and implant design aim to maximize the chance of successful integration (LeGeros & Craig, 1993).

Implant surface chemistry affects the deposition and formation of new bone on the implant surface (LeGeros & Craig, 1993). Titanium is a widely used material in dental and orthopedic applications, due to its high corrosion resistance, biocompatibility and osseointegration capabilities. As a bioinert material, titanium does not induce a physiological reaction when introduced to biological tissue and is therefore suitable for medical purposes. Additionally, osseointegration is promoted for designs that increase bone-implant contact and interlocking of the implant through bone ingrowth (Elsayed, 2019; LeGeros & Craig, 1993). As a result, threaded implants with moderately rough surfaces are widely used due to the increase in surface contact and initial mechanical stability (Berglundh et al., 2003).

1.3.2 Dental Procedures and Outcomes

As previously described, several protocols for single tooth implant placement and loading exist for different types of bone. Conventional protocols consist of a two-stage procedure, where the implant placement occurs during the initial surgery and is followed by a healing period (typically 2 – 6 months) to allow for successful osseointegration. After sufficient healing, a second surgery is performed to open the surrounding soft tissue and expose the implant, in order to place a healing abutment (Gupta et al., 2022). This healing abutment is screwed into the implant and used to shape the contour of the gingiva in the absence of occlusal forces, preventing any accumulation of debris in the implant socket. The healing abutment is eventually replaced by a prosthetic final abutment, onto which the replacement crown is placed. In dentistry, a crown refers to the dental restoration that is used to replace the missing tooth, and is typically made from porcelain, ceramic, or metals such as zirconium oxide. The prosthetic abutment is typically screwed into the implant similar to the healing abutment, while the crown is bonded to the abutment with dental cement.

The anatomy of the mouth is shown in Figure 1.1. The upper and lower jaws are known as the maxilla and mandible, respectively. The mouth is symmetric about the mid-sagittal plane, such that each side of the mouth contains the same number of teeth in the same position. The incisors and canines are classified as anterior teeth, while the premolars and molars are mainly located in the posterior region (Yang et al., 2021).

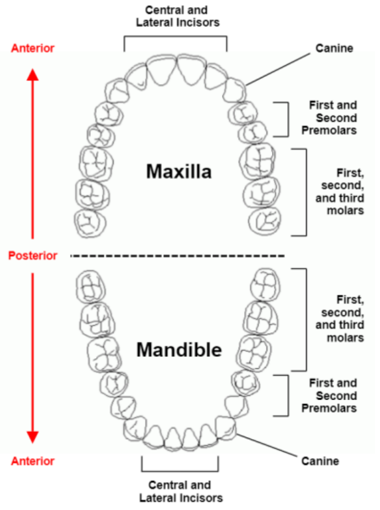

Figure 1.1: Anatomy of the human mouth. Adapted from *What tooth number is this tooth?,* 2011, Specialized Dentistry of New Jersey. https://buildinggreatsmiles.com/blog/what-tooth-number-is-this-tooth/

Apart from sufficient healing time, the success rates of single tooth dental restorations vary depending on the location, which determines the type of tooth, quality of bone, and occlusal forces experienced. For example, the restorations located in the posterior mandible can have a different survival rate than the posterior maxilla and the anterior mandible. Retrospective studies and systematic reviews have found a higher number of occurrences of implant failure in the anterior region and the maxilla. A study by Yang et al. found that molars had the highest survival rate of 97.67%, while anterior teeth had the lowest survival rate of 93.33% (Yang et al., 2021). Hawthan et al. also found higher long-term failure rates for implants placed in the anterior region, citing the common occurrence of misalignment between applied loads and the tooth's long axis (Hawthan et al., 2022).

1.3.3 Dental Implant Stability

Implant stability is strongly correlated to time after surgery and corresponds to changes in stiffness due to the remodelling and formation of surrounding bone (Hiranmayi, 2018). Clinically, implant stability has been defined in two stages: primary and secondary stability, which correspond to the implant before and after osseointegration has taken place (Atsumi et al., 2007; Swami et al., 2016). Primary stability is lost during the following weeks after surgery as the original surrounding bone is resorbed during the bone remodeling process. The onset of osseointegration is indicated by the deposition of new bone onto the implant surface, from which secondary stability begins to develop and increase over the following months.

1.3.3.1 Primary Stability

Primary stability is determined by the mechanical engagement between the bone and implant threads. As there is no developed biological structural connection with the bone during implant placement, stability is initially reliant on the frictional resistance between the two surfaces, bone-implant contact area, and the mechanical properties of the surrounding bone. Therefore, bone quality, implant design, and surgical technique are factors of primary stability (Blume et al., 2021; da Costa Valente et al., 2019; Swami et al., 2016). Insertion torque (IT) is the maximum torque required to seat the implant into its final position in the bone and is a common indicator of primary stability, as it reflects the bone's resistance during placement (Friberg et al., 1999). Recommended IT values range from 20 Ncm to 42 Ncm to prevent implant micromotion during healing (Bedrossian, 2020).

As previously defined, bone quality is determined by its density and cortical bone thickness, and is a main determinant of primary stability (Blume et al., 2021). Cortical bone possesses higher degrees of bone mineralization and bone resistance compared to cancellous bone (Miyamoto et al., 2005). This results in reduced implant micromotion and bone strain, the latter of which is predominantly compressive (Sugiura et al., 2016). During insertion, cortical bone exhibits a strengthening effect to cancellous bone due to its higher mechanical properties, by increasing compression at the implant apex and improving the distribution of occlusal forces (Blume et al., 2021; Chávarri-Prado et al., 2020). This increases the interfacial contact pressure, which improves the anchorage of the implant (Yang et al., 2022). As a result, a positive correlation has been found between the cortical bone thickness and IT (Hong et al., 2012; Wang et al., 2015). Additionally, significantly higher rates of failure for implants placed in the maxilla compared to the mandible (Esposito et al., 1998) have been attributed to the maxilla possessing a lower cortical bone thickness and bone density relative to the mandible (Tanaka et al., 2018).

Another consideration for primary stability is the implant design. Increasing implant diameter can increase the bone-implant contact area and help maintain stability by reducing the stresses at the implant face (Farré-Pagés et al., 2011). Compared to straight-walled cylindrical implants, tapered implants attain greater primary stability than cylindrical implants, as they provide lateral compression of the cortical bone and distribute occlusal forces at a greater degree (Blume et al., 2021). Although implant length affects the bone-implant contact area, its effect on stability is less significant compared to other factors such as implant diameter and geometry (Bedrossian, 2020).

Primary stability is also dependent on factors surrounding surgical preparation and procedures. Various surgical guidelines have been proposed to increase primary stability, especially in compromised bone quality (Blume et al., 2021). Undersized drilling is used to prepare a site lower in diameter than the implant itself. This press-fit between the bone and implant allows for higher levels of insertion torque to be reached (Jimbo et al., 2014). Clinicians must also exercise caution, as mechanical and thermal induced trauma to the osteotomy site can cause bone necrosis and implant failure.

1.3.3.2 Secondary Stability

Secondary stability is developed by osseointegration, where bone deposition on the implant's surface creates a direct structural connection and determines the long-term success of the implant. Compared to primary stability, secondary stability is mainly dependent on the quality of the bone-implant interface. Adequate primary stability is an important precursor to osseointegration, as excessive micromotion can prevent osseointegration and result in the formation of fibrous scar tissue and cancellous bone hypertrophy (Hiranmayi, 2018; Stefano et al., 2021). In this regard, bone quality plays an important role as higher densities correspond to higher primary stability, increasing the likelihood of successful osseointegration. Implant diameter and length also increase secondary stability, albeit to a lesser extent, due to an increase in the area of the osseointegrated surface (Veltri et al., 2014). Cortical bone thickness may also weakly affect secondary stability (Tanaka et al., 2018), but has not been studied in depth in literature (Stefano et al., 2021).

1.3.4 Measuring Implant Stability

Assessing implant stability after installation requires information that indicates the condition of the bone-implant. Several destructive and non-destructive techniques to measure stability exist, listed in Table 1.2.

Table 1.2: Implant stability measurement techniques

Destructive	Non-destructive
Histology	Radiography
Reverse Torque	Computed Tomography Scanning
Pull-Out Testing	Cutting Torque Resistance
Push-Out Testing	Osstell®
	Periotest®

1.3.4.1 Destructive Methods

Histologic analysis determines the amount of surrounding bone and bone-implant contact by removing a section of bone containing the implant and applying a dye (Swami et al., 2016). Reverse torque tests apply an unscrewing torque and characterizes the interfacial stiffness by measuring the amount of torque required for implant removal. The implant is considered stable for torques greater than 20 Ncm (Swami et al., 2016), and reverse torque tests have been used to investigate factors affecting the healing capabilities at the bone-implant interface (Rittel et al., 2017).

Pull-out and push-out tests apply a tensile or compressive load, respectively, parallel to the interface and record the maximum load applied before the implant is dislodged, measuring the interfacial shear strength (Swami et al., 2016). Pull-out tests measure the shear strength of the interfacial bone, while push-out tests measure both the interfacial shear strength and compressive strength of the bone at the implant's apex (Rittel et al., 2017). The pull-out test is more commonly used, as it is more difficult to separately model the compressive and shear properties in push-out tests (Seong et al., 2013). Although axial tensile loads do not normally occur *in-vivo*, the pullout test can still provide insight into the biomechanical properties of the bone-implant interface. While pull-out tests are more suited towards cylindrical non-threaded implants due to their sole dependence on interfacial shear strength for stability, it is recommended by ASTM F543-07 as the standard method to simulate the axial removal of a screw from bone (Rittel et al., 2017).

Due to the destructive nature of these methods they are not clinically feasible for long-term stability monitoring, but are used in nonclinical research to characterize and indicate changes in the interfacial mechanical properties.

1.3.4.2. Non-Destructive Methods

Radiographic analysis and computed tomography (CT) scans are imaging techniques that can be performed at any point to assess the health of the implant in surrounding bone. Radiographs provide qualitative changes in surrounding bone, such as apical bone loss occurring during osseointegration (Salvi & Lang, 2004; Swami et al., 2016). With radiographs however, bone quality and density are not quantifiable, and changes in bone mineral density cannot be detected via this method until 40% of demineralization occurs (Wyatt & Pharoah, 1998). CT scans provide more comprehensive information regarding bone structure than radiographs, but the cost, increased exposure to radiation, and inability to properly image the interfacial region also make it unsuitable for frequent long-term usage (Swami et al., 2016).

Cutting torque resistance analysis measures the energy required by an electric motor to remove a unit volume of bone during implant placement surgery to quantify bone hardness and density (Swami et al., 2016). However, as this technique can only be used during implant surgery, it is not viable for long-term use. As previously mentioned, IT values are used by clinicians as an indicator of the implant's stability at the time of placement. While IT is a strong indicator of primary stability, it is limited to a single measurement at insertion and appears to have no predictive power in predicting the development of secondary stability (Al-Nawas et al., 2006; Cassetta et al., 2022).

Other methods attempt to estimate the degree of osseointegration at the interface by correlating implant stability to the interfacial stiffness and are currently used by clinicians to assess the progressive changes in implant health. Resonance frequency analysis (RFA) and the impact technique are two methods that have been widely used in a research and clinical setting.

RFA was developed based on the fact that the resonance frequency of the bone-implant system is related to the interfacial stiffness (Friberg et al., 1999; Meredith et al., 1997a; Meredith et al., 1997b). For a specific implant system, changes in resonance frequency are indicative of changes in the interface stiffness, which can monitor the progression of osseointegration. The technique consists of attaching a transducer to an implant fixture or abutment and analyzing the first resonance frequency of the system (Figure 1.2), which is dependent on the transducer's design, the stiffness of the fixture and bone-implant interface, and the total effective length above bone level (Sennerby & Meredith, 2008). By exciting the transducer, a bending force is applied to the system and the displacement is measured, providing an estimation of the resonance frequency.

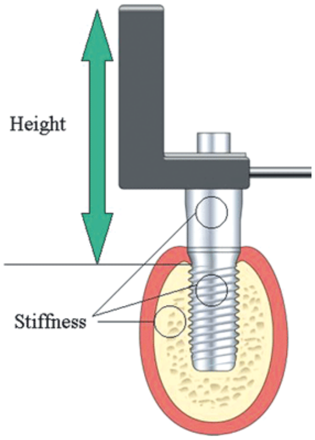

Figure 1.2: Schematic illustrating the concept and set-up for RFA (Sennerby and Meredith, 2008).

The Osstell® (Osstell, Göteborg, Sweden) is a wireless commercial device based on RFA (Sennerby & Meredith, 2008). Stability is indicated with an implant stability quotient (ISQ), ranging from 0 to 100, with larger ISQ values corresponding to greater stability. The device uses a SmartPeg™ as the transducer, which is a metal rod that is screwed into the implant and magnetically excited, causing it to vibrate in two perpendicular directions. Two ISQ values are subsequently obtained, corresponding to the direction of maximum and minimum stability (Swami et al., 2016). The Osstell® has been used as a stability measurement device for dental implants in both clinical (Andersson et al., 2019; Bischof et al., 2004; Farré-Pagés et al., 2011; Turkyilmaz & McGlumphy, 2008; Tanaka et al., 2018; Zix & Hug, 2008) and nonclinical research (Feng et al., 2014; Veltri et al., 2014; Wang et al., 2010; Winter et al., 2010). It has been shown that ISQ values for stable implants tend to increase over time, where implants with low ISQ values pose a significantly greater risk of failing (Salvi & Lang, 2004; Sennerby & Meredith, 2008). However, there lacks a guideline ISQ below which would prompt clinical intervention (Veltri et al., 2014). For example, at the time of implant placement, Turkyilmaz and McGlumphy reported mean ISQ values of around 60 for successful implants (Turkyilmaz & McGlumphy, 2008). However, it was also shown that differences between successful and failed implants were only significant when using a threshold ISQ value of 70 or 75 at the time of implant placement (Andersson et al., 2019).

A major limitation of the Osstell® is that the SmartPeg™ must be directly attached to the implant or abutment. As a result, each type of implant or abutment requires a specific compatible SmartPeg™, and measurements cannot be taken after a prosthetic tooth is installed unless the crown itself is removable. This makes its long-term clinical use difficult or impossible in the case of cemented teeth. Additionally, there is currently uncertainty regarding which parameters affect ISQ values. For example, ISQ values were reported to be significantly higher in the mandible compared to the maxilla (Bischof et al., 2004; Karl et al., 2008). The effect of implant length was found to be significant at placement and after healing in the anterior mandible, but was only significant after healing in the posterior mandible (Karl et al., 2008). Another disadvantage of the Osstell® is that it does not account for the components of the implant system when interpreting resonance frequency. ISQ values appear to be influenced by bone quality and geometry (Bischof et al., 2004; Karl et al., 2008; Liu et al., 2021) but have no statistically significant correlation with marginal bone level (Liu et al., 2021). Moreover, the resonance frequencies of a system do not linearly vary with stiffness. For example, a numerical study conducted by Liu et al. found a diminished change in resonance frequency with increased bonding strength between the implant and bone (Liu et al., 2021). A similar conclusion was also drawn in a separate numerical study by Winter et al. (Winter et al., 2010). This implies that resonance frequencies are not entirely reflective of the interface stiffness and can vary across different patients. Consequently, only patient-specific ISQ trends are meaningful, as a universal threshold ISQ value has not been established.

The Periotest® (Medizintechnik Gulden, Modautal, Germany) is another commercial system that measures stability through impact testing. While originally intended to measure the damping characteristics of the periodontal ligament to assess the mobility (and hence stability) of natural teeth, its use has been extended to endosseous implant systems (Swami et al., 2016). It is a handheld device which uses an electro-magnetically driven and electronically controlled metal rod to impact the system, after which the acceleration experienced by the rod is recorded by a built-in accelerometer and filtered (Figure 1.3). The contact time is obtained by approximating the accelerometer output as a half cycle at the fundamental frequency of the system vibration, and is defined as the duration of contact between the rod and system.

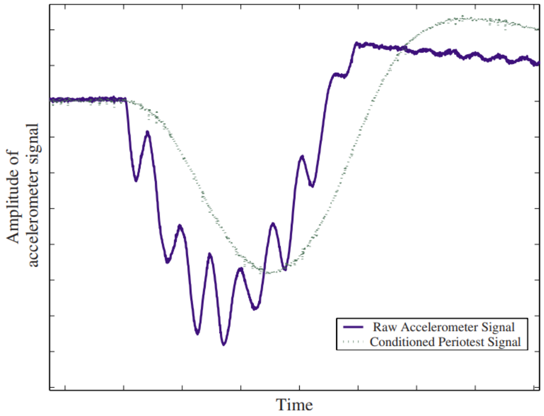

Figure 1.3: Raw and filtered accelerometer output for the Periotest® (Swain et al., 2008a).

Analogous to the ISQ for the Osstell®, the Periotest® provides a Periotest value (PTV) that is calculated based on the contact time (Lukas & Schulte, 1990). The PTV ranges from –8 to +50, with lower values corresponding to higher degrees of stability.

$$\mathrm{PTV} = \begin{cases} \dfrac{(\text{Contact Time})}{2 \times 10^{-5}\ \mathrm{s}} - 21.3 & \mathrm{PTV} < 13 \\ 10\sqrt{\left(\dfrac{CT}{6 \times 10^{-5}\ \mathrm{s}} - 8.493\right)} - 4.17 & \mathrm{PTV} > 13 \end{cases}$$

The advantages of the Periotest® are its simplicity, that it does not need to be attached to the implant system, and that it can be used for any implant system. Similar to the Osstell® however, the Periotest® does not account for differences in implant system components. As shown in Figure 1.3, there are significant differences between the raw and filtered acceleration response. A prominent second high frequency component of the raw signal is removed, resulting in the loss of additional information regarding the system response and distortion of the contact time (Swain et al., 2008a). Different PTVs have been found for different implant locations, bone densities, bone geometries, implant lengths, and abutment lengths (Salvi & Lang, 2004). Since it is a handheld device, the PTV can also be affected by operator variables such as handpiece angle, impact location, and distance between the handpiece and implant system (Zix & Hug, 2008). Since the implant system is unaccounted for, the accuracy of the Periotest® is affected by many confounding variables that could lead to incorrect clinical interpretations.

The AnyCheck® is another impact-based measurement device that measures implant stability based on the contact time (Lee et al., 2020). However, there is limited research on the device's performance (Okuhama et al., 2022; Pyo et al., 2021)

1.3.5 Modelling of Implant Systems

1.3.5.1 Experimental Models

Different approaches in modelling have been adopted due to the cost and relative difficulty of studying stability in human bone. Both synthetic and animal bones are mainly used in mechanical tests to characterize implant stability. Polyurethane foam has been a popular substitute for human bone due to its similar mechanical properties in accordance to ASTM F-1839-08 (ASTM, 2021), and because it is widely available and easier to work with than biological bone. Studies have used different densities of foam as an artificial counterpart to different bone classifications (da Costa Valente et al., 2019; Tumedei et al., 2021). Implant models using polyurethane foam have been used to identify relevant parameters for primary stability (Oliscovicz et al., 2013) and secondary stability (Wang & Lynch, 2017). Bone has also been simulated using cured epoxy resin (Feng et al., 2014; Veltri et al., 2014).

Artificial models simulate osseointegration by bonding the implant to bone using adhesives or embedding the implant in cured resin. Common bonding agents include superglue (Westover et al., 2016a) and various resins (Feng et al., 2014; Veltri et al., 2014; Vien et al., 2019; Westover et al., 2016a). With this approach, a specific adhesive corresponds to the same osseointegration state in terms of interfacial properties. This allows multiple replicates to be made, but limits the number of osseointegration states. As a result, multiple adhesives have been used to model different stages of osseointegration (Feng et al., 2014; Westover et al., 2016a).

Alternatively, studies have used animal models to account for different morphologies in cortical and cancellous bone. Porcine bone is a common choice due to its similar composition, density and size to the human jawbone (Blanc-Sylvestre et al., 2021) and have been used as an implant substrate (Erdogan et al., 2013; Oliscovicz et al., 2013). The use of samples obtained from smaller animals such as rabbits have also been documented (Seong et al., 2013). However, due to the size disparity in the maxillofacial region, bones must be harvested from the extremities (ie. tibia or femur), and porcine models have been deemed as a more suitable animal model for dental implant studies. With animal models, implants are allowed to integrate *in-vivo* before the animal is sacrificed for harvesting (Erdogan et al., 2013; Seong et al., 2013). This allows different osseointegration states to be analyzed by extracting samples at different time points.

1.3.5.2. Computer Models

Computer modelling is mainly used for dynamic analysis, stress analysis, and RFA (Alaqeely et al., 2020; Liu et al., 2021; Rittel et al., 2017). Several approaches for modelling the material properties of human bone are documented in numerical studies. The most commonly used approach assigns homogeneous material properties to distinct regions corresponding to cortical and cancellous bone (Rittel et al., 2017; Sugiura et al., 2016). To account for osseointegration, several methods have been developed to mimic the mechanical behaviour and functionality of the interfacial layer. The most common approach models the interface as a thin uniform layer between the implant and bone and varying its elastic modulus between zero (no integration) and that of the surrounding bone (fully integrated) to represent different degrees of osseointegration (Liu et al., 2021; Wang et al., 2010; Winter et al., 2010). Another approach uses the contact condition at the bone-implant interface to model different stages of osseointegration (Mohamed & Westover, 2022; Yang & Xiang, 2007).

1.3.5.3. Analytical Models

Relatively fewer analytical models of dental implants have been proposed. From a mechanical viewpoint, the process of osseointegration has been described by a progressive change in the modal frequencies of the implant system (Wang et al., 2010; Zanetti et al., 2018). As described by Zanetti et al., the development of the bone-implant interface can be viewed as a set of linear springs, corresponding to newly formed interfacial bone in series with either the surrounding mature cortical and cancellous bone (Zanetti et al., 2018). As shown in Figure 1.4, the interfacial bone stiffness k_1, k_2 gradually increases to that of the surrounding bone, such that $k_1 = k_{cortical}$ and $k_2 = k_{cancellouslar}$ for a fully integrated implant.

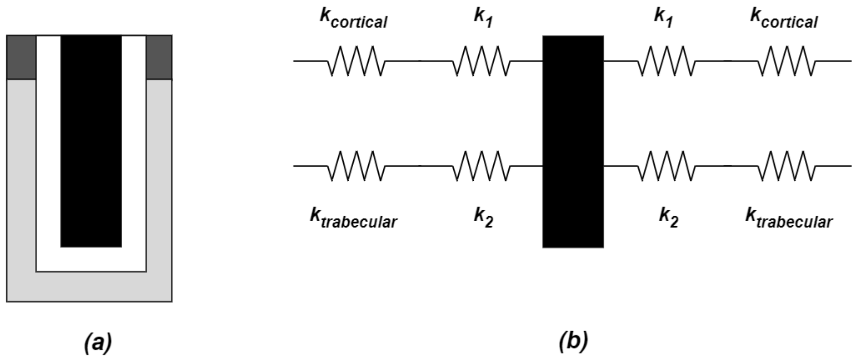

Figure 1.4: (a): Physical model of the implant system consisting of the implant (black), interfacial bone (white), cortical bone (dark gray), and cancellous bone (light gray). (b): Corresponding mechanical model of the system by modelling each bone type as a linear spring with a distinct corresponding stiffness (Zanetti et al., 2018).

The increased prevalence of dental implants has resulted in the development of different methods of monitoring implant stability over time. Out of all the methods described in the sections above, RFA has seen the most success in its implementation in clinical settings as a non-invasive technique due to its simplicity. However, its inherent weaknesses have resulted in contradictory conclusions by researchers, limiting its applicability. To address these weaknesses, the Advanced System for Implant Stability Testing (ASIST) was developed as a device which couples the impact technique used by the PerioTest® with an analytical four degree of freedom vibration model of the implant system. In contrast with the PerioTest®, the ASIST uses the raw, unfiltered acceleration signal measured during impact. By estimating the inertial properties of the system, the signal can be matched to a predicted dynamic response and used to estimate the mechanical stiffness of the bone-implant interface. The ASIST has been previously developed for BAHA implants with promising results in a clinical and research environment. The goal of this research is to use a similar approach for dental implants, with differences in system components and geometries. This requires the development of a dental implant analytical model and investigation of the device's ability to measure and differentiate different levels of stability.

1.4 Thesis Outline

This thesis details the development of the Advanced System for Implant Stability Testing (ASIST), which is a device aimed to measure the stability of dental implants. The ASIST couples an impact technique with an analytical model to estimate the stiffness of the bone-implant interface.

Chapter 1 introduces a background of dental implants and a review of surrounding literature, to establish the clinical significance and current challenges to monitoring implant stability.

Chapter 2 presents the methodology of the ASIST to extract the interfacial stiffness from a measured signal. This includes the details of the analytical model, curve fitting process, and estimation of model parameters.

Chapter 3 evaluates the analytical model and its ability to isolate the interface stiffness.

Chapter 4 compares the ASIST to the Osstell® device and investigates the correlation of both devices with other indicators of stability.

Chapter 5 presents the development and experimental evaluation of a refined analytical model incorporating cortical and cancellous bone, to better reflect the anatomic structure of bone.

Chapter 6 evaluates the refined analytical model by evaluating the effects of the density and thickness of the cortical layer on implant stability. Additionally, the ASIST device is compared with other indicators of stability when a cortical layer is introduced.

Chapter 7 presents a validation of the refined analytical model.

Chapter 8 analyzes the sensitivity of both analytical models with respect to stiffness parameters.

Chapter 9 concludes the thesis and discusses areas of future research.

Chapter 2 : ASIST for Dental Implant Stability

This section describes the ASIST device and how the device estimates stability by measuring the effective stiffness of the interface and its surroundings. The approach is similar to previous work on BAHA implants. However, this chapter describes the development of a new analytical model adapted towards dental implants.

2.1 Overview

The ASIST expands upon the impact technique of the Periotest® and was introduced for BAHA systems (Westover et al., 2016b). The device is operated using an ASIST control unit, handpiece, and computer (Figure 2.1).

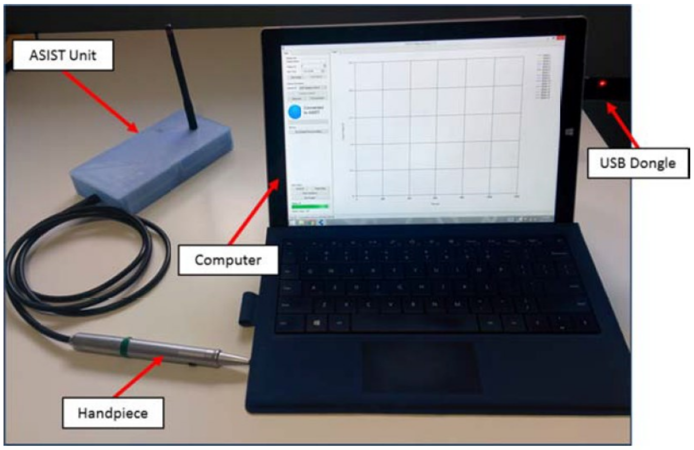

Figure 2.1: ASIST components required for operation (Westover, 2016).

The ASIST design is based upon the Periotest® Classic handpiece (Medizintechnik Gulden, Modautal, Germany), which houses an accelerometer and stainless-steel impact rod (2 mm diameter). The activation button on the handpiece's side propels the impact rod forward through electromagnetic excitation, striking the implant system (Figure 2.2). While the impact rod and superstructure are in contact during each impact, the acceleration of the rod is recorded on the accelerometer and is wirelessly transmitted to the computer via Bluetooth connection. Each measurement consists of 16 individual strikes.

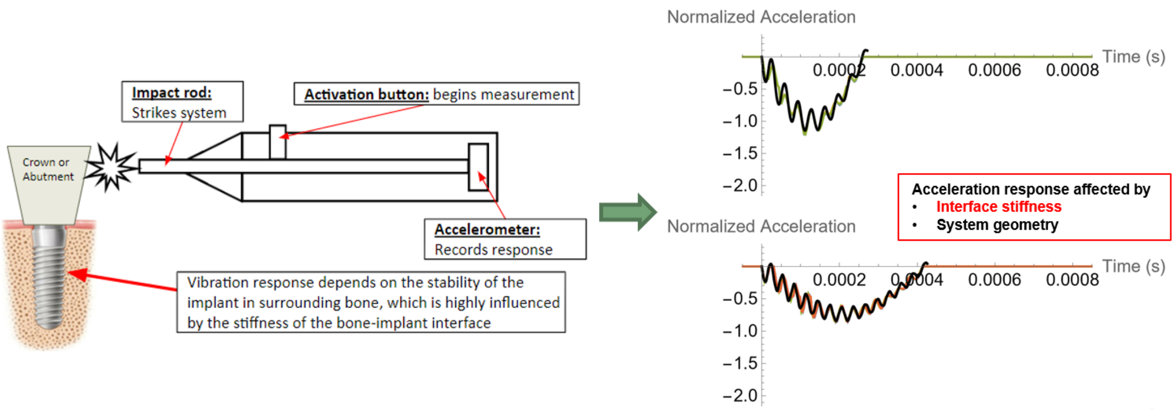

Figure 2.2: Mechanism of action of the ASIST device. The recorded acceleration varies depending on both the interfacial stiffness and system configuration.

2.2 Analytical Model

Bone-level, tapered implants (Institut Straumann, Waldenburg, Switzerland) were used in this work. The ASIST method models the implant system as a four degree of freedom analytical model, originally developed by Swain et al., and later adapted by Westover et al. for hearing aid implants (Swain et al., 2008a, Westover et al., 2016b). The model (Figure 2.3) approximates the implant and abutment as two separate rigid bodies with distinct masses and moments of inertia denoted by m and J, respectively. The impact rod is modelled as a particle with mass m_p, that strikes the system at a height h above bone level. The locations of the implant and abutment's center of gravity G are defined by y_A and y_I with respect to the bottom of the component, while L_I and l_I correspond to the implant's total length and tapered section lengths, respectively.

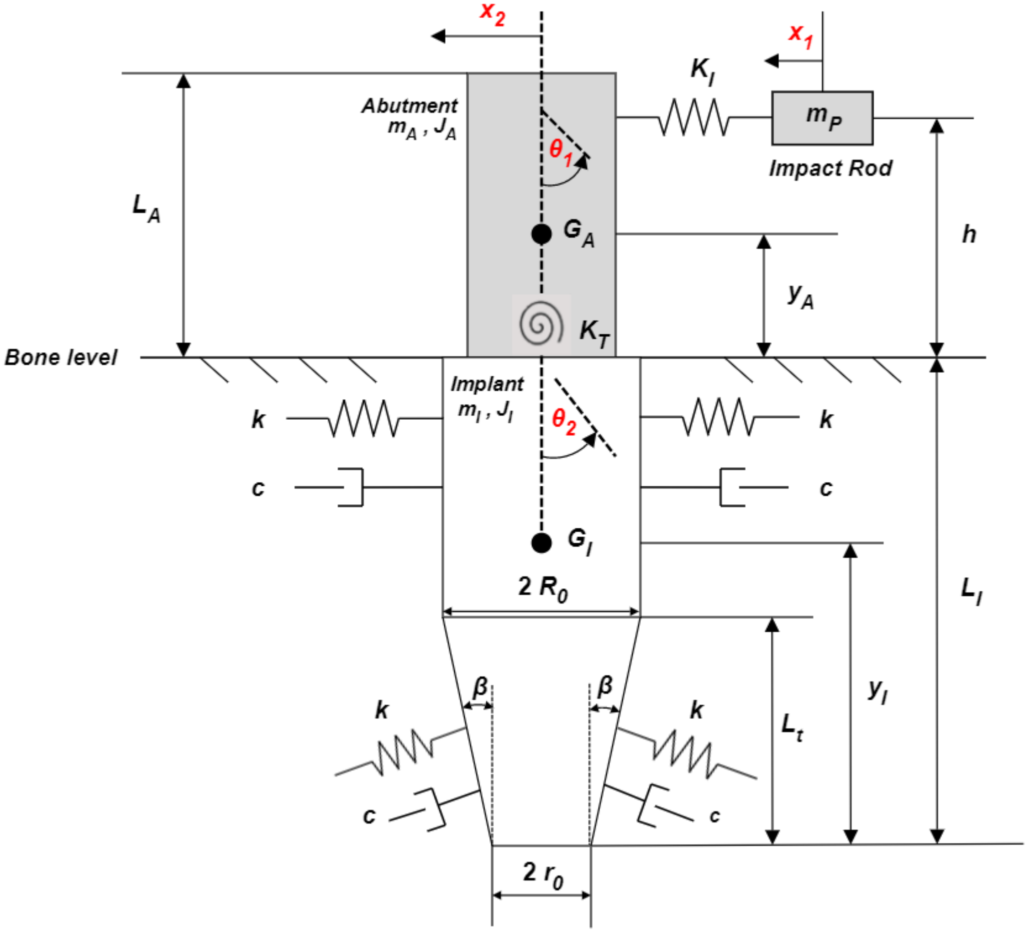

Figure 2.3: Analytical four degree of freedom vibration model of a dental implant system consisting of the impact rod, abutment, and implant.

The impact between the rod and abutment and the implant-abutment connection are represented by a linear spring (K_I) and torsional spring (K_T), respectively, while the effective stiffness of the interface and surrounding bone is represented by a stiffness per unit area k that is uniformly distributed along the surface of the implant below bone level (N/m^3).

To estimate the torsional stiffness, the abutment body is modelled as a rigid cantilever beam (length L, moment of inertia I, and modulus E) with a torsional spring K_T at the support and point load P applied at the free end, such that $K_T\theta = PL$. Then K_T can be estimated using the corresponding deflection of the free end ($\Delta = L\theta = PL^3/3EI$):

$$K_T = \frac{3EI}{L}$$

However, this equation assumes that the abutment is rigidly connected to the implant. In actuality, the abutment and implant are linked with a screw connection. As a result, the actual torsional stiffness is lower than the value calculated from the equation above (Swain et al., 2008a; Westover et al., 2016a). Therefore, a correctional factor $\alpha \in (0,1]$ is introduced below. This is further discussed in Section 2.3.2 and the full derivation is detailed in Appendix A.

.

$$K_T = \alpha\left(\frac{3EI}{L}\right)$$

The system response is described using the displacements of the impact rod (x_1) and abutment (x_2), and angular displacements of the abutment (θ_1) and implant (θ_2).

The system response $\begin{Bmatrix} x_1 \\ x_2 \\ \theta_1 \\ \theta_2 \end{Bmatrix}$ is described by the equations of motion:

$$[M]\{\ddot{x}\} + [C]\{\dot{x}\} + [K]\{x\} = \{0\}$$

Where $[M]$, $[C]$, and $[K]$ correspond to the mass, damping, and stiffness matrices respectively. The mass matrix $[M]$ is defined as:

$$[M] = \begin{bmatrix} m_P & 0 & 0 & 0 \\ 0 & m_A + m_I & m_A y_A - (m_I + m_A)h & -m_I(L_I - y_I) \\ 0 & m_A y_A - (m_I + m_A)h & J_A + m_A(h - y_A)^2 + m_I h^2 & m_I(L_I - y_I)h \\ 0 & -m_I(L_I - y_I) & m_I(L_I - y_I)h & J_I + m_I(L_I - y_I)^2 \end{bmatrix}$$

The stiffness matrix $[K]$ is defined as:

$$[K] = \begin{bmatrix} K_{11} & K_{12} & 0 & 0 \\ K_{21} & K_{22} & K_{23} & K_{24} \\ 0 & K_{23} & K_{33} & K_{34} \\ 0 & K_{42} & K_{43} & K_{44} \end{bmatrix}$$

Where:

$$K_{11} = K_I$$

$$K_{22} = K_I + 4k\left[R_0 L_b + \cos^2(\beta)\left(\frac{2R_0 L_t^2 - (R_0 - r_0)(L_I^2 - L_b^2)}{2L_t}\right)\right]$$

$$K_{33} = k_{33} = K_T + 4kh^2\left[R_0 L_b + \cos^2(\beta)\left(\frac{2R_0 L_t^2 - (R_0 - r_0)(L_I^2 - L_b^2)}{2L_t}\right)\right]$$

$$K_{44} = K_T + \frac{4}{3}k\left[R_0 L_b^3 + \cos^2(\beta)\left(\frac{4R_0\left(L_I^3 - L_b^3\right)L_t - 3(R_0 - r_0)\left(L_I^4 - L_b^4\right)}{4L_t}\right)\right]$$

$$K_{12} = K_{21} = -K_I$$

$$K_{23} = K_{32} = -4kh\left[R_0 L_b + \cos^2(\beta)\left(\frac{2R_0 L_t^2 - (R_0 - r_0)(L_I^2 - L_b^2)}{2L_t}\right)\right]$$

$$K_{24} = K_{42} = -2k\left[R_0 L_b^2 + 2\cos^2(\beta)\left(\frac{3R_0(L_I^2 - L_b^2)L_t - 2(R_0 - r_0)(L_I^3 - L_b^3)}{6L_t}\right)\right]$$

$$K_{34} = K_{43} = -K_T + 2kh\left[R_0 L_b^2 + 2\cos^2(\beta)\left(\frac{3R_0\left(L_I^2 - L_b^2\right)L_t - 2(R_0 - r_0)\left(L_I^3 - L_b^3\right)}{6L_t}\right)\right]$$

Where:

y_A and y_I are the distances between the centre of mass G and the bottom of the abutment or implant, respectively,

r_0 and R_0 are the inner and outer radii of the implant, respectively,

L_I is the implant's total length,

L_b is the length of the straight walled (cylindrical) section of the implant,

$L_t = L_I - L_b$ is the length of the tapered section of the implant,

$\beta = \tan^{-1}\left(\frac{R_0 - r_0}{L_t}\right)$ is the implant's taper angle.

Swain et al. had previously used proportional damping (Swain et al., 2008a); however, this was replaced by a viscous damping model by Westover et al. to better reflect physiological conditions, assuming that damping predominantly occurs at the interface and is negligible elsewhere (Westover et al., 2016b). It is assumed that the damping coefficient per unit area (c) is uniformly distributed along the interface and is negligible elsewhere (Westover et al., 2016).

The damping matrix $[C]$ is given as:

$$[C] = \begin{bmatrix} 0 & 0 & 0 & 0 \\ 0 & C_{22} & C_{23} & C_{24} \\ 0 & C_{32} & C_{33} & C_{34} \\ 0 & C_{42} & C_{43} & C_{44} \end{bmatrix}$$

Where:

$$C_{22} = 2c\left[2R_0L_b + \cos^2(\beta)\left(L_t(R_0 + r_0) - 2L_b(R_0 - r_0)\right)\right]$$

$$C_{33} = 2c\left[2R_0L_b + \cos^2(\beta)\left(L_t(R_0 + r_0) - 2L_b(R_0 - r_0)\right)\right]h^2$$

$$C_{44} = \frac{1}{3}c\left[4R_0L_b^3 + \cos^2(\beta)\left(L_I^3(R_0 + 3r_0) - 3L_IL_b(L_I + L_b)(R_0 - r_0) - L_b^3(7R_0 - 3r_0)\right)\right]$$

$$C_{23} = C_{32} = -2c\left[2R_0L_b + \cos^2(\beta)\left(L_t(R_0 + r_0) - 2L_b(R_0 - r_0)\right)\right]h$$

$$C_{24} = C_{42} = -2c\left[R_0L_b^2 + \frac{\cos^2(\beta)}{3}\left(R_0(L_I^2 - 2L_IL_b - 5L_b^2) + 2r_0(L_I^2 + L_IL_b + L_b^2)\right)\right]$$

$$C_{34} = C_{43} = c\left[2R_0L_b^2 + \frac{2\cos^2(\beta)}{3}\left(R_0(L_I^2 - 2L_IL_b - 5L_b^2) + 2r_0(L_I^2 + L_IL_b + L_b^2)\right)\right]h$$

2.3 Determining the ASIST Stability Coefficient

Using the acceleration of the impact rod, it is possible to determine the interfacial stiffness k by estimating the model parameters and matching the predicted analytical acceleration response $\ddot{x}_1(t)$ to the experimental data. A custom Mathematica code (Wolfram Mathematica 12.3, Champaign, IL, USA) was adapted and used to determine the interface stiffness via numerical optimization. Since the measured acceleration of the impact rod is in volts (V), the data is first curve fitted to determine the relative amplitudes and damping in the signal. Information from the curve fit is then used to normalize the measured response, which is necessary to ultimately match the predicted analytical model response, which has the units of acceleration (m/s^2) rather than volts.

2.3.1 Curve Fitting

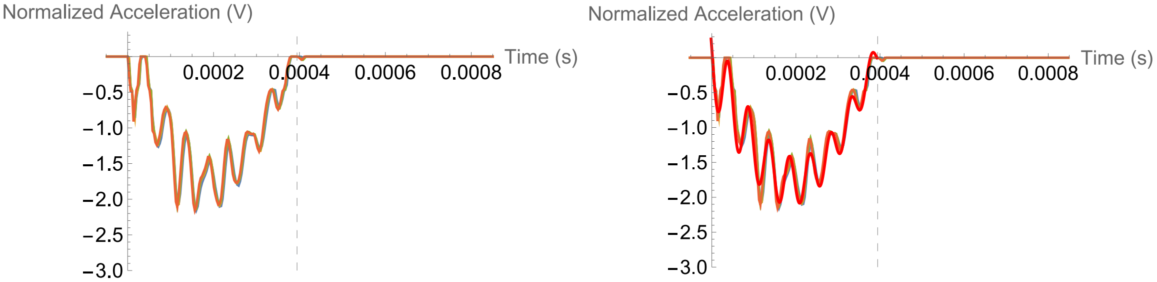

Figure 2.4: Normalized raw acceleration signal (left) and fitted data (right). The dashed line corresponds to the end of the strike and the red line corresponds to the curve fit.

Shown in Figure 2.4, the measured acceleration mainly consists of two dominant frequencies, and it is assumed that the contact time between the impact rod and abutment represents half of a full cycle of the first natural frequency. As a result, the curve fit model is based on a corresponding two degree of freedom (2-DOF) vibration response:

$$x_1(t) = Ae^{-\zeta_1 p_1 t}\sin(\omega_{d1}t + \phi_1) + Be^{-\zeta_2 p_2 t}\sin(\omega_{d2}t + \phi_2)$$

where p represents the natural frequencies and $\omega_{di} = p_i\left(\sqrt{1-\zeta^2}\right)$ represents the damped natural frequency. Since the acceleration of the rod is recorded, the signal is curve fitted by differentiating the above equation to obtain $\ddot{x}_1(t)$. By using the method of least squares, the code determines the values of the parameters in the curve fit model $(A, B, \zeta_1, \zeta_2, p_1, p_2, \phi_1, \phi_2)$ which minimizes the difference between the model and the measured data. Since the signal only contains one half of a cycle of the first natural frequency, there is not enough information to determine the amount of damping in the first mode and ζ_1 is set to 0. The initial condition $\ddot{x}_1(0) = 0$ is also included so that the curve fit reflects the experimental setting.

Normalization is done assuming that the measured voltage is linearly proportional to the acceleration of the impact rod, such that:

$$\ddot{u}(t) = V_{amp}\ddot{x}(t)$$

Where $\ddot{x}(t)$ is the acceleration of the impact rod (m/s^2), $\ddot{u}(t)$ is the normalized acceleration from the accelerometer, and V_{amp} is the proportionality constant. Then, V_{amp} is determined by matching the first mode amplitudes of the measured data and curve fit model.

2.3.2 Determining Analytical Model Parameters

To account for differences in system components, simplified geometries of the implant and abutment were modelled in SolidWorks (Version 2019, Dassault Systèmes, Vélizy-Villacoublay, France) and used to determine their corresponding geometric and inertial properties in the analytical model. Details are covered in Section 3.3.

The curve fit is ultimately used to determine the corresponding predicted analytical model response, which is done through multivariable minimization (Wolfram Language & System Documentation Center). The curve fit approximation and analytical model are matched by selecting the stiffness parameters (k, K_I, K_T) which minimizes the Euclidean norm between the two, and is quantified by an R^2 value. The interfacial stiffness k is the parameter of interest that will be used to determine the ASC score for a given measured signal.

The ASC is reported by normalizing the effective interfacial stiffness by a nominal stiffness at the impact site to provide a non-dimensional parameter for easier interpretation in clinical use:

$$ASC = \frac{k_{eff}}{4 \times 10^6}$$

$$k_{eff} = 4k\left[R_0 L_b + \cos^2(\beta)\left(R_0 L_t - \left(\frac{R_0 - r_0}{2L_t}\right)(L_I^2 - L_b^2)\right)\right]$$

Higher measured stiffnesses yield larger ASC values, indicating greater relative stability. This approach isolates the properties of the interface and allows the ASC to be independent of system geometry.

Chapter 3 : Isolating the Interfacial Stiffness

This chapter details a preliminary evaluation of the ASIST to isolate the interfacial stiffness with respect to SA #1. This chapter will be submitted for publication in the Journal of Biomechanics as:

Jar, C., Archibald, A., Gibson, M., Westover, L. An analytical model to measure dental implant stability with the Advanced System for Implant Stability Testing (ASIST). *Journal of Biomechanics*.

3.1 Introduction

This chapter details the application of the ASIST method to measure the stability of artificial dental implant systems. It is hypothesized that healing abutments or crowns can be modelled as an equivalent body with corresponding geometric and inertial properties, allowing the interfacial stiffness to be estimated independently of the attached superstructure.

3.2 Artificial Implant Systems

Artificial implant models consisted of Straumann bone level tapered dental implants in homogeneous polyurethane foam (Sawbones, Vashon Island, WA, USA). Polyurethane foam is a suitable substitute for human bone due to its similar mechanical properties as stated in ASTM F-1839-08 (ASTM, 2021) and use in previous studies (Oliscovicz et al., 2013a; Tumedei et al., 2021; Wang & Lynch, 2017). Four different bone blocks were used: #10 (ρ = 0.16 g/cm^3), #20 (ρ = 0.32 g/cm^3), #30 (ρ = 0.48 g/cm^3), and #40 (ρ = 0.64 g/cm^3).

Two sizes of bone level tapered Straumann dental implants were used (Straumann, Waldenburg, Switzerland). Both implants have the same length ($L_I = 10\text{ mm}$), but differ in endosteal diameter ($R_0 =$ 3.3 mm or 4.1 mm). Each implant also possesses a different abutment connection design, trademarked as the Narrow CrossFit® (NC) or the Regular CrossFit® (RC) connection design for the 3.3 mm diameter implant or 4.1 mm diameter implant, respectively. Due to the different connection platform, each implant has a specific set of compatible healing and prosthetic abutments (i.e. abutments with an NC design can only be placed on the NC implant).

A set of corresponding Straumann healing abutments and dental crowns were assigned to each implant. Custom dental crowns were manufactured by the University of Alberta Periodontology

Clinic and cemented onto screw-retained Straumann prosthetic abutments. Two different healing abutments, a maxillary lateral incisor crown, and maxillary first premolar crown were assigned to the NC implant, while two different healing abutments and a mandibular first premolar crown were assigned to the RC implant.

The abutments and implants are shown in Figure 3.1, with corresponding nomenclature and properties listed in Table 3.1. Different implant systems are denoted as implant–abutment–substrate. For example, RC-4.5HA-20 corresponds to the RC implant with the 4.5HA abutment in a #20 test block, whereas RC-20 refers to any system with an RC implant and #20 bone block.

Table 3.1: Nomenclature and dimensions of Straumann implants, abutments, and crowns.

Component	Nomenclature	Diameter (mm)	Length (mm)
NC Implant	NC	3.3	10
NC Abutment 1	3.3HA	3.3	3.5
NC Abutment 2	3.6HA	3.6	3.5
Maxillary Incisor	IN	-	13.2
Maxillary Premolar	NCP	-	9.8
RC Implant	RC	4.1	10
RC Abutment 1	4.5HA	4.5	2.0
RC Abutment 2	6.0HA	6.0	4.5
Mandibular Premolar	RCP	-	10.5

Figure 3.1: Implants, abutments, and crowns. From left to right: NC implant, 3.3HA, 3.6HA, IN, NCP, RC implant, 4.5HA, 6.0HA, RCP.

3.3 Determining Analytical Model Parameters

As detailed in Section 2.3, the analytical parameters in the model must be determined in order to obtain an estimate of the interfacial stiffness. Using the acceleration of the impact rod, it is possible to determine the interfacial stiffness k by estimating the model parameters and matching the predicted analytical acceleration response corresponding to $\ddot{x}_1(t)$. A custom Mathematica code (Wolfram Mathematica 12.3, Champaign, IL, USA) was adapted and used to determine the interface stiffness via numerical optimization. Details of the matching process are previously covered in detail (Westover et al., 2016a) and are summarized in Chapter 2. The curve fit approximation of the signal and analytical response is matched by selecting the stiffness parameters (k, K_I, K_T) which minimizes the Euclidean norm between the two and is quantified by an R^2 value.

To estimate the geometric and mass properties of the implants and healing abutments, solid models with the approximate geometries (Figure 3.2) were created in SolidWorks (Version 2019, Dassault Systèmes, Vélizy-Villacoublay, France) and assigned the density of titanium $(\rho = 4.50\,\mathrm{g/cm^3})$ (Winter et al., 2010; Yang & Xiang, 2007). The approximate geometries were determined by measuring the physical implant and abutment specimens with a Vernier caliper with an accuracy of 0.02 mm.

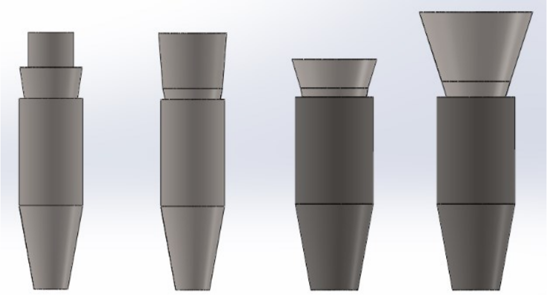

Figure 3.2: Implant-abutment assembly models. Left to right: NC-3.3HA, NC-3.6HA, RC-4.5HA, RC-6.0HA.

Crown STL files were provided by the University of Alberta Periodontology Clinic and imported into SolidWorks. The mass properties of the overall crown-abutment system were estimated by creating assemblies of the crown, prosthetic abutment and dental cement. The crown material (Katana STML Zirconia, Katana, Kuraray Noritake) was approximated as homogeneous with a density of 6.02 g/cm^3 (Kolakarnprasert et al., 2019), the prosthetic abutment was assumed to be titanium (ρ = 4.50 g/cm^3) and the cement density was 1.96 g/cm^3 as specified by the manufacturer

(Multilink Hybrid Abutment Cement, Ivoclar Vivadent AG, Schaan, Liechtenstein). An example of the NC-IN system is shown in Figure 3.3.

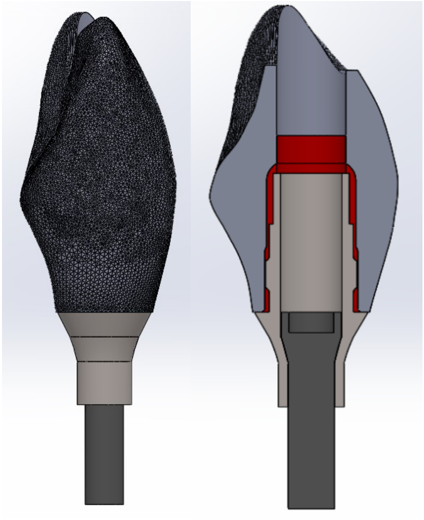

Figure 3.3: Assembly view (left) and internal section view (right) of the NC-IN model assembly, showing the incisor crown (gray) dental cement (red), NC prosthetic abutment (light gray), and abutment screw (dark gray).

Model accuracy was assessed by comparing the approximate and actual masses of each part (Table 3.2) where the actual mass was obtained by a precision mass balance with a resolution of 0.1 mg (ME204, Mettler-Toledo, Greifensee, Switzerland). While the abutment and crown model masses were relatively close to the actual mass, the implant model masses were considerably higher than measured. This is due to the fact that the model does not account for the implant threads, resulting in an overestimation of the implant's volume. As the threads comprise a significant portion of the implant body, it is expected that the model mass would be larger than measured. This was considered acceptable since its effect on the estimated interface stiffness is small compared to the effects of varying the abutment geometry. Note that m_A, J_A and m_I, J_I correspond to the properties of the overall sections of the assembly that would be above and below the substrate surface, respectively. For example, since the entire implant lies below bone level, m_I includes the implant's total mass and the portion of the abutment which is inserted into the implant. In contrast, m_A only includes the portion of the abutment that lies above bone level.

Table 3.2: Estimated model parameters for the implants, healing abutments, and crowns.

Implants	Model Mass (g)	Measured Mass (g)	m_I (g)	J_I (g mm^2)	y_I (mm)
NC	0.2510	0.1788	0.3373	2.55	5.78
RC	0.4355	0.2829	0.5218	4.35	5.75
Abutments/Crowns	Model Mass (g)	Measured Mass (g)	m_A (g)	J_A (g mm^2)	y_A (mm)
3.3HA	0.1625	0.1592	0.0876	0.121	1.48
3.6HA	0.2107	0.1956	0.1312	0.225	1.81
4.5HA	0.2062	0.2030	0.1036	0.140	1.07
6.0HA	0.4159	0.4184	0.3173	0.890	2.34
IN	1.0255	1.0388	1.0080	1.063	6.44
NCP	1.7364	1.8246	1.7190	1.477	5.07
RCP	1.6135	1.5938	1.5616	1.321	5.64

Out of the stiffness parameters (k, K_I, K_T), the interfacial stiffness per unit area k is the parameter of interest that will be used to determine the ASC. The maximum effective torsional stiffness of the implant-abutment connection was determined by modelling the abutment as a rigid cantilever beam (Chapter 2).

$$K_T = 3EI/L$$

Since the abutment and implant are not rigidly connected, the actual torsional stiffness is lower than the theoretical value by a proportionality constant α (Swain et al., 2008a; Westover et al., 2016a).

A sensitivity analysis was conducted for each implant-abutment combination, to investigate the effect of varying the impact stiffness K_I and torsional proportionality constant α, on the measured ASC. The same trends were observed for all implant-abutment combinations and so an example analysis of an RC-6.0HA-20 replicate is shown.

Variations in the impact stiffness K_I affect the ASC and fit between the data and model, as shown in Figure 3.4, where the blue and black lines correspond to the ASC and R^2 values, respectively. Shown in Figure 3.5, the impact stiffness (K_I) has a visible effect on the second mode frequency of the predicted analytical response.

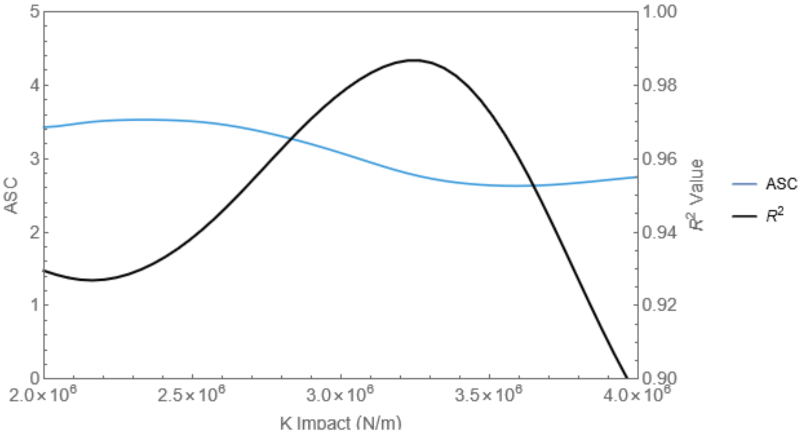

Figure 3.4*:* ASC values (blue line) and R^2 values (black line) for various values of the impact stiffness (K_I) for the RC-6.0HA system.

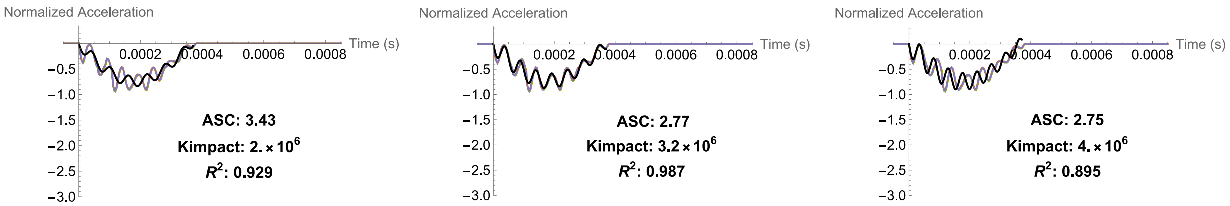

Figure 3.5*:* Effect of varying the impact stiffness on the ASC and R^2 value.

Increasing K_I from 2×10^6 N/m to 3.2×10^6 N/m decreases the ASC by 0.66 (19.2%) and changes the R^2 from 0.929 to 0.986 (6.1%). Further increasing K_I from 3.2×10^6 N/m to 4×10^6 N/m only decreases the ASC by 0.02 (0.7%), but worsens the R^2 to 0.895 (9.3%). Due to this, the impact stiffness was left unfixed in the optimization routine, so that an optimal K_I value can be determined for each signal based on the second mode frequency component. This in turn improves individual estimates of the interfacial stiffness k.

When varying the torsional proportionality constant α, both ASC and R^2 values were sensitive to changes in K_T in the lower region (Figure 3.6). However, both values do not change noticeably past a certain threshold, which corresponds to approximately $\alpha = 0.1$ in the example shown. Therefore, k can be properly estimated if the abutment is adequately tightened into the implant socket because the two components act as a single rigid body, allowing for the impact force to be transferred from the abutment to the implant. Swain et al. found an optimal coefficient for a dental implant-abutment screw connection of $\alpha = 0.26$, which was subsequently used in this study (Swain et al., 2008a). The full analysis is outlined in Appendix B.1.

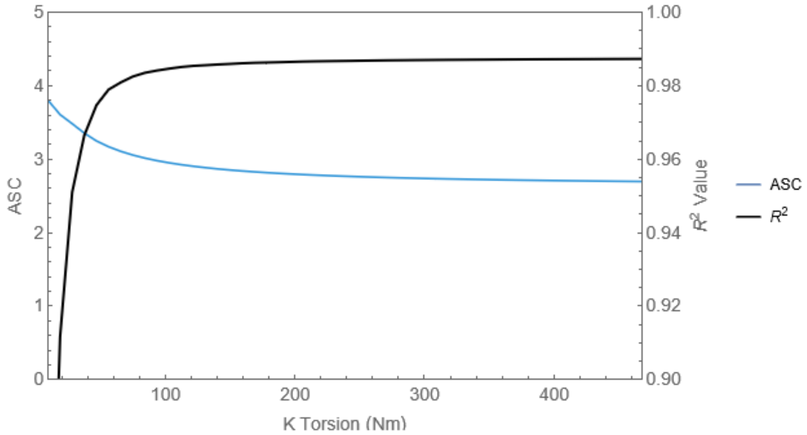

Figure 3.6: ASC values (blue line) and R^2 values (black line) for various values of the torsional stiffness (K_T) for the RC-6.0HA system.

3.4 Experimental Set-up

Implants were installed into test blocks following an outlined surgical manual for Straumann implants (Straumann, 2017). For the NC implant, sites were prepared using a 2.2 mm pilot drill, 2.8 mm drill, 3.3 mm profile drill, and 3.3 mm tap drill. RC implant sites were prepared using a 2.2 mm pilot drill, 2.8 mm followed by a 3.5 mm drill, 4.1 mm profile drill, and 4.1 mm tap drill. Superglue (Canadian Engineering Canada Corporation, Port Coquitlam, BC, Canada) was applied to the implant surface to fix the implant inside the block, simulating secondary stability and allowing multiple abutments to be installed without altering the interface. A total of $n = 5$ replicates were created for each combination of implant and foam density (total $N = 40$ installations). Shown in Figure 3.7, the ASIST was held in a custom stand to maintain a constant striking height and separation distance of 1 mm. While the analytical model assumes a horizontal impact, the ASIST was held at an angle of 5° due to the height constraint of abutment 4.5HA. Previous work has shown that impact measurements are consistent with striking angles between 0 and 5 degrees (Swain et al., 2008a). Each abutment was inserted with 15 Ncm torque, and five repeat ASC measurements were taken.

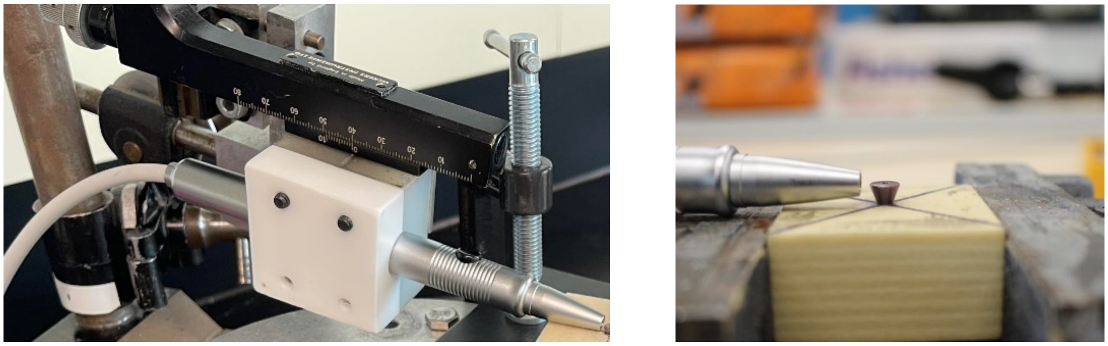

Figure 3.7: Custom stand holding the ASIST (left) and close-up of the RC-6.0HA-40 system.

3.5 Statistical Analysis

Statistical analysis was performed using SPSS software (ver. 29.0, IBM Co., Armonk, NY, USA). ASC values for the NC and RC implant systems were analyzed using mixed two-way repeated measures ANOVA followed by Tukey post-hoc test. Polyurethane density was designated as the between-subjects factor and abutment type as the within-subjects factor. Normality was verified with the Shapiro-Wilk test and sphericity was not violated. For each replicate, an overall estimate for the interfacial stiffness per unit area k was calculated by averaging the values obtained with each superstructure. Two-way ANOVA was performed to evaluate any significant differences in the estimates of k between foam density and implant type. Statistical significance was indicated by a p-value less than 0.05.

3.6 Results

ASC results are shown for the NC implant (Figure 3.8) and RC implant (Figure 3.9). While there are clear differences in the average ASC scores between individual replicates of the same implant and foam density, there is a good agreement in ASC scores obtained with different abutments on the same installation. For the NC implant, the average variation (mean ± standard deviation) in ASC measurements taken with different abutments was found to be 4.7 ± 3.6% (of the average ASC). For the RC implant, changing the superstructure varied the ASC by 6.1 ± 5.9% (of the average ASC).

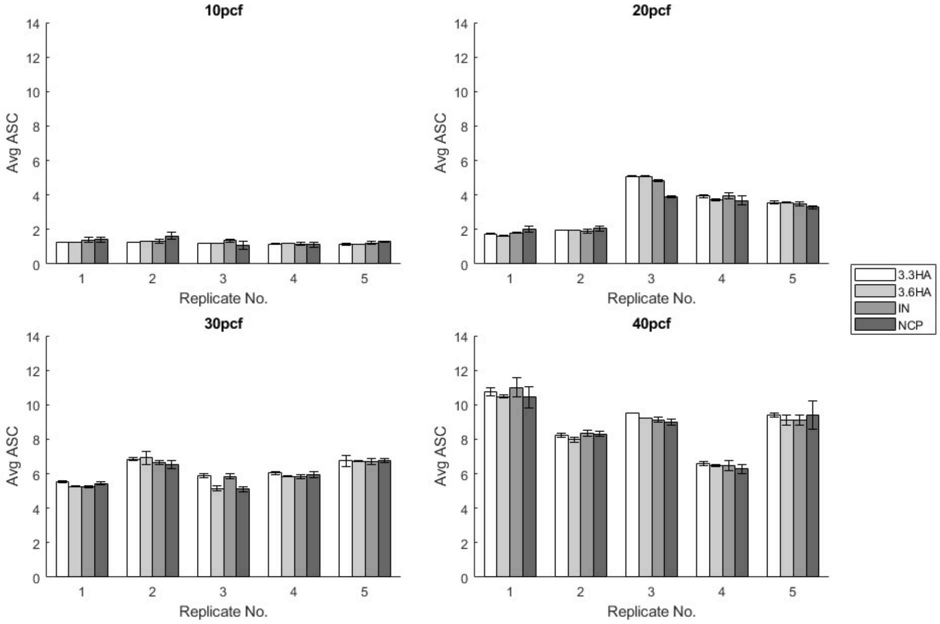

Figure 3.8: ASC measurements for the NC implant system with each superstructure. Bars are grouped by a specific replicate. Error bars represent one standard deviation.

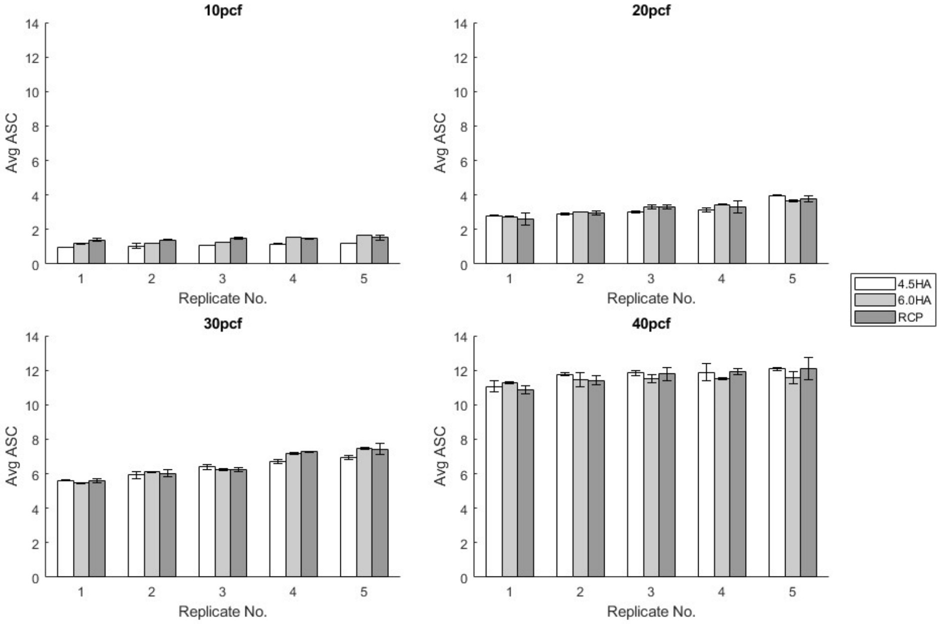

Figure 3.9: ASC measurements for the RC implant system with each superstructure. Bars are grouped by a specific replicate. Error bars represent one standard deviation.

ASC values increased significantly with increasing density but did not differ with abutment type. For the NC implant, there were significant differences in the average ASC scores between each block density ($p < 0.0001$). Abutment type ($p = 0.082$) and interaction effects ($p = 0.737$) were not significant. Similarly, for the RC group, density was significant ($p < 0.0001$), while abutment type ($p = 0.214$) and interaction effects ($p = 0.088$) were not significant.

Despite visually distinct signals obtained with different superstructures, consistent ASC scores were obtained within a specific installation. A representative example is shown by a set of measurements taken on an NC-20 (Figure 3.10) and RC-20 (Figure 3.11) replicate. For the same implant-abutment combination, different signals and ASC values were observed across different densities of polyurethane. This is shown in by an example set of signals taken with the RC-6.0 HA system (Figure 3.12).

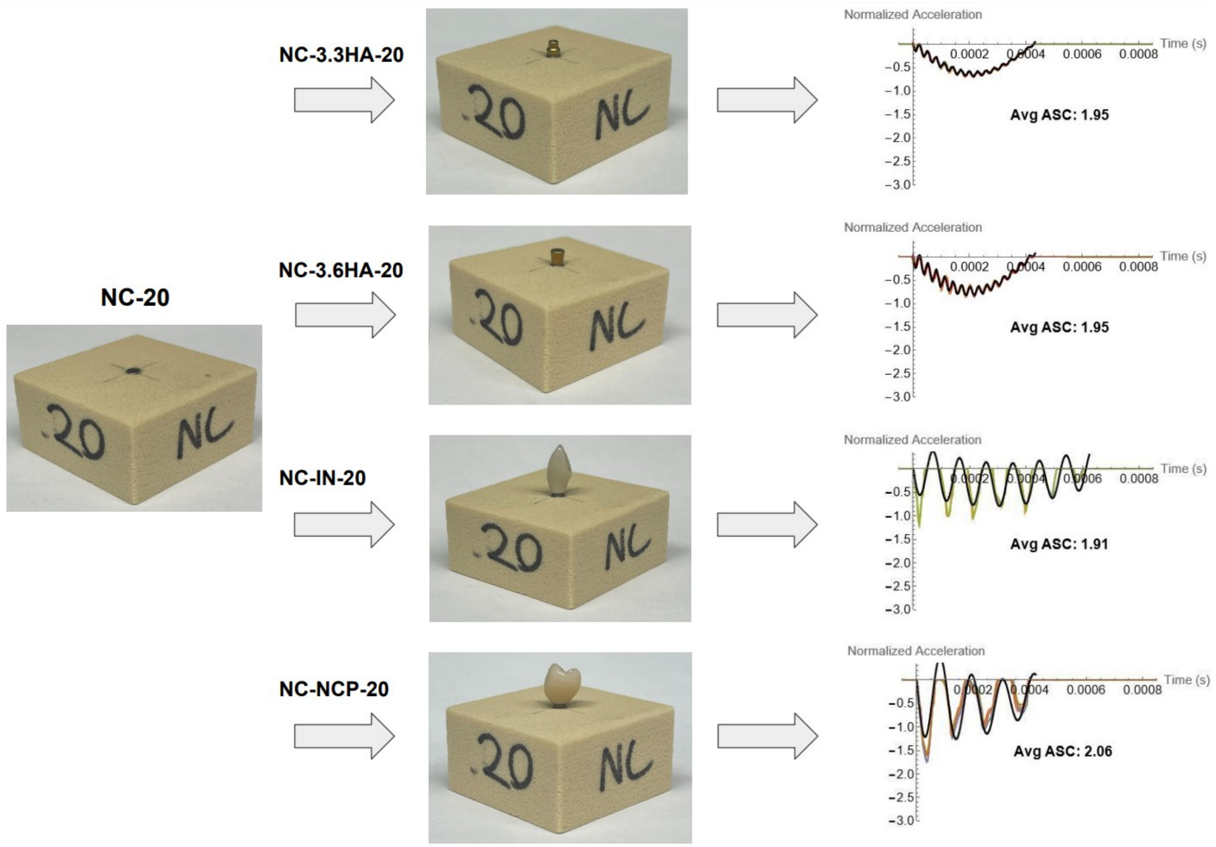

Figure 3.10: Measured signals and ASC values taken with each abutment on the same NC-20 installation replicate.

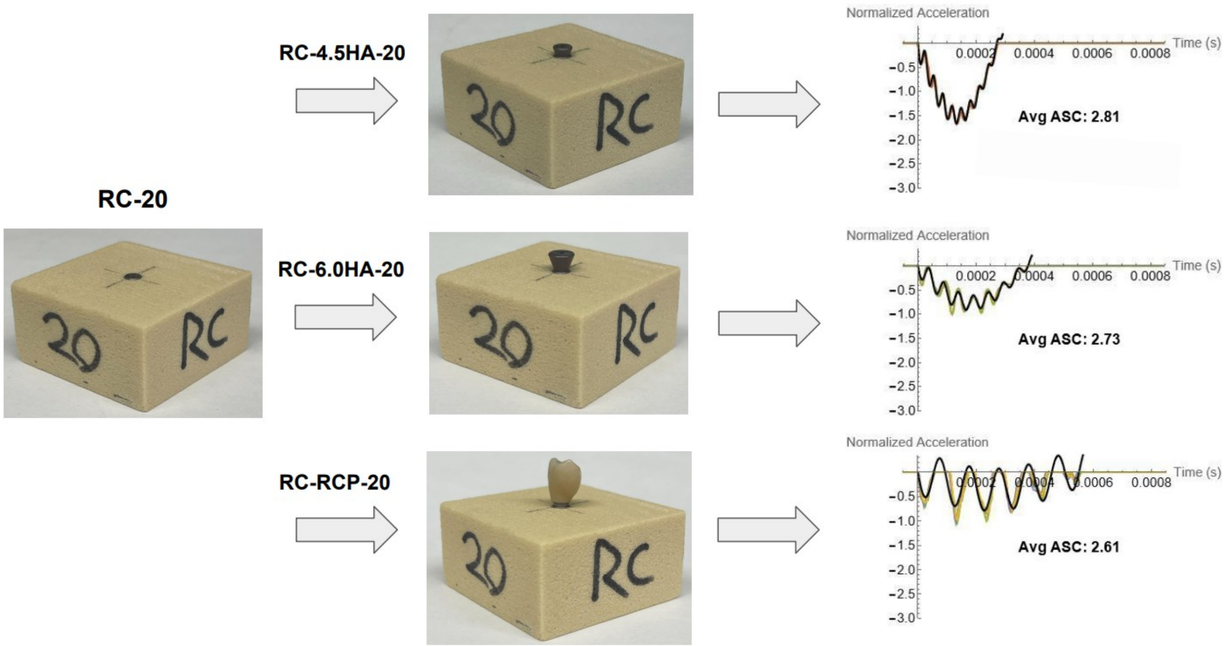

Figure 3.11: Measured signals and ASC values taken with each abutment on the same RC-20 installation replicate.

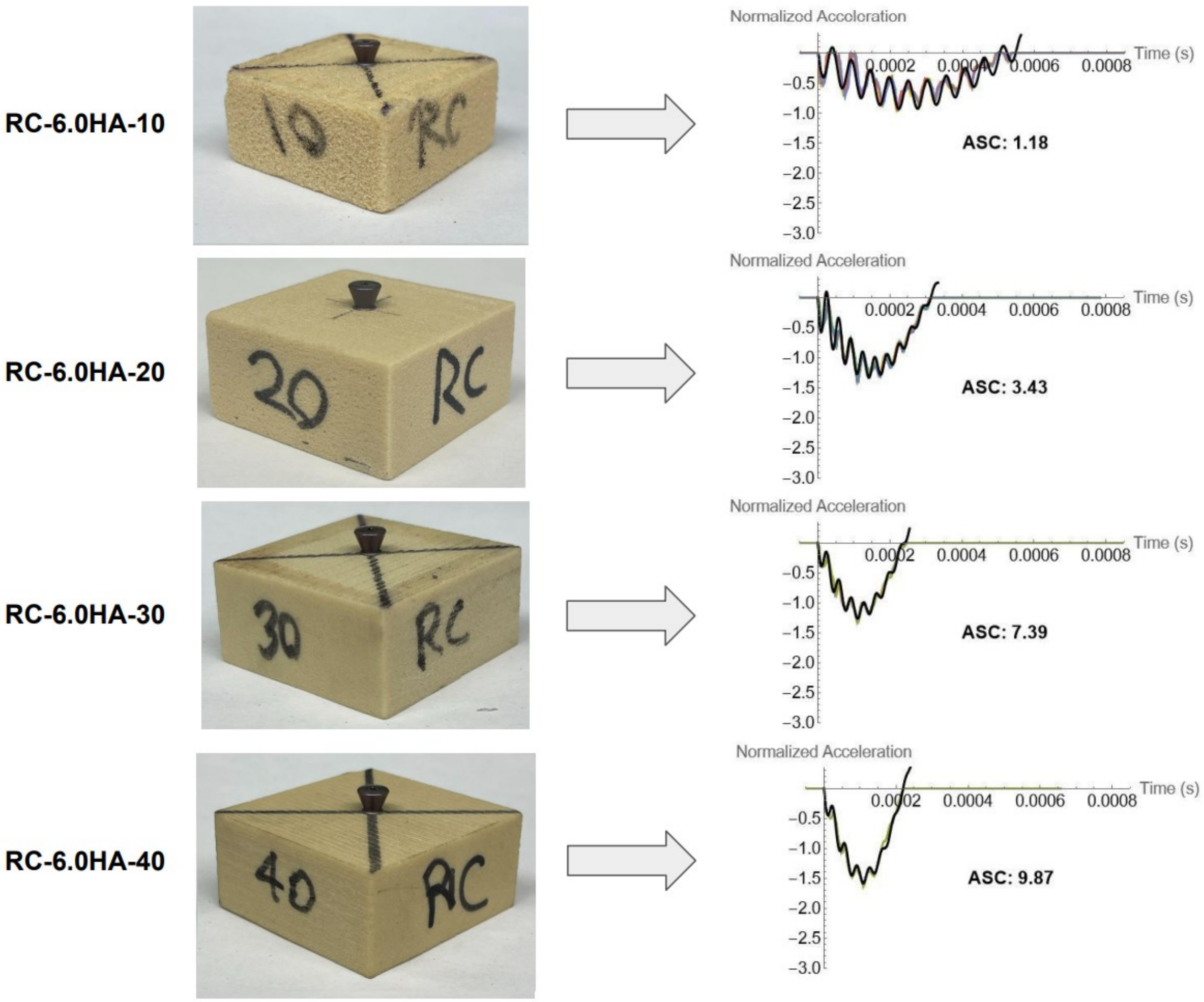

Figure 3.12: Example signals and corresponding ASC values for the RC-6.0HA system for each substrate.

Average values for the interfacial stiffness *k* for each foam density and implant are shown in Figure 3.13. Two-way ANOVA found that the estimates of *k* differed significantly across each density ($p < 0.001$) but did not change with implant type ($p = 0.059$).

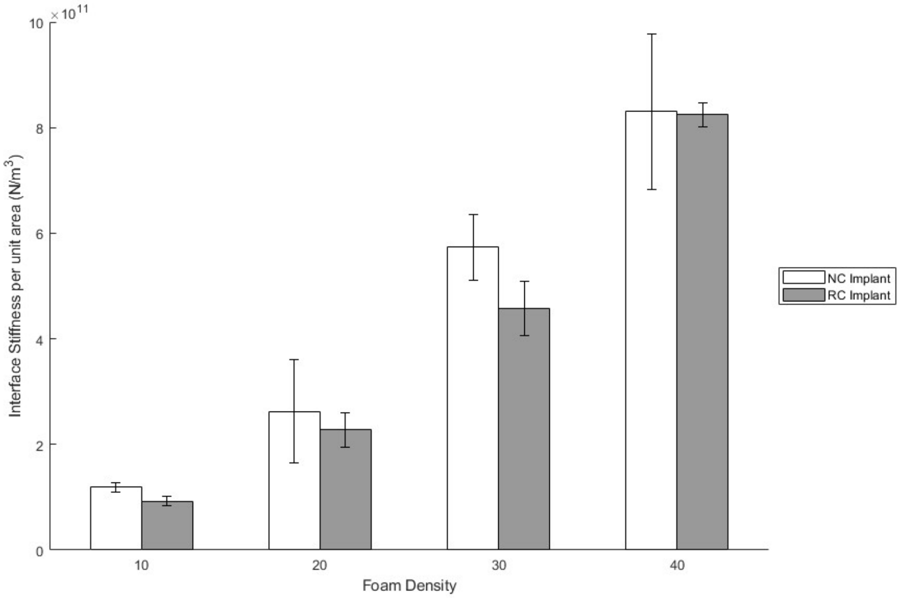

Figure 3.13: Average estimates of the interface stiffness per unit area for each foam density and implant type. Error bars represent one standard deviation between different replicates.

3.7 Discussion

This chapter is a preliminary application of the Advanced System for Implant Stability Testing (ASIST) for measuring dental implant stability. By coupling an impact technique and analytical model, the measured signal can be matched to the response of an equivalent vibration system and provide an estimate of the interfacial stiffness.

Although there is a large variation in the geometry and shape of dental healing abutments and crowns, the signal can be matched to the response of an equivalent model with the same mass and geometric properties. The analytical model was able to provide a good fit for all measurements, with no significant difference in ASC values between different abutments for the same installation despite visually distinct signals. The limitations of other impact-based measurement devices, such as the PerioTest® and AnyCheck®, are illustrated by the differences in the measured signal for different superstructures in Figure 3.10 and Figure 3.11. With different abutments, there is a large variation in contact time, which is used by both methods to gauge stability (Lukas & Schulte, 1990; Lee et al., 2020).

Notably, there is a variability in the ASC between different replicates of the same implant-substrate system, since the amount of glue applied to each implant was not controlled. There is also a distinct increase in the average ASC across different densities of polyurethane foam, with the same range of values between the NC and RC implant systems. However, this does not affect the main conclusion of this study, as there is still a minimal variation in ASC values for a given replicate, which changes significantly across different test blocks. Overall, this implies that the ASC is sensitive to the amount of bonding and mechanical properties of the substrate.

While verifying the validity of fixing the torsional proportionality constant at 0.26 for all measurements, signals were compared from abutments tightened at 10, 15, and 20 Ncm. At each torque, the measured signals were essentially identical. The value of 0.26 was previously found to be the optimal constant for an implant-abutment screw connection for BAHA implants (Swain et al., 2008a). It is assumed that a similar value can be used for dental implants which also use a screw connection. Additionally, this proportionality constant was the same across all systems, as the interior threads of the NC and RC implants were measured and found to be the same. While this may differ from its true value, Figure 3.6 shows that there are minimal changes in the ASC value for variations in α. Furthermore, no significant differences were observed in the average estimate of k between samples with different implants and the same block density. This is consistent with the fact that each interface possesses the same composition (superglue and foam). Additionally, k represents a stiffness per unit area and should not be affected by the implant geometry. Given this, the analytical model appears to be representative of the physical system, and ASC measurements closely reflect the mechanical properties pertaining to the interface and surrounding material.

It is important to consider the limitations within the design of this study. This study does not compare the ASC to another stability metric such as the ISQ. Despite this, there are consistent estimates of the interfacial stiffness, even though there are distinct signals corresponding to different superstructures as shown in Figure 3.10 and Figure 3.11. While a limited number of implants were considered, similar results can be likely obtained by incorporating different implant designs in the analytical model. Additionally, the evaluation of the ASIST was performed using polyurethane foam as an artificial substitute to human bone. Polyurethane foam is not representative of the anatomy or geometry of the human jaw bone. However, polyurethane foam possesses standardized mechanical properties with a lower variability than actual bone. Moreover, polyurethane foam is a suitable substitute for human bone, due to its similar mechanical properties as stated by ASTM F-1839-08 (ASTM, 2021), and has been widely used in studies investigating dental implant stability. It is assumed that the substrate is a continuum medium, so that the bone-implant interface can be defined as a uniform stiffness per unit area. Polyurethane foam and cancellous bone are both porous materials on a microscopic scale, especially at lower densities. From a macroscopic perspective however, these effects can be neglected and it can be assumed that the material is a homogeneous continuum, which has been done in several studies (Liu et al., 2021; Rittel et al., 2017; Sugiura et al., 2016; Zanetti et al., 2018). Furthermore, the analytical model was still able to provide a good match to the experimental data, suggesting that this assumption is acceptable. Due to the visibly different signals collected with each abutment or crown, abutment properties strongly influence the impact acceleration. By modelling these properties, the analytical model was able to predict acceleration responses, specific to each abutment, that provided a good match to the experimental data.

The uniform interface in the analytical model does not reflect the physiological composition of bone, which consists of distinct cortical and cancellous layers. However, it is an accurate description of the homogeneous polyurethane foam used in this study. Compared to real bone, polyurethane foam is more accessible, with smaller variations in morphology and similar mechanical properties. The subsequent chapters in this thesis address the need to cross-validate the ASC with other stability metrics, and to develop an analytical model that accounts for the different stiffnesses of the cortical and cancellous layers.

3.8 Conclusion

This chapter presents the preliminary application of the ASIST to dental implants. Accounting for different implant system components with their corresponding mass and inertial properties provides an estimate of the interfacial stiffness that is sensitive to the properties of the interface and substrate material and independent of the attached superstructure.

Chapter 4 : Cross Validation of the ASIST

The purpose of this chapter is to fulfill SA #2 SA #3 described in Section 1.2, such that ASC values should reflect differences in stability and demonstrate a correlation with other indicators. This chapter will be submitted for publication to the International Journal of Oral and Maxillofacial Implants as:

Jar, C., Archibald, A., Gibson, M., Westover, L. Comparison of an impact technique coupled with an analytical model with insertion torque, RFA, and pullout testing for the in-vitro measurement of dental implant stability. *International Journal of Oral and Maxillofacial Implants*.

4.1 Introduction

This chapter serves as a follow-up to the previous section. With the ASIST, it was shown in Chapter 3 that consistent ASC values were obtained for various superstructures, implying that the interfacial stiffness can be estimated independently of system components. However, correlations between the ASC and other indicators of stability have not yet been investigated. Insertion torque (IT), RFA, and pullout testing were chosen as methods to compare the ASIST device. IT is often used as an indicator of primary stability, as it reflects the bone's resistance during initial placement (Bedrossian, 2020; Wang et al., 2015) and reduces the amount of implant micromotion (Greenstein & Cavallaro, 2017). RFA measures implant stability using the correlations between the resonance frequencies and interfacial stiffness (Atsumi et al., 2007; Meredith et al., 1997a; Meredith et al., 1997b). The Osstell$^{\text{TM}}$ is a commercial RFA device, which outputs the implant stability quotient (ISQ). The pullout test is specified in ASTM F543-23 as the standard method to simulate the axial withdrawal of metallic bone screws (ASTM, 2023), and has been previously used to characterize the mechanical properties of the bone-implant interface (Gehrke et al., 2021; Huang et al., 2020; Oliscovicz et al., 2013a; Oliscovicz et al., 2013b; Rittel et al., 2017; Seong et al., 2013).

Different levels of primary stability were simulated by varying the drill sequence used to prepare the implant bed. Different osteotomy drilling techniques can be used in the case of poor underlying bone quality to improve initial primary stability (Blume et al., 2021). With undersized drilling, the osteotomy is lower in diameter than the implant itself (Delgado-Ruiz et al., 2020). This press-fit between the bone and implant allows for higher levels of insertion torque to be reached (Jimbo et al., 2014).

The purpose of this chapter is to compare the ASIST and Osstell® as non-invasive stability measurement devices by comparing their correlations with IT and pullout strength in artificial implant systems simulating primary and secondary stability. This was done by evaluating the effects of bone density, drill sequence, and implant bonding on the stability of implants installed in artificial bone blocks. It is hypothesized that changes in stability are better reflected in the ASC compared to the ISQ, as the ASC is a mechanical measurement of the interface properties.

4.2 Experimental Groups

Tapered, bone-level Straumann dental implants (Straumann, Waldenburg, Switzerland) with a length of 10 mm and diameter of 4.1 mm were placed into homogeneous polyurethane foam blocks (Sawbones, Vashon Island, WA, USA). Three different types of foam were used: #20 foam (ρ = 0.32 g/cm^3), #30 foam (ρ = 0.48 g/cm^3), and #40 foam (ρ = 0.64 g/cm^3).

Two experimental groups were created in accordance with the objectives of the study. To investigate the effects of density, Group 1 was comprised of implants installed in #20, #30, and #40 test blocks. The effects of implant bonding were evaluated by further dividing Group 1 into two subgroups simulating primary stability (1P) and secondary stability (1S). In Group 1S, superglue (Canadian Engineering Canada Corporation, Port Coquitlam, BC, Canada) was applied to the implant surface before being placed in the test block, while no glue was used for Group 1P. All implant sites were prepared using a drill sequence consisting of a Ø2.2 mm, Ø2.8 mm, and Ø3.5 mm drill, followed by a 4.1 mm profile drill and tap drill (Figure 4.1; Straumann 2017).

Group 2 was divided into four subgroups (2-1, 2-2, 2-3, 2-4) to evaluate the effect of drill sequence on primary stability. Each subgroup consisted of #20 test blocks, and differed with respect to the drill sequence used to prepare the implant bed. The drill sequences used for each group are shown in Figure 4.1. Each experimental condition was replicated $n = 10$ times.

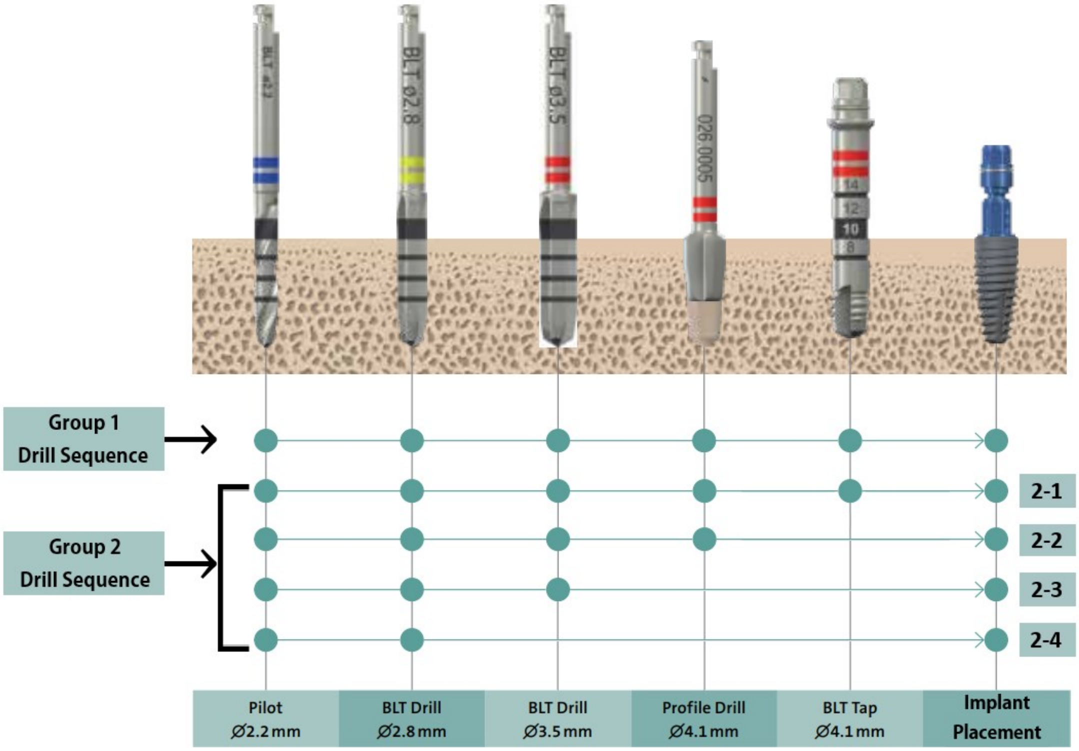

Figure 4.1: Drilling sequence used in each experimental group (Straumann, 2017).

4.3 IT, ISQ, and ASC Measurements

Maximum IT values were recorded during implant placement for groups 1P and 2 using a hand-held torque gauge (FTD2-S, Tohnichi, Tokyo, Japan), while RFA and ASC measurements were conducted on all groups. RFA stability measurements were performed by the Osstell® ISQ by placing a SmartPeg (Type 54, Osstell, Göteborg) in the implant. An average ISQ value for each sample was calculated by orienting the probe in four perpendicular directions and taking four repeat ISQ measurements per direction, for a total of sixteen repeat measurements. Five repeat ASC measurements were taken with the ASIST device by placing an abutment (Straumann, Waldenburg, Switzerland) in the implant. The same healing abutment was used for all ASC measurements (conical shape, 6 mm diameter, 4 mm height). The ASIST was held in a custom stand to control handpiece angulation and positioning (Westover et al., 2016a). The experimental set-up is shown in Figure 4.2.

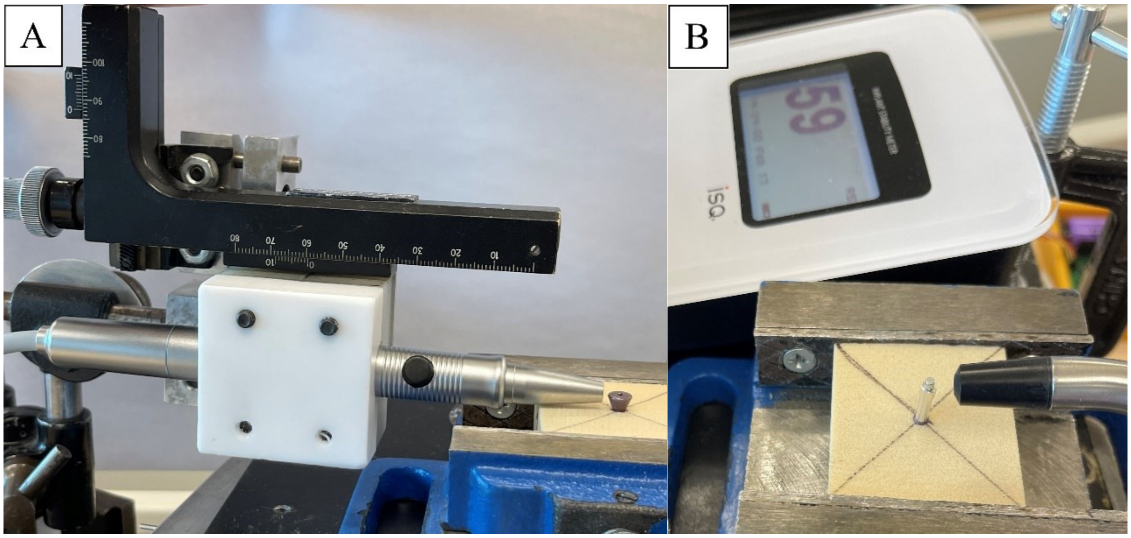

Figure 4.2: Experimental set-up for ASC measurements (A) and ISQ measurements (B).

4.4 Pullout Testing

For each sample, a square washer with approximately the same hole diameter as the implant was aligned and secured to the surface of each block. This was done to ensure that failure occurred along the interface and not within the material itself, especially in the case of Group 1S. Pullout tests were done using a custom bolt fitted to the interior threads of the implant. Blocks were held on the platform by gently tightening wedge clamps to avoid over-compression of the foam (Figure 4.3). Tests were performed with a universal testing machine (Qualitest Quasar 100, Lauderdale, FL, USA) at a rate of 5 mm/min (ASTM, 2023; Gehrke et al., 2021; Huang et al., 2020). A 12.5 kN load cell with 0.5 N resolution was used. The pullout strength was measured using the maximum tensile load required to remove the implant from the test block.

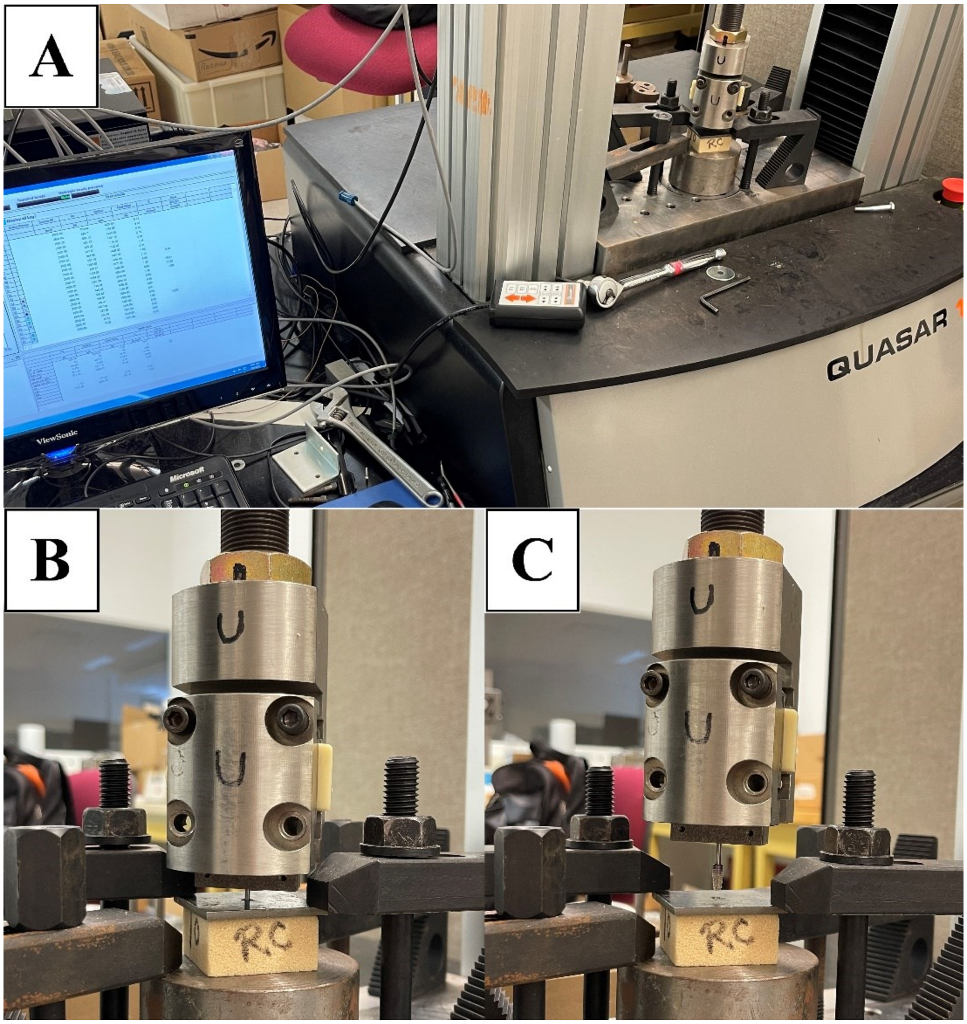

Figure 4.3: Pullout test machine set-up (A); Sample before (B) and after (C) implant pullout.

4.5 Data and Statistical Analysis

SPSS software (ver. 29.0, IBM Co., Armonk, NY, USA) was used to perform statistical analysis. All comparisons were performed using single factor ANOVA. The effects of density and drill sequence on mean IT, ISQ, ASC, and pullout values were investigated by analyzing groups 1P and 2, respectively. A comparison was also done between groups 1P and 1S with respect to their mean ISQ, ASC, and pullout values to evaluate the effects of implant bonding. Normality and homogeneity were verified using the Shapiro-Wilk test and Levene's test, respectively. Significance was indicated by a *p*-value less than 0.05, and values are reported as mean ± standard deviation.

4.6 Results

Stability measurements are summarized in Table 4.1. The pullout force for the #40 test blocks in group 1S was reported using five out of ten samples in group 1S-40. The other five samples could not be measured as the bolt fractured before the implant could be pulled out, which occurred at an average load of 1307.02 N.

Group 1 results are shown in Figure 4.4 and Figure 4.5. Significantly higher stability measurements were observed with increasing density in group 1P and 1S. Implant bonding was also highly influential, as mean pullout, ISQ, and ASC values were significantly higher when comparing blocks of the same density in group 1S to group 1P. All p-values for each comparison were below 0.01.

Group 2 results are shown in Figure 4.6 and Figure 4.7. Mean IT, pullout, and ASC values were significantly different for each drilling sequence in group 2 ($p < 0.001$). ISQ values were significantly different when comparing groups 2-1 and 2-2 to groups 2-3 and 2-4 ($p < 0.001$). However, no significant difference was found in the mean ISQ values when comparing group 2-1 to 2-2 ($p = 0.998$), and group 2-3 to 2-4 ($p = 0.646$).

Table 4.1: Results of IT, ISQ, ASC, and pullout force (mean ± SD) for groups 1 and 2.

Group	Insertion Torque (Ncm)	Pullout (N)	ISQ	ASC
1P-20	5.3 ± 0.5	118.89 ± 10.31	60.80 ± 1.25	1.76 ± 0.16
1P-30	24.8 ± 1.8	380.00 ± 16.51	69.00 ± 0.72	3.38 ± 0.13
1P-40	35.8 ± 2.4	531.88 ± 32.78	70.35 ± 1.53	4.32 ± 0.22
1S-20	-	544.34 ± 44.62	68.68 ± 2.29	3.42 ± 0.26
1S-30	-	1085.07 ± 98.47	72.69 ± 1.94	6.13 ± 0.63
1S-40	-	1213.69 ± 122.56[a]	75.58 ± 2.12	9.85 ± 1.77
2-1	5.3 ± 0.5	118.89 ± 10.31	60.80 ± 1.25	1.76 ± 0.16
2-2	12.9 ± 1.5	168.06 ± 8.60	60.90 ± 1.47	2.09 ± 0.21
2-3	25.2 ± 1.4	259.46 ± 6.76	67.65 ± 0.67	3.26 ± 0.17
2-4	45.9 ± 2.1	429.67 ± 7.98	68.28 ± 1.27	3.75 ± 0.16

[a] Averaged from $n = 5$ measurements.

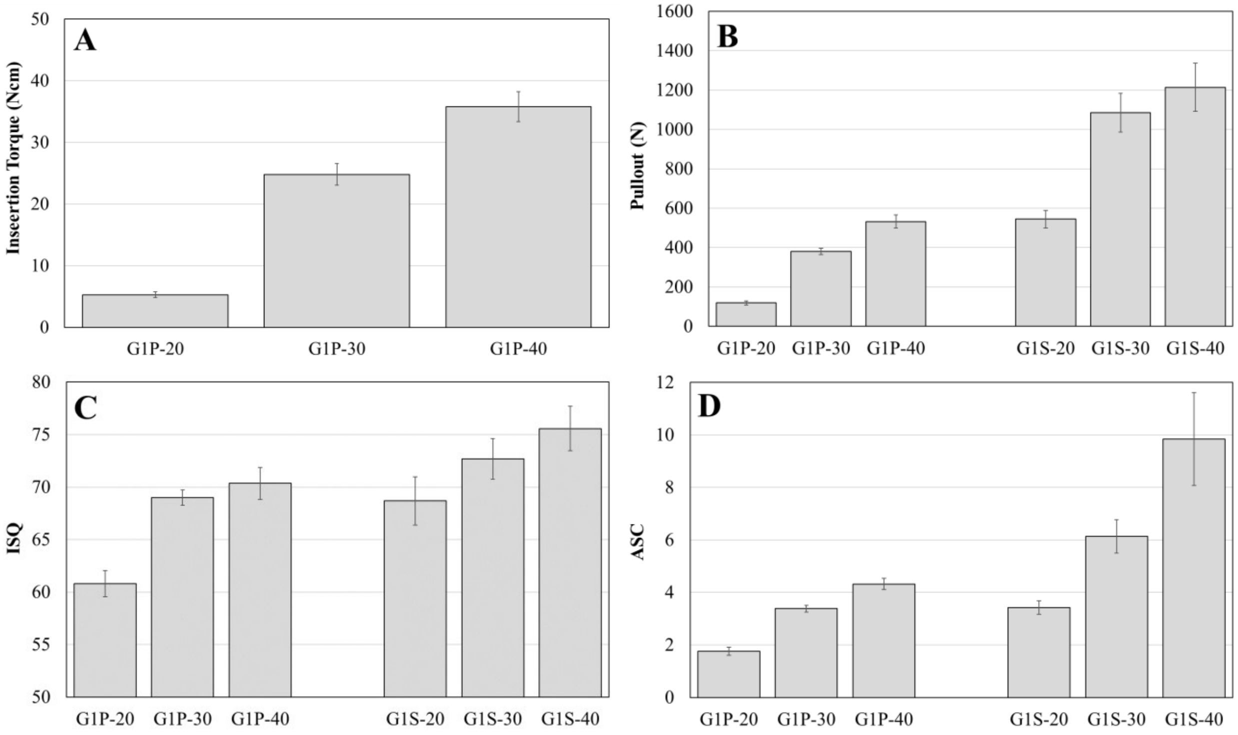

Figure 4.4: Mean IT (A), Pullout (B), ISQ (C) and ASC (D) measurements of Group 1. Error bars represent one standard deviation.

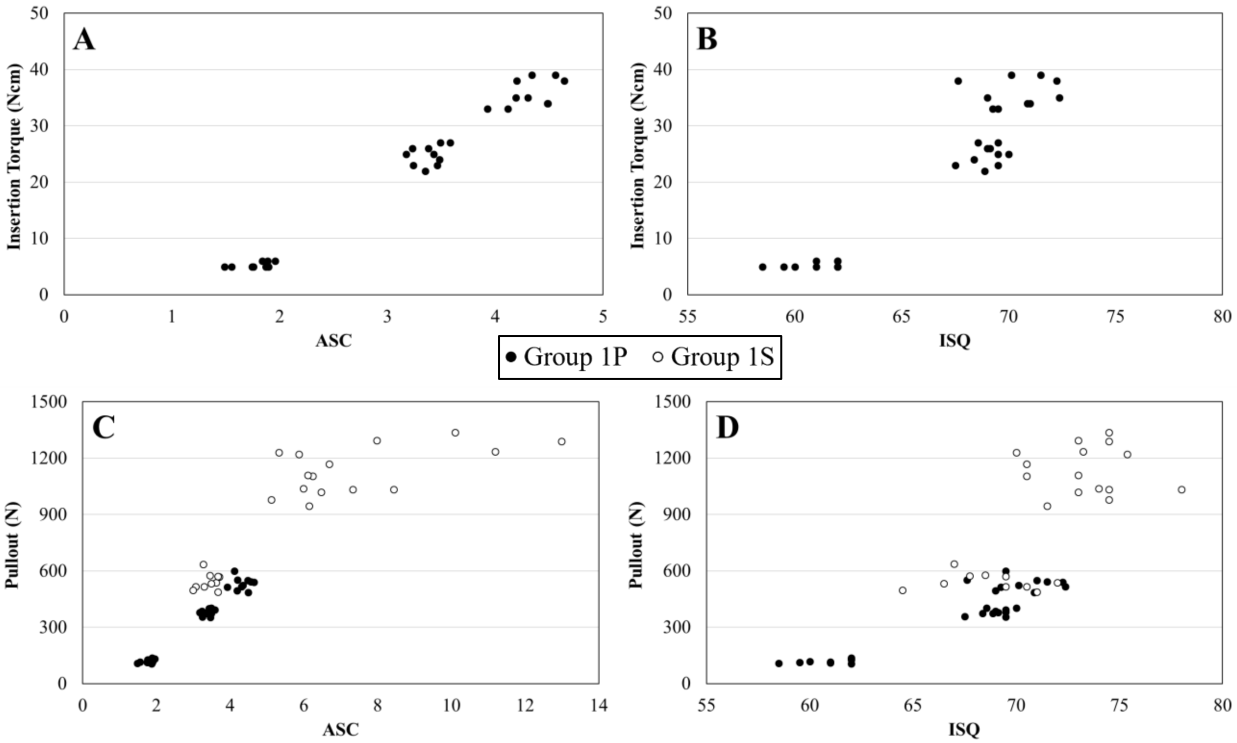

Figure 4.5: Group 1P and 1S scatterplots of IT vs. ASC (A) and ISQ (B), and pullout vs. ASC (C) and ISQ (D).

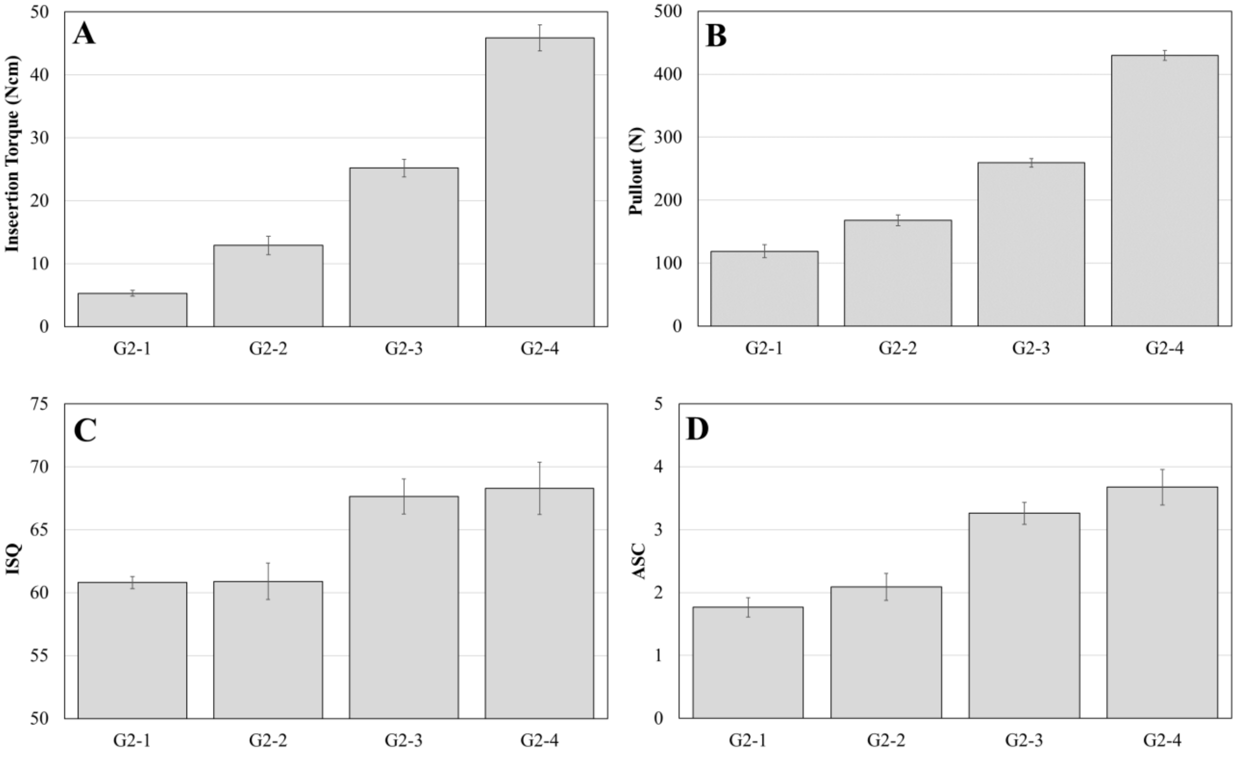

Figure 4.6: Mean IT (A), Pullout (B), ISQ (C) and ASC (D) measurements of group 2. Error bars represent one standard deviation.

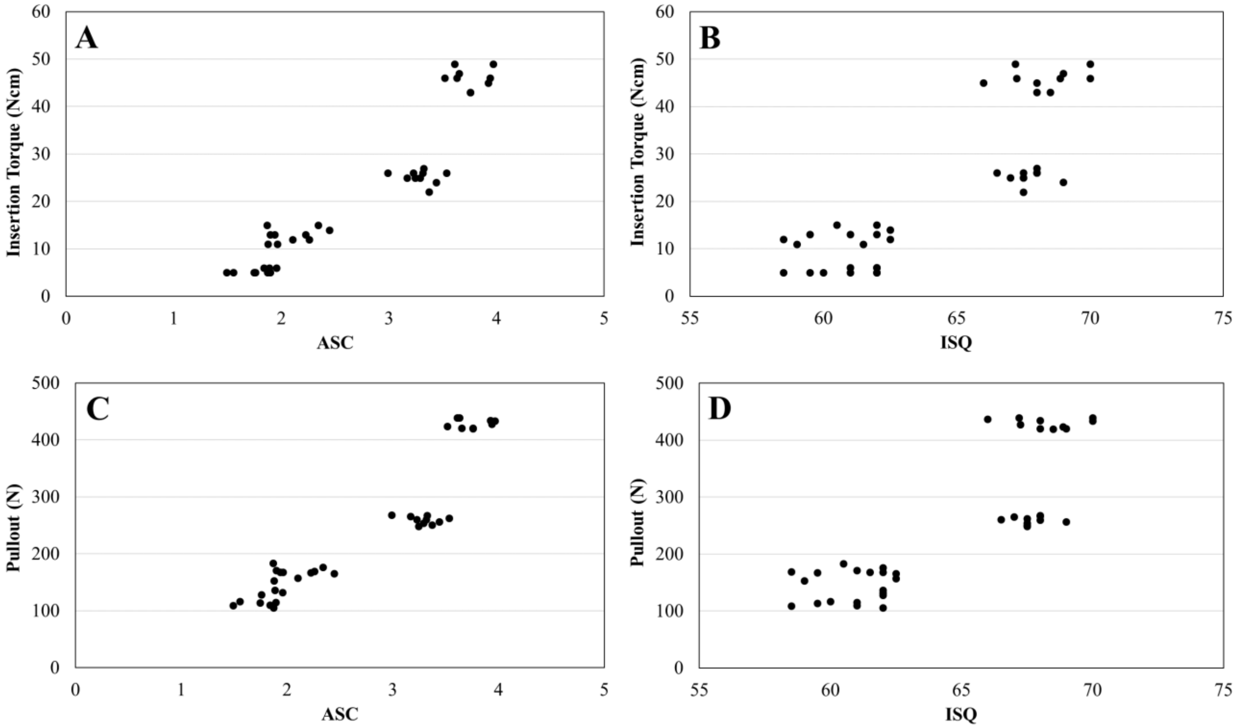

Figure 4.7: Group 2 scatterplots of IT vs. ASC (A) and ISQ (B), and pullout vs. ASC (C) and ISQ (D).

4.7 Discussion

Insertion torque has been used as a standard indicator of primary stability in previous studies (Blume et al., 2021; Friberg et al., 1999; Greenstein & Cavallaro, 2017; Sakoh et al., 2006; Tumedei et al., 2021; Yamaguchi et al., 2020). The pullout test has also previously been used to study implant stability (Gehrke et al., 2021; Huang et al., 2020; Oliscovicz et al., 2013a; Oliscovicz et al., 2013b; Rittel et al., 2017; Seong et al., 2013). Although axial tensile loads do not normally occur *in-vivo*, the pullout test can still provide insight into the biomechanical properties of the bone-implant interface. However, IT is limited to a single measurement at implant placement and the pullout test is not clinically feasible as a destructive mechanical test. RFA addresses these weaknesses by providing a non-invasive method of measuring stability at any given time (until a cemented crown is placed). The ASIST measures stability by using vibrational analysis to estimate the stiffness of the bone-implant interface. This chapter compared the IT, pullout strength, ASIST, and Osstell® ISQ as methods to measure implant stability by evaluating the effects of bone density, implant bonding, and drill sequence in artificial implant systems.

Effects of Bone Density and Implant Bonding

It is generally accepted that bone density is a major determinant of primary stability (Blume et al., 2021; Swami et al., 2016). In the present study, all four stability measurements significantly differed between blocks of different densities in Group 1P. This supports the findings of previous studies using artificial bone block models, where density had a significant effect on IT, pullout force, and ISQ values (Bardyn et al., 2009; Bayarchimeg et al., 2013; da Costa Valente et al., 2019; Gehrke et al., 2021; Oliscovicz et al., 2013a; Oliscovicz et al., 2013b).

The purpose of Group 1S in this study was to simulate the biomechanical differences between primary and secondary stability. Implant bonding also had a significant impact on stability, as a significant increase was observed in the mean pullout force, ISQ, and ASC. While the mean ISQ and ASC values of the #30 blocks in Group 1P was approximately the same as the #20 blocks in Group 1S (ISQ: 69.00 vs. 68.68; ASC: 3.38 vs. 3.42), there was a noticeable difference in the pullout force (380.0 vs. 544.34 N). This can be attributed to the added axial shear resistance provided by the glue, which does not affect the lateral motion measured by the ISQ and ASC.

The use of superglue to model secondary stability does not biologically represent the osseointegration process, nor does it possess equivalent properties of the bone-implant interface *in-vivo*. However, different bonding agents such as epoxy, resin, and glue have been used to simulate an integrated implant in artificial systems in previous work (Veltri et al., 2014; Vien et al., 2019; Westover et al., 2016a). This approach represents a different mechanism of implant stability compared to primary stability by modelling, to some extent, the mechanical stabilization originating from the integration and bonding layer between the implant and bone. The stress and strain distribution at the interface of a newly placed implant is predominantly compressive (Mellal et al., 2004; Sugiura et al., 2016). For a fully bonded implant, stresses tend to be distributed over the entire interface through a combination of compressive and tensile forces (Mellal et al., 2004). This is consistent with the present study, as bonding the implant to the test block resulted in an average ASC increase of 101.3% across each block density, corresponding to a doubling of the interface stiffness. Since the pullout force of the implants bonded to the #40 blocks could not be properly measured in half of the samples, it is expected that the true pullout strength is greater than the reported value (1213.69 ± 122.56 N). Despite this, the pullout force was significantly higher than the other groups and the overall conclusion is unaffected.

The cross validation of artificial secondary stability models in the present study is limited to the ISQ in clinical settings due to the ethics surrounding destructive testing *in-vivo*. However, measured ISQ values were within the range of reported clinical values for newly placed and healed implants. Baftijari et al. reported mean ISQ values of 63.89 ± 6.99 and 69.43 ± 12.72 for implants with primary and secondary stability, respectively (Baftijari et al., 2019). Karl et al. also reported similar mean ISQ values of 69.41 ± 9.34 and 73.42 ± 6.65 for implants in the posterior maxilla at insertion and after healing, respectively (Karl et al., 2008). This suggests that the differences in primary and secondary stability are captured in this study.

Effects of Drill Sequence

IT, pullout force, and ASC values all significantly differed between the four subgroups of Group 2. However, no significant difference was found in the mean ISQ between Groups 2-1 and 2-2, and between Groups 2-3 and 2-4. While the same drill diameter was used in Groups 2-1 and 2-2, the implant beds in Group 2-1 were prepared using a tap drill while the threads in Group 2-2 were cut by the implant itself. The higher stability of Group 2-2 can be attributed to a higher level of mechanical interlocking and bone-implant contact area associated with self-tapping implants. Higher IT values are associated with higher interfacial contact pressure (Yang et al., 2022), which increases the engagement between the implant threads and surrounding material and improves the anchorage of the implant. This is consistent with the fact that the pullout strength of Group 2-2 was also significantly higher than that of Group 2-1. Toyoshima et al. reported higher immediate stability for self-tapping implants, as indicated by IT values and the push-out test, and similarly found no significant difference in RFA measurements (Toyoshima et al., 2011).

Compared to Group 2-3, a smaller drill diameter used for Group 2-4 significantly increased the mean IT, pullout force, and ASC. Previous studies have found a similar conclusion regarding insertion torque and drilling dimension (Bayarchimeg et al., 2013; Coelho et al., 2013; Gehrke et al., 2018). Additionally, IT values that are on the order of the results for Group 2 in the present study, for a similar implant design and drill diameter in #20 polyurethane foam, have been reported in the literature (Gehrke et al., 2021; Hong et al., 2012; Wang et al., 2015). Bayarchimeg et al. varied the final drill diameter for implants (4.1 mm diameter, 11.5 mm length) placed in #20 foam blocks and also found no significant change in ISQ values, despite significant increases in IT with decreasing drill diameter (Bayarchimeg et al., 2013). Sakoh et al. also observed a significant increase in IT and no significant change in ISQ with under-dimensioned drilling for two different implant designs placed in porcine bone (Sakoh et al., 2006).

Overall, the results also suggest that compared to the Osstell®, the ASIST better reflects implant stability as indicated by IT or pullout force values as shown by the scatterplots in Figure 4.7. Additionally, there was no significant difference in ISQ values between Groups 2-1 and 2-2 and between Groups 2-3 and 2-4, despite contradictory results obtained from the other three stability measurements. From Group 2-1 to 2-2, a subsequent increase was observed for the IT from 5.3 to 12.9 Ncm (143.4% increase), pullout force from 118.89 to 168.06 N (41.4% increase), and ASC from 1.76 to 2.09 (18.8% increase). From Group 2-3 to 2-4, a difference in stability was indicated by an increase of IT from 25.2 to 45.9 Ncm (82.1% increase), pullout force from 259.46 to 429.67 N (65.6% increase), and ASC from 3.26 to 3.75 (15.0% increase).

In Group 1P, increasing bone density from 0.32 to 0.48 g/cm^3 increased the IT from 5.3 to 24.8 Ncm (367.9% increase), pullout force from 118.9 to 380.0 N (219.6% increase), and ASC from 1.76 to 3.38 (92.0% increase). Further increasing density from 0.48 to 0.64 g/cm^3 increased the IT to 35.8 Ncm (44.4% increase), pullout force to 531.9 N (40.0% increase), and ASC to 4.32 (27.8% increase). However, for the same subsequent increases in density, the mean ISQ only increases from 60.8 to 69.0 (13.5% increase) and then to 70.35 (1.96% increase). The same trend was seen for when comparing Groups 1P and 1S. For the #20, #30, and #40 foam blocks, bonding the implant increased the mean pullout force by 357.9%, 185.5%, and 128.2%, respectively, and increased the mean ASC by 94.3%, 81.4%, and 128.0%, respectively. The relatively large increase in pullout force for the #20 foam blocks is likely due to the significantly higher shear resistance provided by the superglue. In contrast, bonding the implant increased the mean ISQ of the #20, #30, and #40 foam blocks by 13.0%, 5.3%, and 7.43%, respectively. This suggests that the ISQ is relatively insensitive to changes in stability beyond a certain threshold. Similar conclusions regarding the diminished change in ISQ with increasing stability have been observed in other experimental studies involving polyurethane foam (Bayarchimeg et al., 2013; Tumedei et al., 2021). The ISQ is based on the resonance frequency, and other numerical studies have found a diminished change in resonance frequency with higher bonding strength (Liu et al., 2021; Zanetti et al., 2018). Since the ASIST directly estimates the interfacial stiffness, it does not share the same disadvantage of diminished sensitivity with the Osstell®. This implies that the ASC is more sensitive to changes in stability across a wider range than the ISQ. It can be argued that clinical stability is achieved past a certain threshold (Rowan et al., 2015), and that decreases in sensitivity past this threshold are of less concern. However, it would not then be possible for the ISQ to detect decreases in stability that begin beyond this threshold, and potential risks of late-stage implant failure would not be detected.

A limitation of this study was the use of polyurethane foam, which serves as an approximation of living bone. However, it allows for the standardization of mechanical properties and minimizes its inherent variability in real bone. This is evident by the relatively small variation in pullout force for Groups 1P and 2; the relatively larger variation in Group 1S is likely due to the variation in the amount and distribution of glue applied to the implant face. A similar pattern can be seen in the variation in the corresponding ASC values, which suggests that the ASC closely reflects the condition of the implant's mechanical stability. Another limitation is that the blocks used in this study are not representative of the cortical and cancellous layers of biological bone. However, the use of homogeneous blocks allows for a simpler interface whose mechanical properties are better standardized than real bone. Future work should be done to measure implant stability with the

ASIST in a more realistic substrate. This includes re-developing the analytical model to account for the heterogeneity of real bone and evaluating the correlations between the ASC and other stability measurements.

4.8 Conclusion

This chapter compared the trends in ASC, ISQ, IT, and pullout measurements on the primary stability of dental implants in artificial bone blocks. Bone density, implant bonding, and drill sequence had a significant effect on stability as indicated by IT, pullout force, and ASC values, all of which appear to have a higher sensitivity than the ISQ. Overall, the ASIST device showed a better performance in detecting different levels of stability compared to the Osstell® ISQ. This suggests that compared to RFA, the coupled impact-analytical model technique used by the ASIST more closely reflects the interfacial mechanical properties and is applicable across a broader range of implant stability.

Chapter 5 : Cortical Bone Analytical Model

This chapter details the refinement of the analytical model introduced in Section 2.2 to account for the effects of the cortical bone layer. The refinement of the analytical model was performed to better reflect the physiological structure of bone and improve its suitability in a clinical setting. The analytical model is shown in Figure 5.1. The stiffness and geometric parameters are similar to the previous model outlined in Section 2.2. However, with the addition of the cortical layer, the interfacial stiffness is now represented as a stiffness per unit area that is separated into two components corresponding to the cancellous (k) and cortical bone (k_C). Additionally, the thickness of the cortical layer is defined as L_C.

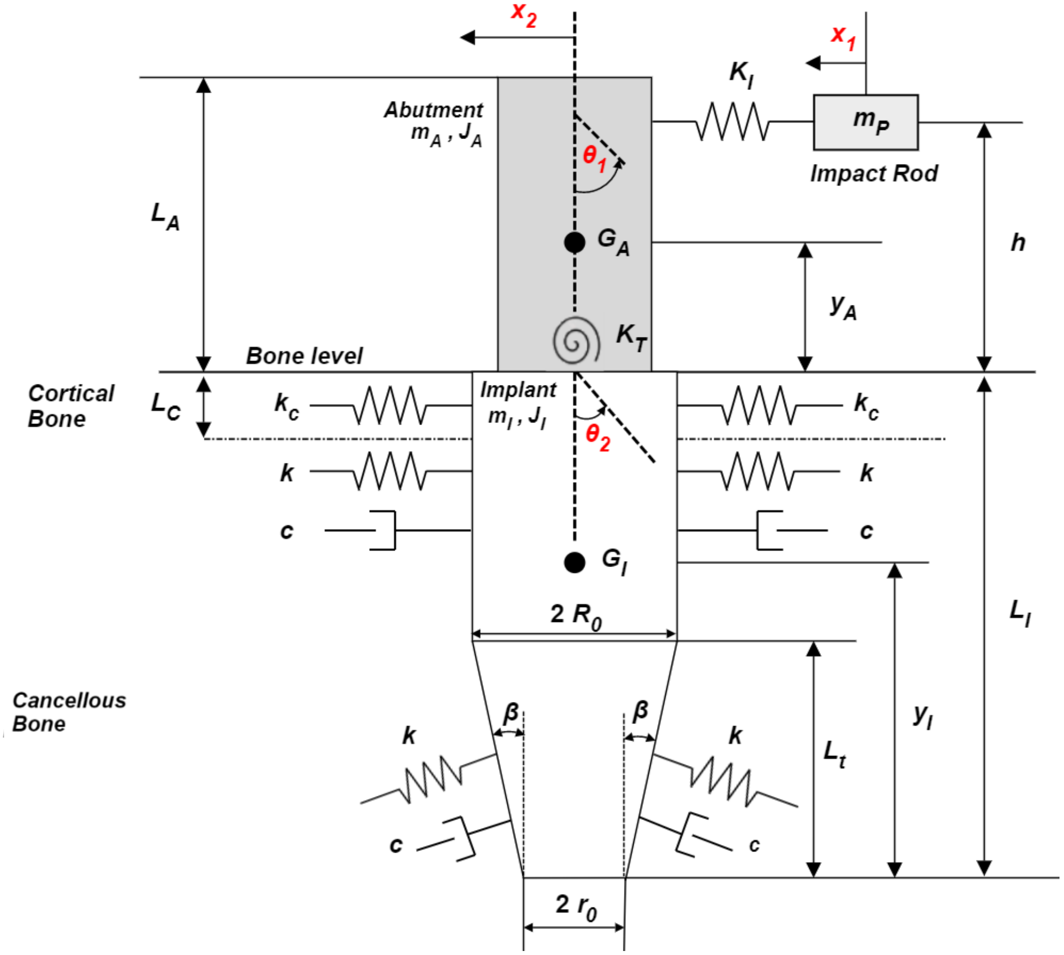

Figure 5.1: Analytical four degree of freedom vibration model of a dental implant system with distinct layers corresponding to cortical and cancellous bone.

The equations of motion are given by:

$$[M]\{\ddot{x}\} + [C]\{\dot{x}\} + [K]\{x\} = \{0\}$$

Where the matrices $[M], [C]$ are identical to the previous model. However, the partitioning of the interfacial stiffness into k and k_C results in a different stiffness matrix:

$$[K] = \begin{bmatrix} K_{11} & K_{12} & 0 & 0 \\ K_{21} & K_{22} & K_{23} & K_{24} \\ 0 & K_{23} & K_{33} & K_{34} \\ 0 & K_{42} & K_{43} & K_{44} \end{bmatrix}$$

Where:

$$K_{11} = K_I$$

$$k_{22} = K_I + 4R_0 \left[k \left(L_b - L_C + L_t \cos^2(\beta) \left(1 - \frac{(L_I^2 - L_b^2)(R_0 - r_0)}{2R_0 L_t^2} \right) \right) + k_C L_C \right]$$

$$K_{33} = K_T + 4R_0 h^2 \left[k \left(L_b - L_c + L_t \cos^2(\beta) \left(1 - \frac{(L_I^2 - L_b^2)(R_0 - r_0)}{2R_0 L_t^2} \right) \right) + k_C L_C \right]$$

$$K_{44} = K_T + \frac{4}{3} R_0 \left[k \left(L_b^3 - L_C^3 + \cos^2(\beta) \left(L_I^3 - L_b^3 - \frac{3(L_I^4 - L_b^4)(R_0 - r_0)}{4R_0 L_t} \right) \right) + k_C L_C^3 \right]$$

$$K_{12} = K_{21} = -K_I$$

$$K_{23} = K_{32} = -4R_0 h \left[k \left(L_b - L_C + L_t \cos^2(\beta) \left(1 - \frac{(L_I^2 - L_b^2)(R_0 - r_0)}{2R_0 L_t^2} \right) \right) + k_C L_C \right]$$

$$K_{24} = K_{42} = -2R_0 \left[k \left(L_b^2 - L_C^2 + \cos^2(\beta) \left(L_I^2 - L_b^2 - \frac{2(L_I^3 - L_b^3)(R_0 - r_0)}{3R_0 L_t} \right) \right) + k_C L_C^2 \right]$$

$$K_{34} = K_{43} = -K_T + 2R_0 h \left[k \left(L_b^2 - L_C^2 + \cos^2(\beta) \left(L_I^2 - L_b^2 - \frac{2(L_I^3 - L_b^3)(R_0 - r_0)}{3R_0 L_t} \right) \right) + k_C L_C^2 \right]$$

The ASC is now calculated by considering the addition of a cortical layer:

$$ASC = \frac{k_{eff}}{4 \times 10^6 \text{ N/m}}$$

$$k_{eff} = 4k_C R_0 L_C + 4k\left(R_0(L_b - L_C) + \cos^2(\beta)\left(R_0 L_t - \left(\frac{R_0 - r_0}{2L_t}\right)(L_I^2 - L_b^2)\right)\right)$$

Chapter 6 : Application of Cortical Bone Model

This chapter details an experimental application of the cortical bone model described in Chapter 5, by evaluating the effects of cortical bone on primary stability using artificial bone blocks. The purpose of this chapter is to validate the refined cortical bone analytical model in a similar manner to the model introduced in Chapter 2, in order to fulfill SA #2 and SA #3 as described in Section 1.2.

This chapter will be submitted for publication to the International Journal of Oral and Maxillofacial Implants as:

Jar, C., Archibald, A., Gibson, M., Westover, L. An in-vitro investigation of the effects of cortical density and thickness on dental implant stability using insertion torque, RFA, pullout testing, and an approach coupling the impact technique with an analytical model. *International Journal of Oral and Maxillofacial Implants*.

6.1 Introduction

The primary stability of dental implants is determined by the mechanical engagement between the bone and implant. Bone quality is a key determinant of primary stability (Blume et al., 2021; Swami et al., 2016), and often dictates preoperative planning and implant selection. An increase in bone density or cortical bone thickness can improve the retention of newly placed implants, which is attributed to a higher degree of bone mineralization and reduction in implant micromotion and bone strain (Miyamoto et al., 2005; Sugiura et al., 2016).

The majority of reported implant failures occur in the early stages and is attributed to poor primary stability in low density bone (Friberg et al., 1991; Mohajerani et al., 2017; Staedt et al., 2020; Yang et al., 2021). Significantly higher failure rates are reported in the maxilla compared to the mandible (Bischof et al., 2004; Brånemark et al., 1977; Esposito et al., 1998; Friberg et al., 1999; Staedt et al., 2020), which has been attributed to the maxilla possessing a lower cortical bone thickness and bone density (Tanaka et al., 2018). This highlights the need for a non-invasive method of monitoring stability to identify implants that are at risk of failure.

Several studies have investigated the effects of cortical bone on primary stability as measured by IT, ISQ, or pullout strength (Bayarchimeg et al., 2013; Chávarri-Prado et al., 2020; Elibol et al., 2020; Hong et al., 2012; Howashi et al., 2016; Merheb et al., 2010; Miyamoto et al., 2005; Tanaka et al., 2018). Chapter 5 described a refined model that accounts for the different mechanical properties of cortical and cancellous bone. This chapter details the application of this model in the ASIST approach by evaluating the effects of cortical bone on primary stability in artificial bone blocks, as measured by ASC, ISQ, IT, and pullout force values.

6.2 Materials

Solid polyurethane foam blocks (Sawbones, Vashon Island, WA, USA) were used as an artificial substitute for bone to standardize bone properties, and in accordance with ASTM standard F1839-08 (ASTM, 2021). Each blocks contained two layers of foam representing cancellous and cortical bone. Cancellous bone in the human jaw was represented using #20 foam (ρ = 0.32 g/cm^3) (Bayarchimeg et al., 2013; Hong et al., 2012). Cortical bone was simulated using #30 foam (ρ = 0.48 g/cm^3), #40 foam (ρ = 0.64 g/cm^3), and #50 foam (ρ = 0.80 g/cm^3) with thicknesses of 1, 2, and 3 mm, for a total of nine different experimental groups. An additional group of homogeneous #20 foam blocks was included as a control group, for a total of ten experimental groups. Each group was denoted by its cortical density in pcf and cortical thickness in mm, and contained 10 replicates.

Bone-level tapered Straumann implants (4.1 mm diameter, 10 mm length) were placed in each block, and a conical-shaped healing abutment (6 mm diameter, 4 mm height) was used for all ASC measurements (Straumann, Waldenburg, Switzerland). Implant beds were prepared using a 2.2 mm pilot drill (740 rpm), 2.8 mm followed by a 3.5 mm drill (740 rpm), and finally a 4.1 mm profile drill (740 rpm) (Figure 4.1; Straumann 2017). The same drilling sequence was used for all groups to control for the effect of drilling dimension on primary stability (Blume et al., 2021; Coelho et al., 2013; Sakoh et al., 2006).

6.3 Primary Stability Measurements

IT, ASC, ISQ and pullout measurements were obtained by following the same protocol outlined in Chapter 4. During implant insertion, the maximum IT value was recorded with a torque gauge (FTD2-S, Tohnichi, Tokyo, Japan). RFA measurements were done using the Osstell® ISQ and SmartPeg (Type 54, Osstell, Göteborg). The probe was oriented across each edge of the block with four repeat ISQ measurements per edge, for a total of sixteen measurements per block. Five repeat

ASC measurements were taken with the ASIST. The device was held in a custom stand and kept at a horizontal position and distance of 1 mm from the top of the abutment (Figure 4.2). Pullout tests were done using a custom bolt fitted to the interior threads of the implant. Blocks were held on the platform by gently tightening wedge clamps to avoid over-compression of the foam. Tests were performed with a universal testing machine (Qualitest Quasar 100, Lauderdale, FL, USA) at a rate of 5 mm/min (Gehrke et al., 2021; Huang et al., 2020). A 12.5 kN load cell with 0.5 N resolution was used. Pullout strength was indicated as the maximum load.

6.4 Determining the ASC

With the addition of a cortical layer, there are now two unknown stiffness parameters (k and k_C) that must be determined when matching the analytical model to the experimental data. However, by relating k and k_C, matching can be done based on a single parameter. Assuming small deformations, Hooke's law can be used to relate the stiffness of each layer to its elastic modulus:

$$\text{Stiffness} = \frac{EA}{L}\ (\text{N/m})$$

where E is the elastic modulus, L is the length of the material along the loading direction, and A is the cross-sectional area. L corresponds to the length of the block in the direction of impact, which is the same for both layers. Additionally, since k_C and k are defined as a stiffness per unit area (N/m^3), the relation is independent of A and the cortical stiffness is proportional to the cancellous stiffness by the ratio of their elastic moduli, defined as γ:

$$k_C = \gamma k, \qquad \gamma = \frac{E_{cortical}}{E_{cancellous}}$$

As there is no bond between the implant and bone, the forces transmitted through the interface are mainly compressive (Sugiura et al., 2016). It is also assumed that the implant (titanium) is rigid relative to bone so that tensile forces on the block due to implant bending can be neglected. As a result, γ can be defined as the ratio of the compressive modulus of each material (Table 6.1).

Table 6.1: Compressive modulus of each foam type.

Foam	Bone	Density (g/cm^3)	Compressive Modulus (MPa)	Theoretical γ
20	Cancellous	0.32	210	
30-20	Cortical – Cancellous	0.48 – 0.32	445 – 210	2.12
40-20	Cortical – Cancellous	0.64 – 0.32	759 – 210	3.61
50-20	Cortical – Cancellous	0.80 – 0.32	1148 – 210	5.47

When determining the ASC for the purely cancellous bone blocks of the control group (#20 foam), γ was set to 1 and L_C was set to 0 mm.

6.5 Data and Statistical Analysis

Statistical analysis was performed using SPSS software (ver. 29.0, IBM Co., Armonk, NY, USA) with a significance level of 0.05. Normality and homogeneity were verified with the Shapiro-Wilk test and Levene's test, respectively. The general effects of cortical thickness and density were analyzed using two-factor ANOVA on the cortical block groups only. Then, t–tests with a Bonferroni adjustment for multiple comparisons were performed to determine differences in IT, pullout force, ISQ, and ASC values between each group (including the control). The Pearson's correlation was used to evaluate the correlations between the IT, pullout strength, ISQ, and ASC.

6.6 Results

Mean values for each group are listed in Table 6.2 and shown in Figure 6.1. Two-factor ANOVA of the cortical block groups found that IT, pullout, and ASC values were significantly influenced by the thickness and density of the cortical layer ($p < 0.001$). ISQ values were significantly affected by the cortical thickness ($p < 0.001$), but not the cortical density ($p = 0.265$).

Table 6.2: Insertion torque, pullout force, ISQ, and ASC values (mean ± SD) for each experimental group.

Group (Foam – Thickness)	IT (Ncm)	Pullout (N)	ISQ	ASC
Control	12.9 ± 1.5	168.1 ± 8.6	60.90 ± 1.47	2.09 ± 0.21
30-1	12.0 ± 1.4	179.1 ± 12.7	64.23 ± 1.56	2.12 ± 0.16
30-2	14.1 ± 1.5	179.5 ± 9.8	65.88 ± 1.53	2.51 ± 0.14
30-3	19.2 ± 1.7	245.0 ± 10.7	66.18 ± 1.62	2.88 ± 0.17
40-1	14.6 ± 1.1	189.3 ± 11.3	65.07 ± 1.48	2.12 ± 0.14
40-2	15.9 ± 1.1	186.7 ± 11.6	64.79 ± 2.50	2.48 ± 0.11
40-3	20.9 ± 3.1	282.0 ± 11.2	66.96 ± 2.20	3.57 ± 0.37
50-1	15.1 ± 0.7	186.7 ± 10.1	64.27 ± 1.97	2.14 ± 0.20
50-2	17.6 ± 2.0	221.1 ± 12.0	66.24 ± 2.18	2.71 ± 0.18
50-3	30.0 ± 3.2	361.3 ± 28.9	67.86 ± 2.14	4.25 ± 0.46

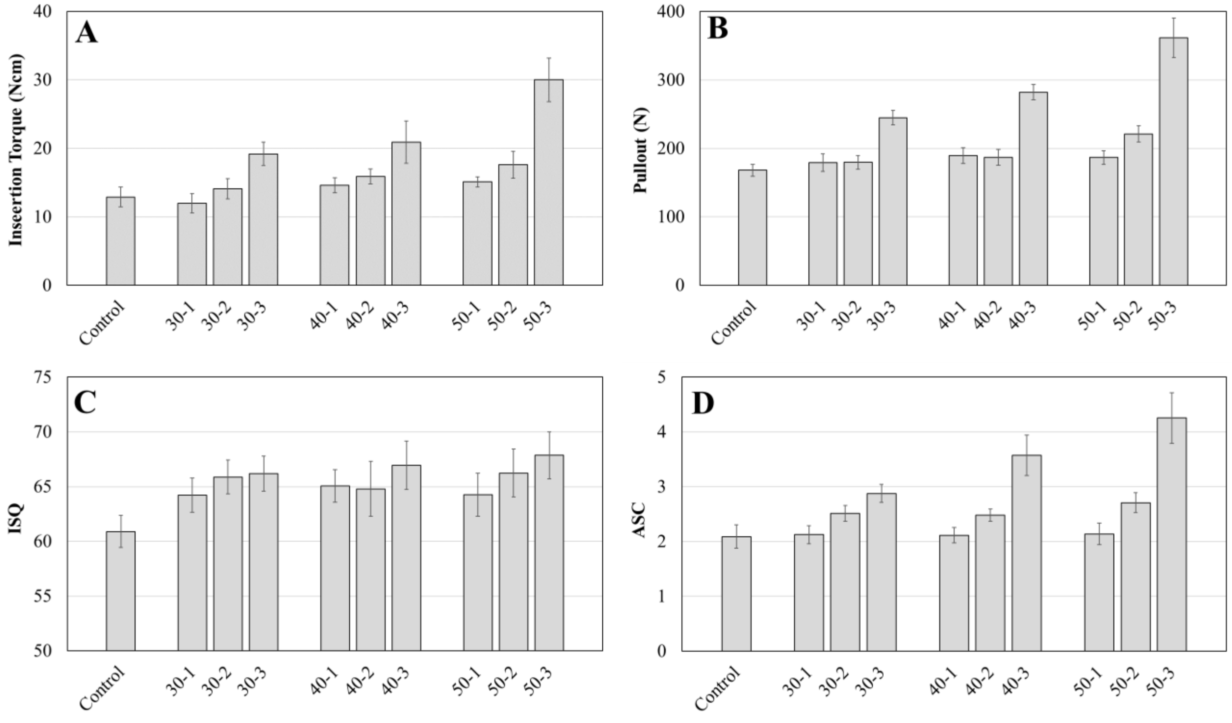

Figure 6.1: Mean IT (A), Pullout (B), ISQ (C) and ASC (D) measurements of each group. Error bars represent one standard deviation.

Significant differences in stability measurements between groups were determined using a *t*–test with a Bonferroni adjustment for multiple comparisons and are shown in Table 6.3. The IT, pullout strength, and ASC values for groups with a 3 mm layer thickness were all significantly higher than groups with the same cortical density but lower thickness ($p < 0.05$). The lowest IT was measured for group 30-1, while the lowest pullout force, ISQ, and ASC values were recorded for the control group. On the other hand, the highest values for each stability measurement was recorded for group 50-3, where the IT, pullout strength, and ASC were significantly higher than every other group ($p < 0.001$). However, the mean ISQ did not significantly differ from groups 30-2, 30-3, 40-1, 40-3, and 50-2 ($p > 0.05$).

With respect to the control group, tests for multiple comparisons found that the mean IT did not differ significantly from groups 30-1, 30-2, 40-1, and 50-1 ($p > 0.40$), while the pullout strength did not vary significantly from groups 30-1, 30-2, 40-2, and 50-1 ($p > 0.10$). While the mean ISQ was significantly lower than every other group ($p < 0.001$), the mean ASC did not significantly differ from groups 30-1, 40-1, and 50-1 ($p > 0.99$).

Table 6.3: Post-hoc multiple comparisons using *t*-tests with Bonferroni correction. Each letter denotes a significant difference in the mean values for the ^{a}Insertion Torque, ^{b}Pullout, ^{c}ISQ, and ^{d}ASC.

	Ctrl	30-1	30-2	30-3	40-1	40-2	40-3	50-1	50-2	50-3
Ctrl		**c**	**c,d**	**a,b,c,d**	**b,c**	**a,c,d**	**a,b,c,d**	**c**	**a,b,c,d**	**a,b,c,d**
30-1			**d**	**a,b,d**		**a**	**a,b,d**	**a**	**a,b,d**	**a,b,c,d**
30-2				**a,b,d**	**d**		**a,b,d**	**d**	**a,b**	**a,b,d**
30-3					**a,b,d**	**a,b,d**	**b,d**	**a,b,d**	**b**	**a,b,d**
40-1							**a,b,d**		**a,b,d**	**a,b,d**
40-2							**a,b,d**		**b**	**a,b,c,d**
40-3								**a,b,d**	**a,b,d**	**a,b,d**
50-1									**a,b,d**	**a,b,c,d**
50-2										**a,b,d**
50-3										

Pearson correlation coefficients between each of the stability measurements are shown in Figure 6.2. The highest correlation coefficient was observed between the IT and pullout strength ($r = 0.946$). However, relatively high correlation coefficients were also observed between the ASC and IT ($r = 0.872$) and between the ASC and pullout strength ($r = 0.917$). In contrast, the ISQ was found to have a weaker correlation to IT ($r = 0.495$) and pullout strength ($r = 0.552$). Additionally, the ASC and ISQ were also found to have a similar correlation ($r = 0.602$). All correlations were statistically significant ($p < 0.01$).

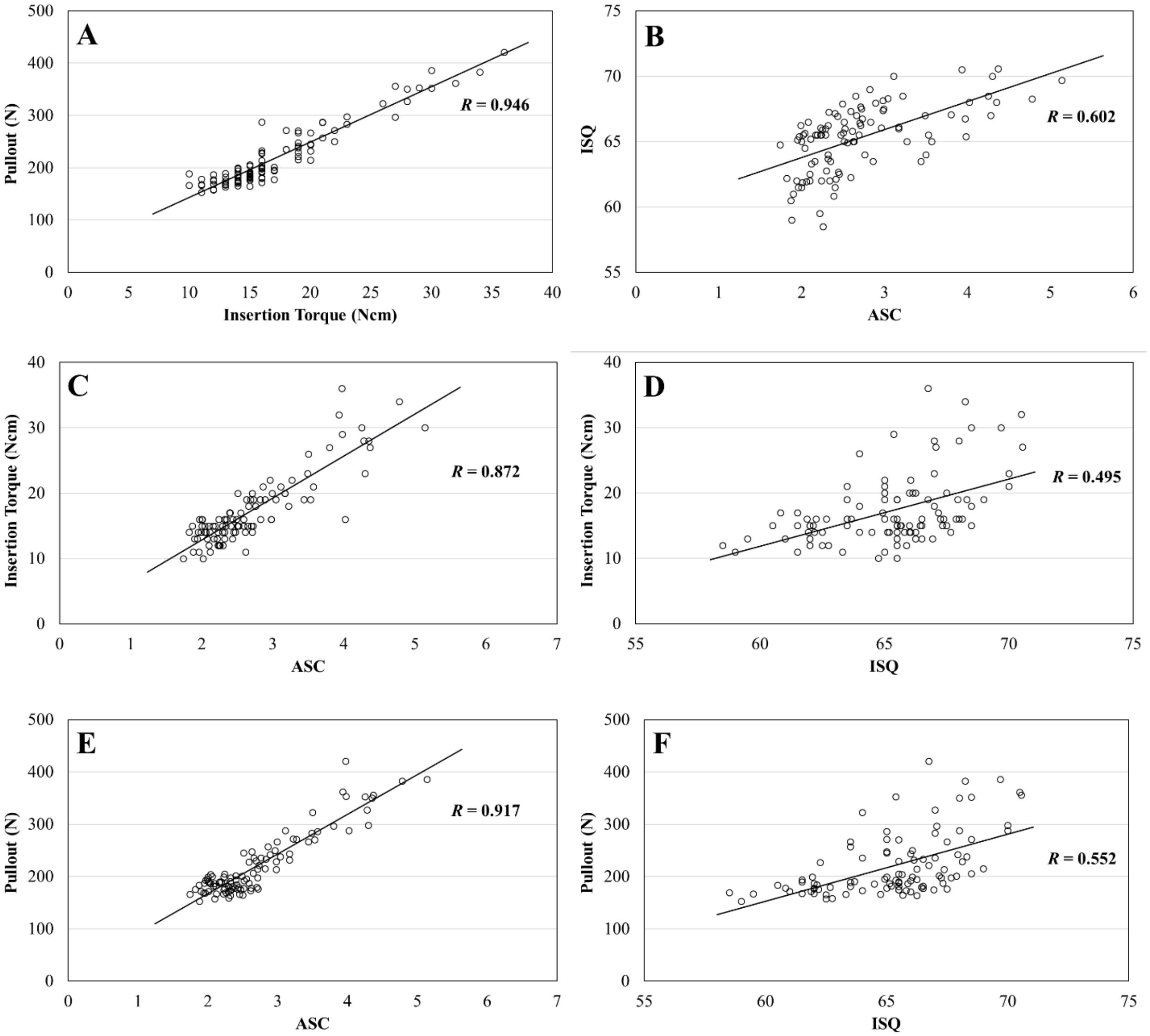

Figure 6.2: Pearson correlation between IT and pullout (A), ASC and ISQ (B), ASC and IT (C), ISQ and IT (D), ASC and pullout (E), and ISQ and pullout (F). All correlations were significant ($p < 0.05$).

6.7 Discussion

IT and pullout tests were included in this study since they both provide a mechanical measurement of implant stability. Clinically, IT has been used to indicate primary stability at implant placement (Blume et al., 2021; Friberg et al., 1991; Greenstein & Cavallaro, 2017; Turkyilmaz & McGlumphy, 2008). While many destructive mechanical tests have been used to characterize implant stability in *ex-vivo* or artificial models, the pullout test is specified by ASTM F543-07e1 as the standard method for axial removal of metallic bone screws (ASTM, 2013) and has been used in several studies (da Costa Valente et al., 2019; Gehrke et al., 2021; Oliscovicz et al., 2013a). However, the IT is limited to a single measurement and the pullout test is clinically infeasible due to its destructive nature. RFA was developed as a non-invasive method of monitoring implant stability over time, and attempts to indirectly measure implant stability using the correlation between the resonance frequency and the interfacial stiffness (Atsumi et al., 2007; Meredith et al., 1997a). However, resonance frequencies have an inherent reduction in sensitivity at higher bonding strength (Liu et al., 2021; Zanetti et al., 2018), and can vary with implant, abutment, and bone geometry (Bischof et al., 2004; Karl et al., 2008; Karl et al., 2008; Westover et al., 2018a). As a result, the ASIST was developed as a method of directly estimating the interfacial stiffness by measuring the dynamic behaviour of the implant system and matching it to the predicted response in a corresponding analytical model. This chapter details the application and validation of the cortical bone analytical model used by the ASIST, and investigates the effects of cortical thickness and density on implant stability.

During insertion, cortical bone exhibits a strengthening effect to cancellous bone due to its higher mechanical properties, by increasing compression at the coronal apex and improving the distribution of occlusal forces (Blume et al., 2021; Chávarri-Prado et al., 2020). While the cortical thickness and density had a significant effect on IT, pullout strength, and ASC values, there are minimal differences in stability between different cortical densities for a thickness of 1 or 2 mm. Additionally, only the cortical thickness had a significant effect on the ISQ. However, Bardyn et al. found that both cortical thickness and density had a significant effect on the ISQ values of Straumann implants (3.3 mm diameter, 12 mm length) in polyurethane foam (Bardyn et al., 2009). This disparity can be attributed to the inclusion of a cortical thickness of 1 mm in the present study. Both studies used Straumann implants, which do not possess any threads in the coronal portion of the implant neck (Figure 6.3). For low thickness cortical bone, its density likely has a minimal effect on implant stability, as there is no engagement between the cortical bone and the implant threads. This is consistent with the noticeably larger increases in IT and pullout force when increasing the cortical thickness from 2 to 3 mm. This is consistent with the results, as there is a small difference in the IT, pullout strength, and ASC values of groups with different cortical densities and a thickness of 1 or 2 mm, yet noticeably larger values when increasing the thickness to 3 mm.

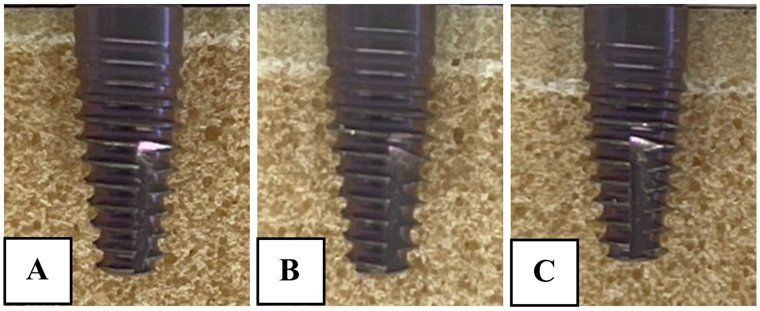

Figure 6.3: Amount of contact between the implant threads and cortical layer for a cortical thickness of 1 mm (A), 2 mm (B), and 3 mm (C).

A numerical study by Alaqeely et al. found that the maximum stresses during insertion and pullout were located in the cortical bone (Alaqeely et al., 2020). The concept of a threshold cortical thickness is also discussed by Elibol et al. on the pullout strength of mini dental implants, who also found a statistically significant effect of the cortical density and thickness on the pullout strength of mini dental implants (Elibol et al., 2020). Other authors have reported a positive correlation between IT and pullout force using polyurethane foam (da Costa Valente et al., 2019; Gehrke et al., 2021). Additionally, previous studies have found a positive relationship between the cortical thickness and IT of dental implants in polyurethane foam (Barros et al., 2022; Bayarchimeg et al., 2013; Chávarri-Prado et al., 2020; Hong et al., 2012).

While the ISQ was only significantly affected by the cortical thickness, the other stability measurements were affected by both density and thickness. This suggests that RFA has a lower sensitivity than the other three methods to changes in stability due to the effects of cortical bone. Additionally, the ASIST demonstrated a stronger correlation to IT and pullout strength compared to the Osstell® device. Similar correlations between IT and ISQ values were reported by Cassetta et al. (*r* = 0.494), do Vale Souza et al. (*r* = 0.457) and Merheb et al. (*r* = 0.57) in human patients at implant placement (Cassetta et al., 2022; do Vale Souza et al., 2021; Merheb et al., 2010). Heitzer et al. also found a similar correlation between the ISQ and IT (r = 0.414) for tapered Straumann implants (4.1 mm diameter, 8 mm length) installed in #20 foam (Heitzer et al., 2022). Seong et al. found a similar Pearson correlation (r = 0.476) between the ISQ and pullout strength (Seong et al., 2013).

A numerical study by Ding et al. found that the stresses from an oblique or lateral load is mainly transferred to the cortical bone (Ding et al., 2009). As a result, the mechanical properties of the cortical layer should affect the dynamic response measured by the ASIST and therefore the ASC value. IT and pullout strength are direct mechanical measurements of specific characteristics of implant stability. Compared to the ISQ, the ASC score was better able to detect differences in mechanical stability, as indicated by IT and pullout strength. A total of 30 comparisons were categorized as having a significant difference in IT. Within this category, a significant difference was also observed in the ASC value for 27 comparisons (90.0%). In contrast, the ISQ only differed significantly in 8 comparisons (26.7%). With respect to the pullout strength, a total of 31 comparisons were categorized as significantly different. Within this category, a significant difference was also observed in the ASC value for 27 comparisons (87.1%), and the ISQ in 8 comparisons (25.8%). Overall, the results suggest that the ASC value is more representative of the implant's mechanical stability of the implant than the ISQ.

The main limitation of this study is the use of polyurethane foam as a substitute for biological bone. However, polyurethane foam allows for better standardized mechanical properties, and is more suitable in controlling for sample variability. This is shown by the relatively low variability in the pullout strength and ASC. However, the evaluation of the ASIST device in real bone to investigate the effects of cancellous and cortical properties is warranted. Additionally, work should be done to investigate the correlations between the ASC and other measures of stability, such as the removal torque and push-in test (Swami et al., 2016).

6.8 Conclusion

This chapter presents an *in-vitro* application of the refined analytical model to measure the effects of cortical bone on primary stability. IT, pullout strength, and ASC values were all significantly affected by the cortical density and thickness. However, only the cortical thickness influenced ISQ values, suggesting that RFA is less sensitive than the other three methods. The ASIST device showed a stronger correlation with IT and pullout measurements than the Osstell®, suggesting that the ASC is more representative of the implant's mechanical stability, and that the analytical model is an accurate representation of the physical system.

Chapter 7 : Cortical Model Validation

7.1 Introduction

In the analytical model, the cortical layer is characterized with a thickness L_C and stiffness proportionality constant γ. The analytical model was evaluated to determine if the model is an accurate representation of the physical system. The analysis was performed using ASIST measurements from Chapter 6, taken on the control group (entirely cancellous, 0.32 g/cm^3 density) and Group 50-3 (0.32 g/cm^3 cancellous bone with a 3-mm thick cortical layer of 80 g/cm^3 density). For example, when inputting a signal obtained from a purely cancellous bone block, the corresponding model response should possess $\gamma = 1$ for a specified non-zero thickness L_C, or a layer thickness of 0 mm for a specified $\gamma > 1$. In contrast, the predicted model response for a signal obtained from the cortical bone blocks should reflect the cortical layer, such that $\gamma > 1$ and $L_C > 0$ mm.

7.2 Methods

A custom Mathematica program (Wolfram Mathematica 12.3, Champaign, IL, USA) was used to determine the interfacial stiffness of a signal by iterating between different values of γ and L_C in the analytical model. The values of γ and L_C that resulted in the highest R^2 value between the signal and model response were then compared to the properties of the actual system.

For the cancellous bone blocks, the best-fit values for L_C and γ were determined. The value for L_C that resulted in the best fit to the experimental data (as quantified by the R^2 value) was determined by arbitrarily setting $\gamma = 3$ and repeating the matching process for values of L_C between 0 and 5 mm. This process was repeated for γ, where L_C was fixed at 3 mm and the fitting process was repeated for γ between 1 and 7.

For the cortical bone blocks, the actual cortical thickness of each block was measured using a shadowgraph profile projector (PH-3515F, Mitutoyo, Sakado, Japan) with a resolution of 0.001 mm. For each block, L_C was set to the measured value and the model was fit to the data for values of γ between 1 and 7. The value of γ that yielded the highest R^2 value was determined for each block.

To evaluate the sensitivity of the model to variations in γ and L_C, best-fit values for the ASC and interfacial stiffness k were recorded during the validation process for each block. These were then compared to the values obtained when setting L_C or γ to their theoretical values as described at the end of Section 6.4. For the cancellous bone blocks, the theoretical values for γ and L_C corresponded to 1 and 0 mm, respectively. For the cortical bone blocks, the theoretical value for γ was set to 5.47, and L_C was set to the measured cortical thickness of each block. The full analysis is given in Appendix C.

7.3 Results

For the cancellous bone blocks, the mean best-fit value of L_C was 0.05 ± 0.07 mm, where γ was fixed at 3 for all cases. A representative example of the validation process for a cancellous bone block replicate is shown in Figure 7.1 to Figure 7.4. Figure 7.1 shows k, ASC, and R^2 values plotted against corresponding values of γ between 1 and 7. Figure 7.2 shows the example fits obtained for γ values at the extremes ($\gamma = 1,7$) and the case resulting in the highest R^2 value.

The mean best-fit value of γ was 1.17 ± 0.08, where L_C was fixed at 3 mm for all cases. Figure 7.3 shows k, ASC, and R^2 values plotted against corresponding values of L_C between 0 and 5 mm. Figure 7.4 shows example fits obtained for layer thicknesses of 0, 3, and 5 mm, where the highest R^2 value was found for a thickness of 0 mm.

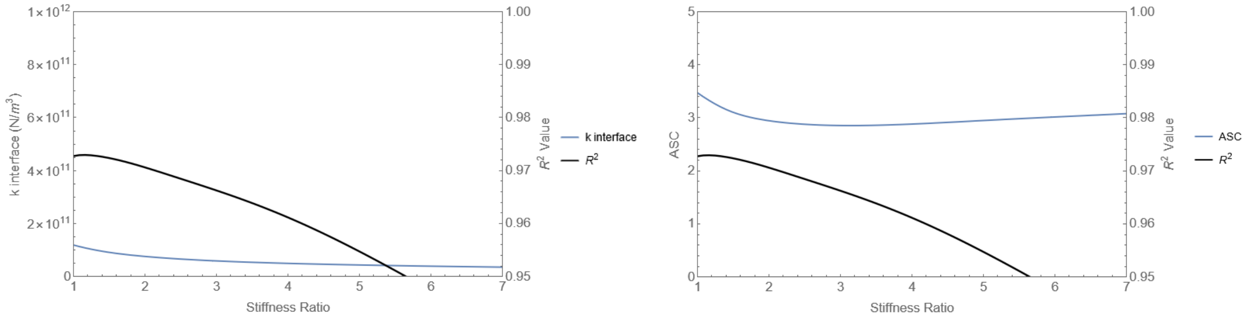

Figure 7.1: k and R^2 values (left) and ASC, R^2 values (right) obtained from the matching process by varying γ between 1 and 7 while holding L_C fixed at 3 mm for cancellous bone blocks.

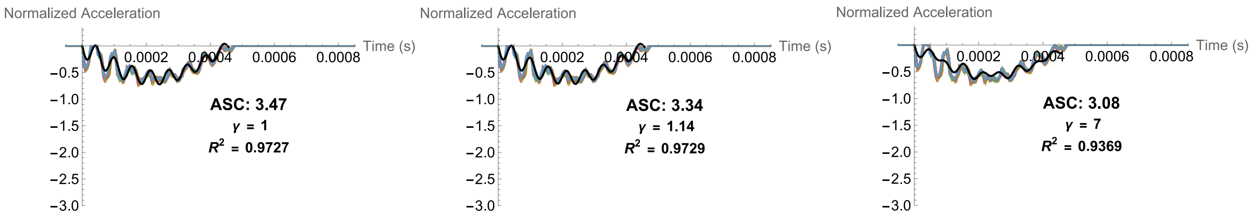

Figure 7.2: Matching model response to the measured signal for $\gamma = 1$ (left), $\gamma = 1.14$ (middle), and $\gamma = 7$ (right), while L_C is fixed at 3 mm in all instances (cancellous bone blocks).

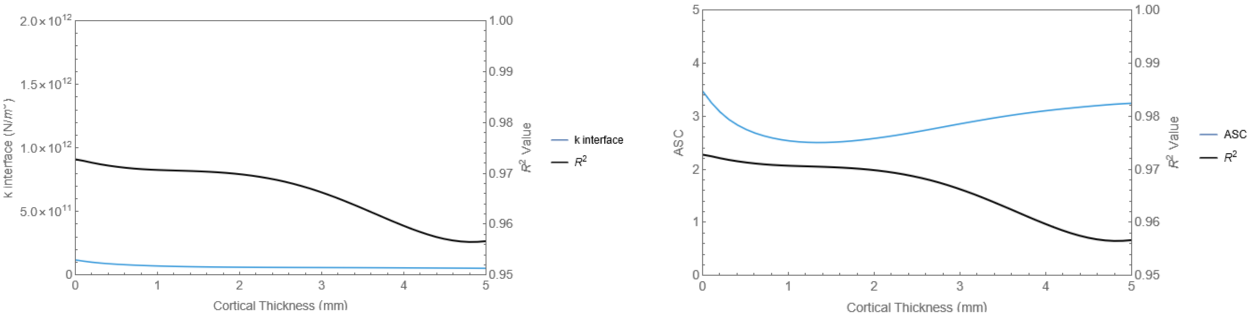

Figure 7.3: k and R^2 values (left) and ASC, R^2 values (right) obtained from the matching process by varying L_C between 0 and 5 mm while holding γ fixed at 3 for cancellous bone blocks.

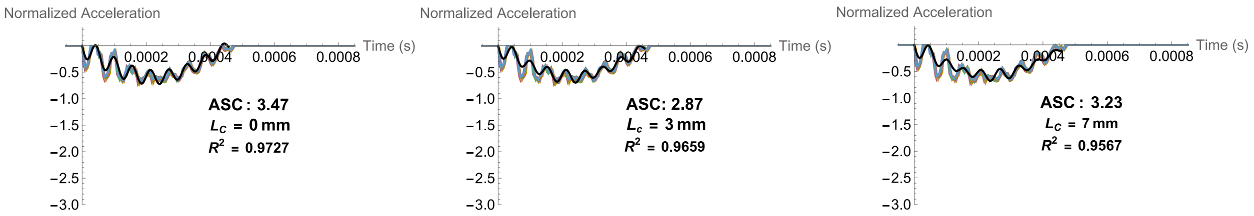

Figure 7.4: Matching model response to the measured signal for $L_C = 0$ mm (left), $L_C = 3$ mm (middle), and $L_C = 5$ mm (right), while γ is fixed at 3 in all instances (cancellous bone blocks).

For the cortical bone blocks, the mean best-fit value of γ was 4.76 ± 0.42, where in each case, L_C was set to the thickness of each block measured with the shadowgraph projector. An example of the analysis for a cortical bone block replicate is shown in Figure 7.5 and Figure 7.6. Figure 7.5 shows k, ASC, and R^2 values plotted against corresponding values of γ between 1 and 7. Figure 7.6 shows example fits obtained for γ values at the extremes ($\gamma = 1,7$) and the case resulting in the highest R^2 value.

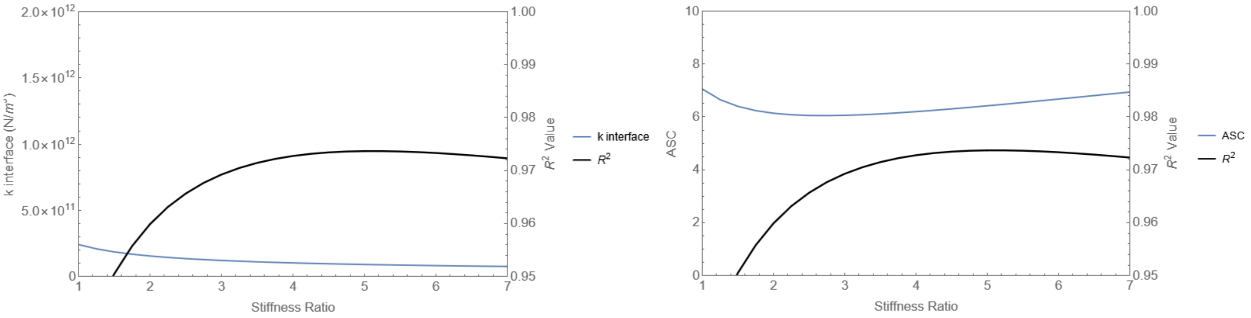

Figure 7.5: k and R^2 values (left) and ASC, R^2 values (right) obtained from the matching process by varying γ between 1 and 7, while setting L_C at the measured thickness of the specific cortical bone block.

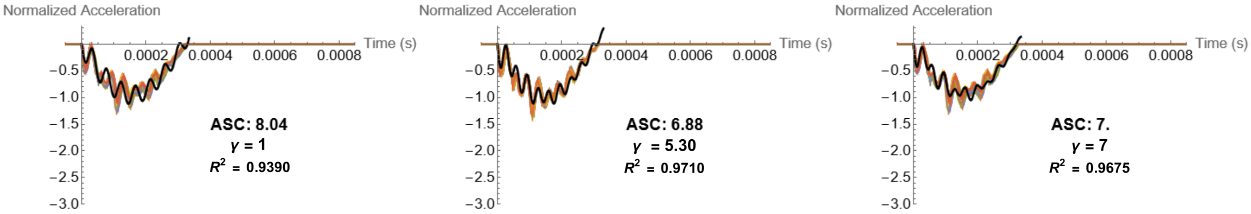

Figure 7.6: Matching model response to the measured signal for $\gamma = 1$ (left), $\gamma = 5.30$ (middle), and $\gamma = 7$ (right), while setting L_C at the measured thickness of the specific cortical bone block.

For the cancellous bone blocks, there was no significant difference between the values for the ASC and interfacial stiffness k (p = 0.099) obtained using theoretical and best-fit values of L_C and γ (Figure 7.7). Similarly, for the cortical bone blocks, no significant difference was observed between the values for the ASC (p = 0.130) and interfacial stiffness k (p = 0.192), obtained using theoretical and best-fit values for γ (Figure 7.8).

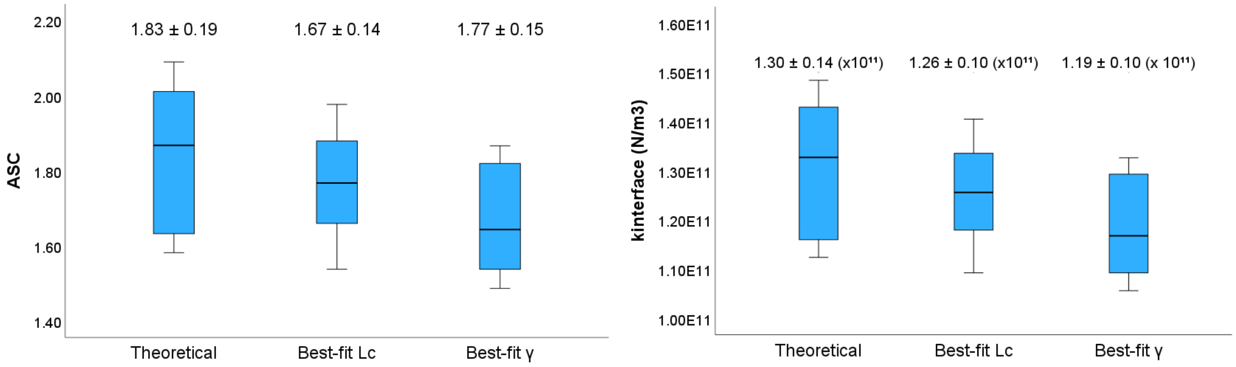

Figure 7.7: Values for the ASC (left) and interfacial stiffness k (right) corresponding to the theoretical and best-fit values for γ and layer thickness L_C for the cancellous bone blocks. Values are shown as mean ± standard deviation.

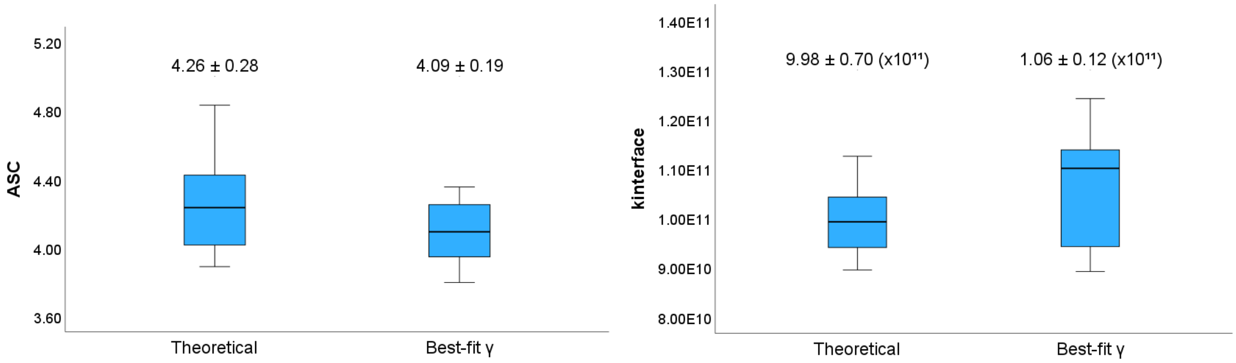

Figure 7.8: Values for the ASC (left) and interfacial stiffness k (right) corresponding to the theoretical and best-fit values for γ for the cortical bone blocks. Values are shown as mean ± standard deviation.

7.4 Discussion

There are promising results from the validation of the analytical model. For the cancellous bone blocks, the value of γ in the model that resulted in the best fit with the measured signal when assuming a non-zero layer thickness was 1.17 ± 0.08. On the other hand, the best-fit value of L_C with an assumed γ of 3 was 0.05 ± 0.07 mm. As a result, the model best matches the cancellous block experimental data when the layer thickness is near zero for values of γ greater than 1, or when γ is approximately 1 for a non-zero layer thickness. In both cases, the best-fit values of γ and L_C correspond to the case of a uniform interface with no distinct cortical layer, which matches the physical properties of the cancellous bone blocks.

For the cortical bone blocks, the thickness of each layer was measured and used to determine a best-fit value of γ, which was found to be 4.76 ± 0.42. The difference between the best-fit value and theoretical value of 5.47 for γ can possibly be attributed to the viscoelastic properties of polyurethane foam. As the analytical model assumes that the implant rotates about the abutment connection, the linear velocity is higher in the lower portion of the implant. With the viscous properties of the foam, the cancellous region has a larger role than expected in stabilizing the implant, which explains why the best-fit value for γ was found to be lower than its theoretical value. Despite this, the best-fit value of γ lies well above 1, which indicates that the data is best represented by including distinct layers in the model. Additionally, there is a clear difference between the best-fit values for γ between the cancellous and cortical bone blocks, while relatively consistent estimates of k, corresponding to the cancellous bone stiffness, were found between the two groups. This is consistent with the fact that the cancellous bone was simulated using #20 foam in both groups. As a result, there is strong evidence to suggest that the properties of the physical system are captured in the analytical model.

Chapter 8 : Parametric Sensitivity Analysis

8.1 Sensitivity of Homogeneous Bone Model to k, K_I, K_T

When determining the ASC score, the measured signal is matched to the analytical model solution, which in turn depends on the impact stiffness (K_I), torsional stiffness (K_T), and interfacial stiffness (k). As a result, it is important to understand how each stiffness parameter affects the natural frequencies of the system, which determines the shape of the predicted analytical response. A sensitivity analysis was performed to determine how variations in k, K_I, and K_T can affect the model solution. This chapter presents an example analysis on the RC-6.0HA implant-abutment system. A full analysis of each combination of implant and healing abutment can be found in Appendix B.

Modal analysis was performed for a low, moderate, and high stiffness value by setting k to 0.1×10^{12} N/m^3, 0.5×10^{12} N/m^3, and 1.0×10^{12} N/m^3, respectively. The first four mode shapes (solid black lines) are shown in Figure 8.1. The initial position of the system is indicated by the gray dashed lines, and the dots represent the positions of the impact rod, abutment at the height of impact, implant-abutment connection, and bottom of the implant.

Out of the four modes, only the first three appear to be sensitive to changes in k. Between the low and moderate stiffness values, there is an increase in p_1 by 889 Hz (84.7 %), p_2 by 10,387 Hz (70.6 %), p_3 by 11,718 Hz (55.0 %), and p_4 by 2079 Hz (2.4 %). Further increasing k from a moderate to high stiffness value increases p_1 by 584 Hz (30.1 %), p_2 by 7697 Hz (30.7 %), p_3 by 13,571 Hz (41.1 %), and p_4 by 3526 Hz (3.9 %). This suggests in the lower stiffness region, p_1 is most sensitive to k, followed by p_2. While there is a decrease in sensitivity to k for both p_1 and p_2 in the upper stiffness region, a moderate increase of approximately 30 percent is still observed for both modes. While p_3 is shown to consistently increase across the entire range of k, the overall contribution of the third and fourth modes to the total response with the given excitation mechanism is considered negligible, as only the first two modes can be seen in the experimental data.

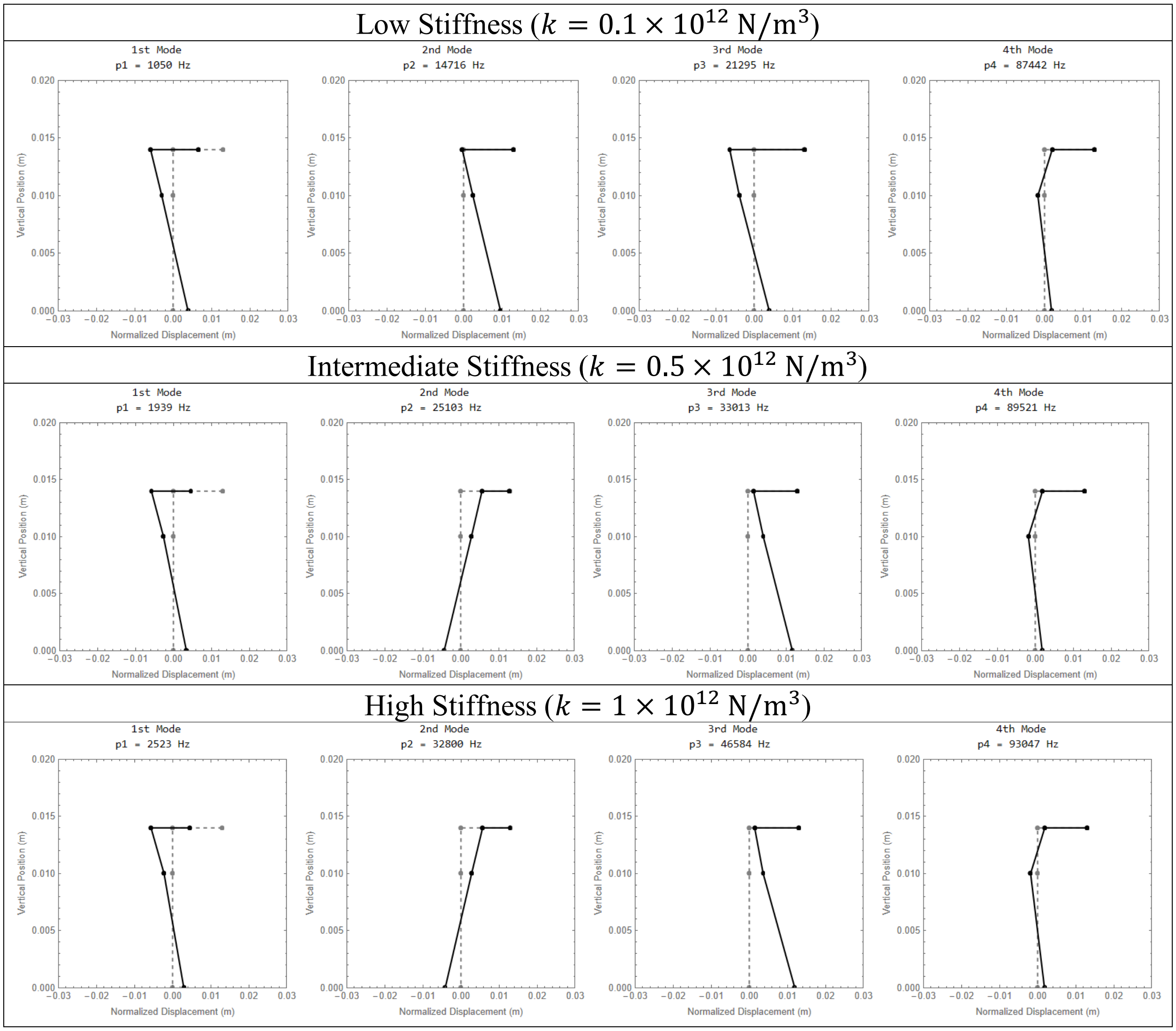

Low Stiffness ($k = 0.1 \times 10^{12}\ \mathrm{N/m^3}$)

Intermediate Stiffness ($k = 0.5 \times 10^{12}\ \mathrm{N/m^3}$)

High Stiffness ($k = 1 \times 10^{12}\ \mathrm{N/m^3}$)

Figure 8.1: Modal analysis of the RC-6.0HA system for a low (top row), moderate (middle row), and high (bottom row) interfacial stiffness. Mode shapes and initial positions are indicated by the solid black and gray dashed lines, respectively. Dots correspond to the position of the impact rod, abutment at the height of impact, implant-abutment connection, and bottom of the implant.

As the frequency response of each measured signal is mainly comprised of the first and second modes, an analysis of the relationship between the stiffness parameters and first and second modal frequencies was performed to observe how p_1 and p_2 change with respect to K_I, K_T, and k. This will improve the interpretation of ASIST measurements by identifying which aspects of the measured signal are sensitive to changes in the mechanical properties of the interface. The relationships between p_1, p_2 and the interfacial stiffness k were evaluated at different values of

K_I. Similarly, the relationships between K_I, K_T and p_1, p_2 were evaluated for a range of values for k to observe trends across a range of implant stability.

The effects of varying k on the first and second mode frequencies are shown in Figure 8.2 for various values of the impact stiffness K_I. In the lower stiffness region, both frequencies are sensitive to changes in k and are approximately the same for each value of K_I. When transitioning to the upper stiffness region, the curves begin to branch off and there is a gradual decrease in stability for both p_1 and p_2. This implies that for low values of k, p_1 and p_2 are mainly affected by k and independent of K_I. Measuring stability may be relatively more difficult for a stiffer interface, as both frequencies are less sensitive to k while their sensitivity to K_I increases. However, changes in k for a stiff interface are not of immediate concern, since the implant is already considered stable to begin with.

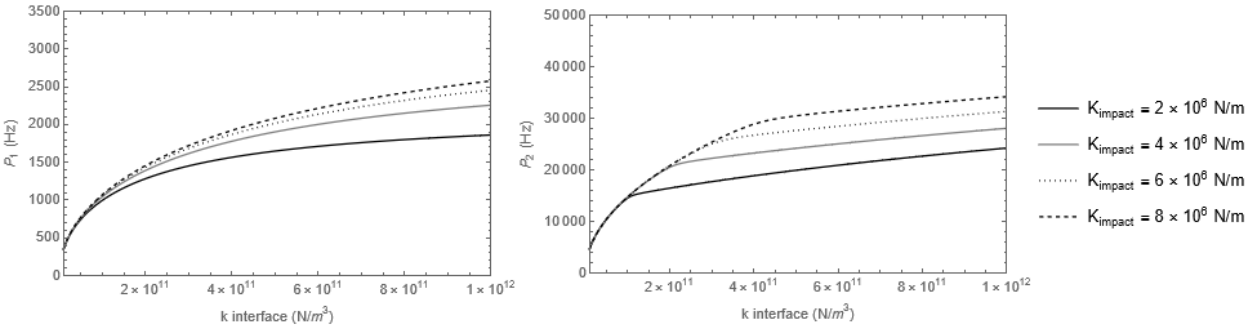

Figure 8.2: Relationship between the interfacial stiffness k and p_1 (left) and p_2 (right) for the RC-6.0HA system for various values of K_I.

The effects of varying K_I on p_1 and p_2 are shown in Figure 8.3 for various values of k. Both subfigures show the previously described trends in the sensitivity of both frequencies. From the plots, K_I has the potential to significantly affect the first and second mode frequencies. The sensitivity of the first mode to changes in K_I increases for larger values of k, as increasing K_I from 2×10^6 N/m to 8×10^6 N/m increases p_1 from 1282 Hz to 1457 Hz (13.6 %) for the lowest interface stiffness ($k = 0.2 \times 10^{12}$ N/m^3), and from 1861 Hz to 2578 Hz (38.5 %) for the highest interface stiffness ($k = 0.8 \times 10^{12}$ N/m^3). Overall, the second mode frequency appears to be more sensitive to K_I than the first mode frequency, as the curves do not plateau to the same extent as those corresponding to p_1. Increasing K_I from 2×10^6 N/m to 8×10^6 N/m increases p_2 from

16,444 Hz to 20,793 Hz (26.4 %) for the lowest interface stiffness ($k = 0.2 \times 10^{12}$ N/m^3), and from 24,224 Hz to 34,187 Hz (41.1 %) for the highest interface stiffness ($k = 0.8 \times 10^{12}$ N/m^3).

Although both frequencies appear to be sensitive to the interface and impact stiffness, it is important to note that in both figures, the curves corresponding to different values of K_I or k do not intersect in their range of expected values. Therefore, p_1 and p_2 in the measured signal can be used separately to determine each possible combination of k and K_I. The combination of values of k and K_I that best match the measured frequencies in the signal can then be determined in order to estimate the interface stiffness.

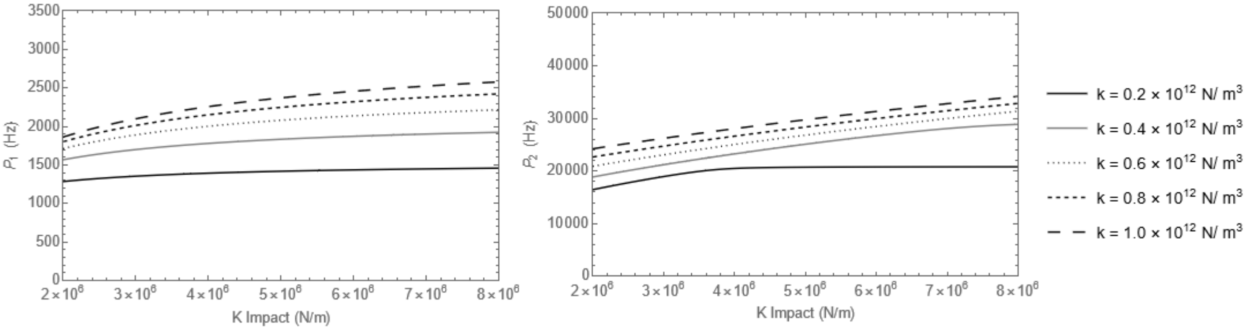

Figure 8.3: Relationship between the impact stiffness K_I and p_1 (left) and p_2 (right) for the RC-6.0HA system for various values of k.

The relationship between the torsional stiffness K_T and the first and second mode frequencies is shown in Figure 8.4 for different values of k. In all cases, significant changes in p_1 and p_2 only occur at low values of K_T. Beyond a certain threshold, there is virtually no change in the frequency response when varying K_T. As K_T increases, the implant-abutment connection becomes more rigid, such that p_1 is increasingly related to the underlying interfacial stiffness k. Physically, if the abutment is sufficiently tightened in the implant, the two bodies essentially move together as a rigid body. This is also seen in the corresponding mode shapes (Figure 8.1), as there is almost no relative rotation between the abutment and implant. The higher sensitivities of p_1 and p_2 at lower values of K_T indicate that the ASIST may be able to detect loosening of the abutment in the implant socket.

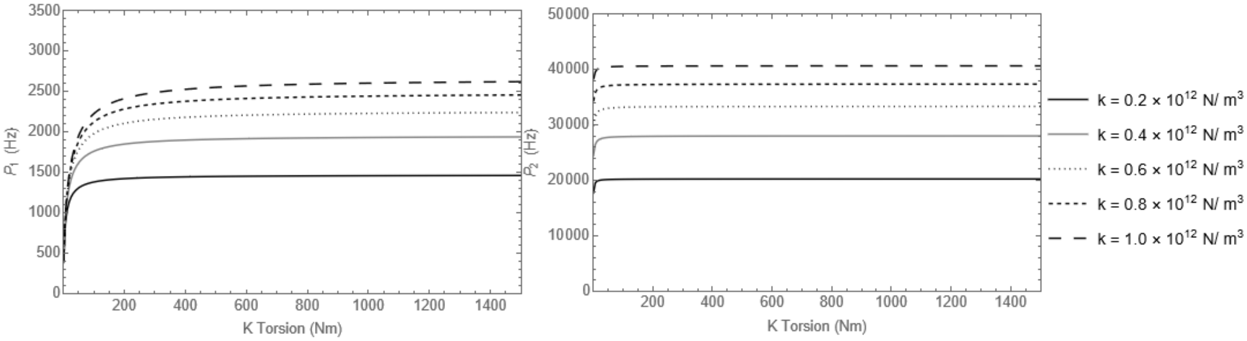

Figure 8.4: Relationship between the torsional stiffness K_T and p_1 (left) and p_2 (right) for the RC-6.0HA system for various values of k.

8.2 Sensitivity of Cortical Bone Model to k_C, L_C

An analysis was performed to determine the sensitivity of the cortical bone model solution to variations in the cortical stiffness per unit area k_C and thickness L_C. An example analysis of the RC-6.0HA system is shown in this chapter. The full analysis can be found in Appendix B.4.

Each parameter was assigned a reference value that corresponds to typical measurements in a clinical setting. Assuming that #20 polyurethane foam is representative of cancellous bone (Comuzzi et al., 2020; Tumedei et al., 2021), a reference cancellous stiffness k_{ref} of approximately 0.25×10^{12} N/m^3 was determined using the average of ASIST measurements taken with #20 bone blocks (ρ = 0.32 g/cm^3). The cortical stiffness reference value (k_{Cref}) was determined by multiplying k_{ref} by the ratio of the elastic moduli of cortical and cancellous bone. An approximate ratio of 10 was found based on reported values in the literature (Nagasao et al., 2002; Sugiura et al., 2016), giving a reference value of 2.5×10^{12} N/m^3 for the cortical stiffness. Based on reported measurements of the cortical thickness in the human jaw, the reference value for the cortical thickness L_{Cref} was set to 1.5 mm (Miyamoto et al., 2005; Stefano et al., 2021).

The first and second mode frequencies were determined for various values of k_C and L_C. While one parameter was varied, the other was held fixed at their reference value. This was performed over a range of values for k and plotted as separate curves. k_{ref} was also included in the analysis, to determine the individual effects of k_C and L_c on p_1 and p_2 when the other parameters are on the order of values expected in clinical situations.

Figure 8.5 shows the effect of varying k_C on p_1, p_2 in the model solution, where the cortical thickness is fixed at its reference value of 1.5 mm. In each subfigure, the red line corresponds to the effects of varying k_C when L_C and k are both set to their reference values.

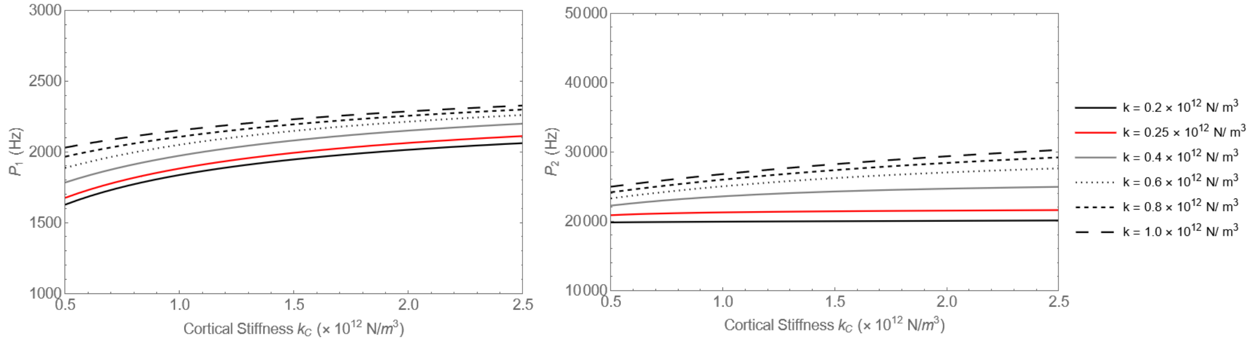

Figure 8.5: Effects of varying the cortical stiffness k_C on p_1 (left) and p_2 (right) with various values of k for the RC-6.0HA system. The cortical thickness is fixed at its reference value of 1.5 mm in all cases.

The profiles and starting positions of each curve suggest that both frequencies are influenced by k_C and k. For p_1, the similar profiles of each curve suggest that the sensitivity of p_1 to k_C is relatively unaffected by k. In contrast, the sensitivity of p_2 to k_C appears to decrease at lower values of k. Additionally, the sensitivities of p_1 and p_2 to changes in k_C are highest at lower values of k_C, and diminish as k_C increases.

For example, consider the case where k is 0.2×10^{12} N/m^3. In the region of low cortical stiffness, increasing k_C from 1×10^{12} to 2×10^{12} N/m^3 increases p_1 from 1837 Hz to 2014 Hz (9.6 %), and increases p_2 from 19,910 Hz to 20,034 Hz (0.6 %). In the region of high cortical stiffness, increasing k_C from 5×10^{12} to 6×10^{12} N/m^3 increases p_1 from 2176 Hz to 2200 Hz (1.1 %) and p_2 from 20,346 Hz to 20,446 Hz (0.5 %).

Next, consider the case for a high cancellous stiffness of 1×10^{12} N/m^3. In the region of low cortical stiffness, increasing k_C from 1×10^{12} to 2×10^{12} N/m^3 increases p_1 from 2152 Hz to 2286 Hz (6.2 %), and increases p_2 from 26,787 Hz to 29,356 Hz (9.6 %). In the region of high cortical stiffness, increasing k_C from 5×10^{12} to 6×10^{12} N/m^3 increases p_1 from 2436 Hz to 2459 Hz (0.9 %) and p_2 from 32,949 Hz to 33,545 Hz (1.81 %).

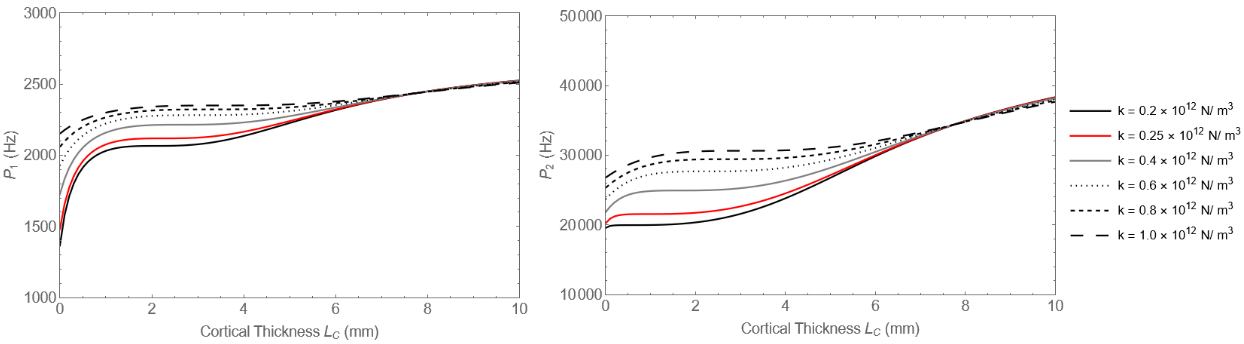

Figure 8.6: Effects of varying the cortical thickness L_C on p_1 (left) and p_2 (right) with various values of k for the RC-6.0HA system. The cortical stiffness is fixed at its reference value of 2.5×10^{12} N/m^3 in all cases.

Figure 8.6 shows the effect of varying the cortical thickness for various values of k on p_1 and p_2, while the cortical stiffness was held at its reference value. In each subfigure, the red line corresponds to the effects of varying L_C when k_C and k are both set to their reference values. At a fixed cortical stiffness, p_1 and p_2 approach a common value for large values of L_C, regardless of k. This is due to the fact that the extreme value of 10 mm for the cortical thickness represents the implant's length. As L_C approaches the implant's length, this common value corresponds to a system where the stiffness per unit area is entirely comprised of k_C.

As k decreases, p_1 and p_2 are shown to vary more sharply when L_C is less than approximately 0.5 to 1 mm. A plateau effect is observed for each curve while the layer thickness is approximately between 1 and 3 mm. Both frequencies begin to further increase past this point, where more noticeable increases are seen with lower values of k.

Assuming that the reference values are representative of a clinical setting, the relevant trends in p_1 and p_2 correspond to the red curves in the leftmost regions of Figure 8.5 and Figure 8.6. This is illustrated in Figure 8.7, where p_1 is increasingly sensitive to both changes in k_C and L_C as the overall interfacial stiffness decreases. This implies that the ASIST most effectively measures stability for compromised bone qualities, which correspond to a lower interfacial stiffness.

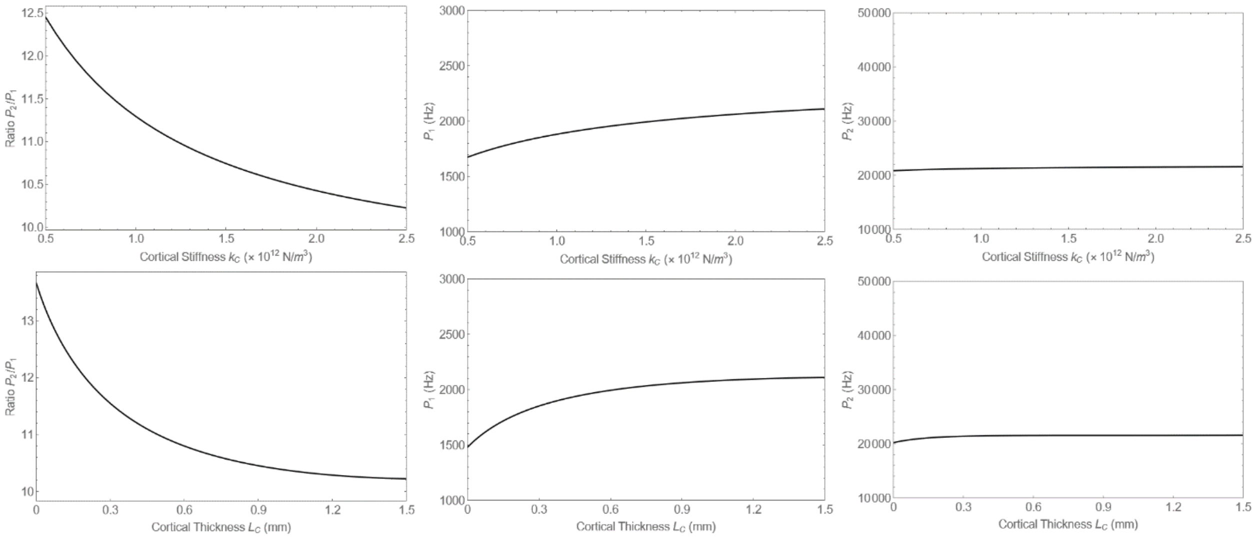

Figure 8.7: Relationship between the ratio p_2/p_1, p_1, and p_2 and the cortical stiffness per unit area k_C and cortical thickness L_C for the RC-6.0HA system in the range of clinically expected values.

Chapter 9 : Summary and Conclusion

9.1 Summary

This thesis details the development of a dental implant analytical model and its experimental application to measure implant stability using the Advanced System for Implant Stability Testing (ASIST). To measure implant stability, the device utilizes an impact technique to obtain the acceleration response of the impact rod when it is in contact with the implant system. By using an analytical model of the implant system, the signal can be matched to the corresponding model response from which the interfacial stiffness can be estimated. The interfacial stiffness is non-dimensionalized and reported as the ASIST Stability Coefficient (ASC). Overall, all three specific aims were fulfilled by the preliminary and refined analytical models.

The ASIST technique was able to provide a consistent estimate of the interfacial stiffness for different superstructures in the same implant installation. Compared to the Osstell® ISQ, which is an RFA measurement device that is currently used by clinicians to monitor implant stability, the ASIST showed a stronger correlation to insertion torque (IT) and pullout strength values. It was also found that the ASC was sensitive to changes at the interface across a wider range of stability, while the sensitivity of the ISQ diminishes with increasing stiffness.

The analytical model was further developed to incorporate the different mechanical properties of the cortical and cancellous bone layers, and evaluated *in vitro* to determine the effects of cortical bone on primary stability. It was found that ASC, ISQ, IT, and pullout strength values all increased significantly in the presence of a cortical layer, suggesting that the ASIST is able to detect changes in stability due to the effects of cortical bone. The analytical model was also able to detect the presence of a cortical layer for a given signal measurement, as the best fit values for the cortical stiffness and thickness were reflective of the actual system's physical properties.

Overall, the ASIST method was shown to properly isolate the interfacial stiffness for the same implant installation with different components, with a stronger correlation to mechanical stability indicators than other contemporary stability measurement devices. *In vitro* experiments and subsequent analyses suggest that both analytical models described in this work are an accurate representation of the physical system. This has strong implications for potential of the ASIST to be used as a non-invasive, stability measurement device in clinical settings.

9.2 Conclusions

- The four degree of freedom analytical model of the ASIST with a uniform interface was developed for dental implant systems.
- The ASIST technique was able to isolate and estimate the interface stiffness, as the analytical model was able to account for differences in the geometric and inertial properties of different components of the implant-abutment system.
- Bone density, insertion torque, implant bonding, and cortical bone were all factors affecting the ASC value.
- Compared to the Osstell® ISQ, which is based on resonance frequency analysis, the ASC was more closely related to the interfacial mechanical properties across a broader range of stability.
- The analytical model was refined to incorporate the mechanical properties of different regions corresponding to cortical and cancellous bone.
- The ASIST was able to detect changes in implant stability due to the presence of a stiffer outer layer, suggesting that the refined analytical model is an accurate representation of a physical system with distinct layers simulating cortical and cancellous bone.
- The first two frequencies in the predicted model response were mainly sensitive to the interfacial stiffness and the impact stiffness, while being virtually insensitive to the torsional stiffness if the abutment is adequately tightened in the implant socket.

9.3 Implications

This work provides a preliminary evaluation of the ASIST device in measuring the stability of dental implant systems. This work provides another method of implant stability measurement that can be used to better understand its mechanical stability over time. This work shows that it is possible to model the impact response of a dental implant system and obtain estimates of the interface stiffness. These estimates are significantly affected by clinically relevant factors, such as bone density and drill protocol, and are also strongly correlated to other mechanical measurements such as insertion torque and pullout force, which are techniques that have been established in a clinical and research setting, respectively. This work also shows that the ASIST is more closely related to these mechanical measurements than the Osstell®, which is a clinically used stability measurement device. As a result, the ASIST can potentially be implemented clinically as a way of estimating the stability of patients over time. Clinicians utilize computer models to plan implant placement surgery. As a result, implant and abutment solid models are readily available to clinicians and can be easily assembled to estimate their properties. Further comparisons can be done with other clinical measurements such as insertion torque and would provide a better understanding of how the ASC is related to implant stability in a clinical setting.

9.4 Future Work

9.4.1 Implant Substrate

The development of the ASIST was performed using polyurethane foam as an artificial substitute to human bone. Although the use of polyurethane foam allows for the standardization of mechanical properties, bone blocks are not representative of the human jaw bone. Further work should be done on implant systems that are more representative of *in-vivo* conditions. The device should be tested using animal models, such as porcine or bovine bone, to address differences in morphology compared to polyurethane foam. Future studies should also be done on substrates that mimic the geometry of the jaw bone. In addition to commercially available biomechanical models, the use of 3D printed models could allow the variation of material properties while controlling for geometric factors.

9.4.2 Application to Other Implant Designs

This work involved Straumann tapered implants that only differed in diameter. Future work should be done with different implant designs, such as cylindrical implants or implants of different length. Additional investigations should be done to determine the effects of different implant surface treatments on the ASC score. This is especially important in primary stability, where no osseointegration has occurred and stability is reliant on the frictional contact and mechanical engagement between the implant and surrounding bone.

9.4.3 Correlation with Other Methods

While pull-out tests have been used to characterize the mechanical properties of the interface, several other destructive test methods exist and should be used to evaluate their correlation with the ASC score. This includes, but is not limited to, removal torque and push-in tests. Additionally, the Osstell® device, which is based on RFA, was used as a means of comparison to the ASIST.

Comparisons should be performed with other devices that also utilize the impact technique, such as the PerioTest® and AnyCheck®.

9.4.4 Longitudinal Clinical Study

The ASIST device should be evaluated *in-vivo* by measuring the stability of implants in a clinical setting to measure the extent of osseointegration. ASC, ISQ, and IT measurements can be taken at the time of implant placement and correlated in a similar manner to the work in this thesis. ASIST and Osstell® measurements can also be compared by evaluating the longitudinal trends during bone remodeling and using imaging techniques, such as CT scans, as a qualitative reference to the extent of osseointegration.

References

Alaqeely, R., Babay, N., & AlQutub, M. (2020). Dental implant primary stability in different regions of the Jawbone: CBCT-based 3D finite element analysis. *The Saudi Dental Journal, 32*(2), 101-107.

Al-Nawas, B., Wagner, W., & Grötz, K. (2006). Insertion torque and resonance frequency analysis of dental implant systems in an animal model with loaded implants. *International Journal of Oral and Maxillofacial Implants, 21*(5), 726-732.

Andersson, P., Verrocchi, D., Volpe, S., Sahlin, H., & Sennerby, L. (2019). Factors influencing resonance frequency analysis (RFA) measurements and 5-year survival of Neoss dental implants. *International Journal of Dentistry*, 3209872.

ASTM. (2023). *Standard F543-23 (2023); Standard specification and test methods for metallic medical bone screws.* West Conshohocken, PA, USA: American Society for Testing and Materials.

ASTM. (2021). *Standard F1839-08 (2021); Standard specification for rigid polyurethane foam for use as a standard material for testing orthopaedic devices and instruments.* West Conshohocken, PA, USA: American Society for Testing and Materials.

Atsumi, M., Park, S., & Wang, H. (2007). Methods used to assess implant stability: current status. *International Journal of Oral and Maxillofacial Implants, 22*(5), 743-754.

Baftijari, D., Benedetti, A., Stamatoski, A., Baftijari, F., Susak, Z., & Veljanovski, S. (2019). Influence of resonance frequency analysis (RFA) measurements for successful osseointegration of dental implants during the healing period and its impact on implant assessed by Osstell mentor device. *Open Access Macedonian Journal of Medical Sciences, 7*(23), 4110-4115.

Bardyn, T., Gedet, P., Hallermann, W., & Buchler, P. (2009). Quantifying the influence of bone density and thickness on resonance frequency analysis: an in vitro study of biomechanical test materials. *International Journal of Oral and Maxillofacial Implants, 24*, 1006-1014.

Barros, L., da Silva, C., Camargos, G., Marcantonio Jr, E., de Oliveira, G., & Barros-Filho, L. (2022). In vitro evaluation of the influence of bone cortical thickness on the primary stability of conventional- and short-sized implants. *Journal of Clinical and Experimental Dentistry, 14*(2), e138-e143.

Bayarchimeg, D., Namgoong, H., Kim, B., Kim, M., Kim, S., Kim, T., . . . Koo, K. (2013). Evaluation of the correlation between insertion torque and primary stability of dental implants using a block bone test. *Journal of Periodontal and Implant Science, 43*, 30-36.

Bedrossian, E. (2020). Do dental implant width and length matter? *Compendium of Continuning Education in Dentistry, 41*(7), e1-e5.

Berglundh, T., Abrahamsson, I., Lang, N., & Lindhe, J. (2003). De novo alveolar bone formation adjacent to endosseous implants. *Clinical Oral Implants Research, 14*, 251-262.

Beschnidt, S., Cacaci, C., Dedeoglu, K., Hildebrand, D., Hulla, H., Iglhaut, G., . . . K, A. (2018). Implant success and survival rates in daily dental practice: 5-year results of a non-interventional study using CAMLOG SCREW-LINE implants with or without platform-switching abutments. *International Journal of Dentistry, 4*(1), 33.

Bischof, M., Nedir, R., Szmukler-Moncler, S., Bernard, J., & Samson, J. (2004). Implant stability measurement of delayed and immediately loaded implants during healing. *Clinical Oral Implants Research, 15*(5), 529-539.

Blanc-Sylvestre, N., Bouchard, P., Chaussain, C., & Bardet, C. (2021). Pre-clinical models in implant dentistry: past, present, future. *Biomedicines, 9*(11), 1538.

Blume, O., Wildenhof, J., Ossto, S., & Probst, F. (2021). Influence of clinical parameters on the primary stability of a tapered dental implant: a retrospective analysis. *International Journal of Oral and Maxillofacial Implants, 36*(4), 762-770.

Brånemark, P., Hansson, B., Adell, R., Breine, U., Lindstrom, J., Hallen, O., & A, O. (1977). Osseointegrated implants in the treatment of the edentulous jaw. Experience from a 10-year period. *Scandinavian Journal of Plastic and Reconstructive Surgery, 16*, 1-132.

Brånemark, P., Zarb, G., & Albrektsson, T. (1985). *Tissue-Integrated Prostheses: Osseointegration in Clinical Dentistry.* Chicago, IL, USA: Quintessence Publishing Company Inc.

Cassetta, M., Brandetti, G., & Altieri, F. (2022). Are the insertion torque value and implant stability quotient correlated, and if so, can insertion torque values predict secondary implant stability? A prospective parallel cohort study. *International Journal of Oral and Maxillofacial Implants, 37*(1), 135-142.

Chávarri-Prado, D., Brizuela-Velasco, A., Diéguez-Pereira, M., Pérez-Pevida, E., Jiménez-Garrudo, A., I, V.-A., . . . Montalbán-Vadillo, O. (2020). Influence of cortical bone and implant design in the primary stability of dental implants measured by two different devices of resonance frequency analysis: An in vitro study. *Journal of Clinical and Experimental Dentistry, 12*(3), e242-e248.

Chugh, T., Jain, A., Jaiswal, R., Mehrotra, P., & Mehrotra, R. (2013). Bone density and its importance in orthodontics. *Journal of Oral Biology and Craniofacial Research, 3*(2), 92-97.

Coelho, P., Marin, C., Teixeira, H., Anchieta, R., Silveira, L., & Bonfante, E. (2013). Biomechanical evaluation of undersized drilling on implant biomechanical stability at early implantation times. *Journal of Oral and Maxillofacial Surgery, 71*(2), E69-E75.

Comuzzi, L., Tumedei, M., Pontes, A., Piattelli, A., & Iezzi, G. (2020). Primary stability of dental implants in low-density (10 and 20 pcf) polyurethane foam blocks: conical vs cylindrical implants. *International Journal of Environmental Research and Public Health, 17*(8), 2617.

da Costa Valente, M., de Castro, D., Shimano, A., & Dos Reis, A. (2019). Influence of an alternative implant design and surgical protocol on primary stability. *Brazilian Dental Journal, 30*(1), 47-51.

Delgado-Ruiz, R., Gold, J., Marquez, T., & Romanos, G. (2020). Under-Drilling versus Hybrid Osseodensification Technique: Differences in Implant Primary Stability and Bone Density of the Implant Bed Walls. *Materials, 13*(2), 390. https://doi.org/10.3390/ma13020390

Ding, X., Liao, S., Zhu, X., Zhang, X., & Zhang, L. (2009). Effect of diameter and length on stress distribution of the alveolar crest around immediate loading implants. *Clinical Implant Dentistry and Related Research, 11*(4), 279-287.

do Vale Souza, J., de Moraes Melo Neto, C., Piacenza, L., Freitas da Silva, E., de Melo Moreno, A., Penitente, P., . . . Goiato, M. (2021). Relation between insertion torque and implant stability quotient: a clinical study. *European Journal of Dentistry, 15*(4), 618-623.

Donos, N., Asche, N., Akbar, A., Francisco, H., Gonzales, O., Gotfredsen, K., . . . Schliephake, H. (2021). Impact of timing of dental implant placement and loading: Summary and consensus statements of Group 1 - The 6th EAO Consensus Conference 2021. *Clinical Oral Implants Research, 32*(21), 85-92.

Elibol, F., Oflaz, E., Buğra, E., Orhan, M., & Demir, T. (2020). Effect of cortical bone thickness and density on pullout strength of mini-implants: An experimental study. *American Journal of Orthodontics and Dentofacial Orthopedics, 157*(2), 178-185.

Elsayed, M. (2019). Biomechanical factors that influence the bone-implant interface. *Research Reports in Oral and Maxillofacial Surgery, 3*, 023.

Erdogan, O., Üstün, Y., Tatli, U., Damlar, I., & Daglioglu, K. (2013). A pig model for the histomorphometric evaluation of hard tissue around dental implants. *Journal of Oral Implantology, 39*(5), 551-557.

Esposito, M., Hirsch, J., Lekholm, U., & Thomsen, P. (1998). Biological factors contributing to failures of osseointegrated oral implants. (I) Success criteria and epidemiology. *European Journal of Oral Sciences, 106*, 527-551.

Farré-Pagés, N., Augé-Castro, M., Alaejos-Algarra, F., Mareque-Bueno, J., Ferrés-Padró, E., & Hernández-Alfaro, F. (2011). Relation between bone density and primary implant stability. *Medicina Oral, Patologia Oal, y Cirugia Bucal, 16*(1), e62-e67.

Feng, S., Lin, C., Chang, W., Lee, S., Cheng, C., & Huang, H. (2014). Influene of simulated bone quality and cortical bone thickness on implant stability detection during resonance frequency and damping factor analysis. *International Journal of Oral and Maxillofacial Implants, 29*(1), 105-112.

Feng, X. (2009). Chemical and biochemical basis of cell-bone matrix interaction in health and disease. *Current Chemical Biology, 3*(2), 189-196.

Florencio-Silva, R., da Silva Sasso, G., Sasso-Cerri, E., Simões, M., & Cerri, P. (2015). Biology of bone tissue: structure, function, and factors that influence bone cells. *Biomedical Research International, 2015*, 421746.

Friberg, B., Jemt, T., & Lekholm, U. (1991). Early failures in 4,641 consecutively placed Brånemark dental implants: a study from stage 1 surgery to the connection of completed prostheses. *International Journal of Oral and Maxillofacial Implants, 6*(2), 142-146.

Friberg, B., Sennerby, L., Linden, B., Grondahl, K., & Lekholm, U. (1999). Stability measurements of one-stage Branemark implants during healing in mandibles. *International Journal of Oral and Maxillofacial Surgery, 28*(4), 266-272.

Ganström, G. (2005). Osseointegration in irradiated cancer patients: an analysis with respect to implant failures. *Journal of Oral and Maxillofacial Surgery, 63*(5), 579-585.

Gehrke, S., Guirado, J., Bettach, R., Fabbro, M., Martinez, C., & Shibli, J. (2018). Evaluation of the insertion torque, implant stability quotient and drilled hole quality for different drill design: an in vitro investigation. *Clinical Oral Implants Research, 29*(6), 656-662.

Gehrke, S., Scarano, A., da Lima, J., Bianchini, M., Dedavid, B., & Da Aza, P. (2021). Effects of the healing chambers in implant macrogeometry design in a low-density bone using conventional and undersized drilling. *Journal of International Society of Preventive and Community Dentistry, 11*(4), 437-447.

Greenstein, G., & Cavallaro, J. (2017). Implant insertion torque: its role in achieving primary stability of restorable dental implants. *Compendium of Continuning Education in Dentistry, 38*(2), 88-95.

Gupta, R., Gupta, N., & Weber, K. (2022). *Dental implants.* Treasure Island, FL, USA: StatPearls Publishing.

Hawthan, M., Chrcanovic, B., & Larsson, C. (2022). Retrospective clinical study of tooth-supported single crowns: a multifactor analysis. *European Journal of Oral Sciences, 130*(4), e12871.

Heitzer, M., Kniha, K., Katz, S., Winnand, P., Peters, F., Möhlhenrich, S., . . . Modabber, A. (2022). The primary stability of two dental implant systems in low-density bone. *International Journal of Oral and Maxillofacial Surgery, 51*, 1093-1100.

Hiranmayi, K. (2018). Factors influencing implant stability. *Journal of Dental Implants, 8*(2), 69-76.

Hong, J., Lim, Y., & Park, S. (2012). Quantitative biomechanical analysis of the influence of the cortical bone and implant length on primary stability. *Clinical Oral Implants Research, 23*(10), 1193-1197.

Howashi, M., Tsukiyama, Y., Ayukawa, Y., Isoda-Akizuki, K., Kihara, M., Imai, Y., . . . Koyano, K. (2016). Relationship between the CT value and cortical bone thickness at implant recipient sites and primary implant stability with comparison of different implant types. *Clinical Implant Dentistry and Related Research, 18*(1), 107-116.

Huang, C., Li, M., Tsai, P., Kung, P., Chen, S., Sun, J., & Tsou, N. (2020). Novel design of additive manufactured hollow porous implants. *Dental Materials, 36*(11), 1437-1451.

Huang, H., Wu, G., & Hunziker, E. (2020). The clinical significance of implant stability quotient (ISQ) measurements: a literature review. *Journal of Oral Biology and Craniofacial Research, 10*(4), 629-638.

Jar, C., Archibald, A., Gibson, M., & Westover, L. (2023a). An analytical model for measuring dental implant stability with the Advanced System for Implant Stability Testing (ASIST). [Unpublished manuscript]. Department of Mechanical Engineering, University of Alberta.

Jar, C., Archibald, A., Gibson, M., & Westover, L. (2023b). Comparison of a new method to measure dental implant stability with the RFA technique in artificial bone blocks. [Unpublished manuscript]. Department of Mechanical Engineering, University of Alberta.

Jayesh, R., & Dhinakarsamy, V. (2015). Osseointegration. *Journal of Pharmacy and BioAllied Sciences, 7*, S226-S229.

Jimbo, R., Tovar, N., Anchieta, R., Machado, L., Marin, C., Teixeira, H., & Coelho, P. (2014). The combined effects of undersized drilling and implant macrogeometry on bone healing around dental implants: an experimental study. *International Journal of Oral and Maxillofacial Surgery, 43*(10), 1269-1275.

Karaer, O., Yamaguchi, S., Imazato, S., & Terzioglu, H. (2023). In silico finite element analysis of implant-supported CAD-CAM resin composite crowns. *Journal of Prosthodontics, 32*(3), 259-266.

Karl, M., Graef, F., Heckmann, S., & Krafft, T. (2008). Parameters of resonance frequency measurement values: a retrospective study of 385 ITI dental implants. *Clinical Oral Implants Research, 19*(2), 214-218.

Kessler-Liechti, G., Zix, J., & Mericske-Stern, R. (2008). Stability measurements of 1-stage implants in the edentulous mandible by means of resonance frequency analysis. *International Journal of Oral and Maxillofacial Implants, 23*(2), 353-358.

Kolakarnprasert, N., Kaizer, M., Kim, D., & Zhang, Y. (2019). New multi-layered zirconias: composition, microstructure and translucency. *Dental Materials, 35*(5), 797-806.

Lee, D., Shin, Y., Park, J., Shim, J., Shin, S., & Lee, J. (2020). The reliability of Anycheck device related to healing abutment diameter. *Journal of Advanced Prosthodontics, 12*, 83-88.

LeGeros, R., & Craig, R. (1993). Strategies to affect bone remodelling: osseointegration. *Journal of Bone and Mineral Research, 8*(2), S583-S596.

Lekholm, U., & Zarb, G. (1985). Patient selection. In P. Brånemark, G. Zarb, & T. Albrektsson, *Tissue-Integrated Prostheses: Osseointegration in Clinical Dentistry* (pp. 199-209). Chicago, IL, USA: Quintessence Publishing Company Inc.

Liu, Y., Sorensen, J., & Shen, I. (2021). Challenges of using resonance frequency analysis to identify stability of a dental implant placed in the mandible. *International Journal of Oral and Maxillofacial Implants, 36*(2), e7-e21.

Lukas, D., & Schulte, W. (1990). Periotest - a dynamic procedure for the diagnosis of the human periodontium. *Clinical Physics and Physiological Measurement, 11*(1), 65-75.

Mellal, A., Wiskott, H., Botsis, J., Scherrer, S., & Belser, U. (2004). Stimulating effect of implant loading on surrounding bone. *Clinical Oral Implants Research, 15*(2), 239-248.

Meredith, N., Book, K., Friberg, B., Jemt, T., & Sennerby, L. (1997a). Resonance frequency measurements of implant stability in vivo. *Clinical Oral Implants Research, 8*(3), 226-233.

Meredith, N., Shagaldi, F., Alleyne, D., Sennerby, L., & Cawley, P. (1997b). The application of resonance frequency measurements to study the stability of titanium implants during healing in the rabbit tibia. *Clinical Oral Implants Research, 8*(3), 234-243.

Merheb, J., Assche, N., Coucke, W., Jacobs, R., Naert, I., & Quirynen, M. (2010). Relationship between cortical bone thickness or computerized tomography-derived bone density values and implant stability. *Clinical Oral Implants Research, 21*(6), 612-617.

Miyamoto, I., Tsuboi, Y., Wada, E., Suwa, H., & Iizuka, T. (2005). Influence of cortical bone thickness and implant length on implant stability at the time of surgery - clinical, prospective, biomechanical, and imaging study. *Bone, 37*(6), 776-780.

Mo, A. (2009). *The impact technique for monitoring intraoral implant stability (M.Sc. Thesis).* Edmonton: University of Alberta.

Mohajerani, H., Roozbayani, R., Taherian, S., & Tabrizi, R. (2017). The risk factors in early failure of dental implants: a retrospective study. *Journal of Dentistry (Shiraz), 18*(4), 298-303.

Mohamed, M., & Westover, L. (2022). Evaluating the dynamic behaviour of bone anchored hearing aids using a finite element model and its applications to implant stability assessment. *Medical and Biological Engineering and Computing, 60*, 2779-2795.

Nagasao, T., Kobayashi, M., Tsuchiya, Y., Kaneko, T., & Nakajima, T. (2002). Finite element analysis of the stresses around endosseous implants in various reconstructed mandibular models. *Journal of Cranio-Maxillofacial Surgery, 30*, 170-177.

Okuhama, Y., Nagata, K., Kim, H., Tsuruoka, H., Atsumi, M., & Kawana, H. (2022). Validation of an implant stability measurmenet device using the percussion response: a clinical research study. *BMC Oral Health, 22*, 286.

Oliscovicz, N., Shimano, A., Marcantonio Jr, E., Lepri, C., & Dos Reis, A. (2013a). Analysis of primary stability of dental implants inserted in different substrates using the pullout test and insertion torque. *International Journal of Dentistry, 2013*, 194987.

Oliscovicz, N., Shimano, A., Marcantonio Jr, E., Lepri, C., & Dos Reis, A. (2013b). Effect of implant design and bone density in primary stability. *Brazilian Journal of Oral Sciences, 12*(3), 158-163.

Pyo, S., Kim, H., Kwon, O., Otgonbold, J., & Lee, K. (2021). Reliability verification of damping capacity assessment through in vitro analysis of implant micromotion in peri-implant bone loss model. *International Journal of Oral and Maxillofacial Implants, 36*(1), 106-114.

Rittel, D., Dorogoy, A., & Shemtov-Yona, K. (2017). Modelling dental implant extraction by pullout and torque procedures. *Journal of the Mechanical Behaviour of Biomedical Materials, 71*, 416-427.

Roumanas, E., Freymiller, E., Chang, T., Aghaloo, T., & Beumer, J. (2002). Implant-retained prostheses for facial defects: an up to 14-year follow-up report on the survival rates of implants at UCLA. *International Journal of Prosthodontics, 15*(4), 325-332.

Rowan, M., Lee, D., Pi-Anfruns, J., Shiffler, P., Aghaloo, T., & Moy, P. (2015). Mechanical versus biological stability of immediate and delayed implant placement using resonance frequency analysis. *Journal of Oral and Maxillofacial Surgery, 73*, 253-257.

Sakoh, J., Wahlmann, U., Stender, E., Al-Nawas, B., & Wagner, W. (2006). Primary stability of a conical implant and a hybrid, cylindric screw-type implant in vitro. *International Journal of Oral and Maxillofacial Implants, 21*, 560-566.

Salvi, G., & Lang, N. (2004). Diagnostic parameters for monitoring peri-implant conditions. *International Journal of Oral and Maxillofacial Implants, 19*, 116-127.

Sennerby, L., & Meredith, N. (2008). Implant stability measurements using resonance frequency analysis: biological and biomechanical aspects and clinical implications. *Periodontology, 47*(1), 51-66.

Seong, W., Grami, S., Jeong, S., Conrad, H., & Hodges, J. (2013). Comparison of push-in versus pull-out tests on bone-implant interfaces of rabbit tibia dental implant healing model. *Clinical Implant Dentistry and Related Research, 15*(3), 460-469.

Staedt, H., Rossa, M., Lehmann, K., Al-Nawas, B., Kämmerer, P., & Heimes, D. (2020). Potential risk factors for early and late dental implant failure: a retrospective clinical study on 9080 implants. *International Journal of Implant Dentistry, 6*(1), 81.

Stefano, D., Arosio, P., Capparè, P., Barbon, S., & Gherlone, E. (2021). Stability of dental implants and thickness of cortical bone: clinical research and future perspectives: a systematic review. *Materials (Basel), 14*(23), 7183.

Straumann. (2017). *Basic Information on the Surgical Procedures for the Straumann Bone Level Tapered Implant.* Institut Straumann AG.

Sugiura, T., Yamamoto, K., Horita, S., Murakami, K., Tsutsumi, S., & Kirita, T. (2016). The effects of bone density and crestal cortical bone thickness on micromotion and peri-implant bone strain distribution in an immediately loaded implant: a nonlinear finite element analysis. *Journal of Periodontal and Implant Science, 46*(3), 152-165.

Swain, R., Faulkner, G., Raboud, D., & Wolfaardt, J. (2008a). A dynamic analytical model for impact evaluation of percutaneous implants. *Journal of Biomechanical Engineering, 130*(5), 051013.

Swain, R., Faulkner, G., Raboud, D., & Wolfaardt, J. (2008b). An improved impact technique for monitoring percutaneous implant integrity. *International Journal of Oral and Maxillofacial Implants, 23*(2), 269-269.

Swami, V., Vijayaraghavan, V., & Swami, V. (2016). Current trends to measure implant stability. *Journal of Indian Prosthodontic Society, 16*(2), 124-130.

Tanaka, K., Sailer, I., Iwama, R., Yamauchi, K., Nogami, S., Yoda, N., & Takahashi, T. (2018). Relationship between cortical bone thickness and implant stability at the time of surgery and secondary stability after osseointegration measured using resonance frequency analysis. *Journal of Periodontal Implant Science, 48*(6), 360-372.

Toyoshima, T., Wagner, W., Klein, M., Stender, E., Wieland, M., & Al-Nawas, B. (2011). Primary Stability of a Hybrid Self-Tapping Implant Compared to a Cylindrical Non-Self-Tapping Implant with Respect to Drilling Protocols in an Ex Vivo Model. *Clinical Implant Dentistry and Related Research, 13*(1), 71-78.

Tumedei, M., Piattelli, A., Falco, A., De Angelis, F., Lorusso, F., Di Carmine, M., & Iezzi, G. (2021). An in vitro evaluation on polyurethane foam sheets of the insertion torque, removal torque values, and resonance frequency analysis (RFA) of a self-tapping threads and round apex implant. *Cellular Polymers, 40*(1), 20-30.

Turkyilmaz, I., & McGlumphy, E. (2008). Influence of bone density on implant stability parameters and implant success: a retrospective clinical study. *BMC Oral Health, 8*, 32.

Veltri, M., González-Martín, O., & Belser, U. (2014). Influence of simulated bone-implant contact and implant diameter on secondary stability: a resonance frequency in vitro study. *Clinical Oral Implants Research, 25*, 899-904.

Vien, B., Chiu, W., Russ, M., & Fitzgerald, M. (2019). A quantitative approach for the bone-implant osseointegration assessment based on ultrasonic elastic guided waves. *Sensors, 19*(3), 454.

Wang, S., Liu, G., Hoang, K., & Guo, Y. (2010). Identifiable range of osseointegration of dental implants through resonance frequency analysis. *Medical Engineering and Physics, 32*(10), 1094-1106.

Wang, T., Lee, M., Wang, J., & Lin, L. (2015). The effect of implant design and bone quality on insertion torque, resonance frequency analysis, and insertion energy during implant placement in low or low to medium density bone. *International Journal of Prosthodontics, 28*(1), 40-47.

Wang, W., & Lynch, J. (2017). IWSHM 2017: Application of guided wave methods to quantitatively assess healing in osseointegrated prostheses. *Structural Health Monitoring, 17*(6), 1377-1392.

Westover, L. (2016). *Evaluation of the interface mechanical properties of craniofacial implants and natural teeth through development of the Advanced System for Implant Stability Testing (ASIST).* [Doctoral dissertation, University of Alberta]. University of Alberta Libraries.

Westover, L., Butz, R., Duke, K., Faulkner, G., Hodgetts, W., & Raboud, D. (2016b). Noninvasive evaluation of periodontal ligament stiffness. *22nd Congress of the European Society of Biomechanics.* Lyon: European Society of Biomechanics.

Westover, L., Faulkner, G., Hodgetts, W., & Raboud, D. (2016a). Advanced system for implant stability testing (ASIST). *Journal of Biomechanics, 49*(15), 3651-3659.

Westover, L., Faulkner, G., Hodgetts, W., & Raboud, D. (2018a). Comparison of implant stability measurement devices for bone-anchored hearing aid systems. *Journal of Prosthetic Dentistry, 119*, 178-184.

Westover, L., Faulkner, G., Hodgetts, W., Kamal, F., Lou, E., & Raboud, D. (2018b). Longitudinal evaluation of bone-anchored hearing aid implant stability using the Advanced System for Implant Stability Testing (ASIST). *Otology and Neurotology, 39*, e489-e495.

Winter, W., Möhrle, S., Holst, S., & Karl, M. (2010). Parameters of implant stability measurements based on resonance frequency and damping capacity: a comparative finite element analysis. *International Journal of Oral and Maxillofacial Implants, 25*(3), 532-539.

Wyatt, C., & Pharoah, M. (1998). Imaging techniques and image interpretation for dental implant treatment. *International Journal of Prosthodontics, 11*(5), 442-452.

Yamaguchi, Y., Shiota, M., Fujii, M., Shimogishi, M., & Munakata, M. (2020). Effects of implant thread design on primary stability - a comparison between single- and double-threaded implants in an artificial bone model. *International Journal of Implant Dentistry, 6*, 42.

Yang, B., Irastorza-Landa, A., Heuberger, P., & Ploeg, H. (2022). Analytical model for dental implant insertion torque. *Journal of the Mechanical Behaviour of Biomedical Materials, 131*, 105223.

Yang, J., & Xiang, H. (2007). A three-dimensional finite element study on the biomechanical behaviour of an FGBM dental implant in surrounding bone. *Journal of Biomechanics, 40*(11), 2377-2385.

Yang, Y., Hu, H., Zeng, M., Chu, H., Gan, Z., Duan, J., & Rong, M. (2021). The survival rates and risk factors of implants in the early stage: a retrospective study. *BMC Oral Health, 21*, 293.

Zanetti, E., Ciaramella, S., Cali, M., Pascoletti, G., Martorelli, M., Asero, R., & Watts, D. (2018). Modal analysis for implant stability assessment: sensitivity of this methodology for different implant designs. *Dental Materials, 34*(8), 1235-1245.

Zix, J., & Hug, S. (2008). Measurement of dental implant stability by resonance fequency analysis and damping capacity assessment: comparison of both techniques in a clinical trial. *International Journal of Oral and Maxillofacial Implants, 23*(5), 525-530.

Appendix A: Analytical Model Parameters

The analytical model for a uniform interface is shown in Figure A.1.

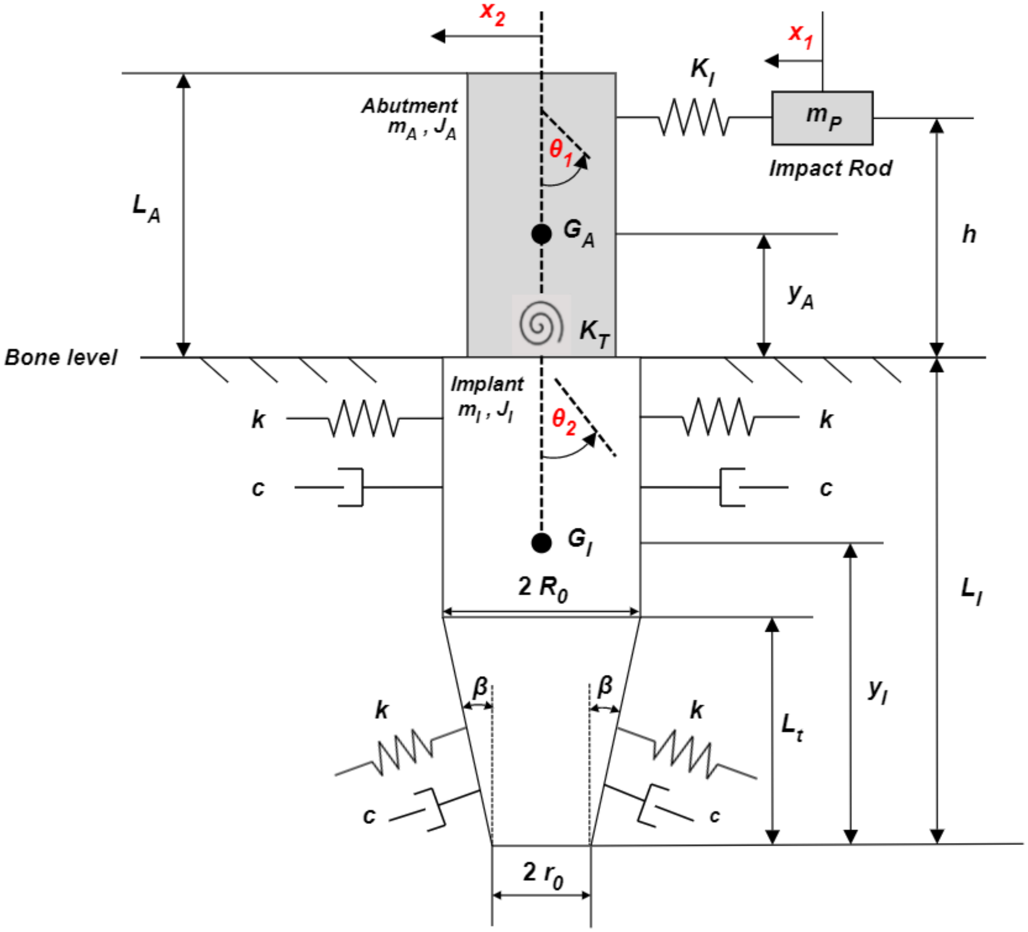

Figure A.1: Four degree of freedom vibration model of a dental implant system in a uniform substrate.

A.1 Derivation of Mass Matrix

The mass matrix was found using inertia influence coefficients m_{ij}, defined as the force required at coordinate i to maintain a unit acceleration at coordinate j, while the accelerations of all other coordinates are maintained at zero.

m_{i1}: Unit acceleration $\ddot{x}_1 = 1$

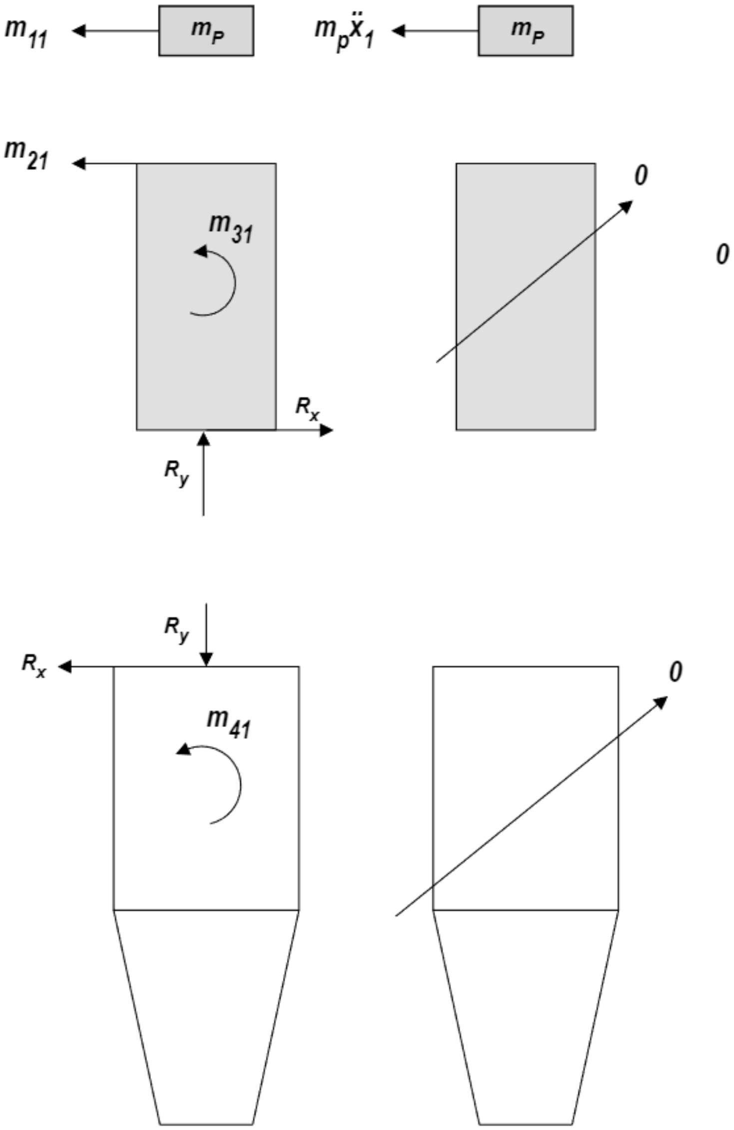

For the impact rod:

$$\leftarrow +\sum F_x = m_p(1) = m_{11}, \qquad m_{11} = m_p$$

For the implant (C refers to the connection point between the implant and abutment):

$$\leftarrow +\sum F_x = R_x = 0$$

$$\circlearrowleft +\sum M_C = m_{41} = 0, \qquad m_{41} = 0$$

For the abutment:

$$\leftarrow +\sum F_x = m_{21} - R_x = 0, \qquad m_{21} = 0$$

$$\circlearrowleft +\sum M_C = m_{31} = 0, \qquad m_{31} = 0$$

m_{i2}: Unit acceleration $\ddot{x}_2 = 1$

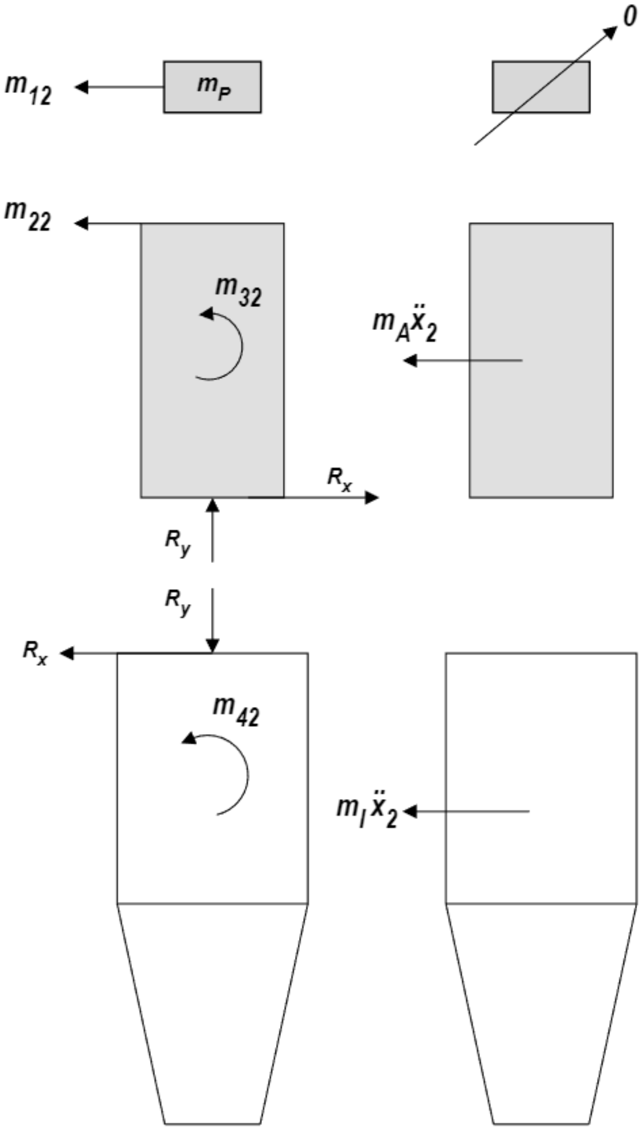

For the impact rod:

$$\leftarrow +\sum F_x = m_{12} = 0, \qquad m_{12} = 0$$

For the implant:

$$\leftarrow +\sum F_x = m_I(1) = R_x, \qquad R_x = m_I$$

$$\circlearrowleft +\sum M_C = m_{42} = -m_I(1)(L_I - y_I), \qquad m_{42} = -m_I(L_I - y_I)$$

For the abutment:

$$\leftarrow +\sum F_x = m_A(1) = m_{22} - R_x = m_{22} - m_I, \qquad m_{22} = m_I + m_A$$

$$\circlearrowleft \sum M_C = m_A(1)y_A = m_{32} + m_{22}h$$

$$m_A y_A = m_{32} + (m_I + m_A)h, \qquad m_{32} = m_A y_A - (m_I + m_A)h$$

m_{i3}: Unit acceleration $\ddot{\theta}_1 = 1$

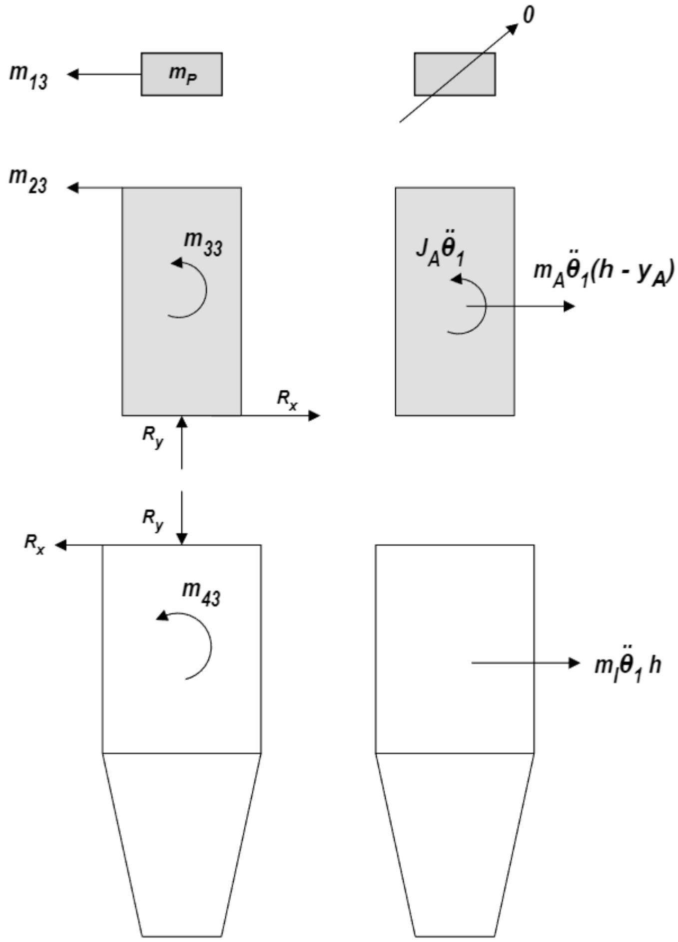

For the impact rod:

$$\leftarrow +\sum F_x = m_{13} = 0, \qquad m_{13} = 0$$

For the implant:

$$\rightarrow +\sum F_x = m_I h = -R_x, \qquad R_x = -m_I h$$

$$\circlearrowleft +\sum M_C = (m_I h)(L_I - y_I) = m_{43}, \qquad m_{43} = m_I h(L_I - y_I)$$

For the abutment:

$$\rightarrow +\sum F_x = m_A(h - y_A) = R_x - m_{23}, \qquad m_{23} = m_A y_A - (m_I + m_A)h$$

$$\circlearrowleft +\sum M_C = J_A - m_A(h - y_A)y_A = m_{33} + m_{23}h, \qquad m_{33} = J_A + m_A(h - y_A)^2 + m_I h^2$$

$$J_A - m_A y_A h + m_A y_A^2 = m_{33} + m_A y_A h - (m_I + m_A)h^2$$

$$m_{33} = J_A + (m_A y_A^2 - 2m_A y_A h + m_A h^2) + m_I h^2$$

$$m_{33} = J_A + m_A(h - y_A)^2 + m_I h^2$$

m_{i4}: Unit acceleration $\ddot{\theta}_2 = 1$

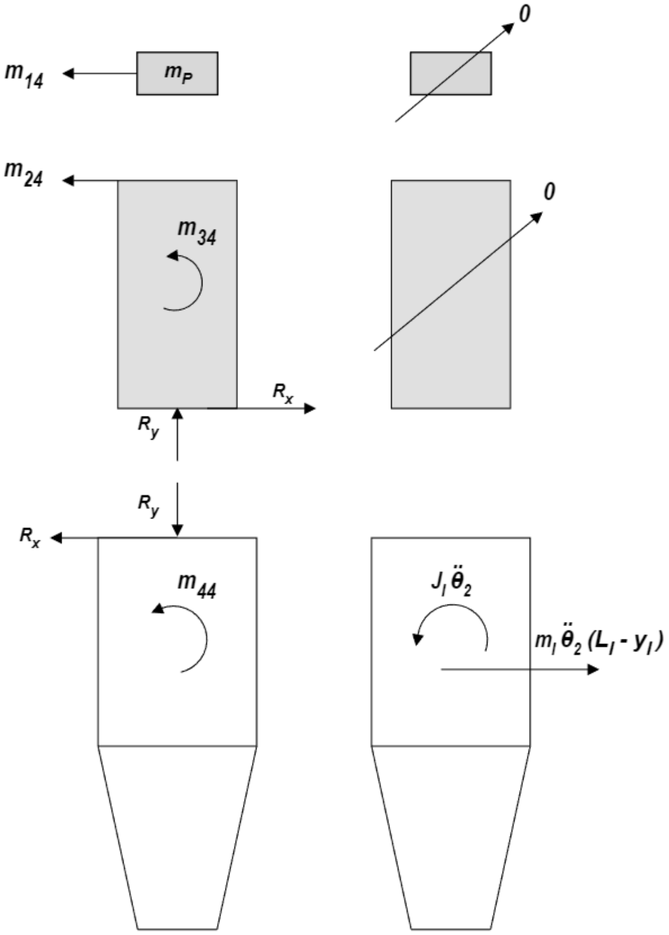

For the impact rod:

$$\leftarrow +\sum F_x = m_{14} = 0, \qquad m_{14} = 0$$

For the implant:

$$\rightarrow +\sum F_x = m_I(L_I - y_I) = -R_x, \qquad R_x = -m_I(L_I - y_I)$$

$$\circlearrowleft +\sum M_C = J_I + m_I(L_I - y_I)(L_I - y_I) = m_{44}, \qquad m_{44} = J_I + m_I(L_I - y_I)^2$$

For the abutment:

$$\leftarrow +\sum F_x = m_{24} - R_x = 0, \qquad m_{24} = -m_I(L_I - y_I)$$

$$\circlearrowleft +\sum M_C = m_{34} + m_{24}h = 0, \qquad m_{34} = m_I h(L_I - y_I)$$

The mass matrix $[M]$ is therefore:

$$[M] = \begin{bmatrix} m_p & 0 & 0 & 0 \\ 0 & m_I + m_A & m_A y_A - (m_I + m_A)h & -m_I(L_I - y_I) \\ 0 & m_A y_A - (m_I + m_A)h & J_A + m_A(h - y_A)^2 + m_I h^2 & m_I(L_I - y_I)h \\ 0 & -m_I(L_I - y_I) & m_I(L_I - y_I)h & J_I + m_I(L_I - y_I)^2 \end{bmatrix}$$

Where:

L_I is the total implant length

y_I is the distance between the implant's centre of mass and bottom of the implant

y_A is the distance between the abutment's centre of mass and bottom of the abutment

h is the striking height measured from the bottom of the abutment

A.2 Stiffness Matrix for Uniform Analytical Model

A.2.1 Effective Interfacial Stiffness

The effective stiffness per unit length of the interface for a general direction must first be determined for the cylindrical and tapered portions of the implant (Figure A.2).

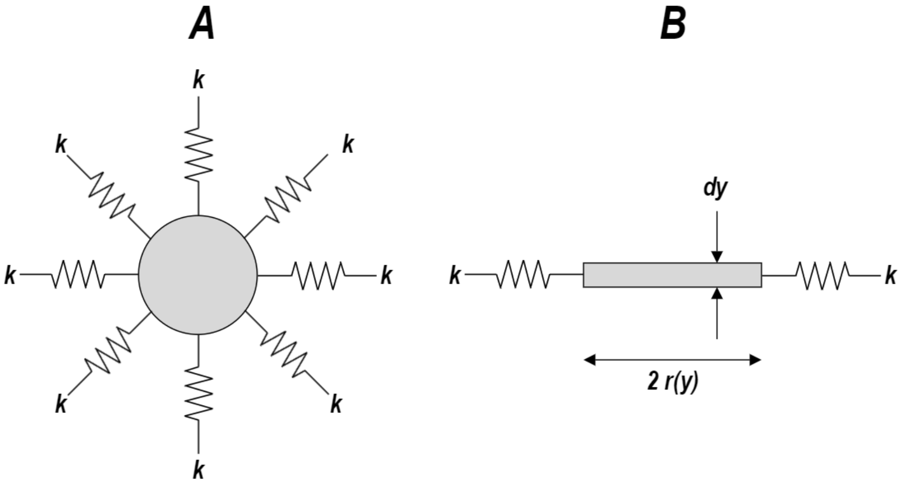

Figure A.2: Cross sectional (A) and side view (B) of a differential disk element of the implant.

The radius of a differential disk element of the implant differs between the cylindrical and tapered portions of the implant, where y is measured from the implant apex:

$$R(y) = \begin{cases} R_0, & 0 \leq y \leq L_b \\ R_0 - \left(\dfrac{R_0 - r_0}{L_t}\right) y, & L_b < y \leq L_I \end{cases}$$

For a unit displacement applied to the implant, the resultant restoring force on a differential element is $dF = k\, r(y) \cos(\theta)\, d\theta dy$.

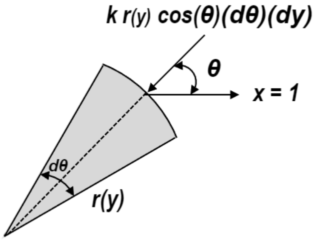

Integrating dF will provide the effective stiffness per unit length of the interface (k_i).

For the cylindrical portion of the implant, $r = R_0$ and k_{ib} is the effective stiffness per unit length.

$$k_{ib} = 2\int_{-\pi/2}^{\pi/2} kR_0\cos(\theta)\,dyd\theta = 2kR_0dy\int_{-\pi/2}^{\pi/2}\cos(\theta)\,d\theta$$

$$k_{ib} = 4kR_0dy$$

For the tapered portion of the implant body, k_{it} is the effective stiffness per unit length:

$$r(y) = R_0 - \left(\frac{R_0 - r_0}{L_t}\right)y$$

It is assumed that the springs act normal to the tapered surface. Therefore, for a displacement in the horizontal direction:

$$k_{it} = 4k\cos^2(\beta)\left(R_0 - \left(\frac{R_0 - r_0}{L_t}\right)y\right)dy$$

Where β is the implant taper angle:

$$\tan(\beta) = \frac{R_0 - r_0}{L_t}$$

Therefore, the effective stiffness per unit length is:

$$k_i = \begin{cases} 4kR_0dy, & 0 \le y \le L_b \\ 4k\cos^2(\beta)\left(R_0 - \left(\frac{R_0 - r_0}{L_t}\right)y\right)dy, & L_b < y \le L_I \end{cases}$$

The total effective stiffness of the interface is obtained by integrating k_i over the implant length:

$$k_{eff} = 4k\left(R_0L_b + \cos^2(\beta)\left(R_0L_t - \left(\frac{R_0 - r_0}{2L_t}\right)(L_I^2 - L_b^2)\right)\right)$$

R_0 is the radius of the cylindrical portion of the implant

r_0 is the radius of the implant base

L_I is the total implant length

L_b is the length of the cylindrical portion of the implant

L_t is the length of the tapered portion of the implant

A.2.2 Derivation of Stiffness Matrix

The method of stiffness influence coefficients was used to determine the stiffness matrix $[K]$ for the model shown in Figure A.1, where k_{ij} is the force required at coordinate i to maintain a unit displacement at coordinate *j* while holding all other coordinates fixed at zero.

k_{i1}: Unit displacement $x_1 = 1$

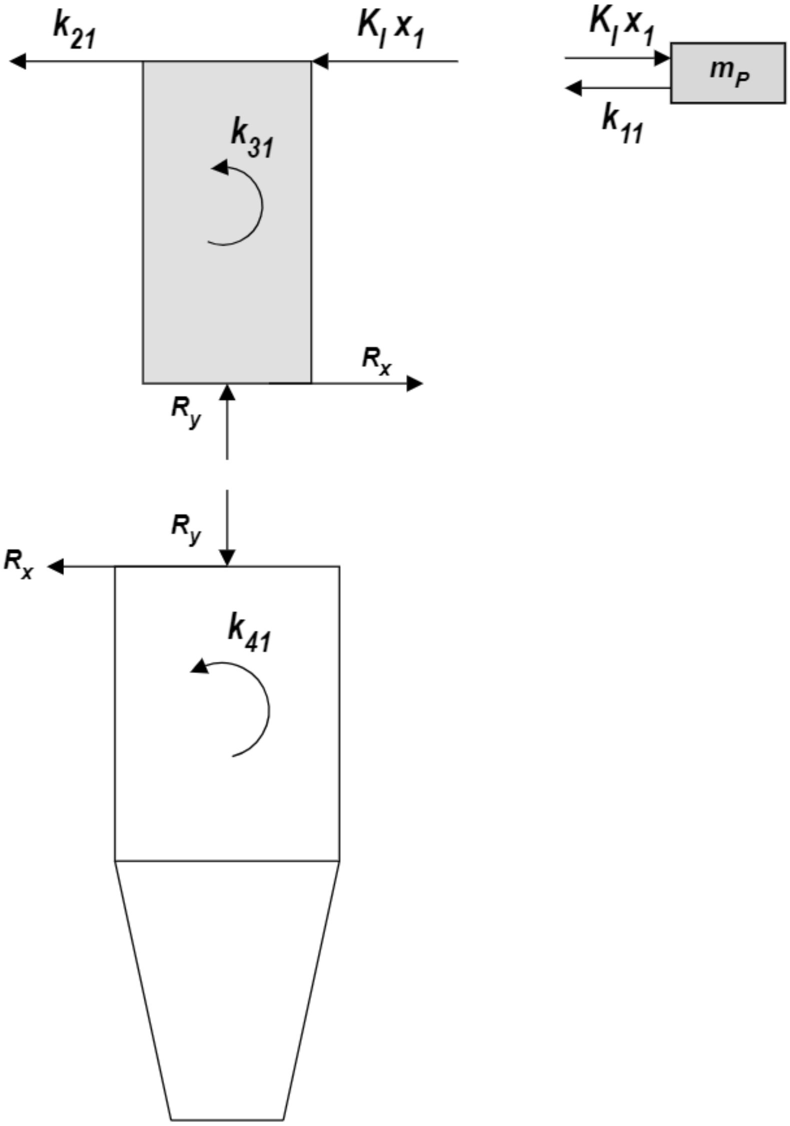

For the impact rod:

$$\leftarrow + \sum F_x = k_{11} - K_I = 0, \qquad k_{11} = K_I$$

For the implant:

$$\leftarrow +\sum F_x = R_x = 0, \qquad R_x = 0$$

$$\circlearrowleft +\sum M_C = k_{41} = 0, \qquad k_{41} = 0$$

For the abutment:

$$\leftarrow +\sum F_x = k_{21} + K_I - R_x = 0, \qquad k_{21} = -K_I$$

$$\circlearrowleft +\sum M_C = k_{31} + (k_{21} + K_I)h = 0, \qquad k_{31} = 0$$

k_{i2}: Unit displacement $x_2 = 1$

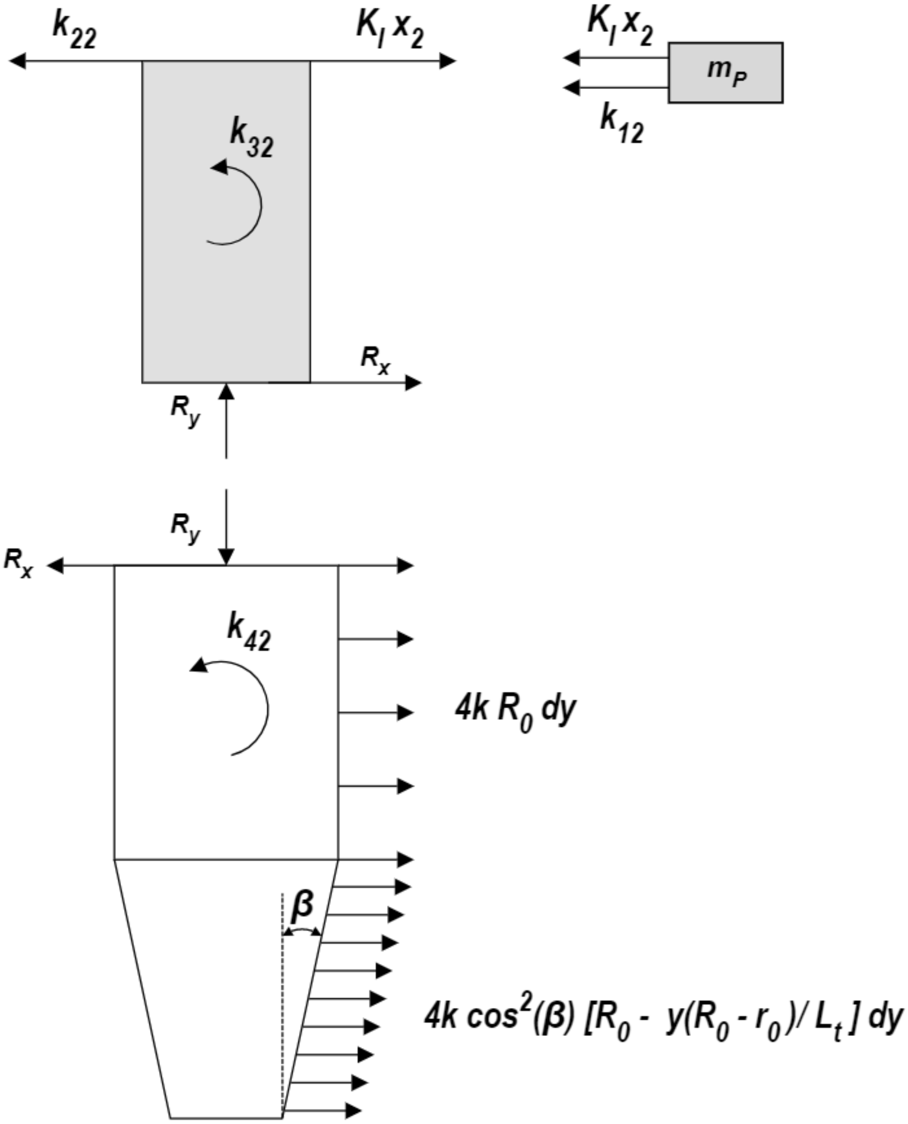

For the impact rod:

$$\leftarrow +\sum F_x = k_{12} + K_I = 0, \qquad k_{12} = -K_I$$

For the implant:

$$\leftarrow +\sum F_x = R_x - \int_{0}^{L_b} 4kR_0 dy - \int_{L_b}^{L_I} 4k\cos^2(\beta)\left(R_0 - \left(\frac{R_0 - r_0}{L_t}\right)y\right)dy = 0$$

$$R_x = 4kR_0L_b + 4k\cos^2(\beta)\left[R_0(L_I - L_b) - \left(\frac{R_0 - r_0}{L_t}\right)\frac{(L_I^2 - L_b^2)}{2}\right]$$

$$R_x = 4k\left[R_0L_b + \cos^2(\beta)\left(\frac{2R_0L_t^2 - (R_0 - r_0)(L_I^2 - L_b^2)}{2L_t}\right)\right]$$

$$\circlearrowleft +\sum M_C = k_{42} + \int_{0}^{L_b} 4kR_0 y dy + \int_{L_b}^{L_I} 4k\cos^2(\beta)\left(R_0 - \left(\frac{R_0 - r_0}{L_t}\right)y\right)y dy = 0$$

$$k_{42} = -2kR_0L_b^2 - 4k\cos^2(\beta)\left[\frac{R_0(L_I^2 - L_b^2)}{2} - \left(\frac{R_0 - r_0}{3L_t}\right)(L_I^3 - L_b^3)\right]$$

$$k_{42} = -2k\left[R_0L_b^2 + 2\cos^2(\beta)\left(\frac{3R_0(L_I^2 - L_b^2)L_t - 2(R_0 - r_0)(L_I^3 - L_b^3)}{6L_t}\right)\right]$$

For the abutment:

$$\leftarrow +\sum F_x = k_{22} - K_I - R_x = 0,$$

$$k_{22} = K_I + 4k\left[R_0L_b + \cos^2(\beta)\left(\frac{2R_0L_t^2 - (R_0 - r_0)(L_I^2 - L_b^2)}{2L_t}\right)\right]$$

$$\circlearrowleft +\sum M_C = k_{32} + k_{22}h - K_Ih = 0$$

$$k_{32} = -4kh\left[R_0L_b + \cos^2(\beta)\left(\frac{2R_0L_t^2 - (R_0 - r_0)(L_I^2 - L_b^2)}{2L_t}\right)\right]$$

k_{i3}: Unit rotation $\theta_1 = 1$

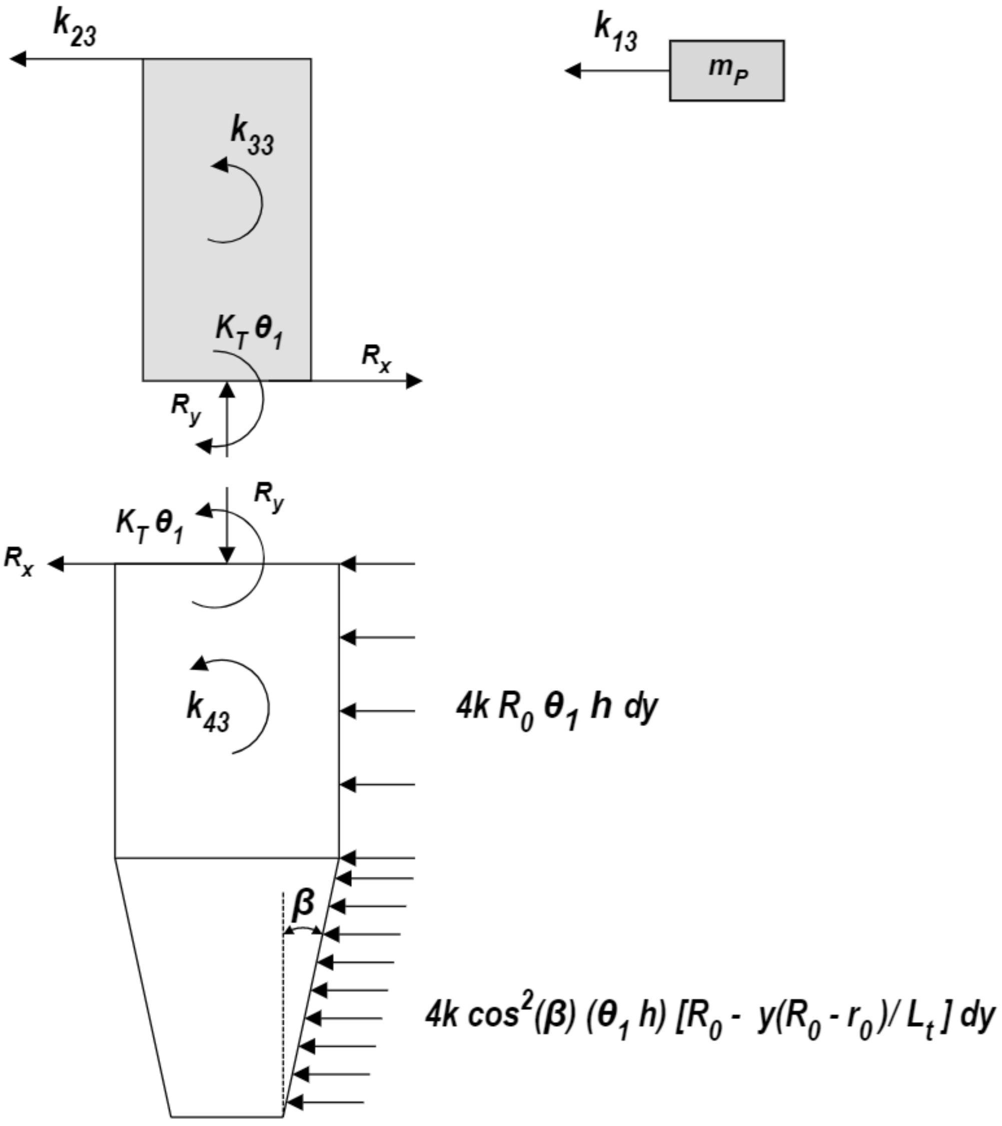

For the impact rod:

$$\leftarrow +\sum F_x = k_{13} = 0, \qquad k_{13} = 0$$

For the implant:

$$\leftarrow +\sum F_x = R_x + \int_0^{L_b} 4kR_0 h\,dy + \int_{L_b}^{L_I} 4k\cos^2(\beta)\,h\left(R_0 - \left(\frac{R_0 - r_0}{L_t}\right)y\right)dy = 0$$

$$R_x = -4khR_0L_b - 4kh\cos^2(\beta)\left(R_0(L_I - L_b) - \left(\frac{R_0 - r_0}{L_t}\right)\left(\frac{L_I^2 - L_b^2}{2}\right)\right)$$

$$R_x = -4kh\left[R_0L_b + \cos^2(\beta)\left(\frac{2R_0L_t^2 - (R_0 - r_0)(L_I^2 - L_b^2)}{2L_t}\right)\right]$$

$$\circlearrowleft +\sum M_C = k_{43} + K_T - \int_0^{L_b} 4khR_0\, ydy - \int_{L_b}^{L_I} 4kh\cos^2(\beta)\left(R_0 - \left(\frac{R_0 - r_0}{L_t}\right)y\right)ydy = 0$$

$$k_{43} = -K_T + kh\left[2R_0L_b^2 + 4\cos^2(\beta)\left(\frac{R_0(L_I^2 - L_b^2)}{2} - \left(\frac{R_0 - r_0}{L_t}\right)\left(\frac{(L_I^3 - L_b^3)}{3}\right)\right)\right]$$

$$k_{43} = -K_T + 2kh\left[R_0L_b^2 + 2\cos^2(\beta)\left(\frac{3R_0(L_I^2 - L_b^2)L_t - 2(R_0 - r_0)(L_I^3 - L_b^3)}{6L_t}\right)\right]$$

For the abutment:

$$\leftarrow +\sum F_x = k_{23} - R_x = 0, \qquad k_{23} = -4kh\left[R_0L_b + \cos^2(\beta)\left(\frac{2R_0L_t^2 - (R_0 - r_0)(L_I^2 - L_b^2)}{2L_t}\right)\right]$$

$$\circlearrowleft +\sum M_C = k_{33} - K_T + k_{23}h = 0$$

$$k_{33} = K_T + 4kh^2\left[R_0L_b + \cos^2(\beta)\left(\frac{2R_0L_t^2 - (R_0 - r_0)(L_I^2 - L_b^2)}{2L_t}\right)\right]$$

k_{i4}**: Unit rotation** $\boldsymbol{\theta_2 = 1}$

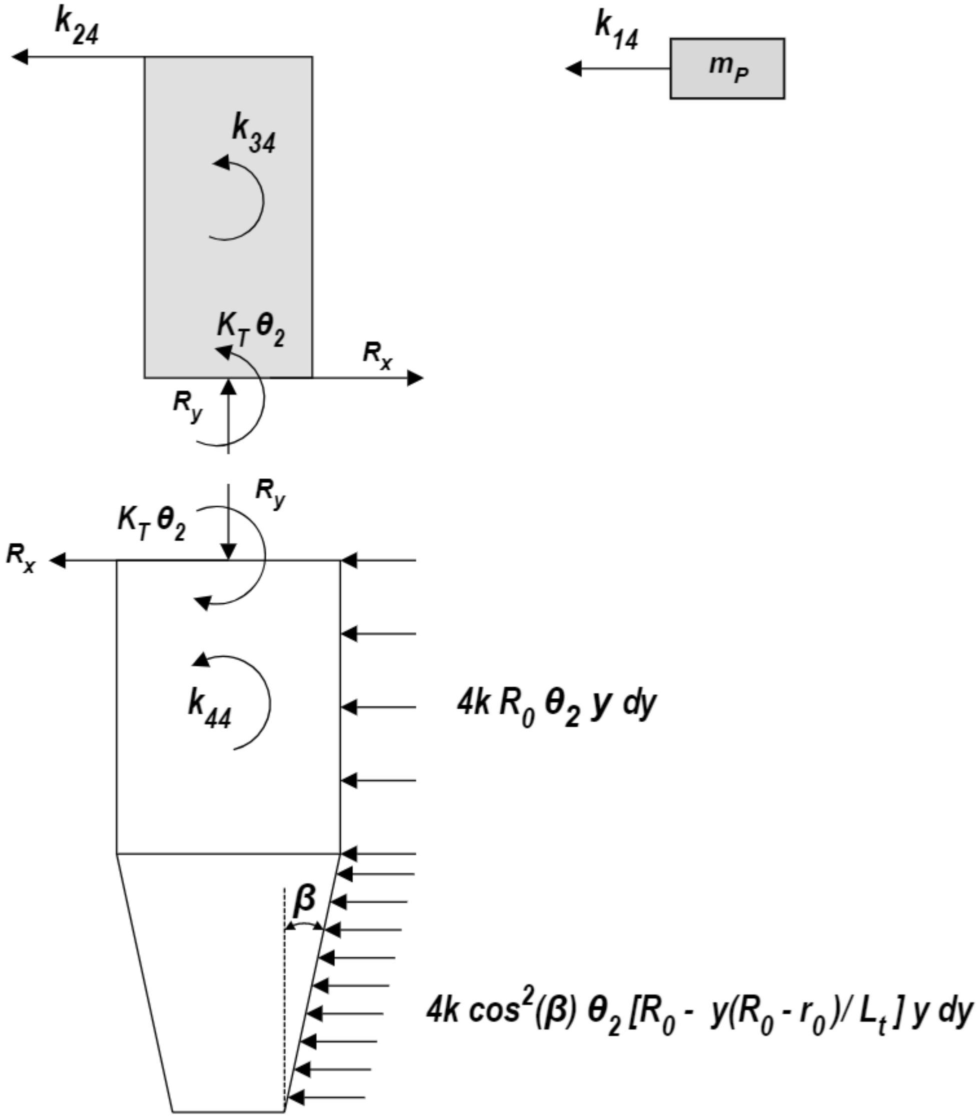

For the impact rod:

$$\leftarrow +\sum F_x = k_{14} = 0, \qquad k_{14} = 0$$

For the implant:

$$\leftarrow +\sum F_x = R_x + \int_0^{L_b} 4kR_0 y dy + \int_{L_b}^{L_I} 4k\cos^2(\beta)\left(R_0 - \left(\frac{R_0 - r_0}{L_t}\right)y\right) y dy = 0$$

$$R_x = -2kR_0 L_b^2 - 4k\cos^2(\beta)\left[R_0\left(\frac{L_I^2 - L_b^2}{2}\right) - \left(\frac{R_0 - r_0}{L_t}\right)\left(\frac{L_I^3 - L_b^3}{3}\right)\right]$$

$$R_x = -2k\left[R_0 L_b^2 + 2\cos^2(\beta)\left(\frac{3R_0(L_I^2 - L_b^2)L_t - 2(R_0 - r_0)(L_I^3 - L_b^3)}{6L_t}\right)\right]$$

$$\circlearrowleft +\sum M_C = k_{44} - K_T - \int_0^{L_b} 4kR_0 y^2 dy - \int_{L_b}^{L_I} 4k\cos^2(\beta)\left(R_0 - \left(\frac{R_0 - r_0}{L_t}\right)y\right)y^2 dy = 0$$

$$k_{44} = K_T + \frac{4kR_0L_b^3}{3} + 4k\cos^2(\beta)\left(\frac{R_0(L_I^3 - L_b^3)}{3} - \left(\frac{R_0 - r_0}{L_t}\right)\left(\frac{L_I^4 - L_b^4}{4}\right)\right)$$

$$k_{44} = K_T + \frac{4}{3}k\left[R_0 L_b^3 + \cos^2(\beta)\left(\frac{4R_0(L_I^3 - L_b^3)L_t - 3(R_0 - r_0)(L_I^4 - L_b^4)}{4L_t}\right)\right]$$

For the abutment:

$$\leftarrow +\sum F_x = k_{24} - R_x = 0$$

$$k_{24} = -2k\left[R_0 L_b^2 + 2\cos^2(\beta)\left(\frac{3R_0(L_I^2 - L_b^2)L_t - 2(R_0 - r_0)(L_I^3 - L_b^3)}{6L_t}\right)\right]$$

$$\circlearrowleft +\sum M_C = k_{34} + k_{24}h + K_T = 0$$

$$k_{34} = -K_T + 2kh\left[R_0 L_b^2 + 2\cos^2(\beta)\left(\frac{3R_0(L_I^2 - L_b^2)L_t - 2(R_0 - r_0)(L_I^3 - L_b^3)}{6L_t}\right)\right]$$

The stiffness matrix is therefore:

$$[K] = \begin{bmatrix} K_{11} & K_{12} & 0 & 0 \\ K_{21} & K_{22} & K_{23} & K_{24} \\ 0 & K_{23} & K_{33} & K_{34} \\ 0 & K_{42} & K_{43} & K_{44} \end{bmatrix}$$

Where:

$$K_{11} = K_I$$

$$K_{22} = K_I + 4k\left[R_0 L_b + \cos^2(\beta)\left(\frac{2R_0 L_t^2 - (R_0 - r_0)(L_I^2 - L_b^2)}{2L_t}\right)\right]$$

$$K_{33} = k_{33} = K_T + 4kh^2\left[R_0 L_b + \cos^2(\beta)\left(\frac{2R_0 L_t^2 - (R_0 - r_0)(L_I^2 - L_b^2)}{2L_t}\right)\right]$$

$$K_{44} = K_T + \frac{4}{3}k\left[R_0 L_b^3 + \cos^2(\beta)\left(\frac{4R_0\left(L_I^3 - L_b^3\right)L_t - 3(R_0 - r_0)(L_I^4 - L_b^4)}{4L_t}\right)\right]$$

$$K_{12} = K_{21} = -K_I$$

$$K_{23} = K_{32} = -4kh\left[R_0 L_b + \cos^2(\beta)\left(\frac{2R_0 L_t^2 - (R_0 - r_0)(L_I^2 - L_b^2)}{2L_t}\right)\right]$$

$$K_{24} = K_{42} = -2k\left[R_0 L_b^2 + 2\cos^2(\beta)\left(\frac{3R_0(L_I^2 - L_b^2)L_t - 2(R_0 - r_0)(L_I^3 - L_b^3)}{6L_t}\right)\right]$$

$$K_{34} = K_{43} = -K_T + 2kh\left[R_0 L_b^2 + 2\cos^2(\beta)\left(\frac{3R_0\left(L_I^2 - L_b^2\right)L_t - 2(R_0 - r_0)\left(L_I^3 - L_b^3\right)}{6L_t}\right)\right]$$

A.3 Stiffness Matrix for Cortical Bone Analytical Model

While the mass matrix $[M]$ does not change in the refined analytical model, the addition of a cortical layer will result in a different formulation of the stiffness matrix. The cortical analytical model is shown in Figure A.3.

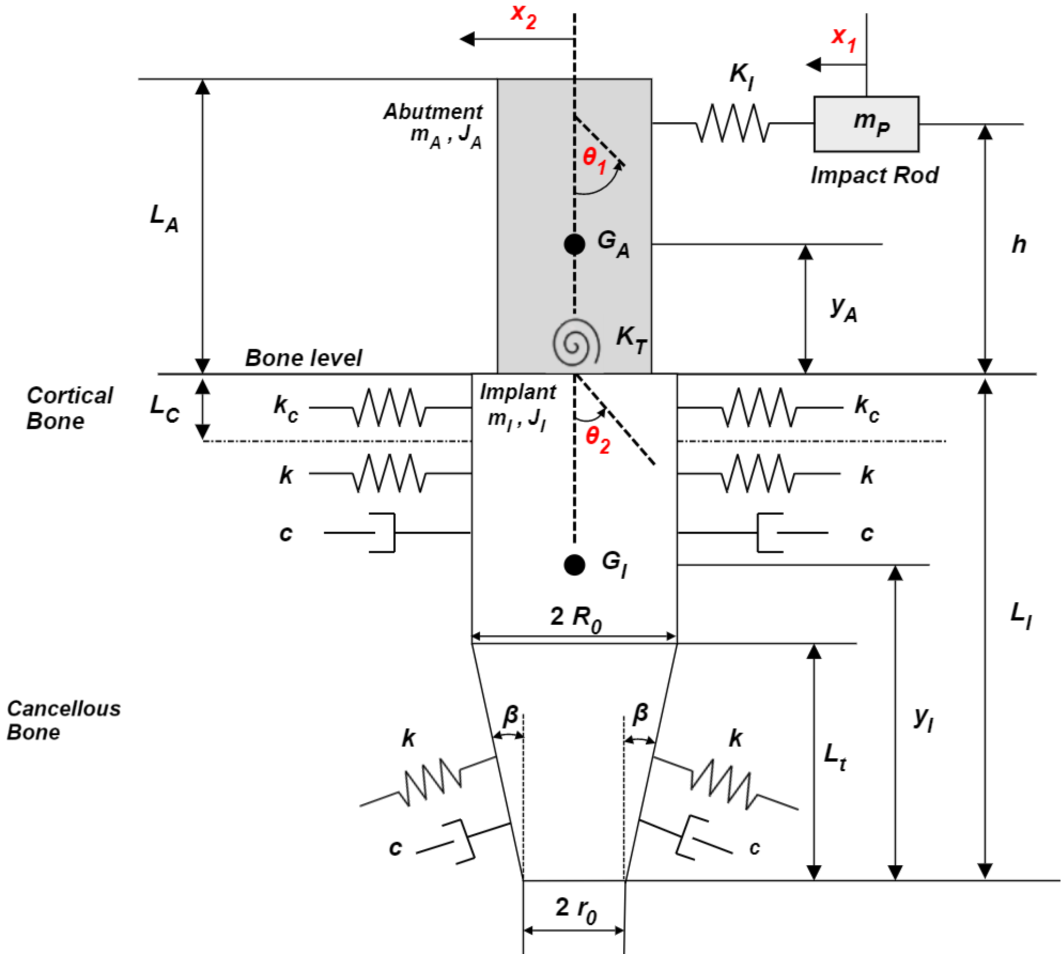

Figure A.3: Four degree of freedom vibration model of a dental implant system with cortical and cancellous bone.

A.3.1 Effective Interfacial Stiffness

In a similar manner to Appendix A.2.1, the effective stiffness per unit length is defined for the cortical and cancellous layers:

$$k_i = \begin{cases} 4k_C R_0 dy, & 0 \leq y \leq L_C \\ 4k R_0 dy, & L_C \leq y \leq L_b \\ 4k\cos^2(\beta)\left(R_0 - \left(\dfrac{R_0 - r_0}{L_t}\right)y\right)dy, & L_b < y \leq L_I \end{cases}$$

Where:

k_C is the stiffness per unit area of the cortical bone

k is the stiffness per unit area of the cancellous bone

L_C is the thickness of the cortical bone

The total effective stiffness of the interface is obtained by integrating k_i over the implant length:

$$k_{eff} = 4k_C R_0 L_C + 4k\left(R_0(L_b - L_C) + \cos^2(\beta)\left(R_0 L_t - \left(\frac{R_0 - r_0}{2L_t}\right)(L_I^2 - L_b^2)\right)\right)$$

R_0 is the radius of the cylindrical portion of the implant

r_0 is the radius of the implant base

L_I is the total implant length

L_b is the length of the cylindrical portion of the implant

L_t is the length of the tapered portion of the implant

A.3.2 Derivation of Stiffness Matrix

The method of stiffness influence coefficients was used to determine the stiffness matrix $[K]$ for the model shown in Figure A.3, where k_{ij} is the force required at coordinate i to maintain a unit displacement at coordinate *j* while holding all other coordinates fixed at zero.

k_{i1}: Unit displacement $x_1 = 1$

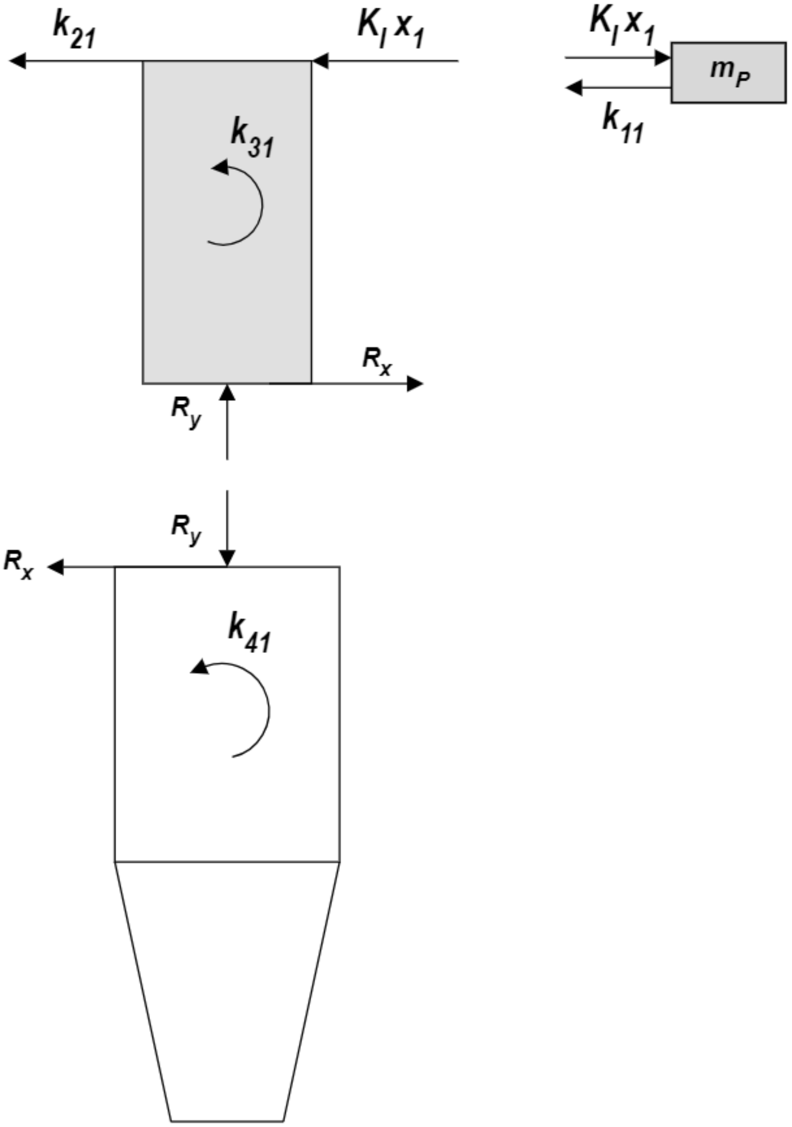

For the impact rod:

$$\leftarrow +\sum F_x = k_{11} - K_I = 0, \qquad k_{11} = K_I$$

For the implant:

$$\leftarrow +\sum F_x = R_x = 0, \qquad R_x = 0$$

$$\circlearrowleft +\sum M_C = k_{41} = 0, \qquad k_{41} = 0$$

For the abutment:

$$\leftarrow +\sum F_x = k_{21} + K_I - R_x = 0, \qquad k_{21} = -K_I$$

$$\circlearrowleft +\sum M_C = k_{31} + (k_{21} + K_I)h = 0, \qquad k_{31} = 0$$

k_{i2}: Unit displacement $x_2 = 1$

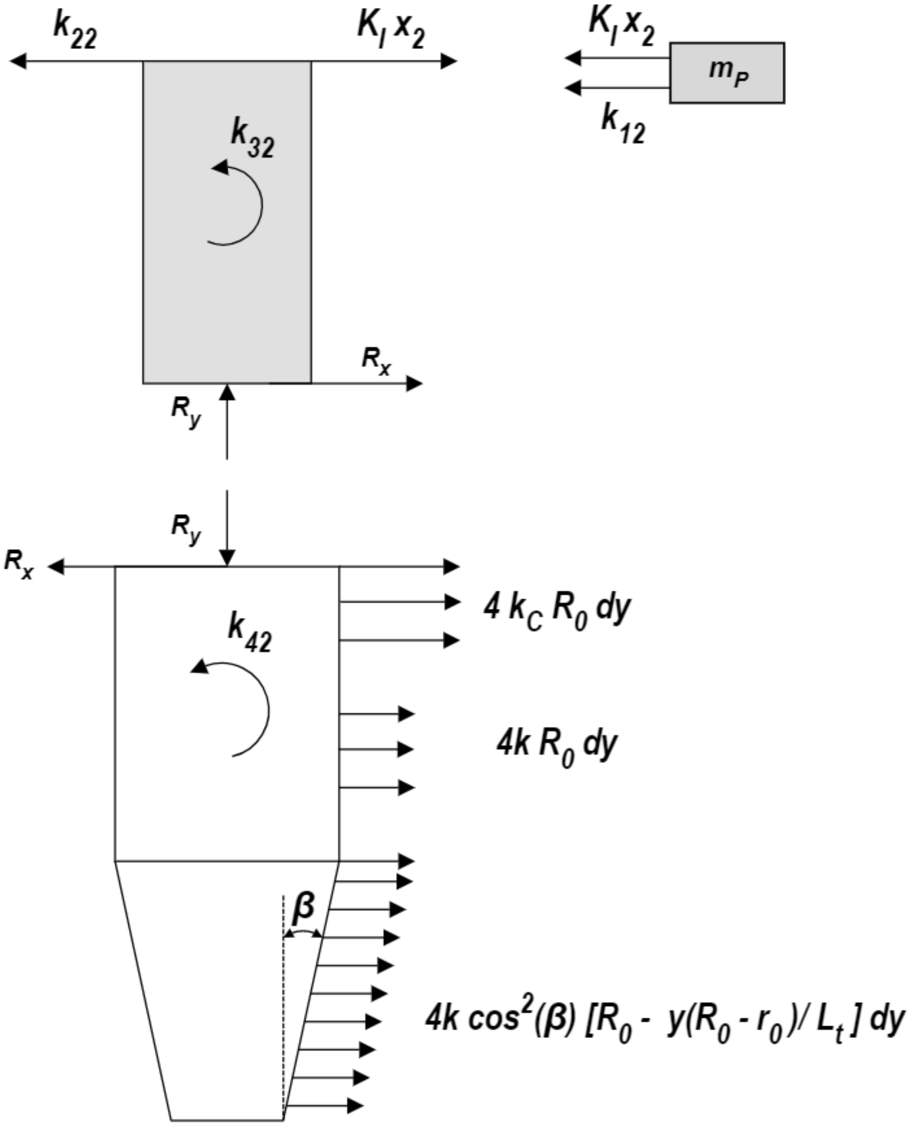

.

For the impact rod:

$$\leftarrow +\sum F_x = k_{12} + K_I = 0, \qquad k_{12} = -K_I$$

For the implant:

$$\leftarrow +\sum F_x = R_x - \int\limits_0^{L_C} 4k_C R_0 dy - \int\limits_{L_C}^{L_b} 4kR_0 dy - \int\limits_{L_b}^{L_I} 4k\cos^2(\beta)\left(R_0 - \left(\frac{R_0 - r_0}{L_t}\right)y\right)dy = 0$$

$$R_x = 4k_C R_0 L_C + 4kR_0(L_b - L_C) + 4k\cos^2(\beta)\left[R_0(L_I - L_b) - \left(\frac{R_0 - r_0}{L_t}\right)\frac{(L_I^2 - L_b^2)}{2}\right]$$

$$R_x = 4\left(k_C R_0 L_C + k\left[R_0(L_b - L_C) + \cos^2(\beta)\left(\frac{2R_0 L_t^2 - (R_0 - r_0)(L_I^2 - L_b^2)}{2L_t}\right)\right]\right)$$

$$\circlearrowleft +\sum M_C = k_{42} + \int\limits_0^{L_C} 4k_C R_0 y dy + \int\limits_{L_C}^{L_b} 4kR_0 y dy + \int\limits_{L_b}^{L_I} 4k\cos^2(\beta)\left(R_0 - \left(\frac{R_0 - r_0}{L_t}\right)y\right)y dy = 0$$

$$k_{42} = -2k_C R_0 L_C^2 - 2kR_0(L_b^2 - L_C^2) - 4k\cos^2(\beta)\left[\frac{R_0(L_I^2 - L_b^2)}{2} - \left(\frac{R_0 - r_0}{3L_t}\right)(L_I^3 - L_b^3)\right]$$

$$k_{42} = -2R_0\left[k\left(L_b^2 - L_C^2 + \cos^2(\beta)\left(L_I^2 - L_b^2 - \frac{2(L_I^3 - L_b^3)(R_0 - r_0)}{3R_0 L_t}\right)\right) + k_C L_C^2\right]$$

For the abutment:

$$\leftarrow +\sum F_x = k_{22} - K_I - R_x = 0,$$

$$k_{22} = K_I + 4\left(k_C R_0 L_C + k\left[R_0(L_b - L_C) + \cos^2(\beta)\left(\frac{2R_0 L_t^2 - (R_0 - r_0)(L_I^2 - L_b^2)}{2L_t}\right)\right]\right)$$

$$k_{22} = K_I + 4R_0\left[k\left(L_b - L_C + L_t\cos^2(\beta)\left(1 - \frac{(L_I^2 - L_b^2)(R_0 - r_0)}{2R_0 L_t^2}\right)\right) + k_C L_C\right]$$

$$\circlearrowleft +\sum M_C = k_{32} + k_{22}h - K_I h = 0$$

$$k_{32} = -4h\left(k_C R_0 L_C + k\left[R_0(L_b - L_C) + \cos^2(\beta)\left(\frac{2R_0 L_t^2 - (R_0 - r_0)(L_I^2 - L_b^2)}{2L_t}\right)\right]\right)$$

$$k_{32} = -4R_0 h\left[k\left(L_b - L_C + L_t\cos^2(\beta)\left(1 - \frac{(L_I^2 - L_b^2)(R_0 - r_0)}{2R_0 L_t^2}\right)\right) + k_C L_C\right]$$

k_{i3}: Unit rotation $\theta_1 = 1$

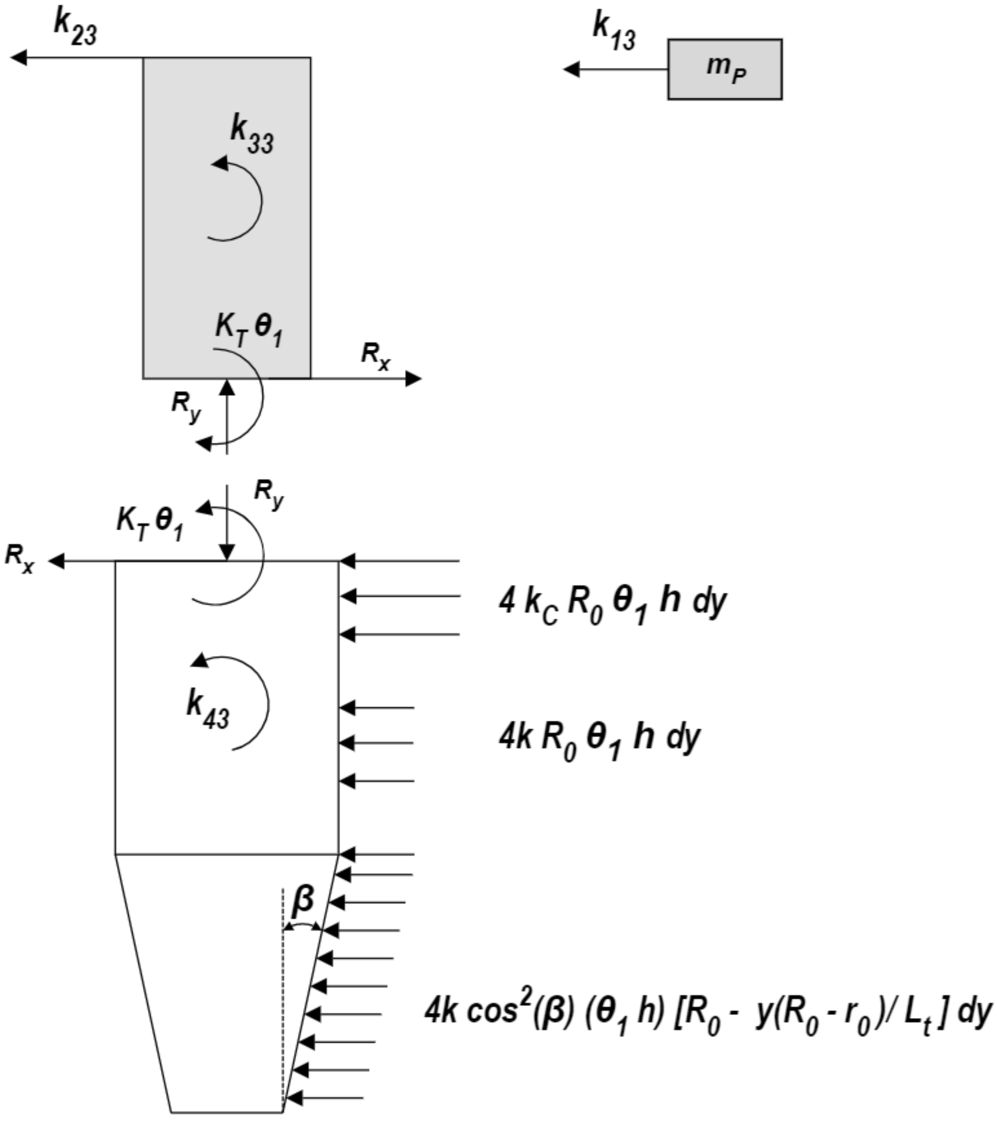

For the impact rod:

$$\leftarrow +\sum F_x = k_{13} = 0, \qquad k_{13} = 0$$

For the implant:

$$\leftarrow +\sum F_x = R_x + \int_{0}^{L_C} 4k_C R_0 h\, dy + \int_{L_C}^{L_b} 4kR_0 h\, dy + \int_{L_b}^{L_I} 4k\cos^2(\beta)\, h\left(R_0 - \left(\frac{R_0 - r_0}{L_t}\right)y\right) dy = 0$$

$$R_x = -4k_C hR_0 L_C - 4khR_0(L_b - L_C) - 4kh\cos^2(\beta)\left(R_0(L_I - L_b) - \left(\frac{R_0 - r_0}{L_t}\right)\left(\frac{L_I^2 - L_b^2}{2}\right)\right)$$

$$R_x = -4h\left(k_C R_0 L_C + k\left[R_0(L_b - L_C) + \cos^2(\beta)\left(\frac{2R_0 L_t^2 - (R_0 - r_0)(L_I^2 - L_b^2)}{2L_t}\right)\right]\right)$$

$$\circlearrowleft +\sum M_C = k_{43} + K_T - \int_{0}^{L_C} 4k_C hR_0 y dy - \int_{L_C}^{L_b} 4khR_0 y dy - \int_{L_b}^{L_I} 4kh\cos^2(\beta)\left(R_0 - \left(\frac{R_0 - r_0}{L_t}\right)y\right) y dy = 0$$

$$k_{43} = -K_T + 2k_C hR_0 L_C^2 + kh\left[2R_0\left(L_b^2 - L_C^2\right) + 4\cos^2(\beta)\left(\frac{R_0\left(L_I^2 - L_b^2\right)}{2} - \left(\frac{R_0 - r_0}{L_t}\right)\left(\frac{\left(L_I^3 - L_b^3\right)}{3}\right)\right)\right]$$

$$k_{43} = -K_T + 2h\left(k_C R_0 L_C^2 + k\left[R_0\left(L_b^2 - L_C^2\right) + 2\cos^2(\beta)\left(\frac{3R_0\left(L_I^2 - L_b^2\right)L_t - 2(R_0 - r_0)\left(L_I^3 - L_b^3\right)}{6L_t}\right)\right]\right)$$

$$k_{43} = -K_T + 2R_0 h\left[k\left(L_b^2 - L_C^2 + \cos^2(\beta)\left(L_I^2 - L_b^2 - \frac{2(L_I^3 - L_b^3)(R_0 - r_0)}{3R_0 L_t}\right)\right) + k_C L_C^2\right]$$

For the abutment:

$$\leftarrow +\sum F_x = k_{23} - R_x = 0$$

$$k_{23} = -4h\left(k_C R_0 L_C + k\left[R_0(L_b - L_C) + \cos^2(\beta)\left(\frac{2R_0 L_t^2 - (R_0 - r_0)(L_I^2 - L_b^2)}{2L_t}\right)\right]\right)$$

$$k_{23} = -4R_0 h\left[k\left(L_b - L_C + L_t\cos^2(\beta)\left(1 - \frac{(L_I^2 - L_b^2)(R_0 - r_0)}{2R_0 L_t^2}\right)\right) + k_C L_C\right]$$

$$\circlearrowleft + \sum M_C = k_{33} - K_T + k_{23}h = 0$$

$$k_{33} = K_T + 4R_0 h^2\left[k\left(L_b - L_C + L_t\cos^2(\beta)\left(1 - \frac{(L_I^2 - L_b^2)(R_0 - r_0)}{2R_0 L_t^2}\right)\right) + k_C L_C\right]$$

k_{i4}: Unit rotation $\theta_2 = 1$

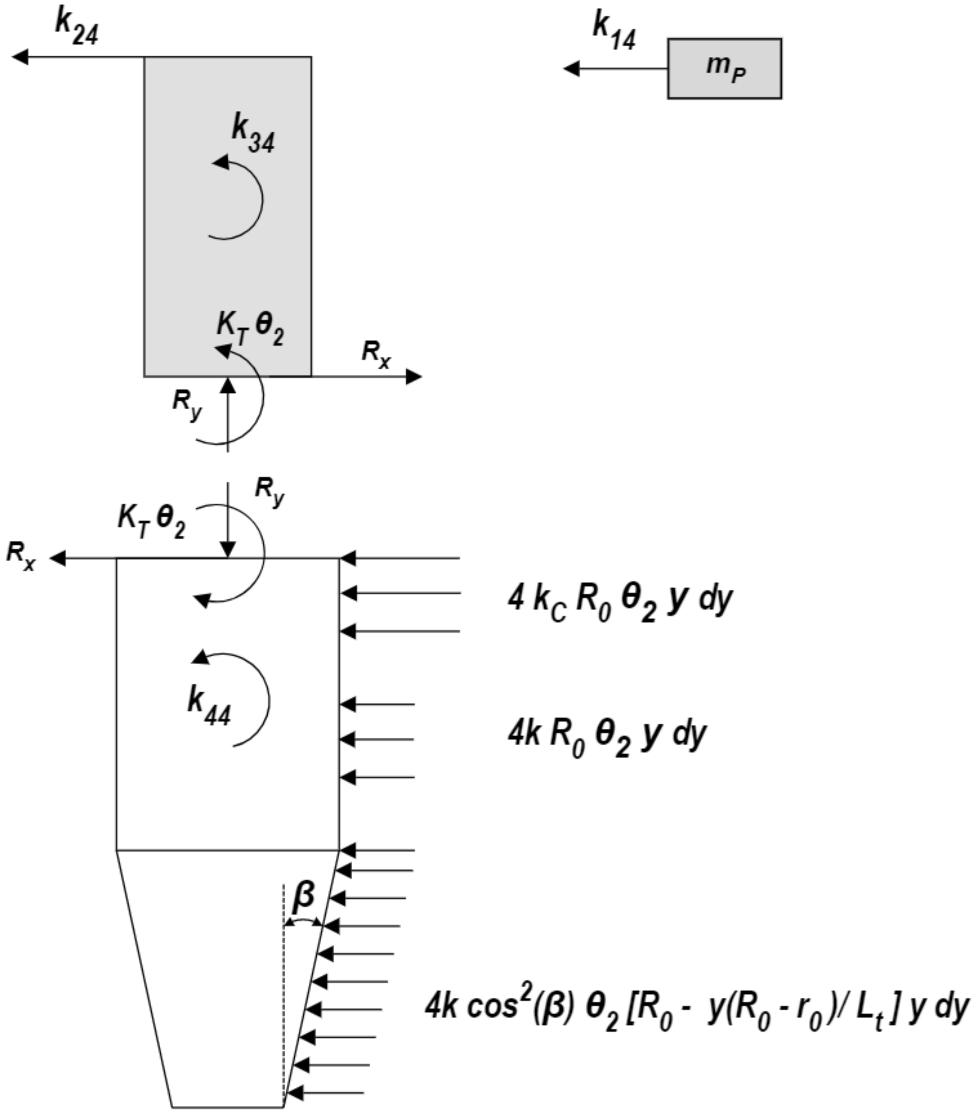

For the impact rod:

$$\leftarrow +\sum F_x = k_{14} = 0, \qquad k_{14} = 0$$

For the implant:

$$\leftarrow +\sum F_x = R_x + \int_0^{L_C} 4k_C R_0 y\,dy + \int_{L_C}^{L_b} 4kR_0 y\,dy + \int_{L_b}^{L_I} 4k\cos^2(\beta)\left(R_0 - \left(\frac{R_0 - r_0}{L_t}\right)y\right)y\,dy = 0$$

$$R_x = -2k_C R_0 L_C^2 - 2kR_0\left(L_b^2 - L_C^2\right) - 4k\cos^2(\beta)\left[R_0\left(\frac{L_I^2 - L_b^2}{2}\right) - \left(\frac{R_0 - r_0}{L_t}\right)\left(\frac{L_I^3 - L_b^3}{3}\right)\right]$$

$$R_x = -2\left(k_C R_0 L_C^2 + k\left[R_0\left(L_b^2 - L_C^2\right) + 2\cos^2(\beta)\left(\frac{3R_0\left(L_I^2 - L_b^2\right)L_t - 2\left(R_0 - r_0\right)\left(L_I^3 - L_b^3\right)}{6L_t}\right)\right]\right)$$

$$\circlearrowleft +\sum M_C = k_{44} - K_T - \int_0^{L_C} 4k_C R_0 y^2\,dy - \int_{L_C}^{L_b} 4kR_0 y^2\,dy - \int_{L_b}^{L_I} 4k\cos^2(\beta)\left(R_0 - \left(\frac{R_0 - r_0}{L_t}\right)y\right)y^2\,dy = 0$$

$$k_{44} = K_T + \frac{4k_C R_0 L_C^3}{3} + \frac{4kR_0\left(L_b^3 - L_C^3\right)}{3} + 4k\cos^2(\beta)\left(\frac{R_0\left(L_I^3 - L_b^3\right)}{3} - \left(\frac{R_0 - r_0}{L_t}\right)\left(\frac{L_I^4 - L_b^4}{4}\right)\right)$$

$$k_{44} = K_T + \frac{4}{3}R_0\left[k\left(L_b^3 - L_C^3 + \cos^2(\beta)\left(L_I^3 - L_b^3 - \frac{3\left(L_I^4 - L_b^4\right)\left(R_0 - r_0\right)}{4R_0 L_t}\right)\right) + k_C L_C^3\right]$$

For the abutment:

$$\leftarrow +\sum F_x = k_{24} - R_x = 0$$

$$k_{24} = -2R_0\left[k\left(L_b^2 - L_C^2 + \cos^2(\beta)\left(L_I^2 - L_b^2 - \frac{2\left(L_I^3 - L_b^3\right)\left(R_0 - r_0\right)}{3R_0 L_t}\right)\right) + k_C L_C^2\right]$$

$$\circlearrowleft +\sum M_C = k_{34} + k_{24}h + K_T = 0$$

$$k_{34} = -K_T + 2R_0 h\left[k\left(L_b^2 - L_C^2 + \cos^2(\beta)\left(L_I^2 - L_b^2 - \frac{2\left(L_I^3 - L_b^3\right)\left(R_0 - r_0\right)}{3R_0 L_t}\right)\right) + k_C L_C^2\right]$$

The stiffness matrix is therefore:

$$[K] = \begin{bmatrix} K_{11} & K_{12} & 0 & 0 \\ K_{21} & K_{22} & K_{23} & K_{24} \\ 0 & K_{23} & K_{33} & K_{34} \\ 0 & K_{42} & K_{43} & K_{44} \end{bmatrix}$$

Where:

$$K_{11} = K_I$$

$$k_{22} = K_I + 4R_0 \left[k \left(L_b - L_C + L_t \cos^2(\beta) \left(1 - \frac{(L_I^2 - L_b^2)(R_0 - r_0)}{2R_0 L_t^2} \right) \right) + k_C L_C \right]$$

$$K_{33} = K_T + 4R_0 h^2 \left[k \left(L_b - L_c + L_t \cos^2(\beta) \left(1 - \frac{(L_I^2 - L_b^2)(R_0 - r_0)}{2R_0 L_t^2} \right) \right) + k_C L_C \right]$$

$$K_{44} = K_T + \frac{4}{3} R_0 \left[k \left(L_b^3 - L_C^3 + \cos^2(\beta) \left(L_I^3 - L_b^3 - \frac{3(L_I^4 - L_b^4)(R_0 - r_0)}{4R_0 L_t} \right) \right) + k_C L_C^3 \right]$$

$$K_{12} = K_{21} = -K_I$$

$$K_{23} = K_{32} = -4R_0 h \left[k \left(L_b - L_C + L_t \cos^2(\beta) \left(1 - \frac{(L_I^2 - L_b^2)(R_0 - r_0)}{2R_0 L_t^2} \right) \right) + k_C L_C \right]$$

$$K_{24} = K_{42} = -2R_0 \left[k \left(L_b^2 - L_C^2 + \cos^2(\beta) \left(L_I^2 - L_b^2 - \frac{2(L_I^3 - L_b^3)(R_0 - r_0)}{3R_0 L_t} \right) \right) + k_C L_C^2 \right]$$

$$K_{34} = K_{43} = -K_T + 2R_0 h \left[k \left(L_b^2 - L_C^2 + \cos^2(\beta) \left(L_I^2 - L_b^2 - \frac{2(L_I^3 - L_b^3)(R_0 - r_0)}{3R_0 L_t} \right) \right) + k_C L_C^2 \right]$$

A.4 Derivation of Torsional Stiffness

The torsional stiffness of the implant-abutment connection is based on previous work with the ASIST approach (Swain et al., 2008a; Westover et al., 2016a). The abutment was approximated as a cantilever beam (Figure A.4), and the impact is simulated as a point load P at a distance L, which corresponds to the striking height.

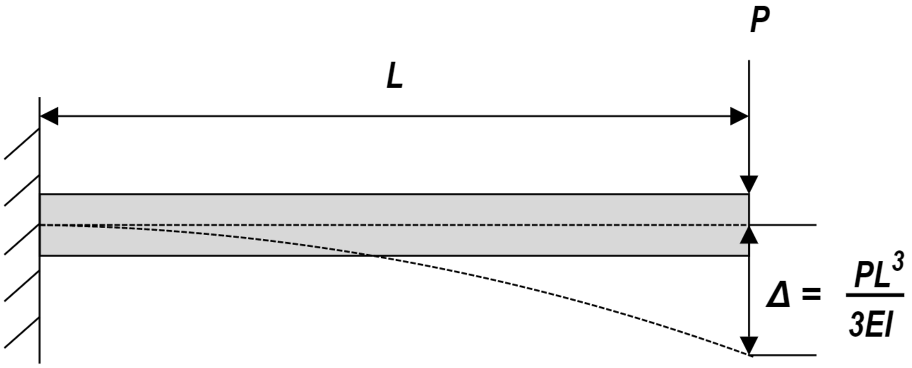

Figure A.4: Cantilever beam (length L) with point load P applied at the end.

The deflection is given as:

$$\Delta = \frac{PL^3}{3EI}$$

Where E is the Young's modulus and I is the cross-section's second moment of area. This relation can be used to define the rotation of the abutment if it is assumed that the abutment is rigid with a torsional spring K_T at the end (Figure A.5):

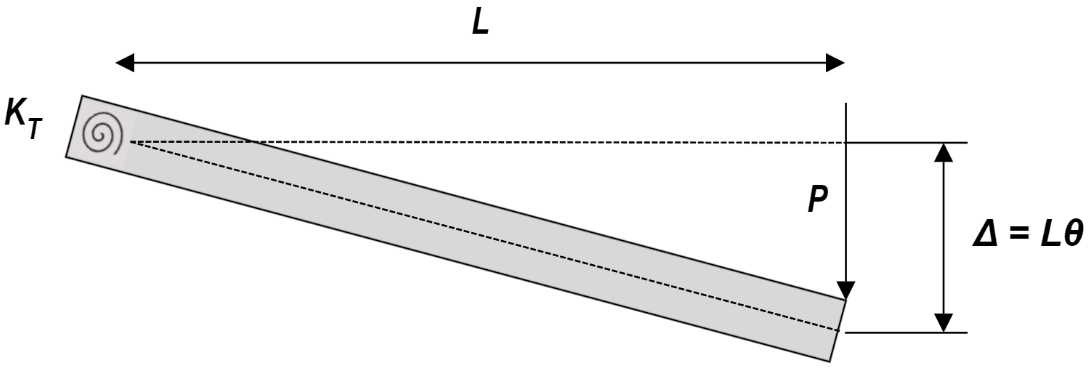

Figure A.5: Deflection of a rigid beam due to applied load P with torsional spring K_T at the end.

The corresponding deflection of the end is:

$$PL = K_T\theta$$

$$\Delta = L\theta, \qquad \theta = \frac{PL^2}{3EI}$$

$$PL = K_T\left(\frac{PL^2}{3EI}\right)$$

Using this, the torsional stiffness can be approximated as:

$$K_T = \frac{3EI}{L}$$

This approximation is based on the deflection corresponding to a rigid connection. In actuality, the abutment and implant are linked with a screw connection. As a result, the actual torsional stiffness is lower than the value calculated from the equation above (Swain et al., 2008a). Therefore, a correctional factor $\beta \in (0,1)$ is introduced:

$$K_T = \alpha\left(\frac{3EI}{L}\right) = \alpha K_{Tmax}$$

The K_{Tmax} was determined for each healing abutment (Figure A.6) using their corresponding geometric approximations (Figure A.7).

Figure A.6: From left to right: healing abutments 3.3HA, 3.6HA, 4.5HA, 6.0HA.

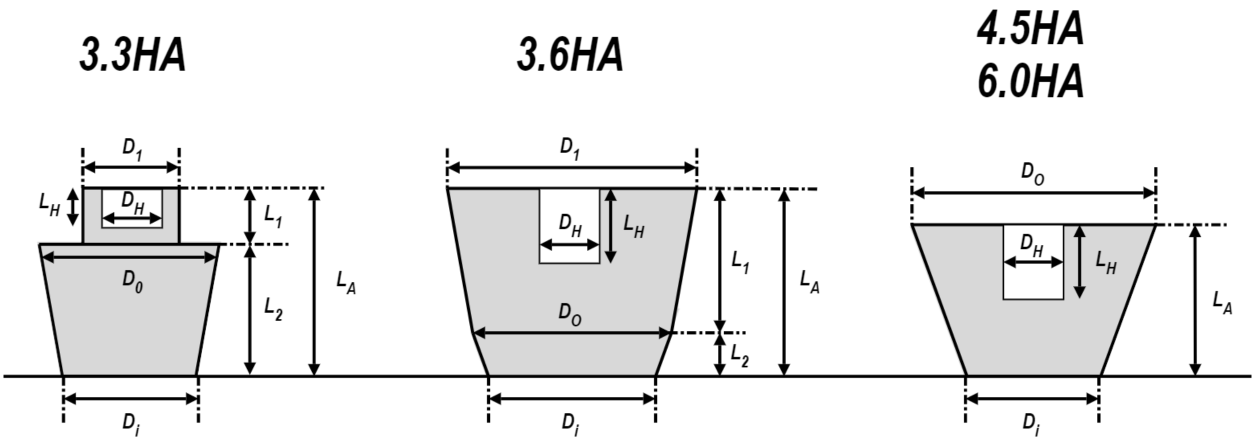

Figure A.7: Geometric approximations of healing abutments.

Since the abutments possess a non-uniform cross section across its length, the total strain energy of the abutment was found in terms of the applied load P and used to find the deflection of the free end using Castigliano's method. An example calculation is shown for abutment 6.0HA using geometry C.

$D(x)$ corresponds to the cross-sectional diameter at a distance x from the fixed end of the abutment.

$$E = 105 \text{ GPa} = 1.1 \times 10^{11} \text{ Pa}$$

$$D_0 = 6 \text{ mm}, \qquad D_i = 3.43 \text{ mm}, \qquad D_H = 1.3 \text{ mm}$$

$$L_A = 4 \text{ mm}, \qquad L_H = 0.8 \text{ mm}$$

$$I_1(x) = \frac{\pi}{64}[D(x)]^4$$

$$I_2(x) = \frac{\pi}{64}\left[\left(D(x)\right)^4 - D_H^4\right]$$

$$D(x) = D_i + \left(\frac{D_0 - D_i}{L_A}\right)x$$

The strain energy due to bending of a beam is:

$$dU = \frac{M^2}{2EI}dx$$

Where M is the applied bending moment at a distance x from the fixed end. For an applied point load:

$$M(x) = -P(L_A - x), \qquad M^2 = P^2(L_A - x)^2$$

The strain energy of the abutment is therefore:

$$U = \int_{0}^{L_A - L_H} \frac{P^2(L_A - x)^2}{2EI_1(x)}dx + \int_{L_A - L_H}^{L_A} \frac{P^2(L_A - x)^2}{2EI_2(x)}dx$$

$$= \frac{P^2}{2E}\left(\int_{0}^{0.0032} \frac{(0.006 - x)^2}{\frac{\pi}{64}(0.00343 + 0.6425x)^4}dx + \int_{0.0032}^{0.004} \frac{(0.006 - x)^2}{\frac{\pi}{64}[(0.00343 + 0.6425x)^4 - 0.0013^4]}dx\right)$$

$$U = (8.547 \times 10^{-9})P^2$$

The deflection of the free end is given as:

$$\Delta = \frac{\partial U}{\partial P} = (1.709 \times 10^{-8})P$$

The maximum K_T is determined as:

$$K_{Tmax} = \frac{PL_A^2}{\Delta} = 936 \text{ Nm}$$

Table A.1: Maximum torsional stiffness values for each healing abutment.

Abutment	Maximum K_T (Nm)
3.3HA	267
3.6HA	400
4.5HA	1367
6.0HA	936

The geometries of each crown and their corresponding prosthetic abutment were approximated as symmetric with simple geometries, as shown in Figure A.8 to Figure A.10. The maximum torsional stiffness was estimated in a similar manner to the healing abutments. However, the abutment is now modelled as a composite beam with respect to the different material properties of the crown (Katana STML Zirconia, Katana, Kuraray Noritake) and abutment (titanium).

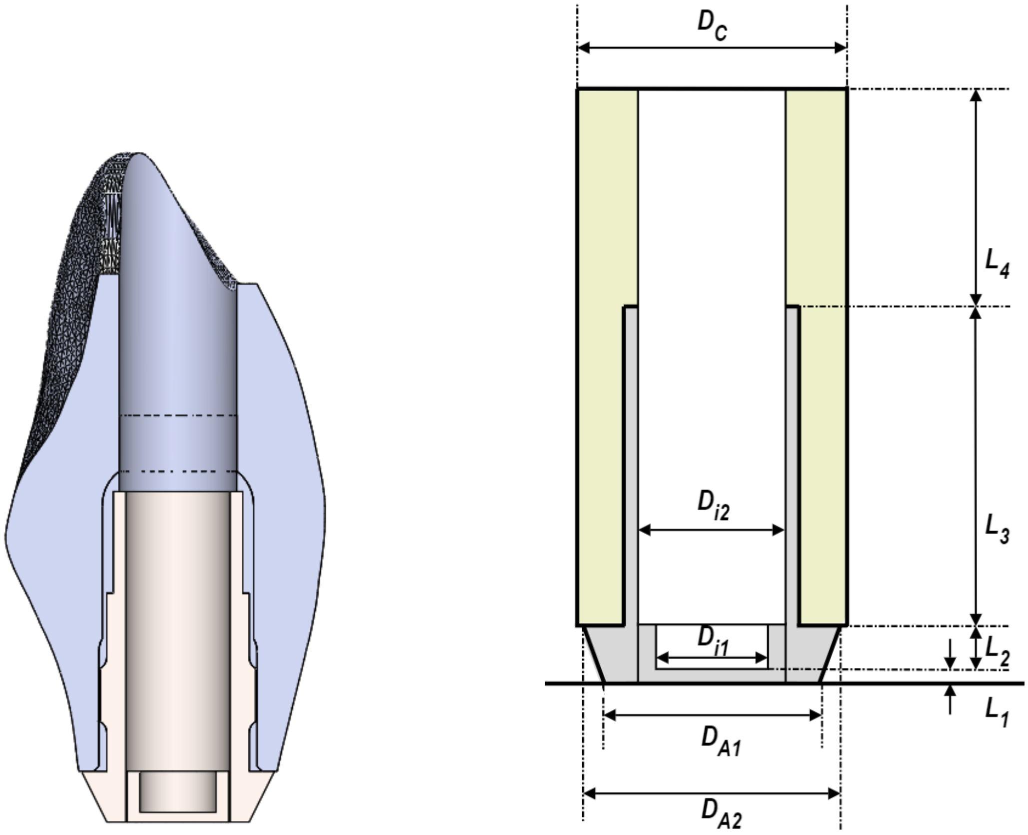

Figure A.8: Actual geometry (left) and approximated geometry (right) of the NC lateral incisor. The abutment material (titanium) is shaded in gray, while the crown material (zirconia composite) is shaded in light green.

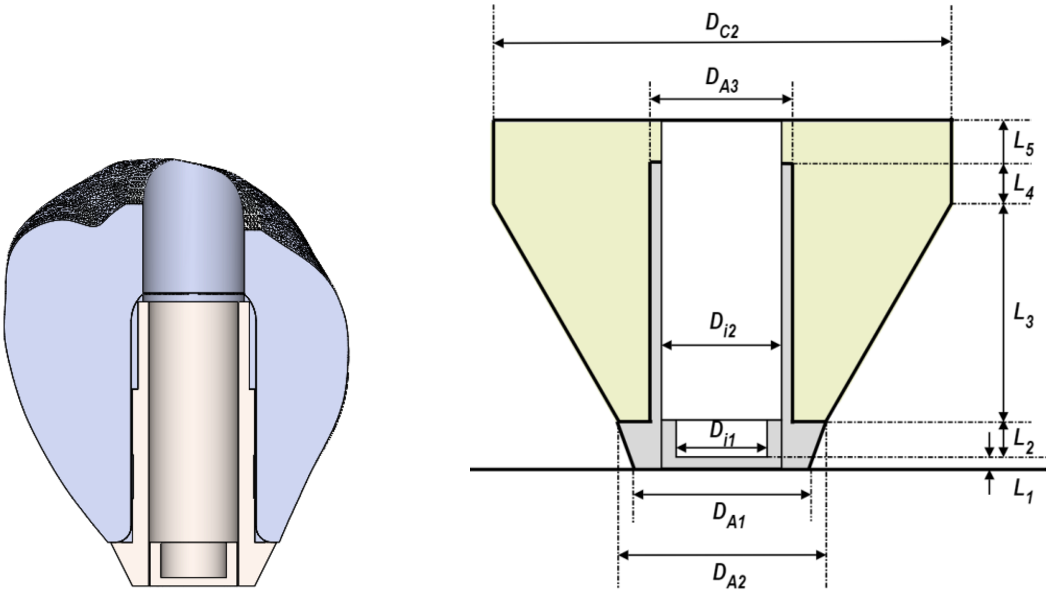

Figure A.9: Actual geometry (left) and approximated geometry (right) of the NC first premolar. The abutment material (titanium) is shaded in gray, while the crown material (zirconia composite) is shaded in light green.

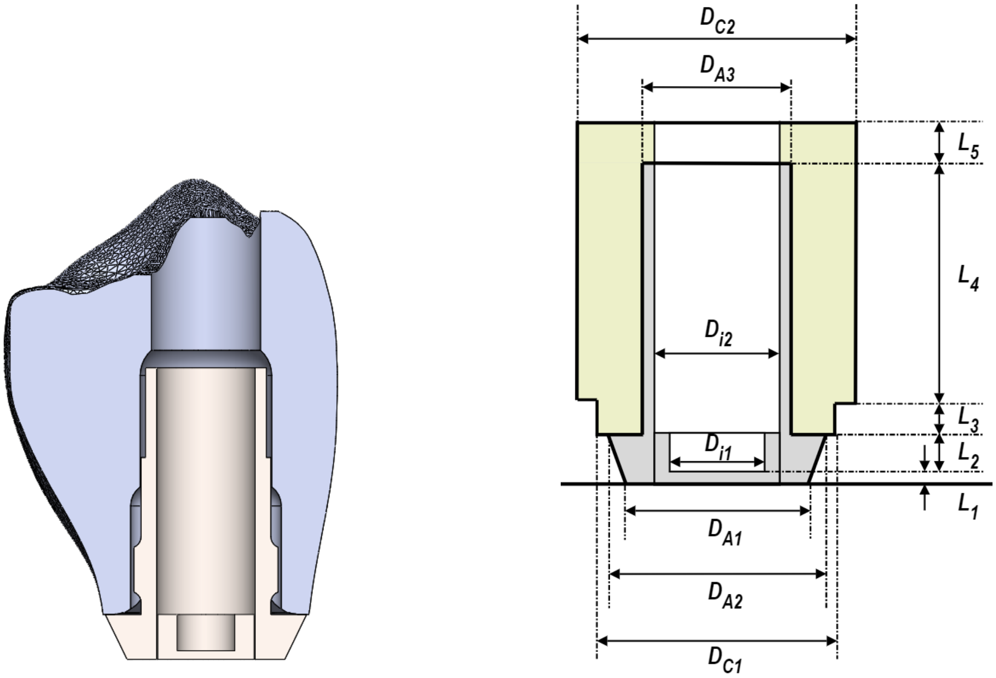

Figure A.10: Actual geometry (left) and approximated geometry (right) of the RC first premolar. The abutment material (titanium) is shaded in gray, while the crown material (zirconia composite) is shaded in light green.

An example analysis is shown for the RC first premolar crown-abutment assembly. It is assumed that the abutment screw and body are a single solid body.

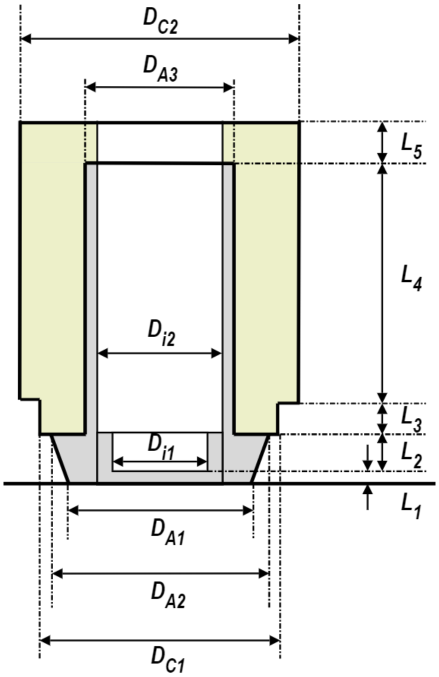

The abutment dimensions were measured and estimated as:

$$D_{A1} = 2.7\text{ mm}, \qquad D_{A2} = 4.5\text{ mm}, \qquad D_{i1} = 1.3\text{ mm}, \qquad D_{i2} = 2.2\text{ mm},$$

$$D_{C1} = 4.6\text{ mm}, \qquad D_{C2} = 8\text{ mm}$$

$$L_1 = 0.2\text{ mm}, \qquad L_2 = 0.8\text{ mm}, \qquad L_3 = 1.5\text{ mm}, \qquad L_4 = 4\text{ mm}, \qquad L_5 = 4\text{ mm}$$

D corresponds to the inner diameter (D_i) or outer diameters of the abutment (D_A) and crown (D_C). L corresponds to the length of sections obtained by partitioning the assembly at changes in the cross-section.

For a composite cross-section, analysis was done on an equivalent beam that is entirely made of titanium. This was done by scaling the width of the crown material by E_2/E_1, where E_1 and E_2 correspond to the elastic modulus of the abutment and crown, respectively. The crown material was assumed to have an elastic modulus of 29 GPa (Karaer et al., 2023), while the abutment was assumed to be titanium ($E_1 = 110$ GPa). An example of the transformed cross section in the segment L_4 is shown.

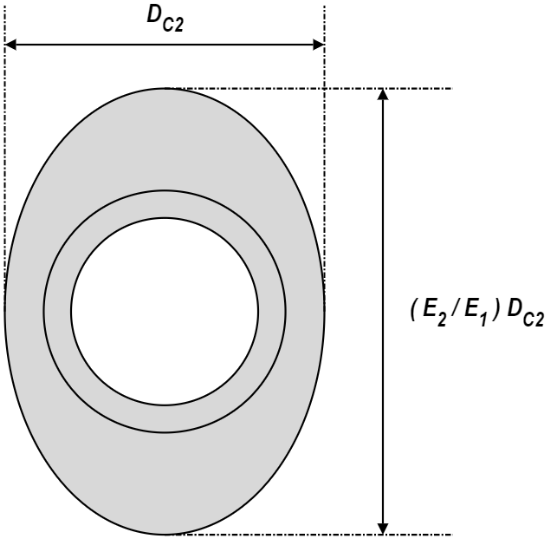

The second moment of area was defined as:

$$I(x) = \begin{cases} \dfrac{\pi}{64}[D_1(x)]^4 & 0 \le x \le L_1 \\ \dfrac{\pi}{64}\left[\left(D_1(x)\right)^4 - d_{i1}^4\right] & L_1 < x \le L_1 + L_2 \\ \dfrac{\pi}{64}\left[(D_{C1})^3\left(\dfrac{E_2}{E_1}\right)(D_{C1}) - d_{i2}^4\right] & (L_1 + L_2) < x \le (L_1 + L_2 + L_3) \\ \dfrac{\pi}{64}\left[(D_{C2})^3\left(\dfrac{E_2}{E_1}\right)(D_{C2}) - d_{i2}^4\right] & (L_1 + L_2 + L_3) < x \le (L_1 + L_2 + L_3 + L_4) \\ \dfrac{\pi}{64}(D_{C2}^4 - d_{i2}^4) & (L_1 + L_2 + L_3 + L_4) < x \le (L_1 + L_2 + L_3 + L_4 + L_5) \end{cases}$$

Where:

$$D_1(x) = D_{A1} + \left(\frac{D_{A2} - D_{A1}}{L_1 + L_2}\right)x, \qquad 0 \le x \le (L_1 + L_2)$$

The strain energy was determined as:

$$U = \frac{P^2}{2}\left(\int_0^{L_1} \frac{(L_A - x)^2}{E_1 I_1(x)}dx + \int_{L_1}^{L_1+L_2} \frac{(L_A - x)^2}{E_1 I_2(x)}dx + \int_{L_1+L_2}^{L_1+L_2+L_3} \frac{(L_A - x)^2}{E_1 I_3(x)}dx \right.$$
$$\left. + \int_{L_1+L_2+L_3}^{L_1+L_2+L_3+L_4} \frac{(L_A - x)^2}{E_1 I_4(x)}dx + \int_{L_1+L_2+L_3+L_4}^{L_1+L_2+L_3+L_4+L_5} \frac{(L_A - x)^2}{E_2 I_5(x)}dx \right)$$

Where L_A is the total height of the abutment and crown. For the RC premolar:

$$L_A = 10.5 \text{ mm}$$

The strain energy is:

$$U = (6.16 \times 10^{-8})P^2$$

The deflection of the free end is given as:

$$\Delta = \frac{\partial U}{\partial P} = (1.23 \times 10^{-7})P$$

The maximum K_T is determined as:

$$K_{Tmax} = \frac{PL_A^2}{\Delta} = 343 \text{ Nm}$$

Table A.2: Maximum torsional stiffness values for each dental crown.

Crown	Maximum K_T (Nm)
NC Incisor	296
NC Premolar	291
RC Premolar	343

Appendix B: Parametric Sensitivity Analysis

B.1 Sensitivity of Quality of Fit to Stiffness Parameters

This section evaluates the sensitivity of the matched analytical response for a given signal to variations in the impact stiffness K_I and torsional stiffness K_T. The quality of fit between the measured signal and model solution was quantified by an R^2 value. For each implant-abutment combination, a sample measurement from each of the uniform bone blocks (#10, #20, #30, #40 foam) was used to determine the ASC and R^2 values across a range of values for K_I and K_T. For each data set, the matching process was repeated for values of K_I between 2×10^6 N/m to 8×10^6 N/m, and for the torsional stiffness proportionality constant β was varied between 0.01 and 1.

When varying K_I, a distinct peak can be seen in the R^2 value for each implant-abutment system (Figure B.4 to Figure B.10), which corresponds to the best-fit between the experimental data and model solution. An example is shown in Figure B.1 for a sample measurement taken on a replicate of the RC-6.0HA-20 system, where the blue and black lines correspond to the ASC and R^2 values, respectively.

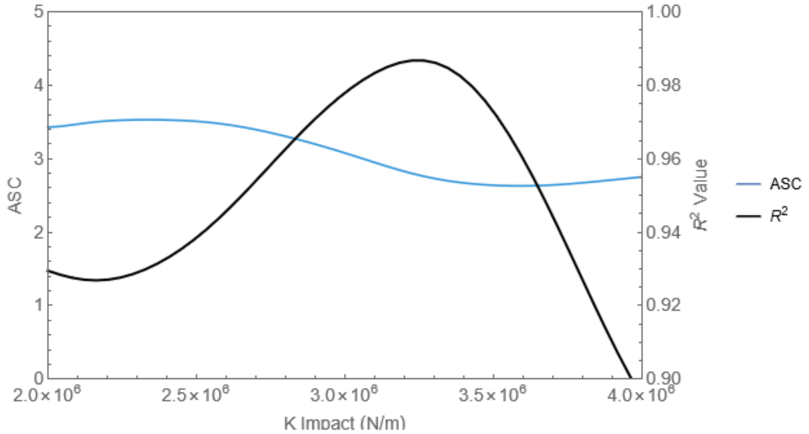

Figure B.1*:* **ASC values (blue line) and R^2 values (black line) for various values of the impact stiffness (K_I) for the RC-6.0HA system.**

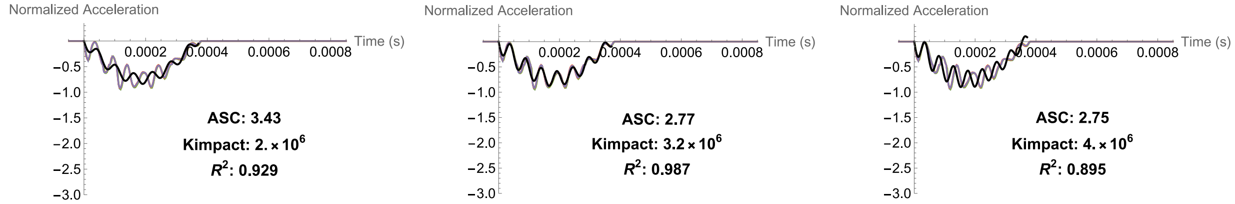

Figure B.2*:* Effect of varying the impact stiffness on the ASC and $\mathbf{R^2}$ value.

Shown in Figure B.2, the impact stiffness (K_I) has a visible effect on the second mode frequency of the predicted analytical response. Increasing K_I from 2×10^6 N/m to 3.2×10^6 N/m decreases the ASC by 0.66 (19.2%) and changes the R^2 from 0.929 to 0.986 (6.1%). Further increasing K_I from 3.2×10^6 N/m to 4×10^6 N/m only decreases the ASC by 0.02 (0.7%), but worsens the R^2 to 0.895 (9.3%). Due to this, the impact stiffness was left unfixed, so that the ASIST is better able to properly determine the corresponding analytical response by selecting the value of K_I that provides the closest fit to the experimental data. This in turn improves individual estimates of the interfacial stiffness k.

At lower foam densities (Figure B.4 to Figure B.10), there is an increasingly narrower range of K_I values which provide a satisfactory quality of fit. This suggests that the device is better able to measure the stability at lower interfacial stiffnesses. In a clinical setting, the ASIST would be increasingly effective for implants that become gradually more unstable, which would allow clinicians to pre-emptively detect implants with an increasingly higher risk of failure.

When varying the torsional proportionality constant α, both ASC and R^2 values were sensitive to changes in K_T in the lower region (Figure B.4 to Figure B.10). An example is shown for the RC-6.0HA-20 system in Figure B.3, where R^2 and ASC do not change noticeably past a certain threshold, corresponding to approximately $\alpha = 0.1$. Therefore, estimates of k are not affected by K_T if the abutment is adequately tightened into the implant socket, because the two components act as a single rigid body and allow for the impact force to be transferred from the abutment to the implant. This can also be seen in the mode shapes shown in Appendix B.2; in the first and second modes, there is a minimal amount of relative motion between the implant and abutment.

A notable exception to this trend is seen for abutment 3.3HA in the #10 test block (Figure B.4) and abutment 3.6HA in the #10 and #20 test blocks (Figure B.5), where there is a distinct peak in R^2 values rather than a flat curve. Despite this, ASC values remain essentially constant past the previously described threshold for K_T, which shows that the interfacial stiffness can still be properly estimated for variations in the assumed K_T if the abutment is sufficiently tightened in the implant.

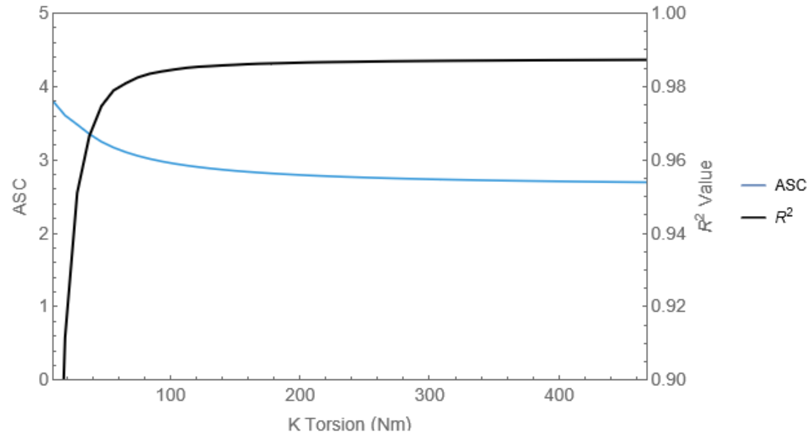

Figure B.3: ASC values (blue line) and R^2 values (black line) for various values of the torsional stiffness (K_T) for the RC-6.0HA system.

#10 (ρ = 0.16 g/cm^3)

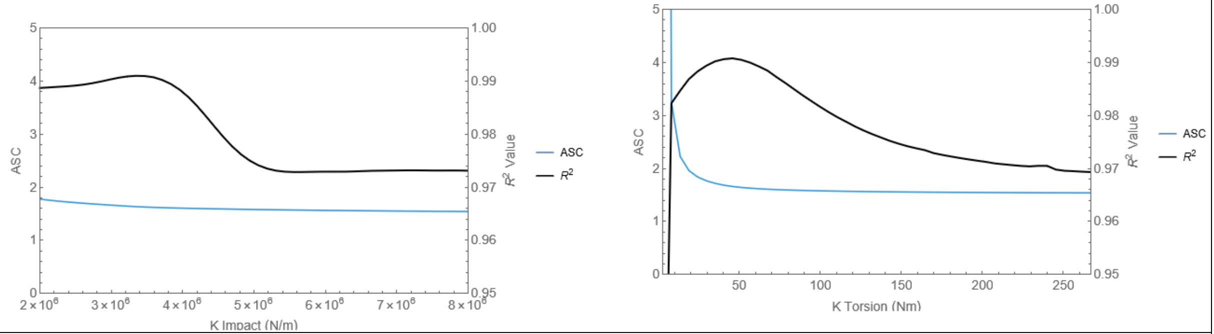

#20 (ρ = 0.32 g/cm^3)

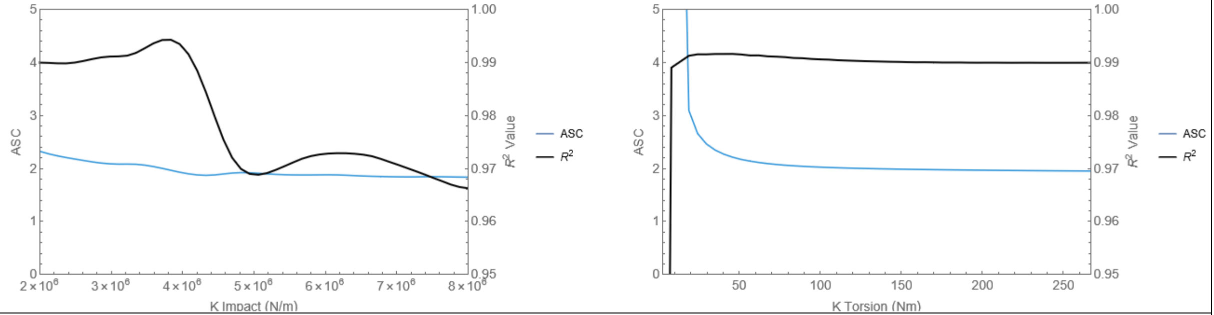

#30 (ρ = 0.48 g/cm^3)

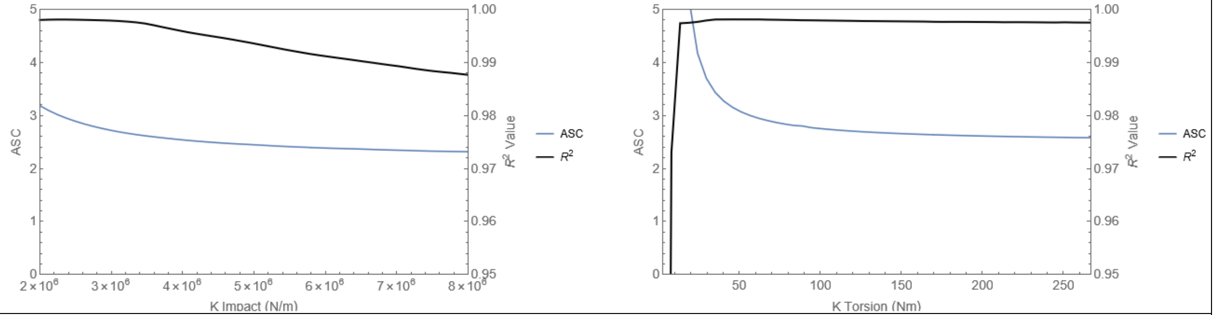

#40 (ρ = 0.64 g/cm^3)

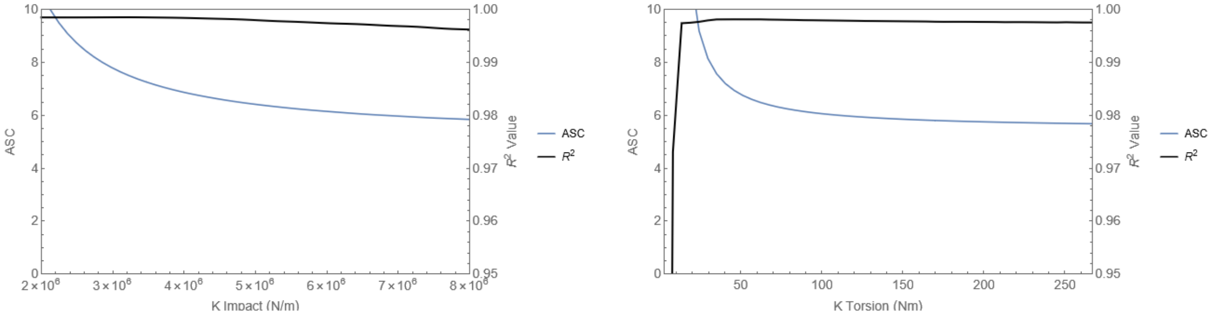

Figure B.4: Changes in ASC (blue line) and R^2 values (black line) by varying K_I (left) and K_T (right) for the NC-3.3HA implant system in various substrates (#10, #20, #30, #40 bone blocks).

#10 (ρ = 0.16 g/cm^3)

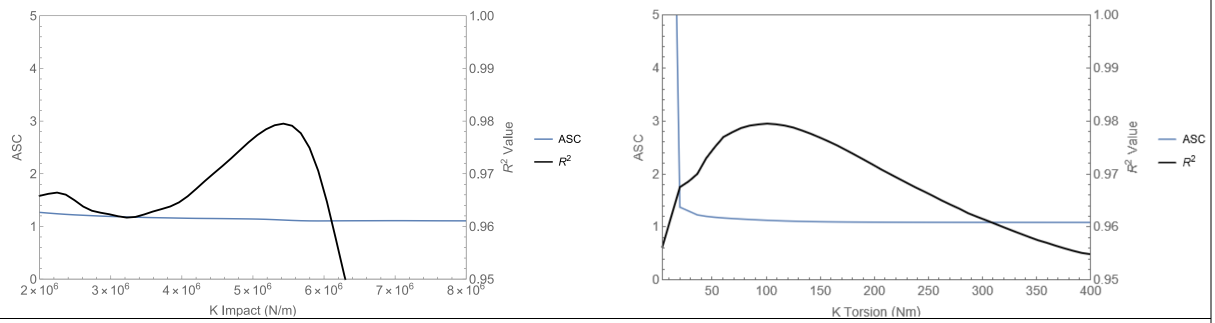

#20 (ρ = 0.32 g/cm^3)

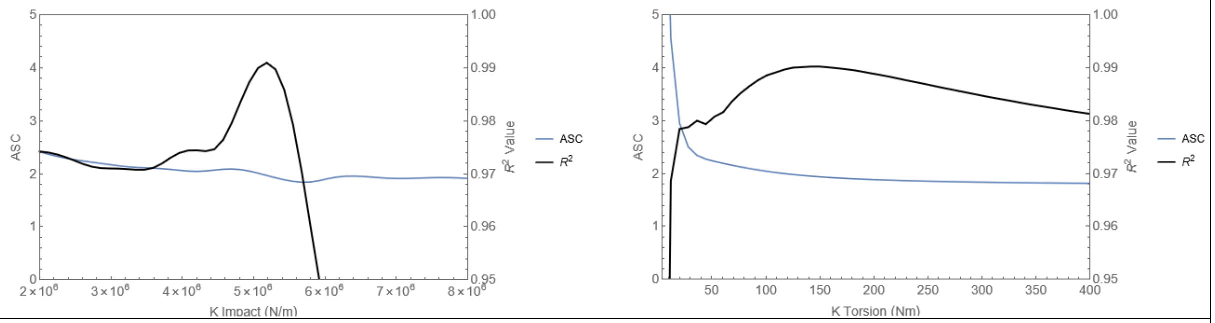

#30 (ρ = 0.48 g/cm^3)

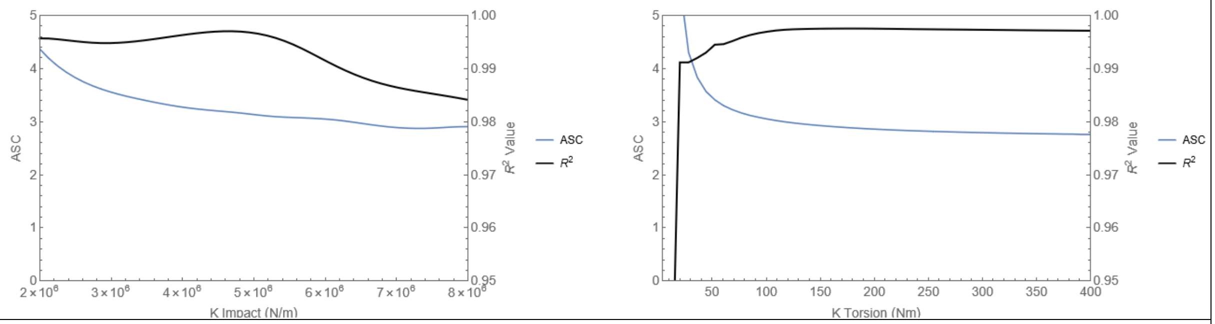

#40 (ρ = 0.64 g/cm^3)

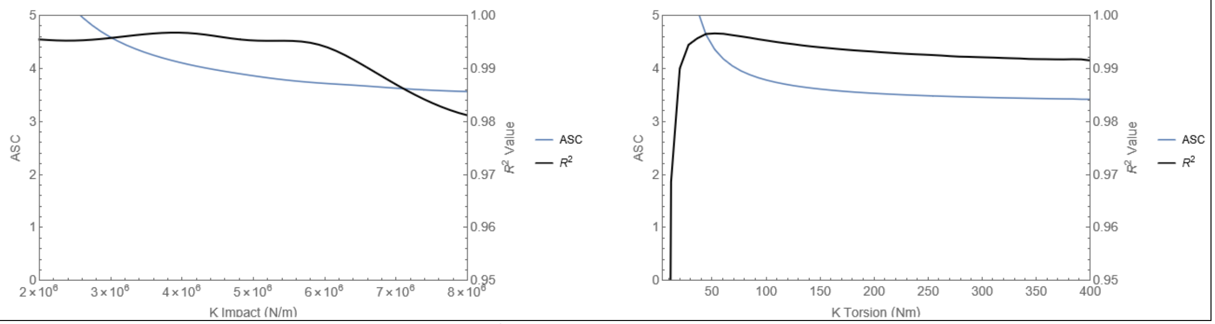

Figure B.5: Changes in ASC (blue line) and R^2 values (black line) by varying K_I (left) and K_T (right) for the NC-3.6HA implant system in various substrates (#10, #20, #30, #40 bone blocks).

#10 (ρ = 0.16 g/cm^3)

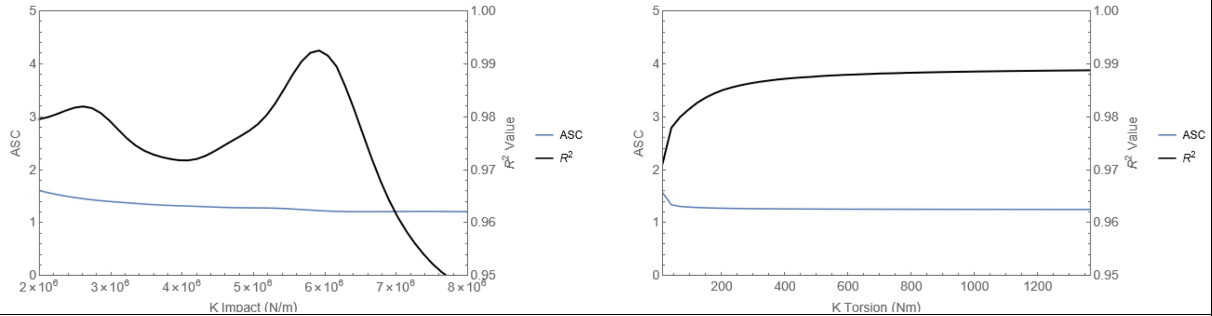

#20 (ρ = 0.32 g/cm^3)

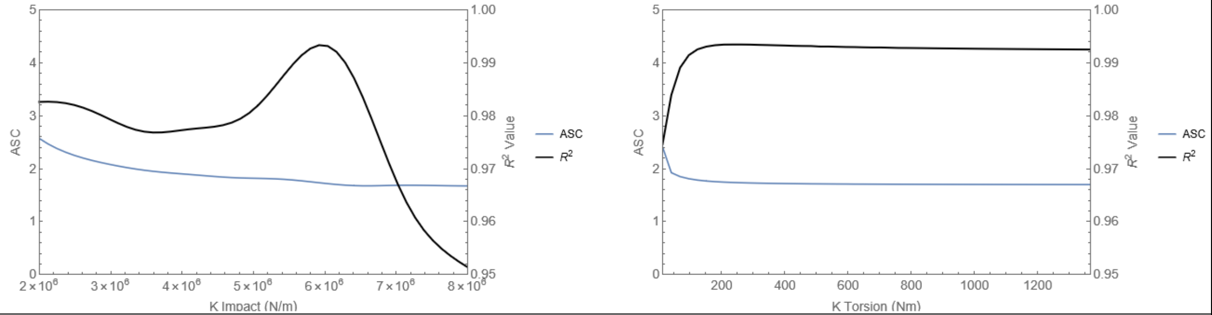

#30 (ρ = 0.48 g/cm^3)

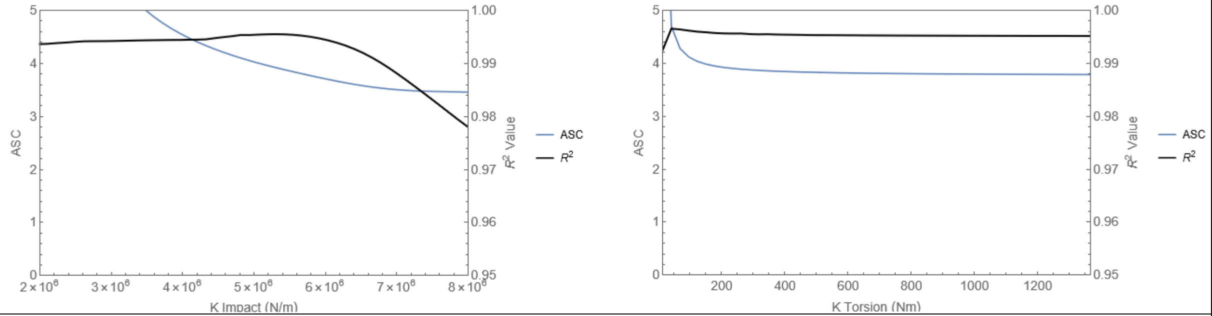

#40 (ρ = 0.64 g/cm^3)

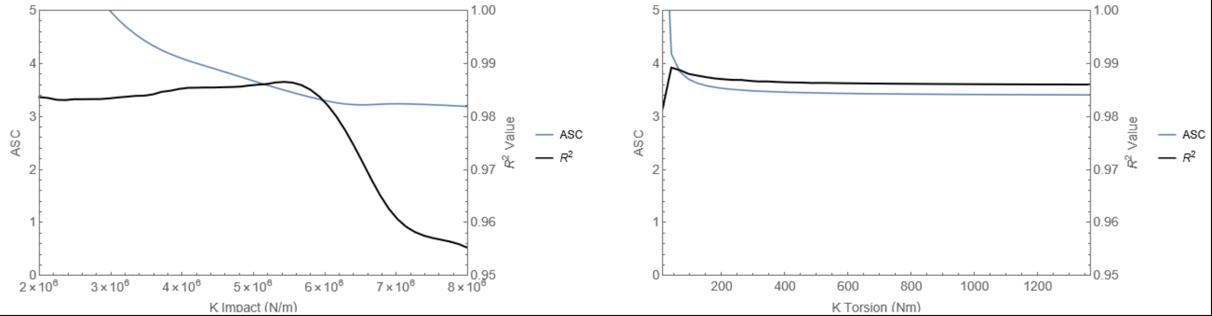

Figure B.6: Changes in ASC (blue line) and R^2 values (black line) by varying K_I (left) and K_T (right) for the RC-4.5HA implant system in various substrates (#10, #20, #30, #40 bone blocks).

#10 (ρ = 0.16 g/cm^3)

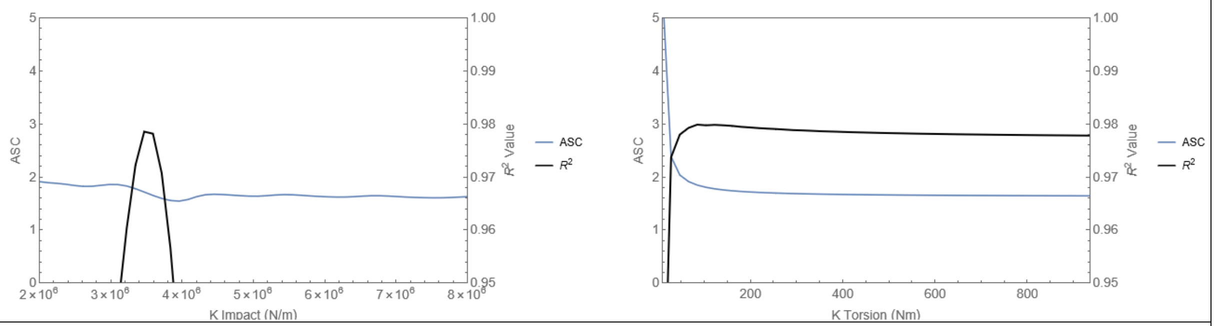

#20 (ρ = 0.32 g/cm^3)

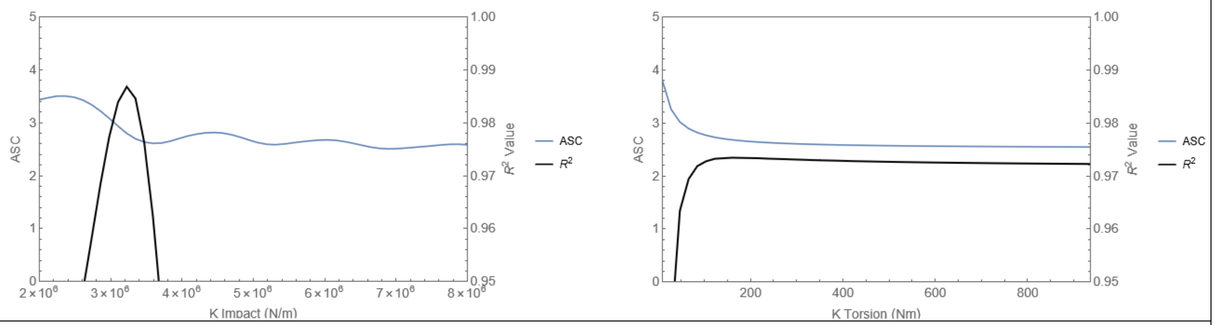

#30 (ρ = 0.48 g/cm^3)

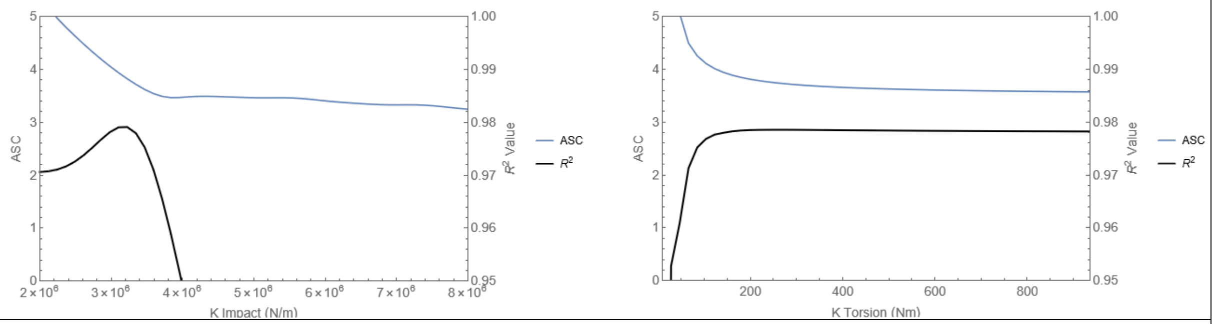

#40 (ρ = 0.64 g/cm^3)

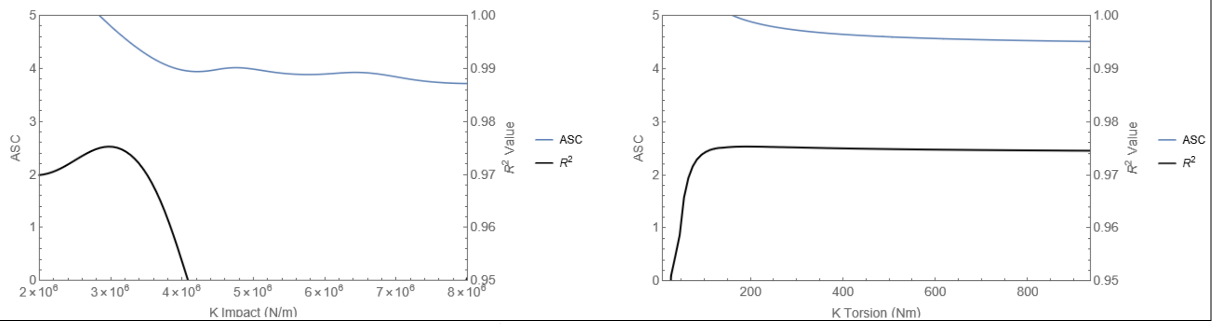

Figure B.7: Changes in ASC (blue line) and R^2 values (black line) by varying K_I (left) and K_T (right) for the RC-6.0HA implant system in various substrates (#10, #20, #30, #40 bone blocks).

#10 (ρ = 0.16 g/cm^3)

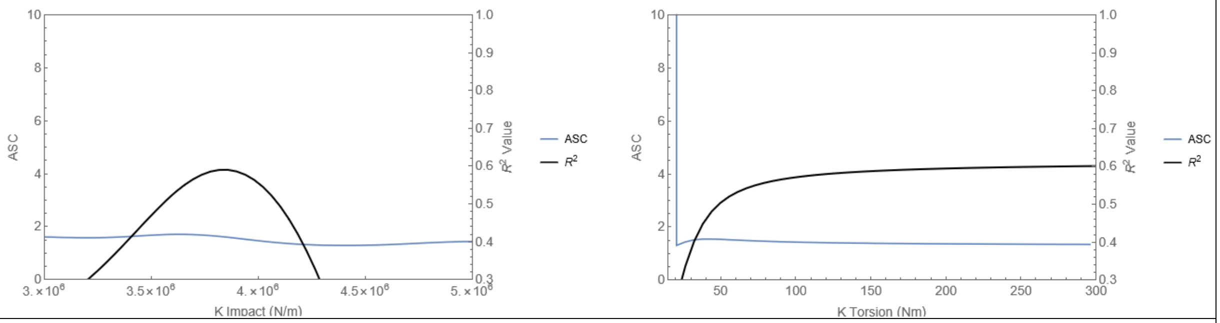

#20 (ρ = 0.32 g/cm^3)

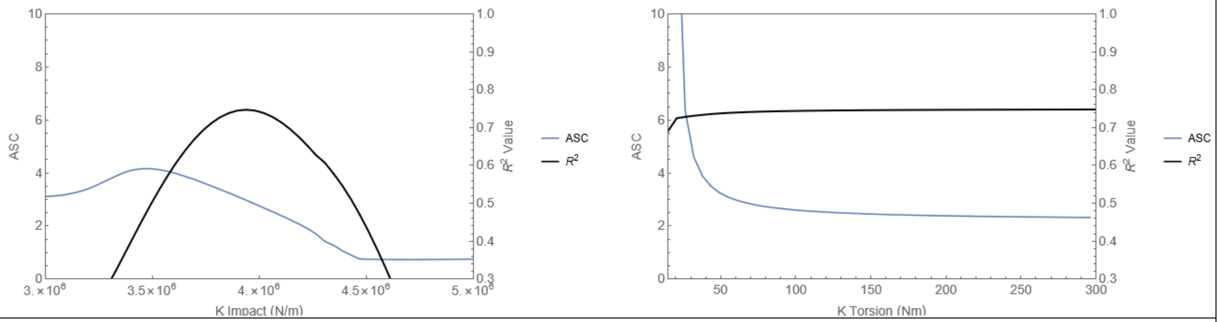

#30 (ρ = 0.48 g/cm^3)

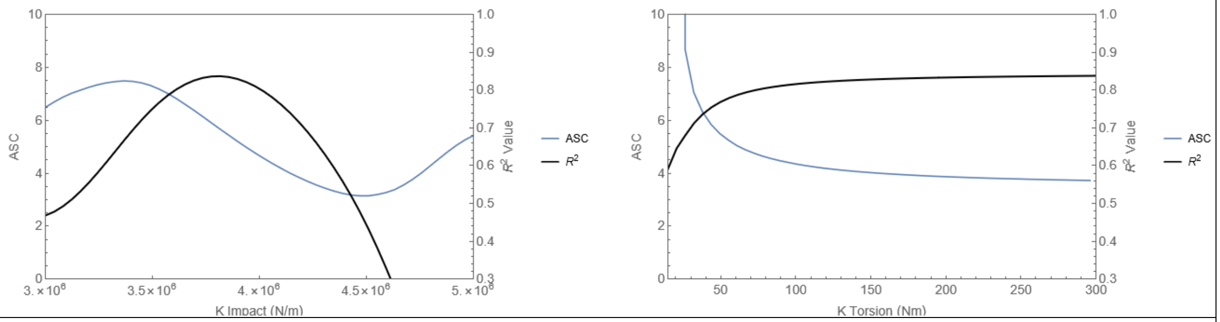

#40 (ρ = 0.64 g/cm^3)

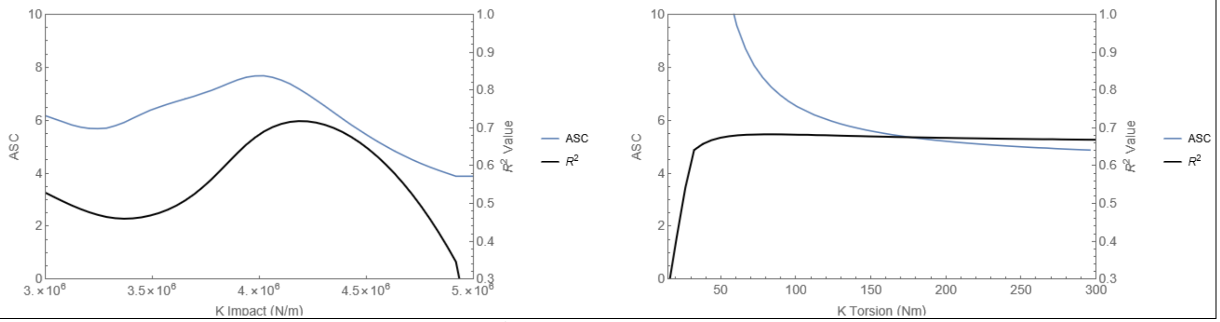

Figure B.8: Changes in ASC (blue line) and R^2 values (black line) by varying K_I (left) and K_T (right) for the NC-IN implant system in various substrates (#10, #20, #30, #40 bone blocks).

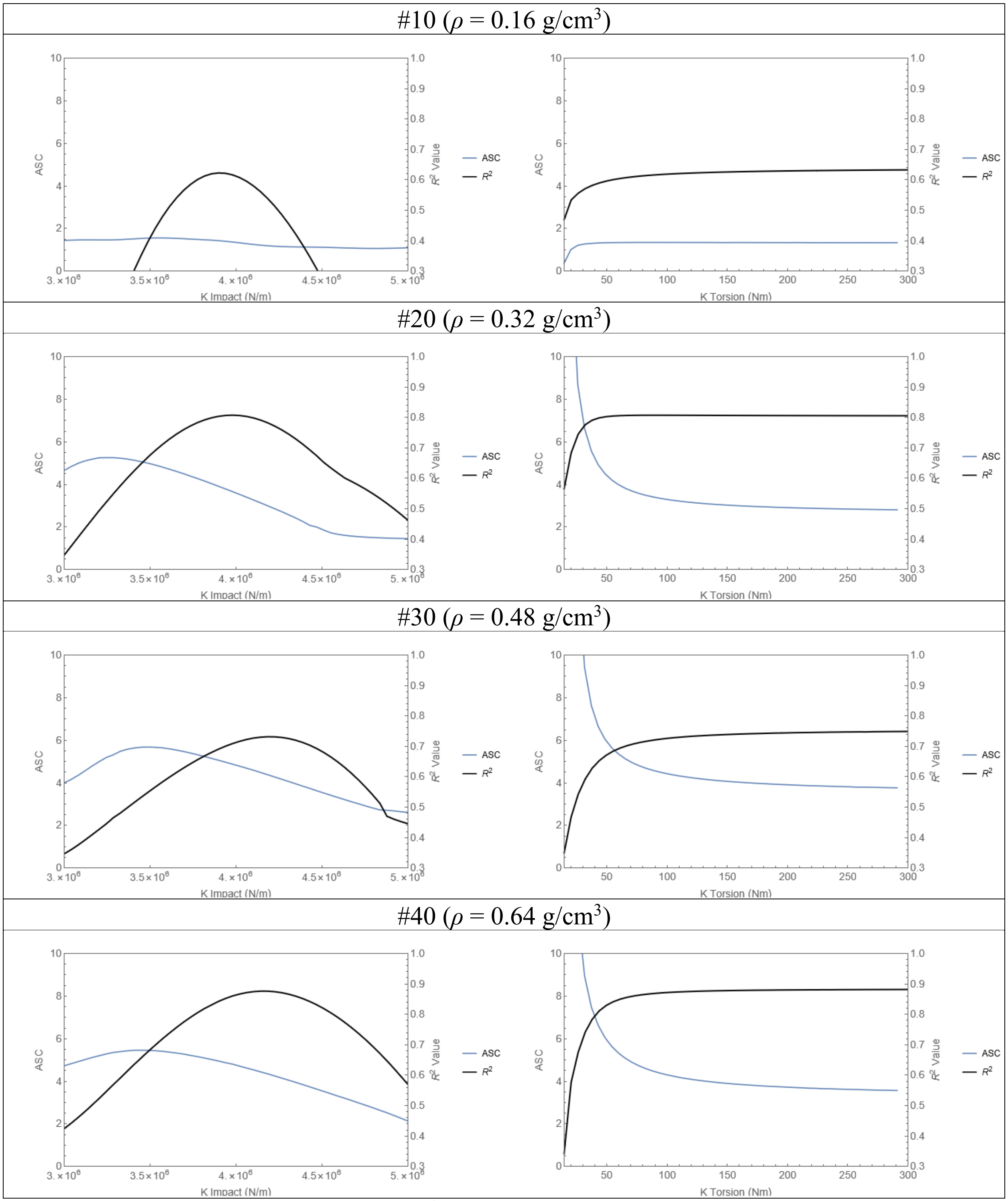

Figure B.9: Changes in ASC (blue line) and R^2 values (black line) by varying K_I (left) and K_T (right) for the NC-NCP implant system in various substrates (#10, #20, #30, #40 bone blocks).

#10 (ρ = 0.16 g/cm^3)

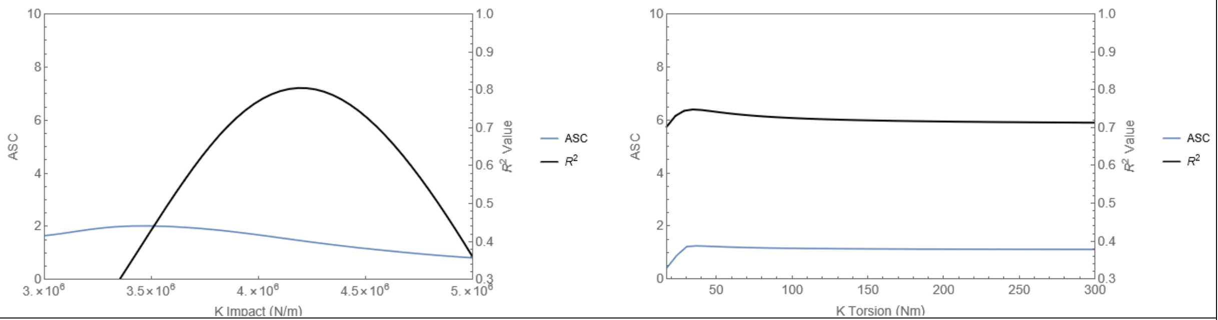

#20 (ρ = 0.32 g/cm^3)

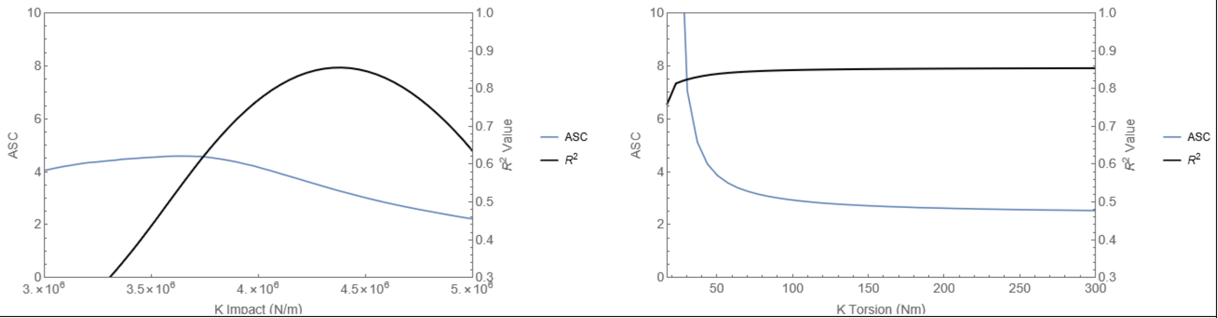

#30 (ρ = 0.48 g/cm^3)

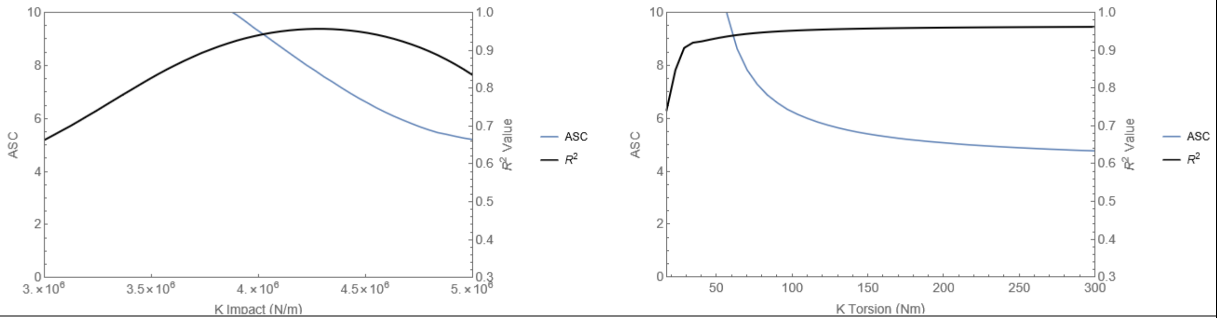

#40 (ρ = 0.64 g/cm^3)

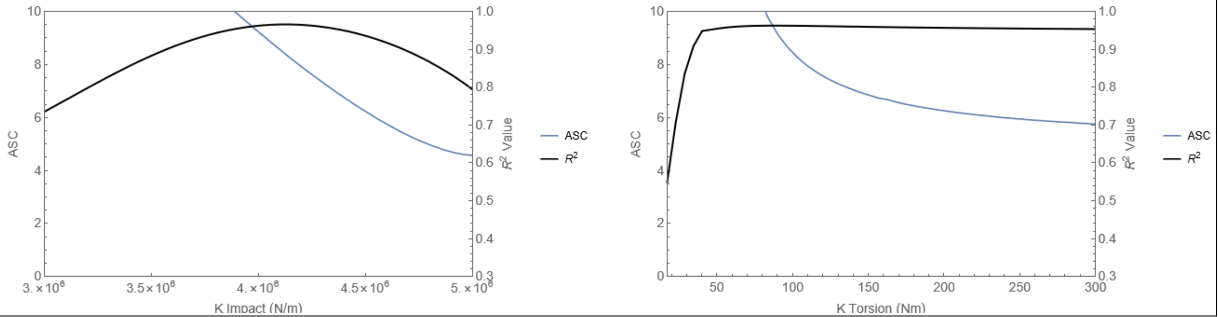

Figure B.10: Changes in ASC (blue line) and R^2 values (black line) by varying K_I (left) and K_T (right) for the RC-RCP implant system in various substrates (#10, #20, #30, #40 bone blocks).

B.2 Modal Analysis

The natural frequencies and mode shapes of each implant-abutment system were determined for three different interfacial stiffnesses (low: $k = 0.1 \times 10^{12}$ N/m^3; medium: $k = 0.5 \times 10^{12}$ N/m^3; high: $k = 1 \times 10^{12}$ N/m^3). A custom Mathematica program (Wolfram Mathematica 12.3, Champaign, IL, USA) was used to implement each implant (NC, RC), abutment (3.3HA, 3.6HA, 4.5HA, 6.0HA), and crown (IN, NCP, RCP). The mode shapes are shown below from Figure B.11 to Figure B.17.

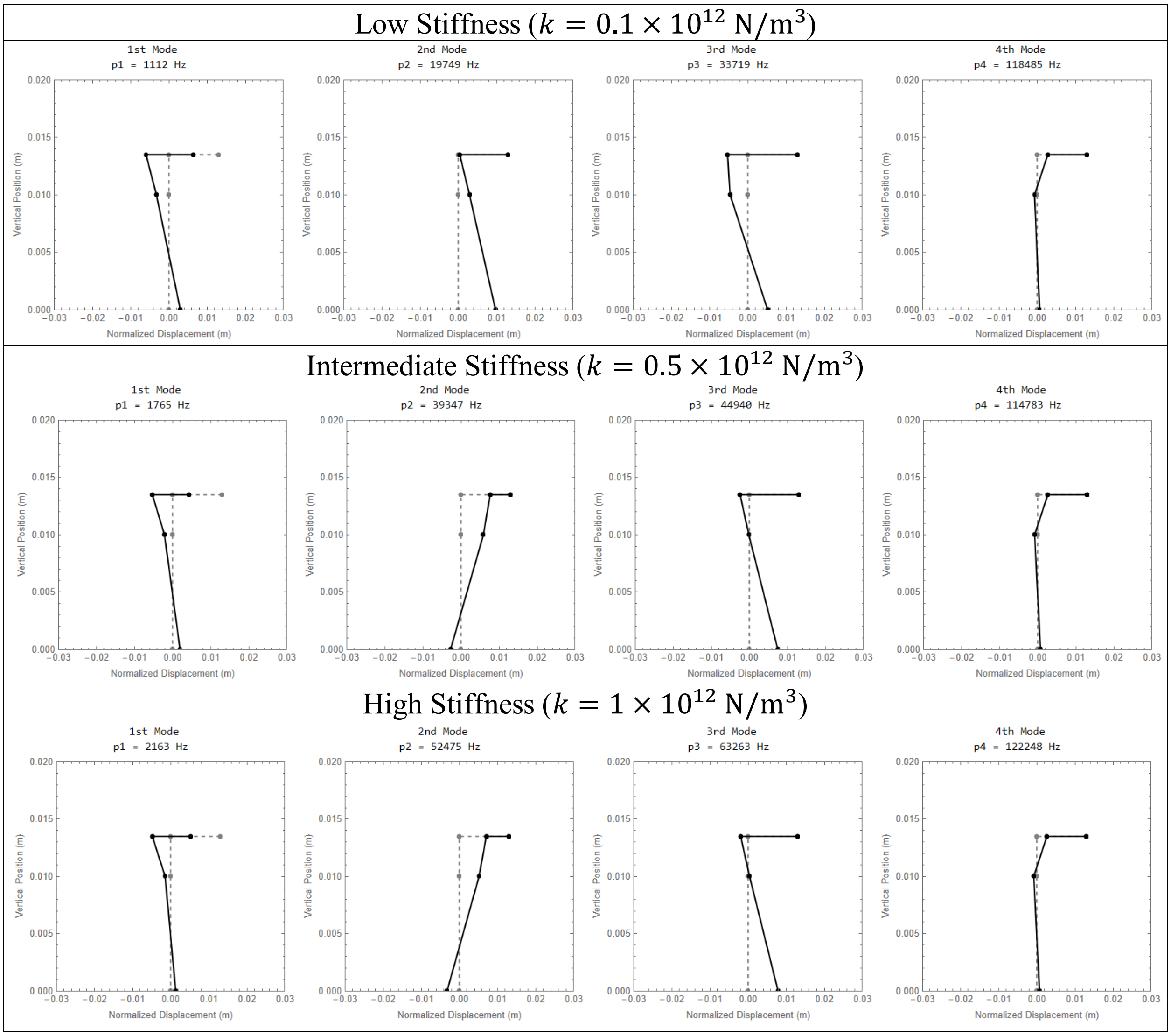
Low Stiffness ($k = 0.1 \times 10^{12}$ N/m^3)

1st Mode p1 = 1112 Hz; 2nd Mode p2 = 19749 Hz; 3rd Mode p3 = 33719 Hz; 4th Mode p4 = 118485 Hz

Intermediate Stiffness ($k = 0.5 \times 10^{12}$ N/m^3)

1st Mode p1 = 1765 Hz; 2nd Mode p2 = 39347 Hz; 3rd Mode p3 = 44940 Hz; 4th Mode p4 = 114783 Hz

High Stiffness ($k = 1 \times 10^{12}$ N/m^3)

1st Mode p1 = 2163 Hz; 2nd Mode p2 = 52475 Hz; 3rd Mode p3 = 63263 Hz; 4th Mode p4 = 122248 Hz

Figure B.11: Mode shapes and natural frequencies for the NC-3.3HA system for low (top row), moderate (middle row), and high (bottom row) interfacial stiffness.

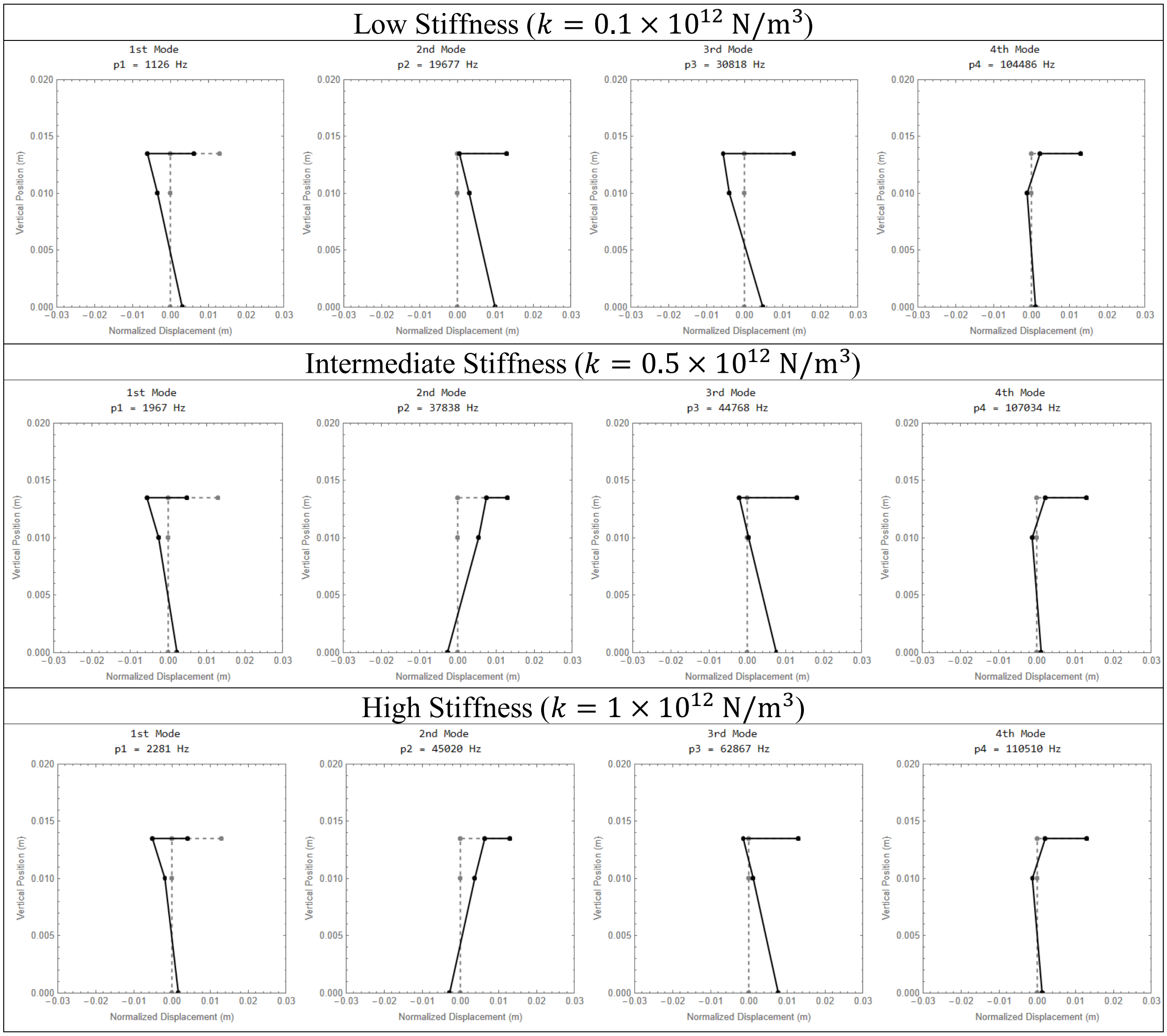

Figure B.12: Mode shapes and natural frequencies for the NC-3.6HA system for low (top row), moderate (middle row), and high (bottom row) interfacial stiffness.

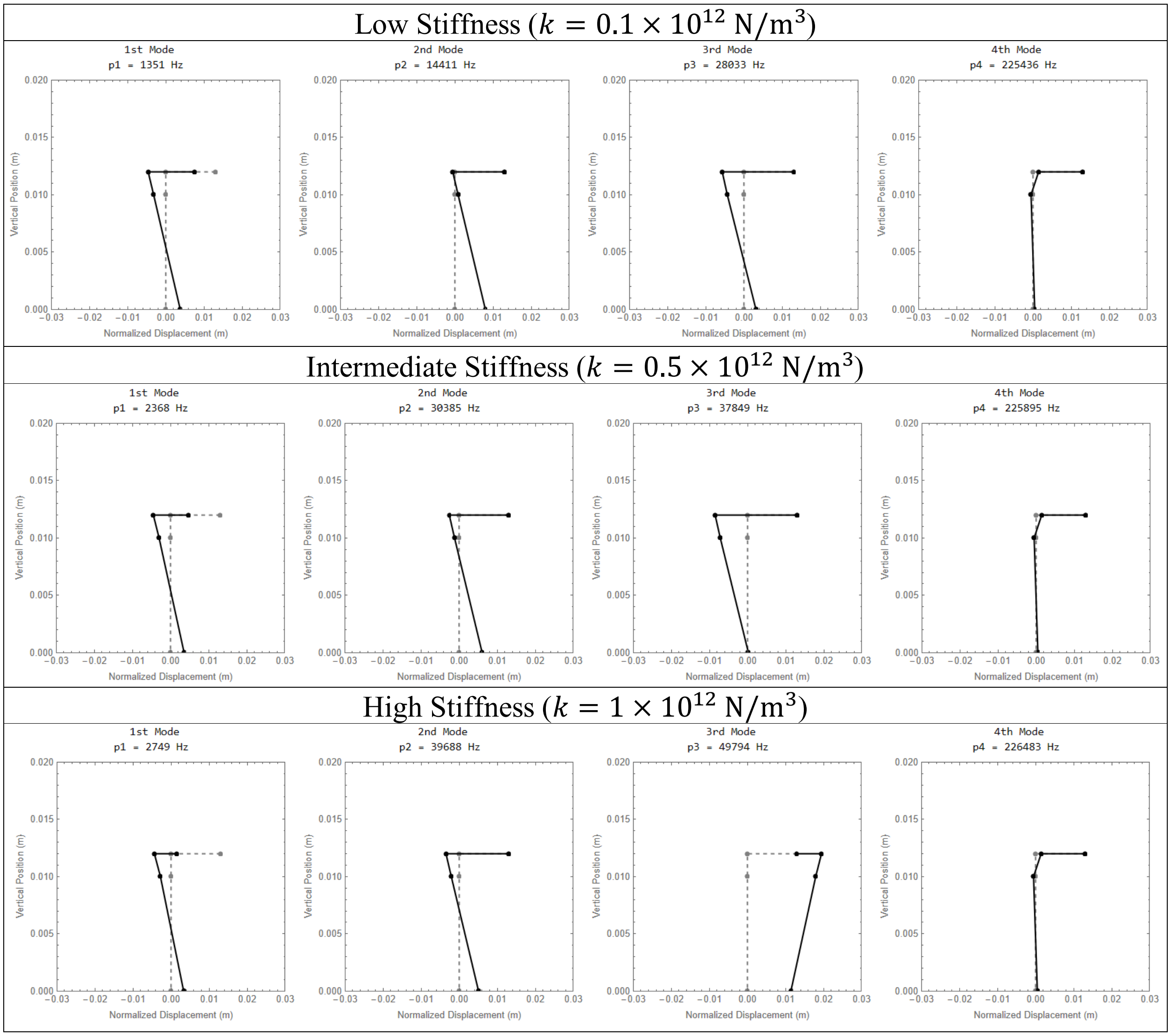

Figure B.13: Mode shapes and natural frequencies for the RC-4.5HA system for low (top row), moderate (middle row), and high (bottom row) interfacial stiffness.

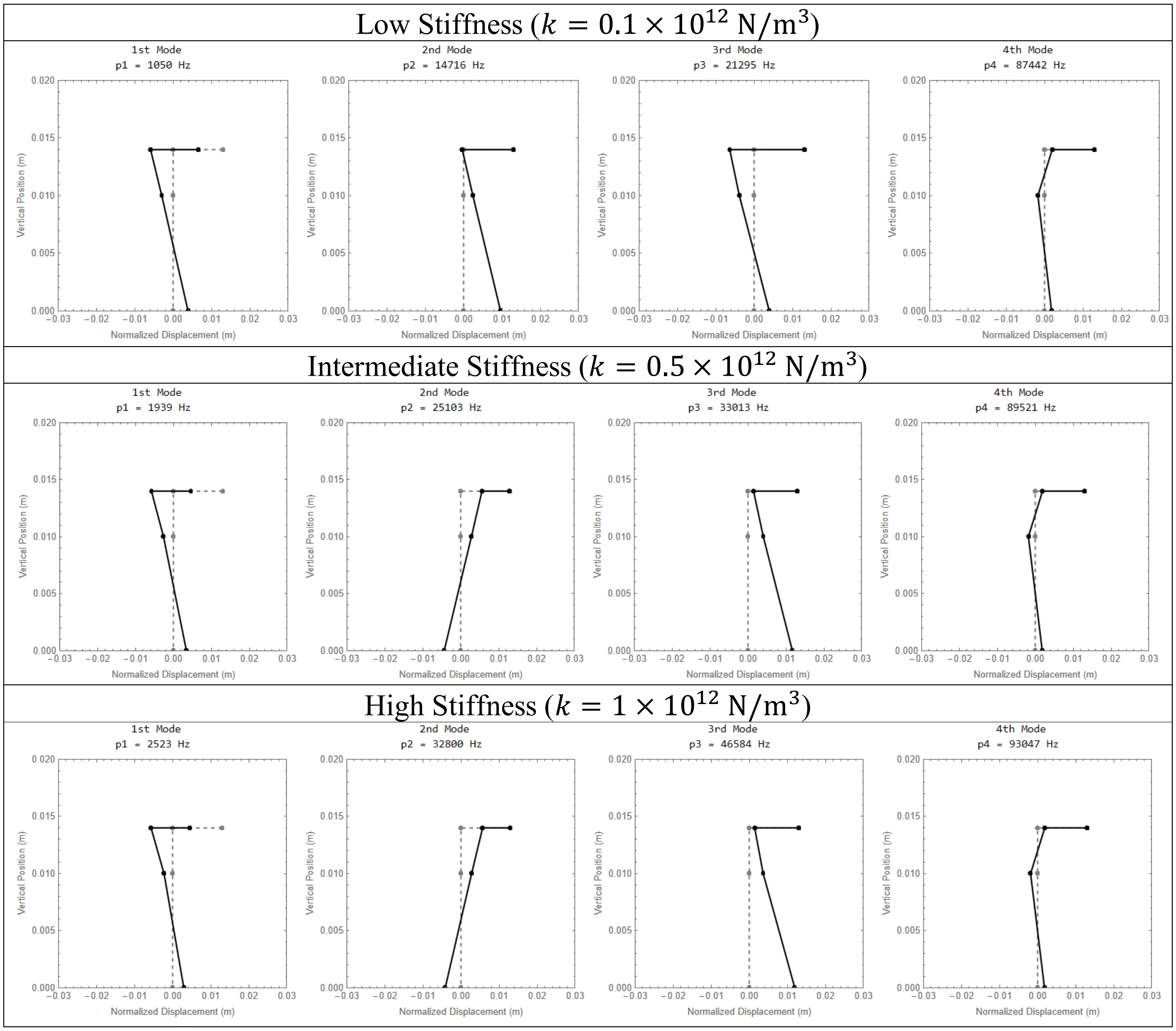
Low Stiffness ($k = 0.1 \times 10^{12}\ \mathrm{N/m^3}$)

Intermediate Stiffness ($k = 0.5 \times 10^{12}\ \mathrm{N/m^3}$)

High Stiffness ($k = 1 \times 10^{12}\ \mathrm{N/m^3}$)

Figure B.14: Mode shapes and natural frequencies for the RC-6.0HA system for low (top row), moderate (middle row), and high (bottom row) interfacial stiffness.

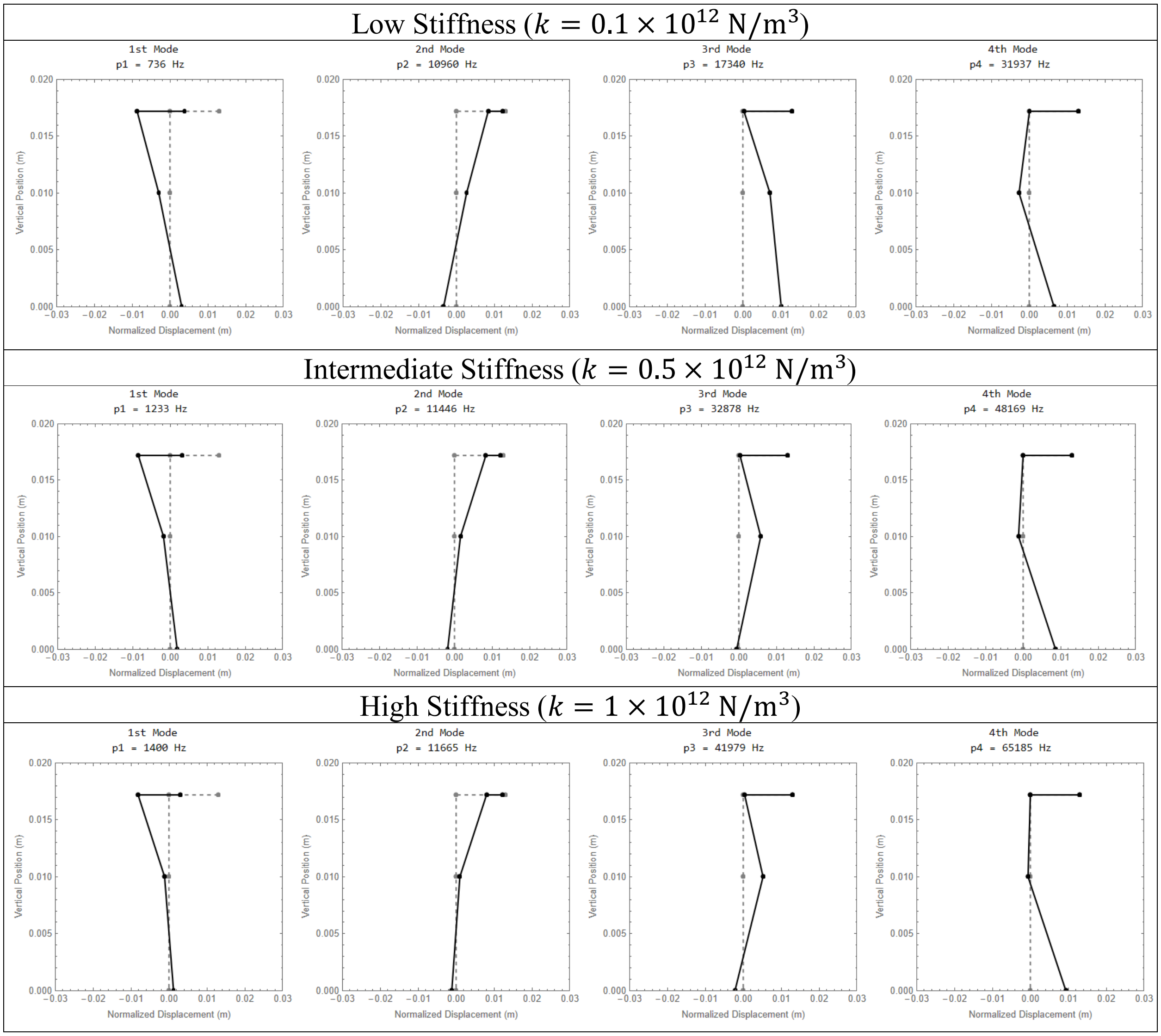

Figure B.15: Mode shapes and natural frequencies for the NC-IN system for low (top row), moderate (middle row), and high (bottom row) interfacial stiffness.

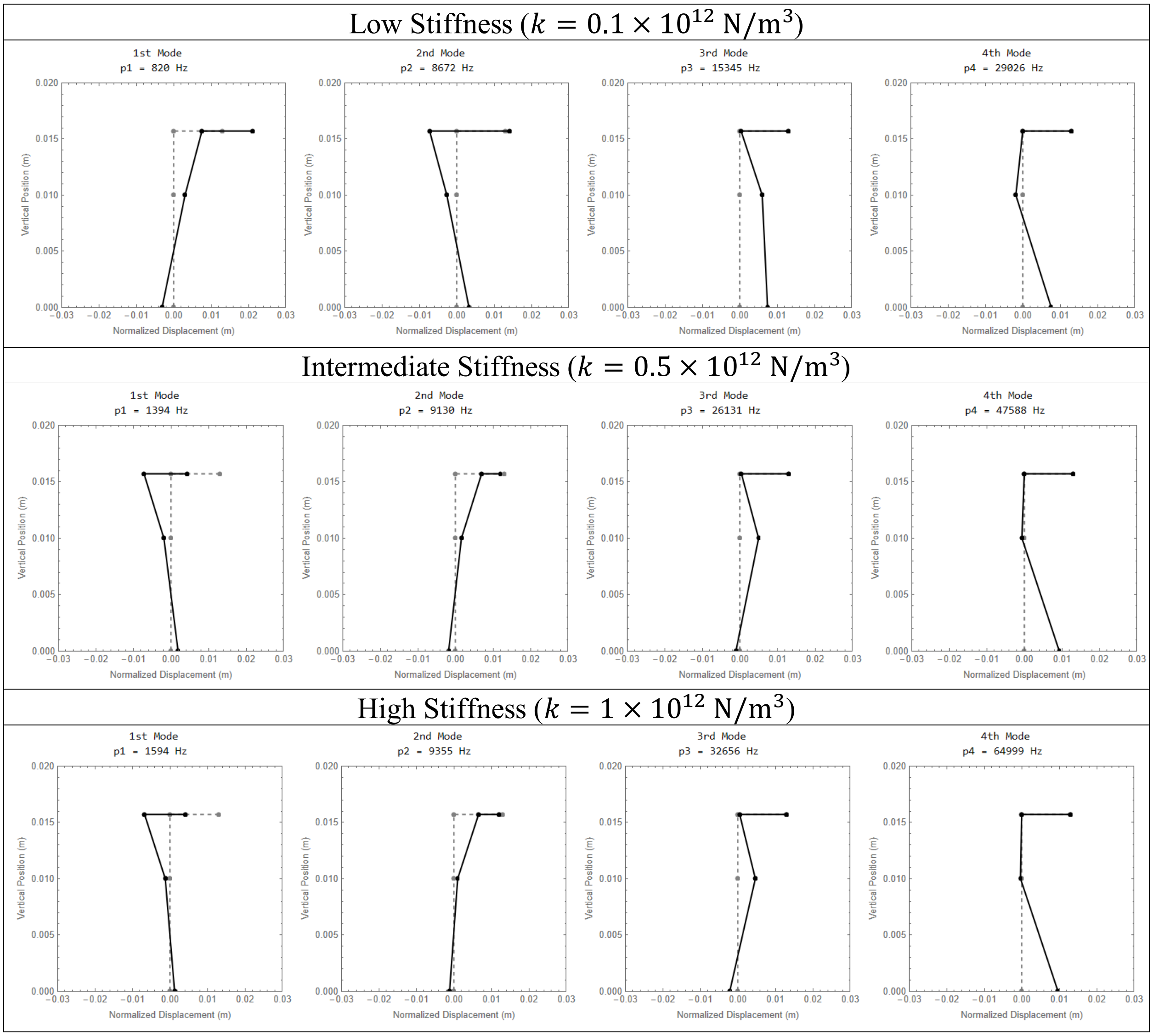

Figure B.16: Mode shapes and natural frequencies for the NC-NCP system for low (top row), moderate (middle row), and high (bottom row) interfacial stiffness.

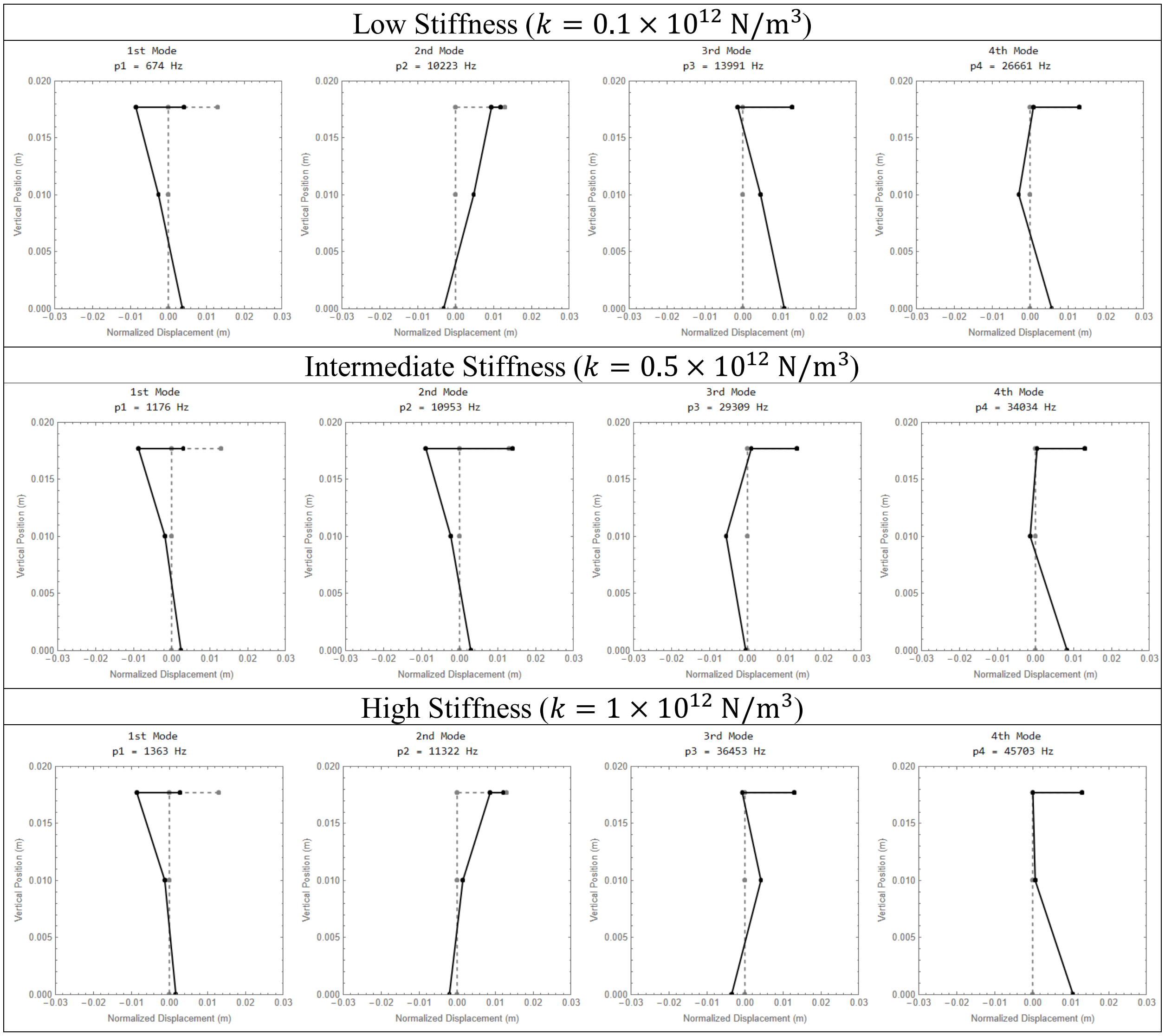

Figure B.17: Mode shapes and natural frequencies for the RC-RCP system for low (top row), moderate (middle row), and high (bottom row) interfacial stiffness.

B.3 Sensitivity of Analytical Frequency Response to Stiffness Parameters

For the analytical model of a uniform interface, a sensitivity analysis was performed to investigate the effects of varying k, K_I, and K_T on the first and second frequencies of the analytical model solution. The effect of varying the interfacial stiffness k on the first and second mode frequencies are shown in Figure B.18, for various values of the impact stiffness K_I (2×10^6 to 8×10^6 N/m). Figures B.19 and B.20 show the effects of varying the impact stiffness K_I and K_T on the first and second mode frequencies, respectively.

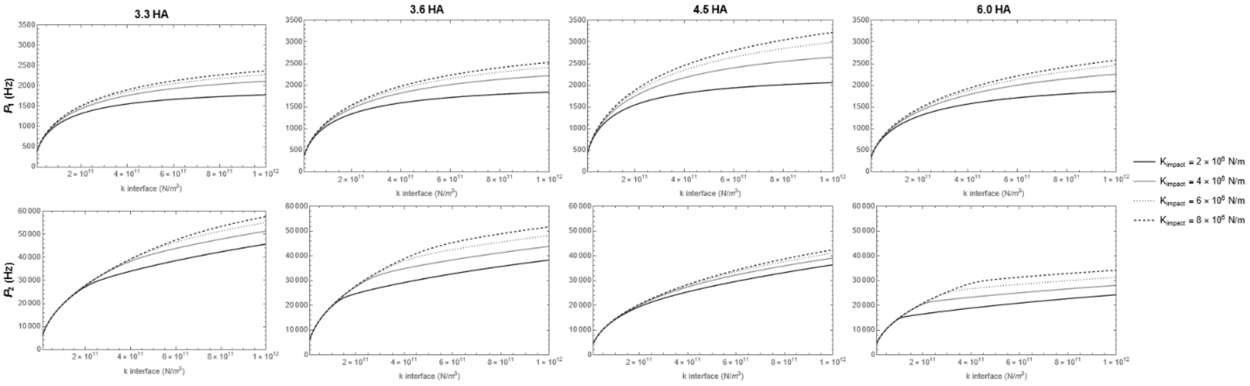

Figure B.18: Relationship between the interfacial stiffness k and p_1 (top row) and p_2 (bottom row) for each implant-abutment combination (individual columns).

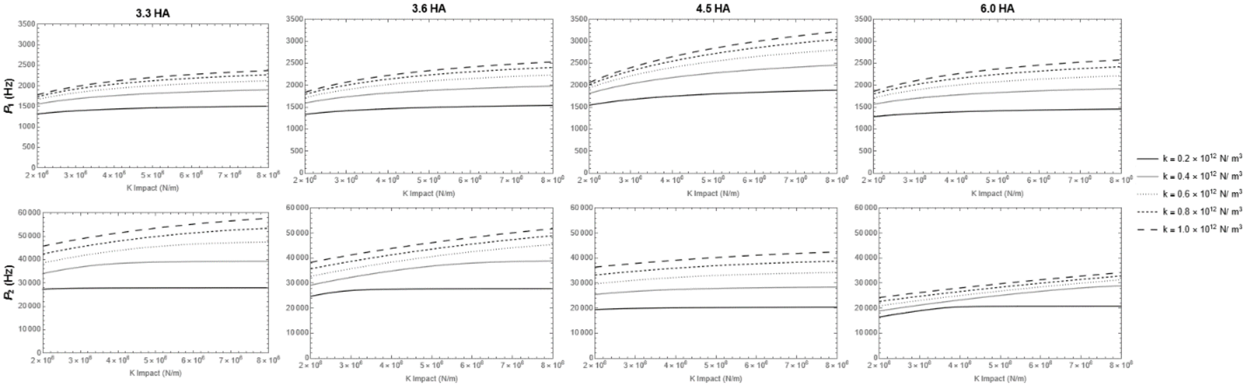

Figure B.19: Relationship between the impact stiffness K_I and p_1 (top row) and p_2 (bottom row) for each implant-abutment combination (individual columns).

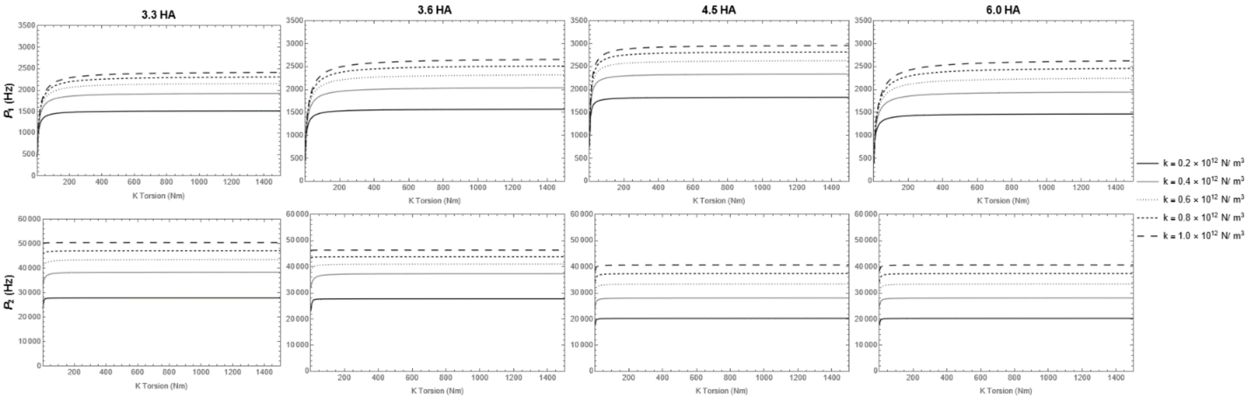

Figure B.20: Relationship between the torsional stiffness K_T and p_1 (top row) and p_2 (bottom row) for each implant-abutment combination (individual columns).

B.4 Sensitivity of Analytical Frequency Response to Cortical Stiffness and Thickness

In the cortical bone analytical model, there are two additional parameters k_C, L_C corresponding to the stiffness and thickness of the cortical layer, respectively. A sensitivity analysis was performed to investigate the effects of varying k_C and L_C on the first and second frequencies of the analytical model solution, for various values of the cancellous stiffness k.

Each parameter was assigned a reference value that corresponds to typical measurements in a clinical setting. Assuming that #20 polyurethane foam is representative of cancellous bone (Comuzzi et al., 2020; Tumedei et al., 2021), a reference cancellous stiffness k_{ref} of approximately 0.25×10^{12} N/m^3 was determined using the average of ASIST measurements taken with #20 bone blocks (ρ = 0.32 g/cm^3). The cortical stiffness reference value (k_{Cref}) was determined by multiplying k_{ref} by the ratio of the elastic moduli of cortical and cancellous bone. An approximate ratio of 10 was found based on reported values in the literature (Nagasao et al., 2002; Sugiura et al., 2016), giving a reference value of 2.5×10^{12} N/m^3 for the cortical stiffness. Based on reported measurements of the cortical thickness in the human jaw, the reference value for the cortical thickness L_{Cref} was set to 1.5 mm (Miyamoto et al., 2005; Stefano et al., 2021).

While one parameter was varied, the other was held fixed at their reference value. This was performed over a range of values for k and plotted as separate curves. Figures B.21 to B.28 show the changes in p_1 and p_2 when varying k_C or L_C for each implant-abutment system (NC-3.3HA, NC-3.6HA, RC-4.5HA, RC-6.0HA). In each figure, the red line indicates the case when k is also set to its reference value. This illustrates the trends in p_1 and p_2 with respect to k_C or L_C while all other parameters are in the range of clinically expected values.

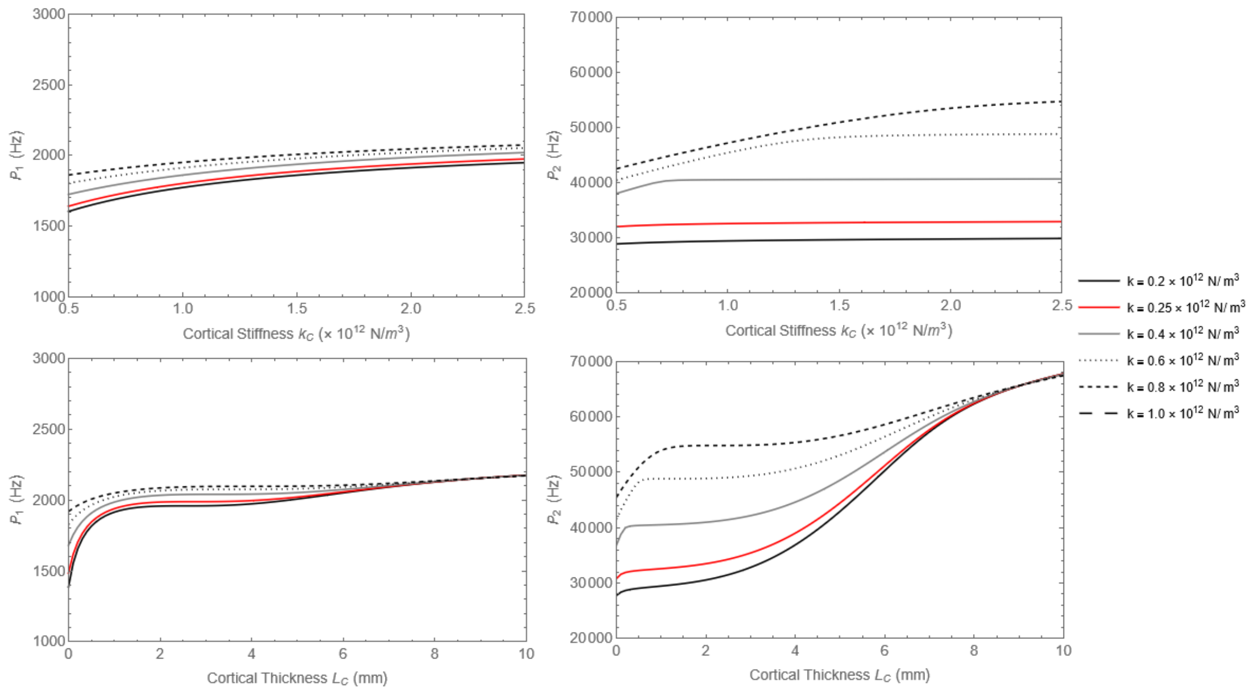

Figure B.21: Effect of varying the cortical stiffness k_C (top row), and cortical thickness L_C (bottom row), on p_1 (left) and p_2 (right), for the NC-3.3HA system and various values of k.

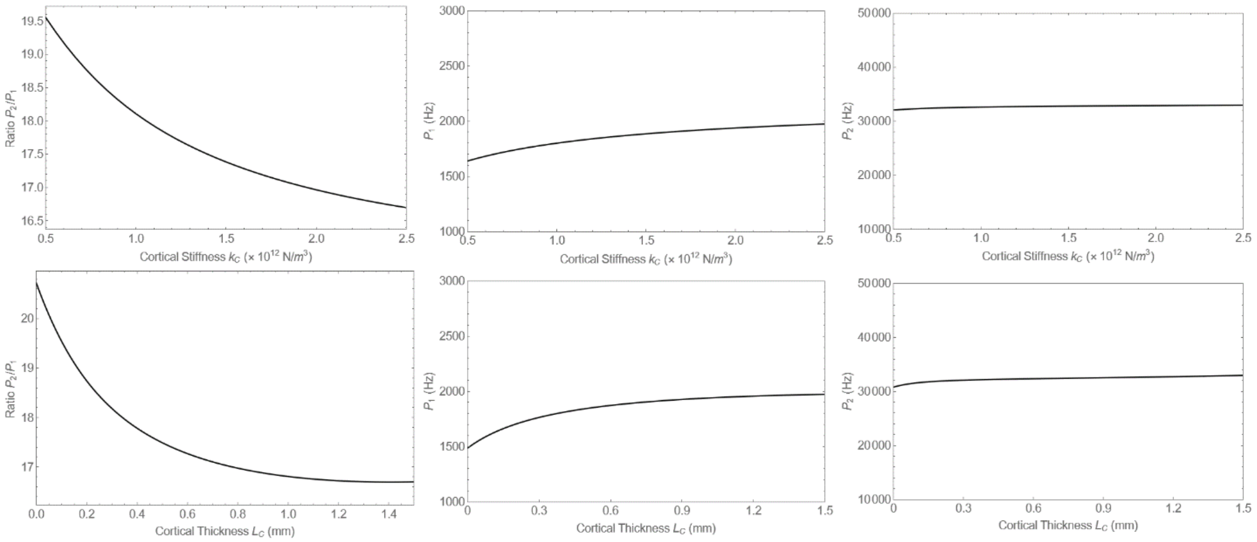

Figure B.22: Relationship between the ratio p_2/p_1, p_1, and p_2 and the cortical stiffness per unit area k_C and cortical thickness L_C for the NC-3.3HA system in the range of clinically expected values.

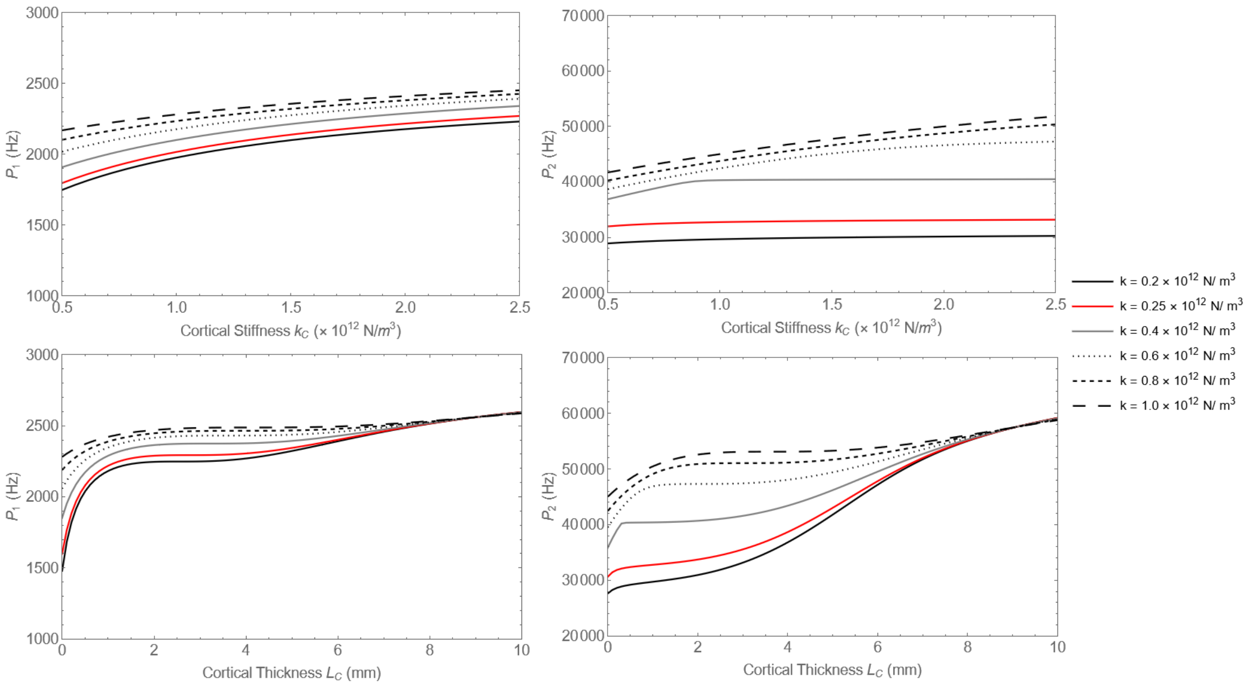

Figure B.23: Effect of varying the cortical stiffness k_C (top row), and cortical thickness L_C (bottom row), on p_1 (left) and p_2 (right), for the NC-3.6HA system and various values of k.

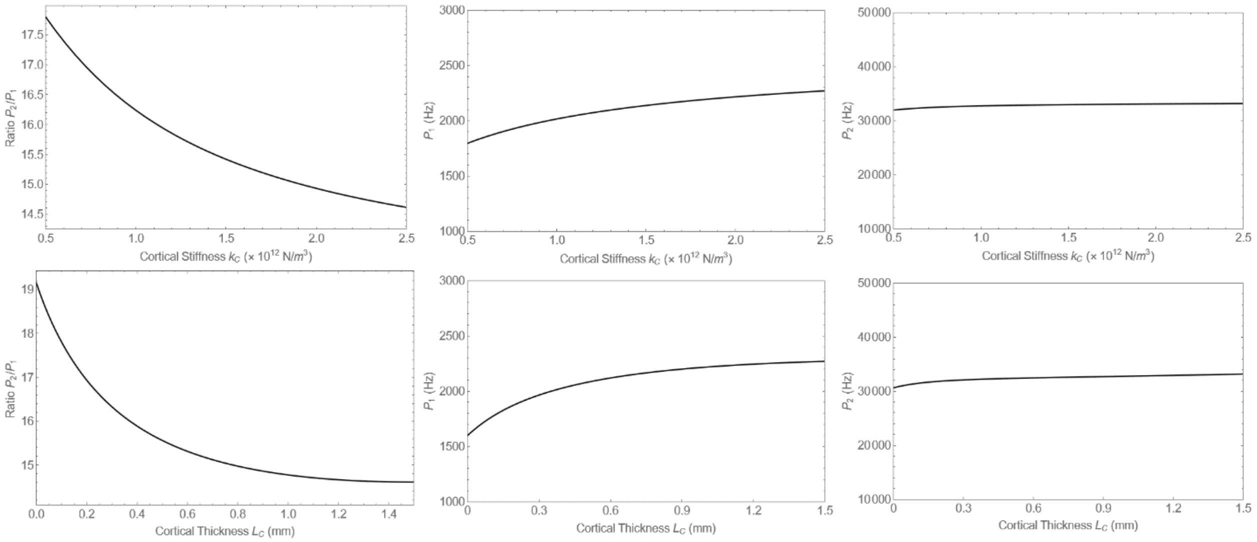

Figure B.24: Relationship between the ratio p_2/p_1, p_1, and p_2 and the cortical stiffness per unit area k_C and cortical thickness L_C for the NC-3.6HA system in the range of clinically expected values.

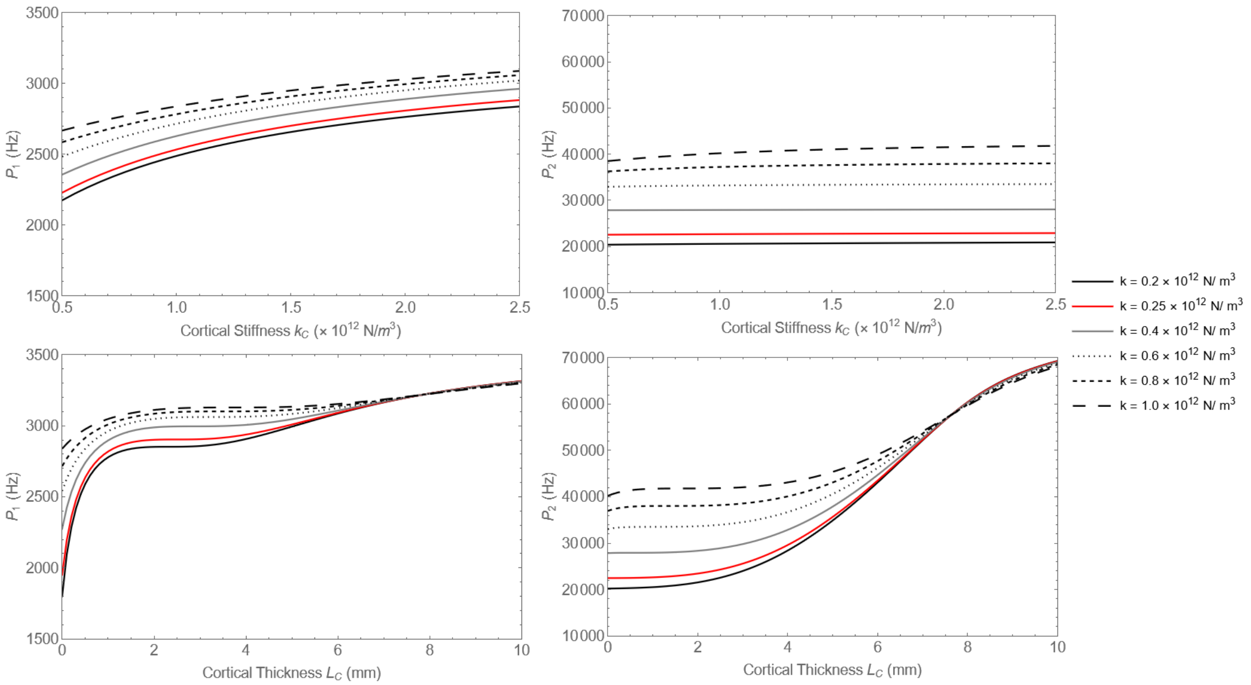

Figure B.25: Effect of varying the cortical stiffness k_C (top row), and cortical thickness L_C (bottom row), on p_1 (left) and p_2 (right), for the RC-4.5HA system and various values of k.

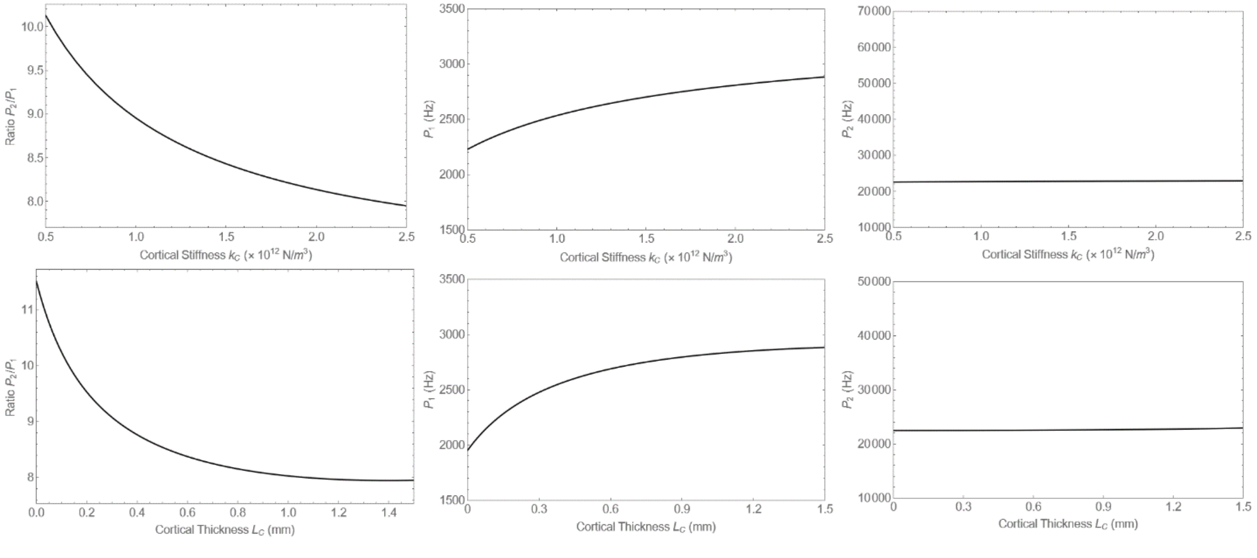

Figure B.26: Relationship between the ratio p_2/p_1, p_1, and p_2 and the cortical stiffness per unit area k_C and cortical thickness L_C for the RC-4.5HA system in the range of clinically expected values.

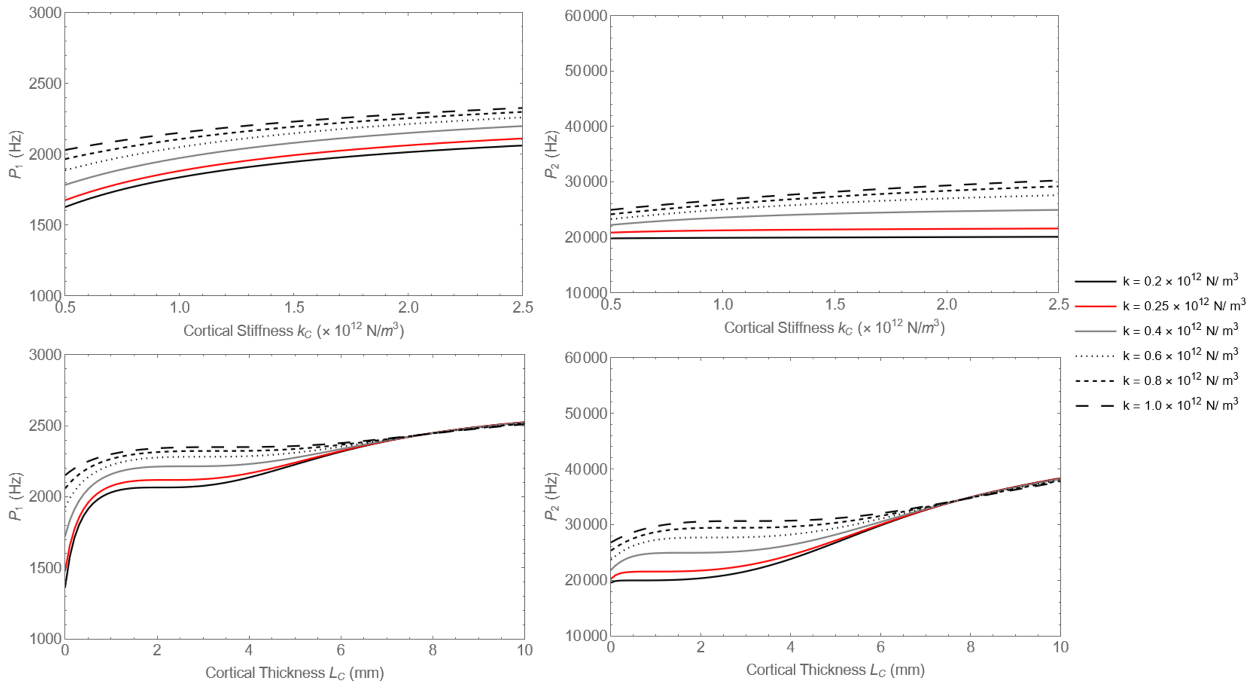

Figure B.27: Effect of varying the cortical stiffness k_C (top row), and cortical thickness L_C (bottom row), on p_1 (left) and p_2 (right), for the RC-6.0HA system and various values of k.

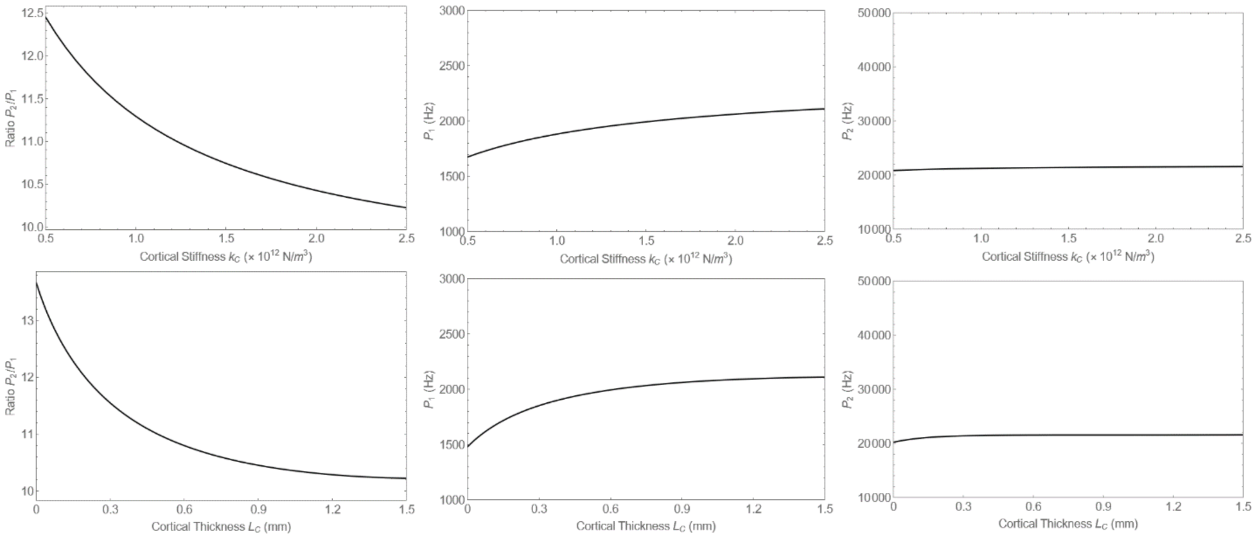

Figure B.28: Relationship between the ratio p_2/p_1, p_1, and p_2 and the cortical stiffness per unit area k_C and cortical thickness L_C for the RC-6.0HA system in the range of clinically expected values.

Appendix C: Validation of Cortical Bone Model

The cortical bone analytical model was evaluated to determine if the model is an accurate representation of the physical system. In the model, the cortical layer is characterized with a thickness L_C and stiffness proportionality constant γ, which defines the ratio of the cortical stiffness k_C to the cancellous stiffness k. For each of the implant installations created in Chapter 6, a custom Mathematica program (Wolfram Mathematica 12.3, Champaign, IL, USA) was used to fit the analytical model to the experimental data by iterating between different values of γ and L_C. The values of γ and L_C that resulted in the highest R^2 value between the signal and model response were then compared to the properties of the actual system.

For the cortical group, the value of L_C was fixed at the measured thickness of each block while varying γ in the model, with an average best-fit value for γ of 4.76 ± 0.42. Figure C.1 shows the variations in k and the R^2 value with γ, where L_C was fixed to the measured cortical thickness of the corresponding block. In each case, R^2 values start to decrease significantly as γ moves further away from the best-fit value. This is visually shown in Figure C.2.

For the cancellous bone blocks, γ was fixed at 3 when varying L_C, while L_C was fixed at 3 mm when varying γ. The average best-fit values of γ and L_C were found to be 1.17 ± 0.08 and 0.05 ± 0.07 mm, respectively. Figure C.3 shows the effect of varying γ on the R^2 value and predicted value of k, respectively. Shown in Figure C.3 and Figure C.4, R^2 values begin to sharply decrease as γ and L_C move further away from their respective best-fit values. This is visually shown in Figure C.5.

The results strongly suggest that the analytical model is an accurate representation of the physical system. For the cortical group, there is a distinct range of values for γ that provide a good fit to the experimental data, which fall in the range of the theoretical value of γ. For the cancellous group, the best-fit value of 1.17 for γ indicates the model provides a good fit to the data when k_C and k are approximately the same; this is essentially equivalent to a uniform interface with a stiffness per unit area of k. In contrast, the best-fit value of 0.05 mm for L_C reflects that when k_C and k are assumed to be different, the model best matches the data when the cortical thickness is essentially zero. As a result, both best-fit values of γ and L_C for the cancellous group reflect an interface of entirely cancellous bone, which matches the physical properties of the actual system.

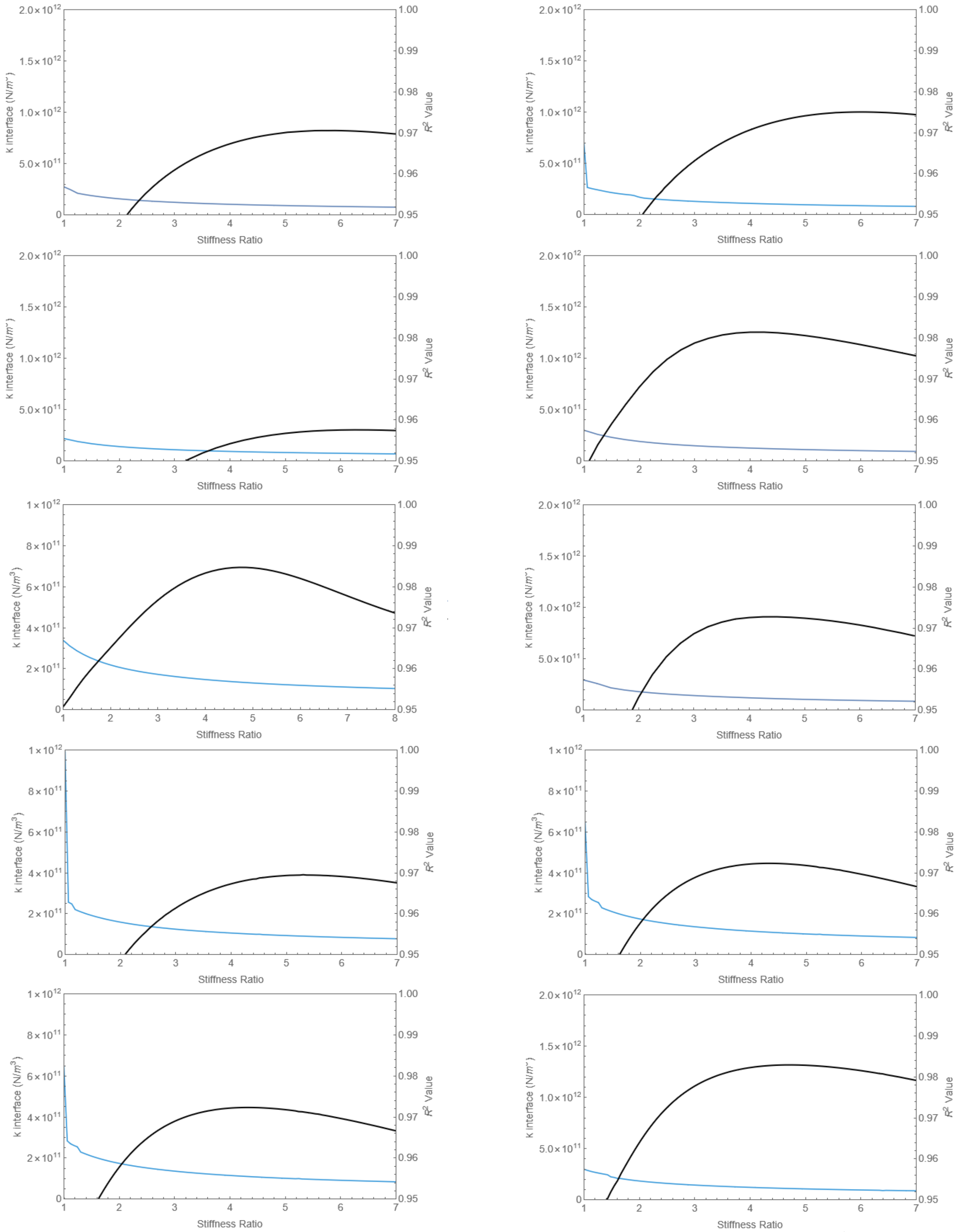

Figure C.1: Analysis of cortical bone blocks. Interface stiffness per unit area (blue line) and R^2 (black line) values obtained from the matching process by varying γ between 1 and 7 while holding L_C fixed at 3 mm.

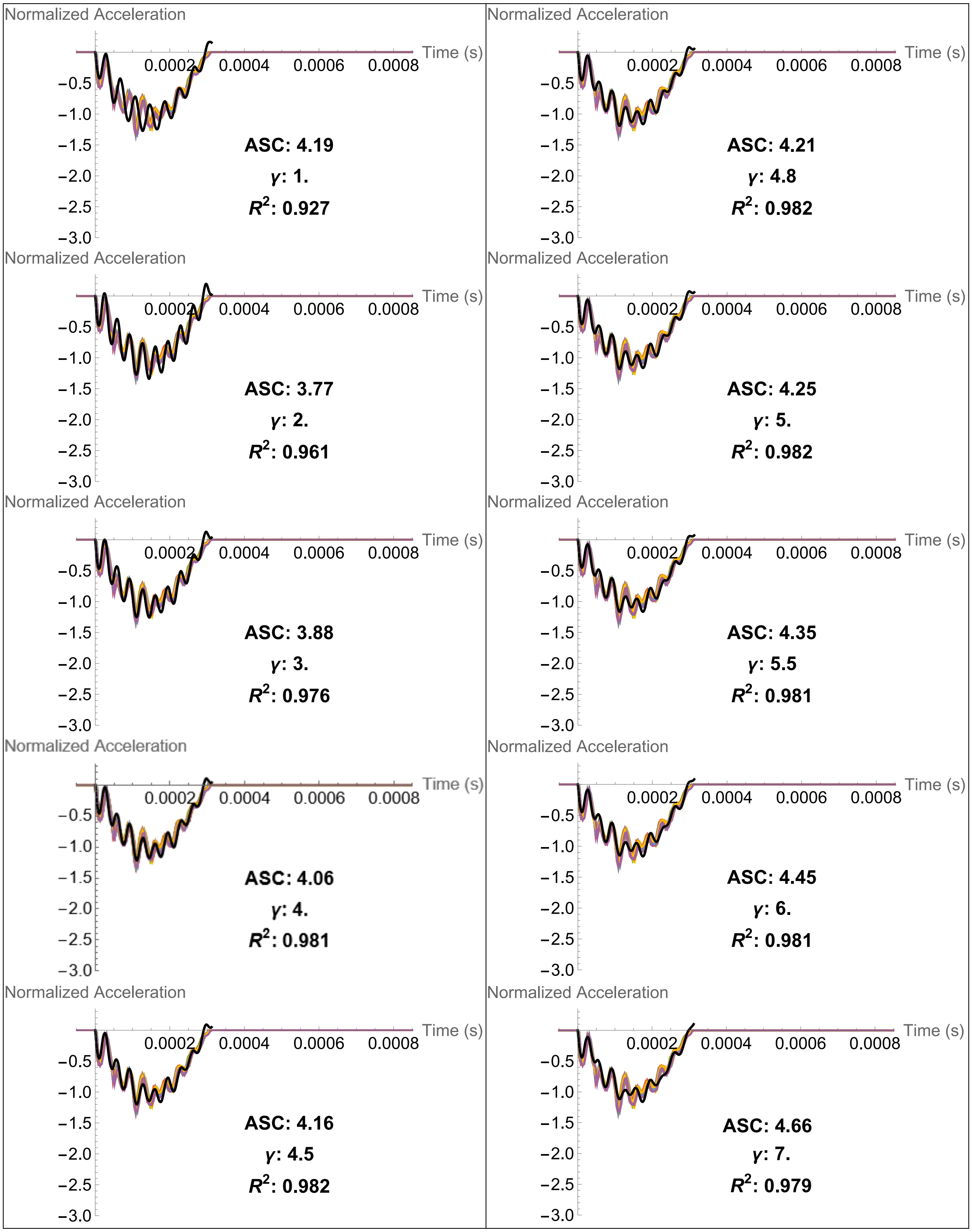

Figure C.2: Fitting of analytical model (black line) to cortical bone experimental data (coloured lines). ASC and R^2 values are shown for various values of γ.

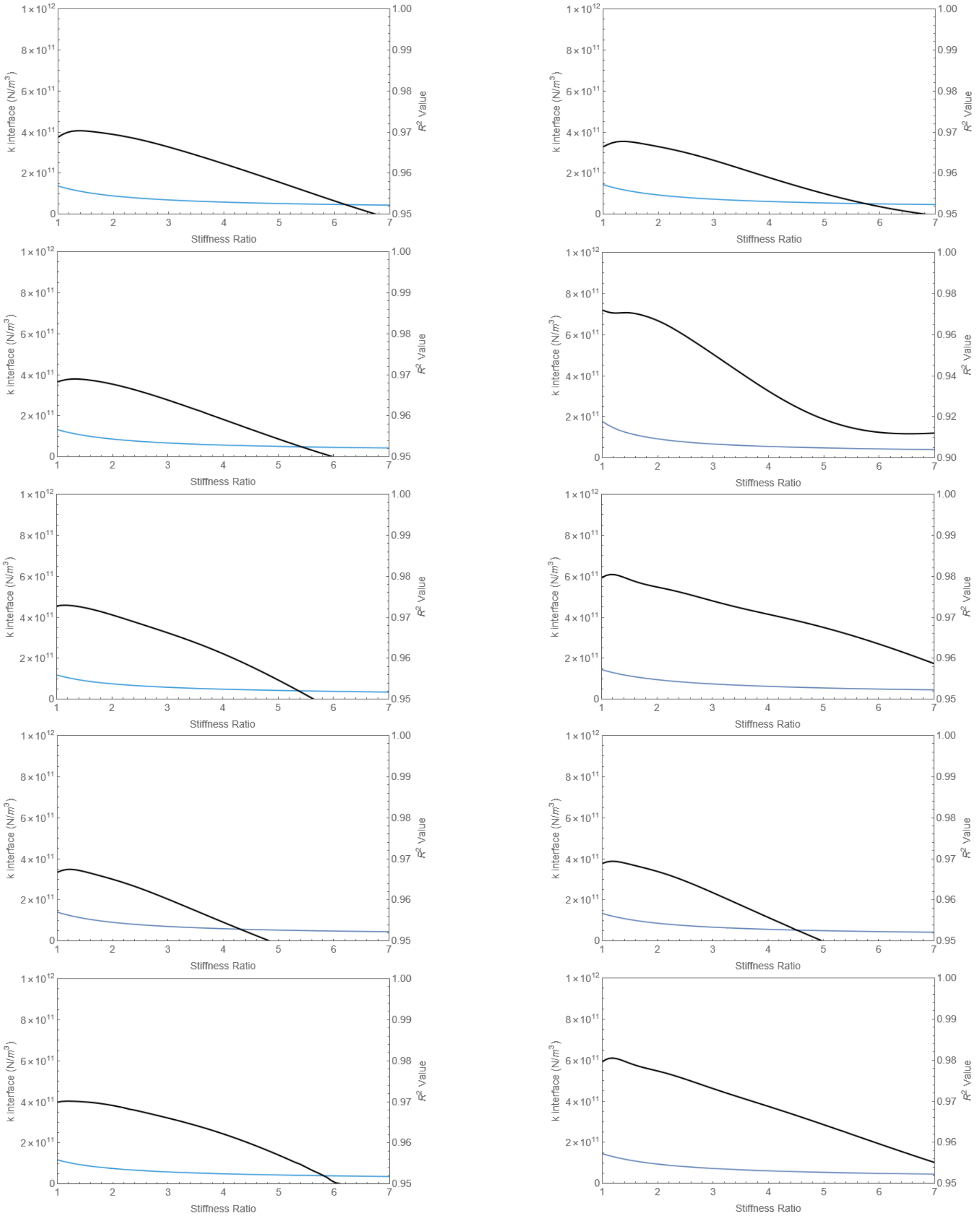

Figure C.3: Analysis of cancellous bone blocks. Interface stiffness per unit area (blue line) and R^2 (black line) values obtained from the matching process by varying γ between 1 and 7 while holding L_C fixed at 3 mm.

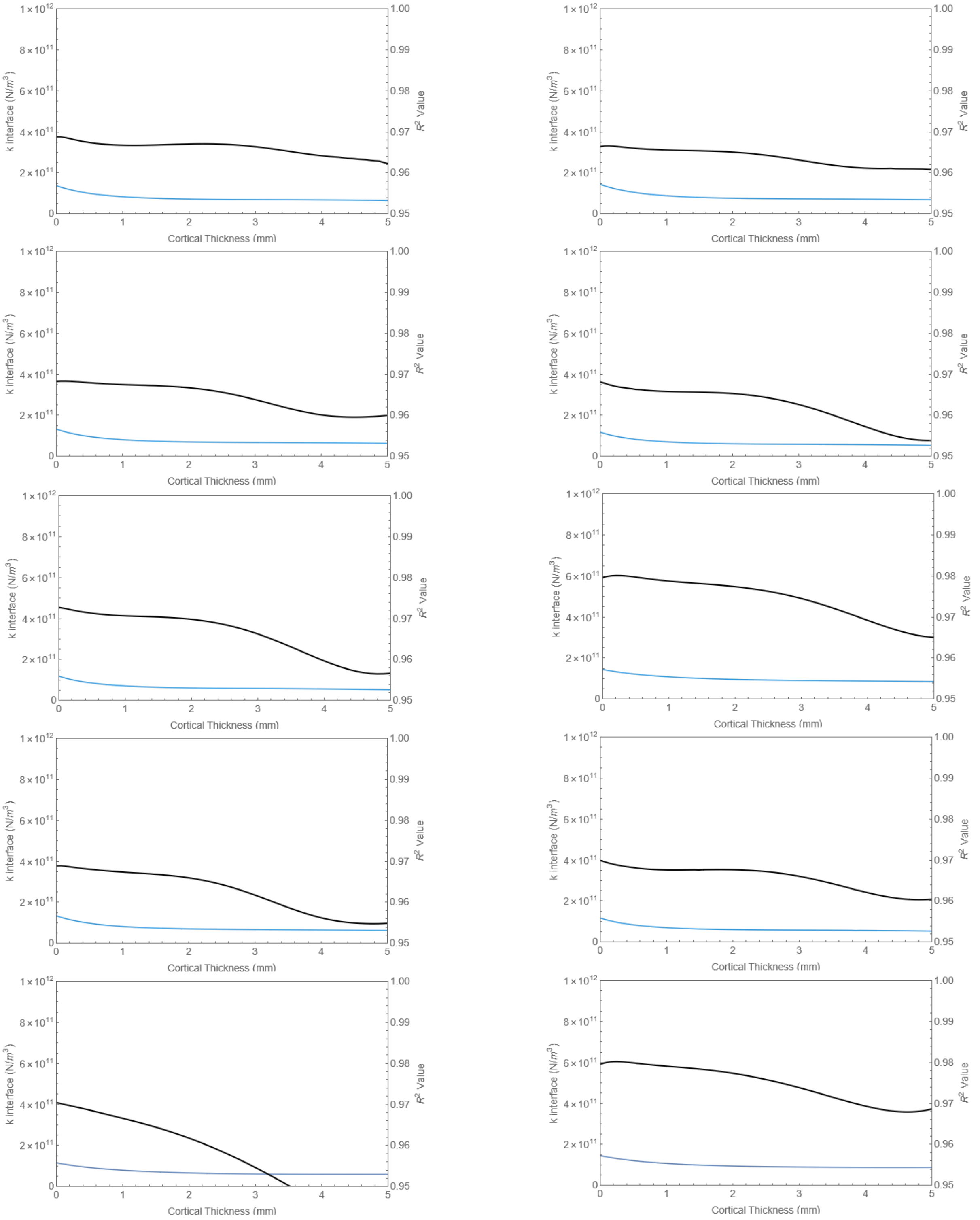

Figure C.4: Analysis of cancellous bone blocks. Interface stiffness per unit area (blue line) and R^2 (black line) values obtained from the matching process by varying L_C between 0 and 3 mm while holding γ fixed at 3.

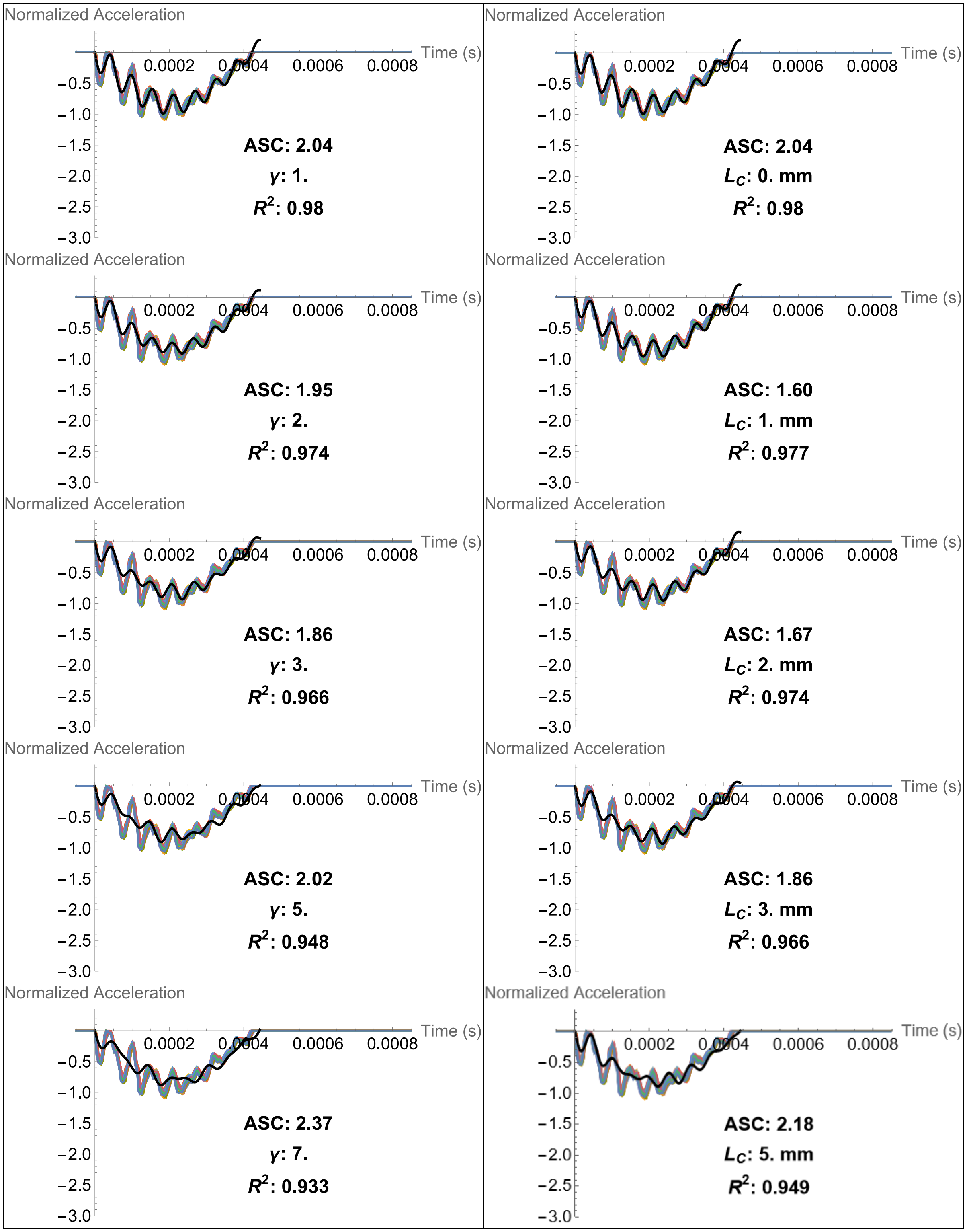

Figure C.5: Fitting of analytical model (black line) to cancellous bone experimental data (coloured lines). ASC and R^2 values are shown for various values of γ while L_C is fixed at 3 mm (left) and various values of L_C while γ is fixed at 3 (right).